

Preclinical MRI in Neurological Diseases

Development of MRI Methods for Non-Invasive Investigation of Experimental Epilepsy

zur Erlangung des akademischen Grades eines
Doktors der Ingenieurwissenschaften (Dr.-Ing.)

von der KIT-Fakultät für Maschinenbau
des Karlsruher Instituts für Technologie (KIT)
angenommene

Dissertation

von

Niels Leonard Schwaderlapp

Tag der mündlichen Prüfung: 21.01.2020

Erster Gutachter: Prof. Dr. Jan G. Korvink

Zweiter Gutachter: Prof. Dr. Dr. h.c. Jürgen Hennig

Autor Niels Leonard Schwaderlapp
niels.schwaderlapp@uniklinik-freiburg.de
Universitätsklinikum Freiburg
Klinik für Radiologie, Medizin Physik
Killianstraße 5a
79106 Freiburg im Breisgau

Gutachter Prof. Dr. Jan G. Korvink
Institut für Mikrostrukturtechnik
Karlsruher Institut für Technologie
Hermann-von-Helmholtz Platz 1
76344 Eggenstein-Leopoldshafen

Prof. Dr. Dr. h.c. Jürgen Hennig
Universitätsklinikum Freiburg
Klinik für Radiologie, Medizin Physik
Killianstraße 5a
79106 Freiburg im Breisgau

Prüfungsvorsitzender Prof. Dr. Frank Gauterin
Institut für Fahrzeugsystemtechnik
Teilinstitut Fahrzeugtechnik
Karlsruher Institut für Technologie
Rintheimer Querallee 2
76131 Karlsruhe

Tag der Disputation 21. Januar .2020



Statement of Authorship

I declare that this thesis has been composed solely by myself and that it has not been submitted, in whole or in part, in any previous application for a degree. All sources have been listed in the bibliography and identified as references. I confirm that the work submitted is my own, except where work which has formed part of a jointly-authored publication has been included. The collaborative contributions have been indicated clearly and acknowledged.

The rules for safeguarding good scientific practice of the KIT Karlsruhe were followed.

Ethical Statement

All institutional and national guidelines for the care and use of laboratory animals were followed.

Data Availability Statement

The acquired data and self-written software used to support the results of this work have been secured at the group of Medical Physics, University Medical Center Freiburg. Requests for access should be made to niels.schwaderlapp@uniklinik-freiburg.de.

Acknowledgement

This work was supported by the German Research Foundation as part of the Cluster of Excellence ‘BrainLinks-BrainTools’ within the framework of the German Excellence Initiative (grant number EXC 1086).

Niels L. Schwaderlapp

Summary

Among the strengths of MRI is its versatility. Among the weaknesses are the somewhat unspecific results as the contrast in MRI is based on water molecules and not for example on cell-specific molecules. For example, MRI is not able to verify epilepsy, because neuronal epileptic activity can only be identified by EEG. Some alterations in epilepsy are however well established, like the increased signal intensity in an epileptic focus, so that MRI has become the method of choice in order to diagnose epilepsy and various neurological disorders in general. Other aspects that can be assessed by MRI, such as the structural and functional connectivity between different brain areas, are so far rather preliminary. Further research is needed to elucidate the exact relation between the underlying pathological changes and the MR measures. Only then could these MR features be used as a clear indication for further patient treatment. Translational research is essential for this task because it bridges the gap between precise, very specific basic research in animal models and clinical studies. Animal models offer the additional benefit that aspects of a disease can be studied that are not accessible in humans but promise to reveal new insights for the treatment of patients. In the context of epilepsy this particularly applies to the process of epileptogenesis and the observation of epileptic seizures by functional MRI. In this work, MRI methods were optimized and developed to study these aspects in a mouse model of temporal lobe epilepsy (TLE).

The experimental work of this thesis comprises three chapters. In the first part, methods were optimized in order to monitor the longitudinal developments during epileptogenesis in the kainate mouse model of TLE. This animal model replicates structural changes like hippocampal sclerosis and granule cell dispersion very similar to changes known in human TLE. These changes were quantified during epileptogenesis by means of T₂-weighted MRI, diffusion MRI and MR spectroscopy of metabolite concentrations. These results were retrospectively validated by EEG and immunohistochemistry. Some of the MR quantities were able to describe the longitudinal development of the epilepsy, such as granule cell dispersion, and may be used as so-called biomarkers to predict the final outcome already at an early time point. Hippocampal specimens, which were resected from epilepsy patients for therapeutic measures, were scanned ex-vivo and showed very similar alterations, which proves that the results from the longitudinal study in the mouse model could be translated to human research.

In the second part, BOLD fMRI was used to investigate epileptic activity and connectivity differences between healthy and epileptic mice. Spontaneous seizures occur too rarely to allow studying them by fMRI. Therefore, epileptic activity was induced by optogenetic stimulation. At first, in order to make such a study feasible, methods were developed to allow optogenetic stimulation during fMRI and provide at the same time

stable physiological conditions of the animal and a high sensitivity of the fMRI scan. The results showed clearly stronger seizure activity in epileptic mice in comparison to healthy controls and these differences could be related to alterations in the resting-state fMRI connectivity.

The third part explored the possibility to detect metabolic activity directly. Metabolite concentrations of glutamate and GABA had been detected in the first part of this thesis and showed alterations in epileptic mice. The meaning of these changes with respect to epileptic activity, however, remains elusive as the BOLD fMRI contrast, as used in the second part to study functional activity, is based on hemodynamic processes and is just an indirect measure of neuronal activity. Thus, CEST MRI was made sensitive to glutamate and changes during epileptic seizures were measured. Epileptic activity in particular is usually associated with an excessive release of the excitatory neurotransmitter glutamate. The insights and methods of the first two chapters thus built the ideal platform to investigate glutamate-based CEST fMRI, which could lead to new discoveries compared to BOLD fMRI.

Zusammenfassung

Zu den Stärken der MRT gehört die Vielseitigkeit der Anwendungen, zu den Schwächen allerdings die teilweise unspezifischen Ergebnisse da der Kontrast in MRT Aufnahmen in der Regel auf Wassermoleküle zurückgeht, und nicht etwa auf zellspezifische Moleküle. Zum Beispiel kann man mit MRT auch keinen tatsächlichen Nachweis für Epilepsie liefern, da neuronale epileptische Aktivität nur mit EEG messbar ist. Einige Veränderungen in Epilepsie sind aber bereits so gut etabliert, wie zum Beispiel eine erhöhte Signalintensität im Fall eines epileptischen Fokus, so dass MRT die Methode der Wahl geworden ist um auch epileptische, oder allgemein neurologische Erkrankungen zu identifizieren. Andere Aspekte, die mit MRT untersucht werden können, wie z.B. die Konnektivität zwischen verschiedenen Gehirnregionen, sind bisher nicht so gut etabliert. Diese müssen weiter erforscht werden mit dem Ziel den genauen Zusammenhang zwischen den grundlegenden pathologischen Veränderungen und den gemessenen MRT Ergebnissen zu kennen, so dass man diese als klare Indikation für die weitere Behandlung einsetzen kann. Hierfür ist die translationale Forschung hilfreich, denn sie schlägt die Brücke zwischen präziser, sehr spezifischer Grundlagenforschung in Tiermodellen und klinischen Studien. Tiermodelle bieten den weiteren Vorteil, dass Aspekte einer Krankheit untersucht werden können, die möglicherweise wesentlich neue Erkenntnisse für die Behandlung einer Krankheit liefern, die aber im Menschen nicht ausreichend untersucht werden können. Bei Epilepsie gehören dazu der Prozess der Epileptogenese und das Beobachten epileptischer Anfälle mittels funktioneller MRT. In dieser Arbeit wurden MRT Methoden optimiert und entwickelt, um diese beiden Punkte in einem Mausmodell für Temporallappen Epilepsie untersuchen zu können.

Der experimentelle Teil dieser Arbeit umfasst drei Kapitel. Im ersten Teil wurden Methoden optimiert, um in einer longitudinalen Studie die Entstehung von chronischer Epilepsie im Mausmodell erkennen zu können. Strukturelle Veränderungen wie hippocampale Sklerose und Körnerzelldispersion werden in dem Mausmodell sehr ähnlich zu bekannten Veränderungen in Epilepsie Patienten repliziert. Mittels T_2 -gewichteter MRT, diffusions-MRT und MR-Spektroskopie wurden diese Prozesse während der Epileptogenese quantifiziert, was im Anschluss durch EEG und Immunohistochemie validiert wurde. Einige der MR Ergebnisse konnten die kontinuierlichen Entwicklungen, z.B. der Körnerzelldispersion, sehr gut beschreiben und können als sogenannte Biomarker eingesetzt werden, um die finalen Veränderungen bereits zu einem frühen Zeitpunkt vorherzusagen. Hippokampale Gewebeproben, die aus therapeutischen Gründen von Epilepsie Patienten entfernt wurden, wurden ex-vivo untersucht und zeigten ähnliche Veränderungen, was zeigt, dass die Ergebnisse aus der longitudinalen Studie im Mausmodell teilweise auf den Menschen übertragbar sind.

Im zweiten Teil wurden mittels BOLD fMRT epileptische Aktivität und Konnektivitätsunterschiede zwischen gesunden und epileptischen Mäusen untersucht. Da spontane Anfälle zu selten auftreten, um sie mit fMRT systematisch untersuchen zu können, wurden mittels optogenetischer Stimulation Anfälle induziert die möglichst ähnliche Erscheinungsformen haben sollen. Damit diese Studie machbar wurde, mussten Methoden entwickelt werden für die optogenetische Stimulation während der fMRT Messungen unter stabilen physiologischen Bedingungen und möglichst guter fMRT Sensitivität. Die Ergebnisse zeigten eine deutlich stärker ausgeprägte Anfallsaktivität in epileptischen Tieren im Vergleich zu den Kontroll-Tieren und diese Unterschiede konnten durch Unterschiede in der Gehirnkonnektivität, die während den Ruhephasen gemessen wurde, erklärt werden.

Im dritten Teil wurde untersucht ob es möglich ist die metabolische Aktivität direkt zu detektieren. Im ersten Teil dieser Arbeit wurden mit MR Spektroskopie Veränderungen in den Neurotransmitter Konzentrationen von Glutamat und GABA in epileptischen Tieren gemessen. Welche Rolle diese Veränderungen allerdings auf die Aktivität während epileptischer Anfälle haben, wie sie im zweiten Teil untersucht wurde, ist unklar, denn der genutzte BOLD fMRT Kontrast basiert lediglich auf hämodynamischen Prozessen und ist nur ein indirektes Maß für Aktivität. Für die Messung von Glutamat wurde die CEST MRT Methode genutzt und damit Veränderungen während epileptischer Anfälle gemessen. Gerade epileptische Anfälle werden üblicherweise mit starker exzitatorischer Aktivität in Verbindung gebracht. Die Erkenntnisse und Methoden der ersten beiden Ergebnissteile schafften so die ideale Plattform, um zu testen ob man Glutamat Metabolismus während einer Aktivität mittels CEST fMRT detektieren kann, was neue Erkenntnisse im Vergleich zu BOLD fMRT bringen könnte.

Table of Contents

Summary	i
Zusammenfassung	iii
Table of Contents.....	v
1 Introduction	1
1.1 Motivation and Objectives.....	1
1.2 Organization and Key Results in Brief.....	3
2 Principles of Magnetic Resonance Imaging	5
2.1 Basics of Signal Formation and Image Encoding	5
2.1.1 Origin of the NMR Signal.....	5
2.1.2 Spatial Encoding by Imaging Gradients.....	7
2.1.3 Signal-to-Noise Ratio and Image Quality	10
2.1.4 MRI sequences: RARE	12
2.1.5 MRI sequences: Echo Planar Imaging	14
2.2 Contrast for Neurological MRI Applications	15
2.2.1 Diffusion MRI.....	15
2.2.2 In-vivo ¹ H-NMR Spectroscopy	22
2.2.3 Functional MRI	24
2.2.4 Chemical Exchange Saturation Transfer (CEST)	30
3 Neuroscientific Fields for MRI.....	33
3.1 Epilepsy	33
3.1.1 About Epilepsy.....	33
3.1.2 Animal Models in Epilepsy Research	34
3.1.3 Temporal Lobe Epilepsy and the Kainate Model.....	35
3.2 Optogenetics	37
3.2.1 Basic Principles.....	37
3.2.2 Optogenetics in Epilepsy Research	39
4 Using High-Resolution Diffusion MRI and ¹H-MRS to Monitor Epileptogenesis	41
4.1 Introduction	41
4.2 Monitoring of Epileptogenesis by MRI and MRS – State of the Art.....	42
4.3 Methods	44
4.3.1 Experimental Design.....	44
4.3.2 Preclinical in-vivo MR measurements	45
4.3.3 Ex-vivo MRI of human hippocampal tissue	55
4.4 Results	56
4.4.1 Histochemical and Electrophysiological Characterization of Animals.....	56
4.4.2 T ₂ -weighted MRI and ¹ H MRS: Early Quantification of Sclerosis.....	57
4.4.3 Diffusion MRI: Development of Granule Cell Dispersion (GCD).....	62
4.4.4 Diffusion MRI in Ex-Vivo Human Tissue: Validation of GCD	66
4.4.5 Combination of MR Modalities	68
4.5 Discussion.....	69
4.6 Conclusions and Outlook.....	70

5	Optogenetic fMRI	73
5.1	Introduction.....	73
5.2	State of the Art.....	73
5.3	Methods.....	75
5.3.1	Optogenetic Setup.....	75
5.3.2	fMRI Setup and Acquisition.....	77
5.3.3	Mouse Brain Atlas	80
5.4	Results I: Methodological Characterization.....	81
5.4.1	Side Effects in ofMRI: Visual Stimulation and Thermal Effects.....	81
5.4.2	Optogenetic-fMRI Block Design.....	82
5.4.3	Resting State fMRI	84
5.4.4	Sliding Window Analysis of Resting State fMRI.....	87
5.4.5	Comparison of Single-Echo and Multi-Echo fMRI.....	90
5.4.6	Dynamic fMRI Response of Epileptic Seizures	91
5.5	Results II: Epileptic networks	92
5.5.1	fMRI during Optogenetically-Induced Epileptiform Activity.....	92
5.5.2	Resting State fMRI Connectivity Changes.....	98
5.5.3	Epileptic Networks and Seizure Propagation	106
5.6	Discussion	110
5.7	Conclusions and Outlook	113
6	CEST fMRI.....	115
6.1	Introduction.....	115
6.2	Glutamate CEST fMRI - Hypothesis.....	116
6.3	Methods.....	118
6.4	Results I – Establishment of GluCEST MRI	119
6.4.1	Proof-of-Principle	119
6.4.2	Optimization of sensitivity	120
6.4.3	In-vivo validation: Reduction of Glu after KA-induced status epilepticus	121
6.5	Results II – GluCEST fMRI.....	123
6.5.1	GluCEST response during induced epileptic seizures in naïve mice	123
6.5.2	GluCEST response during continuous stimulation in naïve mice.....	126
6.5.3	GluCEST response in epileptic mice.....	127
6.6	Discussion.....	127
6.7	Conclusions and Outlook	128
7	Concluding remarks	129
	Bibliography	131
	List of Figures	145
	List of Tables	147
	List of Abbreviations	148
	Danksagung	153

1 Introduction

1.1 Motivation and Objectives

Hundreds of millions of people worldwide are affected by some form of a neurological disorder (WHO, 2019a). Among the most prevalent disorders are epilepsy, Alzheimer's disease or other dementias, Parkinson's disease, multiple sclerosis and depression. Around 50 million people worldwide are affected by epilepsy, whereby nearly 80% of them live in low- and middle-income countries where they do not receive appropriate medical care. Especially in these regions, providing access for every person to cost-effective, anti-seizure medicines would reduce the burden of epilepsy. The majority (up to 70%) of epilepsy patients can become seizure-free with anti-epileptic drugs (AEDs). However, even in high-income countries, the use of AEDs has limitations; AEDs may produce side-effects and because they only treat the symptoms they may have to be taken for an indefinite time. In cases of focal epilepsies, which are particularly often refractory to AEDs, surgical removal of the seizure focus may be a true cure. However, this is only pursued if the expected improvements after surgery surpass the possible negative consequences due to the highly invasive operation. In recent years, electrical stimulation of brain regions to interfere with neurological diseases has been explored (Miocinovic et al., 2013). As a prerequisite to consider electrical brain stimulation, the long-term reliability of the stimulation devices and electrodes must be investigated and ensured for safe applications (Coffey, 2009). Deep brain stimulation (DBS) did show positive effects for example in depression (Mayberg et al., 2005) and Parkinson's disease (Krack et al., 2003; Deuschl et al., 2006). However, the effectiveness and fundamental functionality of DBS has to be investigated further (Lozano et al., 2019).

A precise analysis of the abnormal alterations in diseases is thus not only required for an accurate diagnosis but also needed to improve the treatment approaches. Non-invasive evaluation in humans is routinely performed by EEG and MRI. In the context of epilepsy for example, an epileptic focus reveals increased MRI signal intensity in T₂-weighted images, altered water diffusivities in diffusion MRI maps and altered metabolite concentrations as detected by MR spectroscopy (see section 4.2). Alterations of brain connectivity in focal epilepsy have been assessed by diffusion MRI, functional MRI and EEG (Parker et al., 2017; Englot et al., 2016; van Mierlo et al., 2014). Spontaneous epileptic seizures can be studied by EEG. However, due to the limited time of an MRI session, only resting-state patterns and interictal events can be studied by fMRI in the large majority of cases. There are also further restrictions in the study of neurological diseases in humans. Many disorders are acquired and develop over time. However, at the time point affected people seek treatment, the disorder has already been established. Prospective studies, including the time before the disease onset and the later longitudi-

nal developments, are limited to heterogeneous and/or small patient cohorts and have to span years or even decades. Furthermore, patient treatment is only allowed according to medical indications. Systematic experiments, which are needed to drive the methodological advancements, are not possible in humans.

Animal models offer the possibility to study aspects of a disease that cannot be studied in humans. For example, the initial onset of a disease in humans is in general not known. In animal models however, the disease is induced at a particular time point which allows the investigation of early developments. In this work, preclinical MRI is used to explore the kainate mouse model of mesial temporal lobe epilepsy, as one example of a neurological disorder. Preclinical MR methods are developed to characterize the structural-, metabolic- and functional-alterations at different time scales. The term “epileptogenesis” refers to the development of fundamental, permanent changes that eventually manifest the chronic state of epilepsy. These changes are however triggered at an earlier time point. The first objective of this work is to exploit various MR contrasts and identify which biological alterations during epileptogenesis can be detected by current state of the art MRI/MRS. The MR results are validated by histochemistry and EEG with the aim to provide biomarkers that allow the prediction of the developments already at an early time point before the state of chronic epilepsy is established.

In the future, such biomarkers for epilepsy may be used to start medication in order to prevent the development of chronic epilepsy in the first place. This would be the ideal therapy but is currently not possible. The alternative is to interfere with the immediate consequences of the disease during the chronic state. If for example, the severity of epileptic seizures could be alleviated or the seizures even suppressed, this would represent a major improvement in the treatment of patients. It is assumed that structural abnormalities in epilepsy promote spontaneous epileptic activity and differences in functional connectivity may indicate possible targets for interference. For this, it is important to understand how these areas are involved during the propagation of epileptic activity across the brain. Seizures in humans can only be studied using EEG with high temporal, but low spatial resolution. fMRI during epileptic seizures is not usually possible in humans but would be extremely helpful to better describe the spread of activity and identify possible hub regions that can be targeted by stimulation. Therefore, the second objective of this work is to employ optogenetic stimulation to induce epileptic activity in mice and analyze these seizures by fMRI. Furthermore, resting-state fMRI is used to relate different seizure patterns in healthy and epileptic mice to corresponding functional connectivity differences.

This thesis lays the foundation for upcoming work on disease interference by e.g. optogenetic inhibition. By applying the developed methods, the effect of the interventions can be characterized with the aim to identify new targets for treatments.

1.2 Organization and Key Results in Brief

All necessary background information is described in chapters 2 and 3. They include the principles of MRI and information about epilepsy in general, animal models in epilepsy research and basics about optogenetics, which is a technique used to induce neuronal activity. The chapters 4 to 6 present the experimental work of this thesis.

Chapter 4 demonstrates the possibility to use MR measurements (T_2 , DTI and MRS) to track the developments during epileptogenesis (figure 1.1). MRI/MRS was able to quantify the progress of known alterations in epilepsy, like hippocampal sclerosis and granule cell dispersion, which was retrospectively validated by EEG and histochemistry. Epileptogenesis may span a decade in humans and is thus not immediately detectable. However, evaluating resected tissue from patients with different levels of epilepsy severity showed similar alterations. In the future, the process of epileptogenesis may thus also be detectable and predictable in humans. These results were published in (Janz et al., 2017) and additionally covered by an insight article (Gröhn and Sierra, 2017).

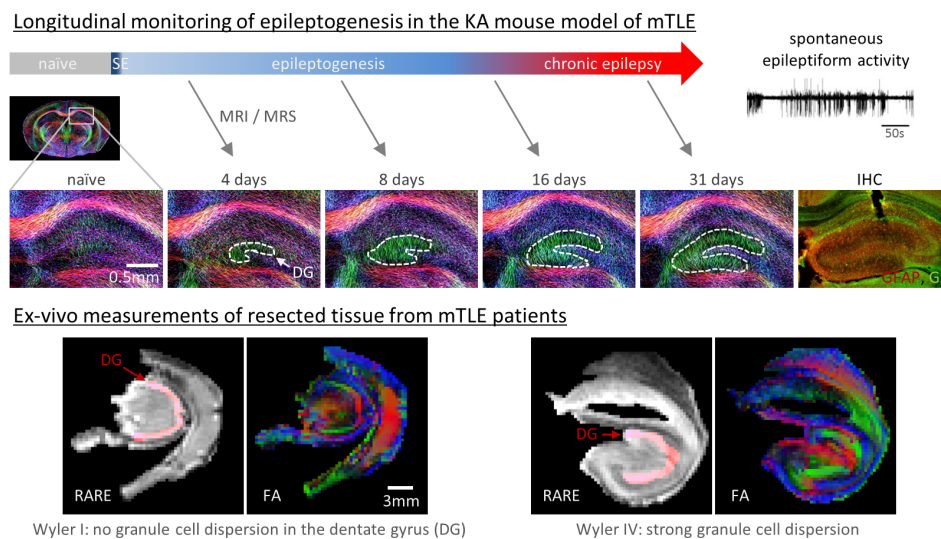


Figure 1.1: Longitudinal study of experimental epilepsy and ex-vivo analysis of resected tissue from epilepsy patients. Top) Kainate injection into the right septal hippocampus provoked a status epilepticus (SE). After a silent period of 1-2 weeks, these mice developed chronic epilepsy where spontaneous seizures occurred. MRI/MRS was performed at several time points to cover the development of the pathology. **Bottom)** Resected hippocampal specimens graded in different Wyler scores show radially oriented diffusion in the DG and differently dispersed granule cell layers in the DG, which is very similar to the mouse model.

Chapter 5 focuses on functional aspects assessed by BOLD fMRI. Optogenetic stimulation is used to induce neuronal activity in animals. This allows using fMRI to describe the propagation of activity during epileptic seizures. For the first time, this is done not only in healthy but also in epileptic mice. Differences between the animal groups in seizure spread and resting-state connectivity point to regions critically involved in epilepsy.

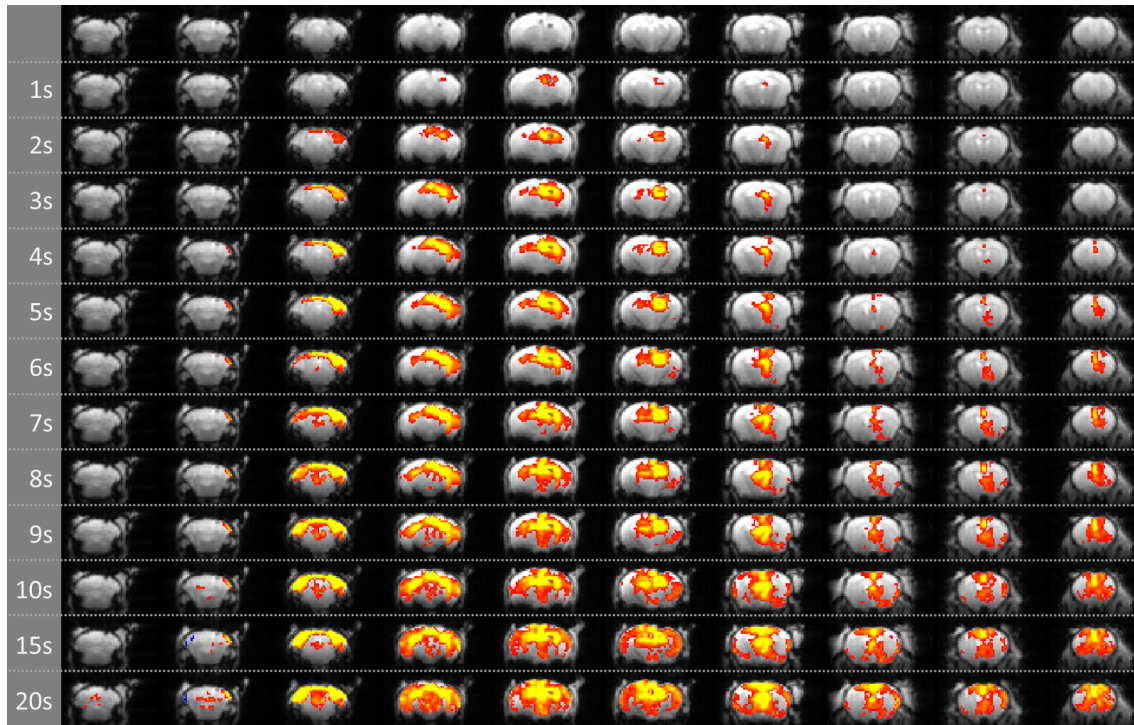


Figure 1.2: fMRI shows the propagation of an optogenetically induced seizure in an epileptic mouse. Left column) Time after stimulation onset. Rows) Brain slices along the rostral-caudal direction (positive fMRI response in red-yellow).

Chapter 6 indicates the possibility to detect glutamate metabolism during induced activity. The concentration of the excitatory neurotransmitter glutamate is altered in epileptic mice (measured in chapter 4), however there is currently no way to relate the BOLD fMRI results in chapter 5 to neurotransmitter activity. Therefore, CEST fMRI was used to explore the feasibility of concurrently detecting BOLD and glutamate changes directly.

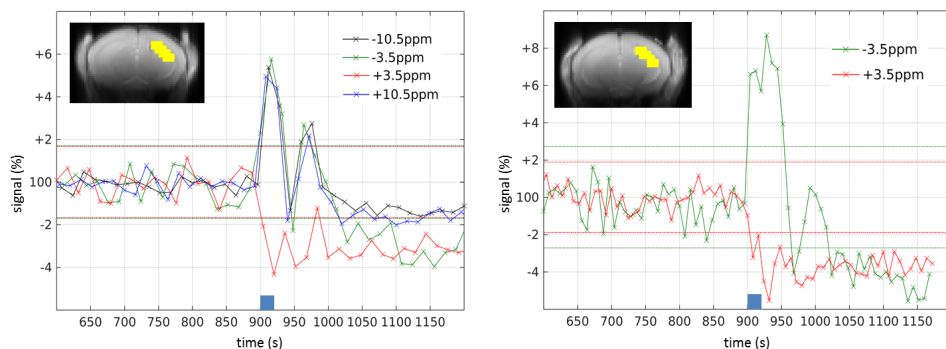


Figure 1.3: CEST fMRI response during optogenetically induced epileptic seizures. The different time courses represent different saturation pulse offsets. Glutamate CEST fMRI effects are frequency specific and can only be visible at +3.5ppm, whereas the other time courses show only BOLD (two experiments sampled with 4 (figure left) and 2 (figure right) saturation frequencies, respectively).

2 Principles of Magnetic Resonance Imaging

2.1 Basics of Signal Formation and Image Encoding

The discovery of the principles of magnetic resonance and the further development into a routine device for imaging began at the end of the 20th century. Some pioneers of the field were rewarded with the Nobel Prize like Isidor Rabi in physics in 1944, Felix Bloch and Edward Purcell in physics in 1952, and Paul Lauterbur and Sir Peter Mansfield in physiology or medicine in 2003. The principles of MRI may not be as straightforward as alternative imaging techniques. In X-ray for comparison, radiation is directed from a source towards the object and absorption by the object yields a direct negative image on a plane behind the object. MRI is fundamentally different.

The first two sections in this chapter explain how the MR signal is created and how the spatial information is encoded into the signal in order to achieve an image of the object. Subsequently, general points on the image quality and the two MRI sequences RARE and EPI are explained. These sequences were developed during the 1980s and paved the way for rapid imaging. Even though there are faster alternatives nowadays, they are fundamental and still among the most frequently used sequences in MRI.

2.1.1 Origin of the NMR Signal

The signal for all magnetic resonance methods employed in this work originates from the hydrogen (¹H) nuclei. By a fortunate coincidence of nature, ¹H is the most sensitive nucleus for MRI, has a natural abundance of close to 100% and is present in the water throughout the human body in high concentrations. Hydrogen consists of one electron in the shell and a single proton as nucleus.

The behavior of a particle – like an electron or proton – can, in addition to the more well-known properties like mass, electrical charge and magnetism, be described by its spin. The spin refers to a kind of angular momentum, which is however an intrinsic property and does not result from motion. The spin of the proton nucleus can be illustrated by a vector; the axis and the direction of the vector indicate the axis of the angular momentum and the magnetic moment, respectively. In the absence of a magnetic field, the vector may point in any direction in space and an ensemble of many spins shows an isotropic distribution leading to a total net magnetization of zero. When placed in a

magnetic field B_0 , the spins precess around B_0 with a characteristic frequency, the so-called Larmor frequency ω_0 :

$$\omega_0 = \gamma B_0 \quad (2.1)$$

The gyromagnetic ratio γ is a constant specific to each particle ($\gamma_{1H} \approx 42.6 \text{ MHz/T}$). The spins precess on cones with arbitrary but constant angles depending on the initial polarization (Hanson, 2008; Levitt, 2008). The motion of the molecules and the influence of the microscopic field fluctuations provoke small changes of the precession angles. A magnetic moment in general tends to align parallel to a magnetic field so as to minimize the potential energy. A preferred direction therefore exists when the precession angle is altered. This leads over time to an anisotropic distribution and a net-magnetization in the B_0 direction. The time constant describing the formation of the magnetization is referred to as longitudinal or spin-lattice relaxation and is denoted by T_1 .

The precession angle of the spins can be rotated by applying an oscillating magnetic field perpendicular to B_0 , which is called excitation of the spins. The degree of the rotation depends on the duration and amplitude (B_1) of the excitation pulse and is called flip angle. An appropriate excitation pulse may cause a flip angle of 90° and as all of the spins are equally affected, the total magnetization is rotated from the longitudinal direction into the transverse plane. After the excitation pulse is turned off, the spins – and thereby also the net-magnetization – precess again around B_0 . The individual spins are losing their phase coherence during the precession because of microscopic magnetic field fluctuations. This dephasing leads to a decay of the net-magnetization. The time constant describing the irreversible decay of the transversal magnetization is referred to as spin-spin relaxation and is denoted by T_2 . Microscopic magnetic field fluctuations are caused by interactions at the molecular level and therefore they induce a random and irreversible dephasing. Macroscopic field inhomogeneities induce an even faster dephasing, which is described by the relaxation constant T_2^* . However, these perturbations are stationary and the thereby caused dephasing is reversible.

The precession of magnetization perpendicular to B_0 can induce a detectable voltage in a nearby coil. As the first person who detected the magnetic resonance phenomenon in this manner, Felix Bloch introduced the relaxation time constants and developed equations describing the components of the magnetization during their return to equilibrium (Bloch, 1946; Bloch et al., 1946). The signal after a single pulse oscillates at the frequency ω_0 and decays with T_2^* . This form of the signal is called free induction decay (FID). A subsequent second pulse, which may have a flip angle of 180° , inverts the phase evolution. The dephasing components are thereby refocused and create a spin echo (Hahn, 1950). The de- and rephasing can also be enforced by gradients (which are described in the next section). This produces so-called gradient (-recalled) echoes, which are under the envelope of the T_2^* decay (Figure 2.1).

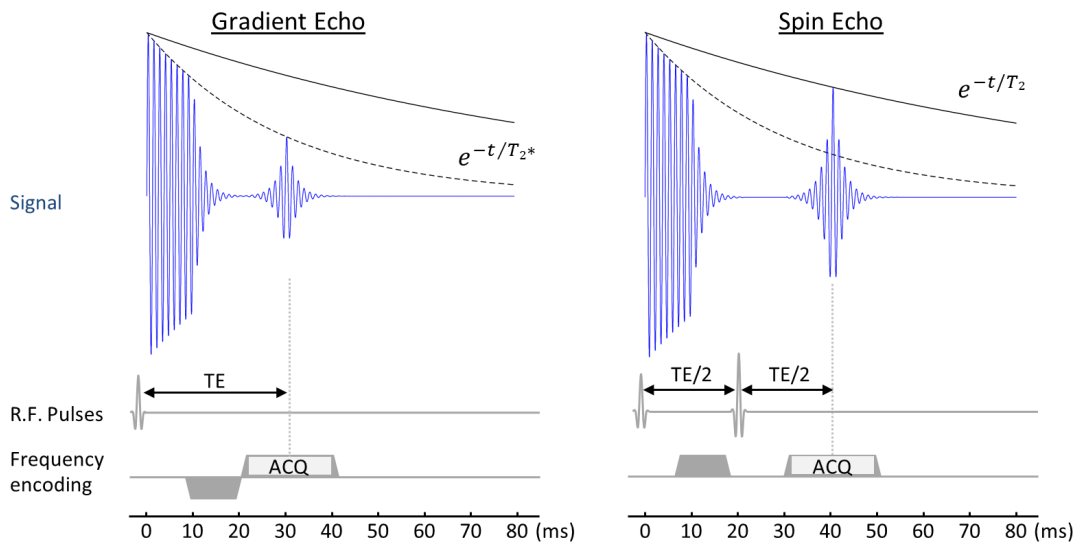


Figure 2.1: Signal evolution for Gradient and Spin Echoes. Gradient Echo formation, left) The signal (blue line) after the r.f. excitation pulse decays under the envelope of T_2^* as indicated by the black dashed line. The first gradient (labeled “frequency encoding”) induces a fast dephasing and the subsequent gradient with opposite polarity leads to a rephasing and the occurrence of an echo signal after the echo time (TE). **Spin Echo formation, right)** The phase evolution is refocused by an r.f. pulse. In that case dephasing due to static magnetic field inhomogeneities is also refocused and the echo is formed under the envelope of T_2 decay (black solid line). ACQ = Acquisition. (Figure inspired by www.mriquestions.com/gradient-echo.html (Elster, 2019)).

2.1.2 Spatial Encoding by Imaging Gradients

The previous section illustrated how a net-magnetization is created in the static magnetic field and that, after excitation by a pulse, the precession of the magnetization leads to a detectable NMR signal. The receiver coil thereby accumulates all signal sources in its sensitive volume. This section describes how magnetic field gradients are used to encode spatial information in the MR signal in order to allow the reconstruction of an image. Basic principles are the selection of a slice and frequency- and phase-encoding to resolve the in-plane information. The fundamental basis of MRI is the direct relation between the acquired gradient-encoded signal and the spatial frequencies of the image. This is the concept of the so-called “k-space” from which the image of the object can be reconstructed.

MRI systems employ sets of coils to create magnetic field gradients along the x-, y, and z-directions, where z refers to the direction along the static magnetic field B_0 . The magnetic field of each of these gradients is directed along the z-direction, but the amplitude of this z-component varies linearly along each respective direction. If such a gradient is turned on, the gradient field adds to the B_0 field yielding a local variation of the resonance condition which depends on the position along the gradient. The gradients are centered on the isocenter, adding on one side to the magnetic field and subtracting on the other, respectively.

In a 2D MRI experiment, a unique slice is selected by applying a gradient perpendicular to the desired slice orientation and simultaneously applying a frequency-selective r.f. pulse for excitation of that slice. If the bandwidth and shape of the excitation pulse is kept constant, then the thickness of the slice is determined by the gradient strength. The available signal originates from this single slice. In order to obtain an image, the signals within the plane then have to be resolved, which is described in the following.

Let us consider spins along the x-axis and assume a gradient in this direction is applied during signal acquisition. This is referred to as frequency encoding and read-out of the signal. At the onset of the gradient all spins precess with equal frequencies and are in-phase. The gradient imposes a linear frequency variation along the gradient-direction and with that a change in the phases. After a time t , the spins at position x have accumulated a phase difference proportional to the gradient field $G(x)$ times t . The distance between spins that have accumulated a phase difference of 2π , and hence are in-phase again, is denoted by the wavelength λ . The reciprocal of the wavelength is the wave-number $k=1/\lambda$, which describes a wave by the number of cycles per unit distance. The phase differences evolve with the time during which the gradient is applied and hence the wavelength λ gets shorter and k increases. The signal acquired over time is therefore proportional to spatial frequencies k (Figure 2.2). The mathematical tool to convert time domain signals into their frequency components is the Fourier transform. As the digitized MR signal already represents the Fourier transform of the imaged object, an inverse Fourier transform will yield the image (in one dimension).

The information in the second dimension is obtained by phase encoding. Prior to the read-out in x-direction, a gradient is temporarily applied in the y-direction. After the gradient is turned off, the spins return to their original precession frequency but the acquired phase differences persist. A single phase-encoding step doesn't permit to resolve the spatial information as only the average signal in the y-direction is detected. Phase encoding thus employs multiple measurements with a variation of the gradient strength. The amount of the phase shifts depends on the local gradient strength; the stronger the gradient and the local field the faster the change of the phases. The rate of the change of the phase is related to a frequency that can be identified by a Fourier transform. After acquiring many phase encoding steps, a (second) Fourier transform in the y-direction yields the spin distribution along the y-direction.

In a 2D imaging experiment, the spatial frequencies of the object are represented in the so-called k-space (Figure 2.3), which contains the raw digitized MR signals. The rows of the k-space are filled with the signal during the read-out, showing the strongest signal at the position of the echo (most often at the center). Each line corresponds to a different phase encoding step. The strength of the phase encoding gradient, and with that the signal reduction caused by the gradient-induced dephasing, increases towards the top and bottom of k-space. A 2D Fourier transform reconstructs the image from the k-space.

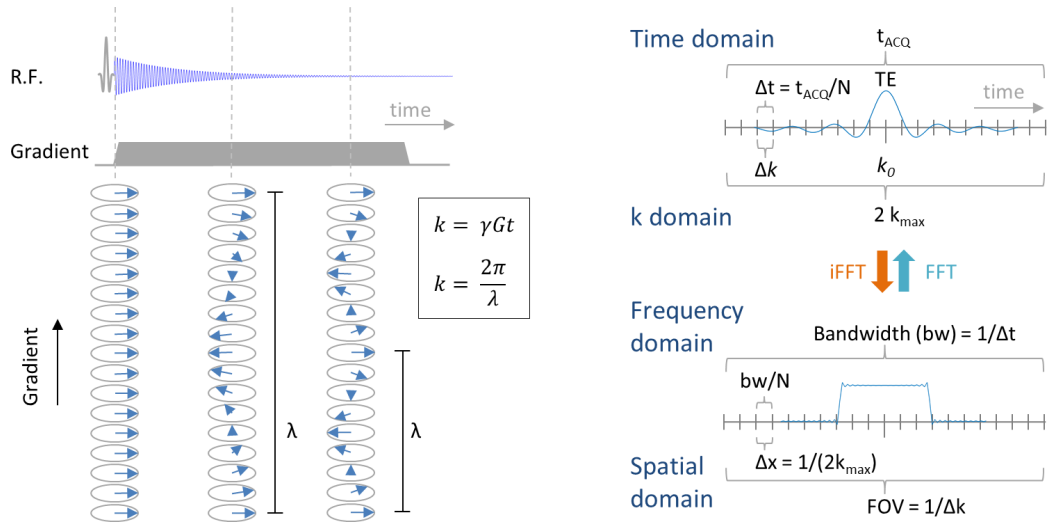


Figure 2.2: Spatial Encoding by Gradients. Left) Spins are aligned in the direction in which the read-out gradient is applied and they are in-phase at the onset of the gradient. The individual spins gain a relative phase advance proportional to the gradient strength $G(x)$ and time t . Therefore, higher spatial frequencies k are sampled with increasing time (adapted from (Callaghan, 2009)). Right) Relations between time and frequency domain. Abbreviations: Acquisition time t_{ACQ} , number of sampling points N , ACQ dwell time Δt (adapted from a presentation by J. Hennig, 2017).

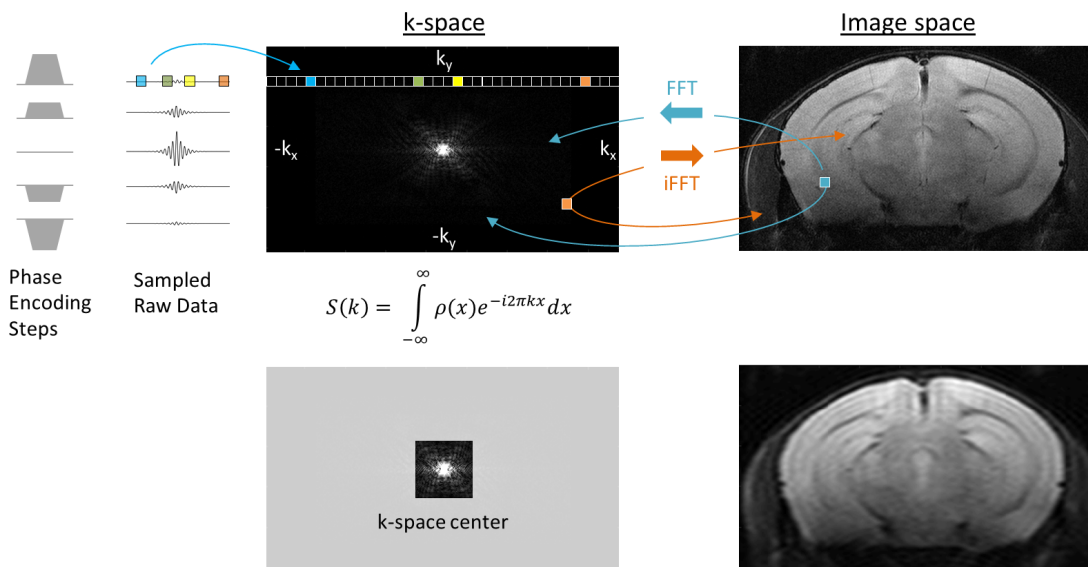


Figure 2.3: Relation between k-space and image space. Each k-space row corresponds to the echo signal S acquired during the application of the read-out gradient and different rows correspond to different previously applied phase encoding gradients strengths. The signal S is the Fourier transform of the spin density distribution $\rho(x)$. The single pixels in the k-space do not correspond to single pixels in the image. Because spatial frequencies are acquired, any pixel in k-space holds information about every pixel in image space and vice versa. Taking only the center of k-space, containing the high intensity but low frequency signals, results in an image with low resolution. This cut off also shows the enhanced so-called truncation, ringing or Gibbs artefact which is a result of the truncation of the Fourier series. (Figure inspired by www.mriquestions.com/data-for-k-space.html (Elster, 2019)).

2.1.3 Signal-to-Noise Ratio and Image Quality

The available signal for imaging is the voltage induced in the receiving coil. This is based on the macroscopic magnetization M , which is proportional to the number of nuclei in the sample (N), their gyromagnetic ratio (γ), the inverse of the temperature (T) of the sample and the magnetic field strength (B_0):

$$M \sim \frac{N\gamma^2}{T} B_0 \quad (2.2)$$

For in-vivo imaging the sample is given and the temperature is fixed. Only B_0 can – within certain limits – be freely chosen. Nowadays, human brain imaging is often performed at 3 T or (if available) 7 T. Most preclinical MRI systems are in the range of 7 to 15 T. The employed sequence and acquisition parameters (TR, TE, b-value ...) of course determine how efficient the available signal is used. But the decisive factor in MRI is the ratio of the induced signal voltage to the received noise voltage or signal-to-noise ratio (SNR). The noise voltage V_{Noise} may be expressed by:

$$V_{Noise} \sim \sqrt{T_R R \Delta\nu} \quad (2.3)$$

where T_R denotes the temperature of the noise resistance and $\Delta\nu$ the acquisition bandwidth. The resistance R sums up all loss mechanisms (Haase et al., 2000). As can be seen from the above, increasing the resolution, and thereby reducing N within each voxel, leads to a direct proportional reduction in SNR. Averaging the signal from many repetitions increases the SNR but only with the square root of the number of averages and hence is a very time-consuming method. A more efficient approach is to use an optimized probe head.

The probe head consists of the coil and the preamplifier. The (loaded) coil has to be tuned to the resonance frequency and matched to the impedance of the transmitter to avoid power reflection during transmission/reception. In order to assess the performance of the coil the principle of reciprocity was established. It states that the field strength B_1 produced by the current I during transmission is equivalent to the sensitivity of the coil during detection. Therefore, the coil has to produce the largest possible B_1 field in the sample at a given transmission power. This is achieved by a high filling factor, for which the coil geometry has to be optimally adapted to the volume-of-interest. A second quantitative factor – the quality factor – encompasses all loss mechanism during transmission, which is related to noise during reception: the ohmic resistance of the wires and losses in the sample due to the magnetic and electrical coupling. In MRI of small samples, like in preclinical MRI and MR microscopy, the thermal noise of the resistances is the dominant loss mechanism. In this case, reducing the temperature is an effective means to increase the SNR. The CryoProbe employed in this work uses a closed cycle helium cooler to reduce the temperature of the coil and preamplifier to $\approx 20-77$ K, which

can increase the SNR by a factor of 2-5 (according to Bruker, Germany). A further increase in SNR is achieved by using two orthogonal coils in quadrature mode. The second coil detects the same MR signal shifted by 90° . The noise in the two channels is uncorrelated, combining the two channels therefore increases the SNR by a factor of $\sqrt{2}$ compared to a single coil.

A good image quality is characterized by a high SNR and also by the absence of severe artifacts (Figure 2.4). Among the many possible origins of MR artifacts a few of them are addressed here. First, motion during the acquisition reduces the image quality. Periodic motion like respiration may lead to discrete artifacts. Non-periodic motion reduces the overall SNR depending on the amplitude of the motion. Because the acquisition time in the frequency encoding direction is significantly shorter than in the phase encoding direction, artifacts are often more pronounced in the latter direction. The best strategy in preclinical MRI to reduce motion artifacts is first to minimize the motion by anesthesia and fixation, and in addition to trigger the image acquisition to the detected respiratory cycle. A related artifact is the Nyquist $N/2$ ghost in EPI. Phase errors between different lines in k-space create ghosts of the image shifted in the phase encoding direction. Causes can be motion, poor shimming or eddy currents. The effect of eddy currents may be reduced by avoiding oblique slices because these require all three gradient directions. Improving the magnetic field homogeneity by shimming reduces many problems, but susceptibility artifacts cannot always be avoided. Inserting electrodes/implants into the brain, as described in chapter 5, causes local field distortions and signal loss due to T_2^* -dephasing. This can be alleviated by improving the shim as much as possible, choosing less sensitive sequences (spin-echo instead of gradient-echo) and adapting the material of the electrodes in order to reduce the susceptibility difference to the tissue.

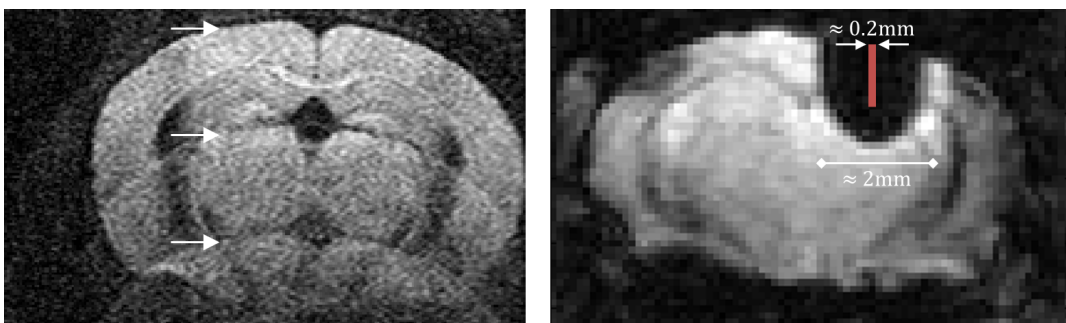


Figure 2.4: Image Artifacts. **Left)** Motion artifact in a segmented acquisition of a diffusion-weighted spin echo EPI. K-space was filled in three repetitions whereby each EPI train acquired every third k-space line. Phase differences between the three segments led to ghost images shifted in the phase direction by $FOV/3$. **Right)** The gradient echo EPI of a mouse brain with an inserted platinum electrode (red) shows significant signal dropout around the electrode.

2.1.4 MRI sequences: RARE

Rapid acquisition with relaxation enhancement (RARE) is an imaging sequence that uses a train of spin echoes in order to accelerate the imaging time (Hennig et al., 1986). After a 90° r.f. excitation, multiple $\leq 180^\circ$ refocusing pulses produce spin echoes that are each encoded differently. Thus, multiple k-space lines can be filled upon a single excitation which reduces the necessary number of repetitions and thereby the total acquisition time. The sequence is illustrated in figure 2.5.

In the case of the acquisition of a single spin echo, assuming a receiver bandwidth (BW) of 32 kHz and 256 points (N) in the read direction are sampled, then the sampling time t_{ACQ} for one echo is 8 ms ($t_{ACQ} = N/BW$) (Bernstein et al., 2004). However, for sequences that employ spin echoes it is the T_2 relaxation that indicates the time during which the transverse magnetization is available for imaging and this is in the order of 100 ms. Thus, utilizing only one echo in each TR interval leaves most of the time unused. It is more efficient to employ an echo train, which is possible as long as no substantial T_2 decay occurs. The number of echoes in each TR interval determines the echo train length (ETL) and the acceleration or RARE factor, which is typically in the order 4-16.

Because each echo in the train is used for a different phase encoding step, all gradient effects have to be compensated within one echo cycle. Before the first refocusing pulse, a prephasing gradient centers the echo of the first acquisition. In each echo cycle, a phase encoding gradient is applied before the read-out and a converse phase rewinding gradient is applied directly after it. The refocusing pulses lead to identical readout directions in k-space. All r.f. pulses, at least partially, rotate the magnetization and reverse the phase evolution. Therefore, many signals arise in an echo train. The goal of RARE is to eliminate disturbing signals and use only the (primary and stimulated) echoes that have the same phase. This is achieved by evenly positioned pulses; the echo spacing (ESP) is constant and twice as long as the time between the excitation and the first refocusing pulse. Crusher gradients surrounding the refocusing pulses destroy unwanted signals.

The repetition time is in the order of seconds which is much longer than the ETL. In a 2D experiment different slices can therefore be acquired during this wait time. A Fourier transform can be applied to reconstruct the image from the rectilinear k-space.

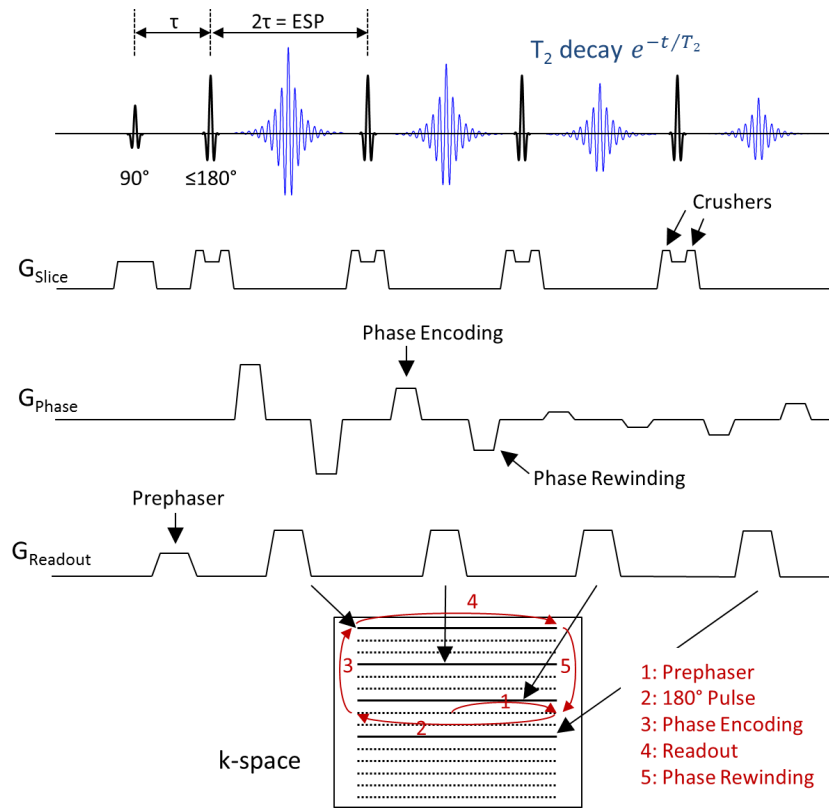


Figure 2.5: RARE (adapted from Bernstein et al., 2004)

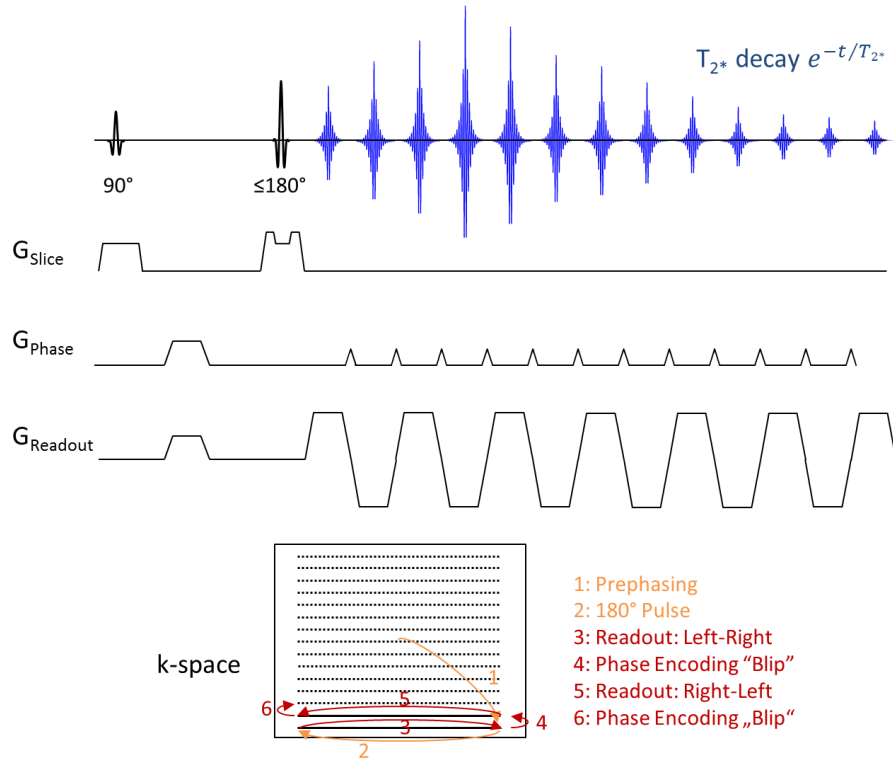


Figure 2.6: EPI (adapted from Bernstein et al., 2004)

2.1.5 MRI sequences: Echo Planar Imaging

Echo planar imaging (EPI) refers to imaging sequences that employ a characteristic gradient echo train for a fast read-out (Mansfield, 1977). The principle is similar to RARE with the difference that gradient echoes are encoded instead of spin echoes. But just as in RARE, each echo in the train is differently encoded in order to sample multiple k-space lines upon a single excitation. The same notations for the echo train length (ETL) and echo spacing (ESP) can be used for EPI. Also, the number of echoes in the ETL is directly related to the acceleration and reduction of the scan time.

The sequence is illustrated in figure 2.6. The slice selection and signal generation can be realized by a conventional r.f. spin echo or gradient echo. A prephasing gradient determines the initial position in k-space. This gradient can be placed before the refocusing pulse in a spin echo preparation in order to save time before the read-out. The polarity of the gradient has to be reversed in this case to counteract the phase reversal by the r.f. pulse. During the readout, a series of gradient echoes is produced. The second half of each gradient acts as prephaser for the following. The polarity of successive gradients therefore has to alternate – the readout gradient oscillates throughout the echo train. For the phase encoding, short so-called blips are applied before each gradient cycle to allow different k-space lines to be sampled. The effect of these blips, which have usually the same polarity and area, accumulates during the ETL. Unlike in RARE, there is no need for a phase rewinder. The lines in k-space are sampled with an alternating direction because the readout gradient alternates its polarity from echo to echo. Every second line therefore has to be flipped along the readout direction before the reconstruction. This row flipping might enhance phase difference between lines in k-space leading to ghost artifacts. This can be corrected using a reference scan. There, no phase encoding is applied and thus all echoes should be in-phase. Any detected phase inconsistency can be used to correct the phase errors in the actual scan.

With RARE, echoes can be generated and encoded until significant T_2 decay occurs, whereas EPI is subject to the faster T_2^* decay. However, gradient echoes can be generated with a much faster rate than spin echoes. Compared to RARE with an ESP of 10-20 ms, the ESP in EPI of less than 1 ms allows a much longer ETL. Imaging matrices of 64-96 may be sampled with a single excitation. Wide receiver bandwidth (100-300 kHz) are used to minimize the sampling time for a single echo ($t_{ACQ} = N/BW$) and to maximize the ETL.

2.2 Contrast for Neurological MRI Applications

The contrast in routine MR images, for example the contrast between gray and white matter in the brain, depends on the relaxation parameters T_1 and T_2 of the tissue. Images based on T_1 and T_2 contrast allow identifying brain structures and anatomical abnormalities in the case of a disease. Quantification of the relaxation constants is also possible, but these remain MR parameters without a direct equivalent in biophysiology. Instead of hoping that a specific finding in a disease, e.g. the increase of T_1 , can be translated one to one from basic research in animals to the clinic, the characterization of the underlying physiological changes may provide a better understanding and a more reliable translation of the results obtained from basic research. More valuable for this are MR measures that more precisely characterize the kind of physiological change that is observed. This chapter describes such methods. From diffusion MRI, the direction of neuronal fibers can be reconstructed, for example, MRS and CEST can be correlated with metabolite concentrations and functional MRI can be correlated with neuronal activity. However, these are indirect measures and need to be validated by established methods. For research in experimental animal models, non-invasiveness is not the key premise and several methods like optical microscopy, histology and electrophysiology allow thorough investigations. But if the detected MR features were validated, non-invasive preclinical MRI can contribute to basic research by making longitudinal studies and whole-brain analysis possible.

2.2.1 Diffusion MRI

Diffusion is the random motion of molecules driven by their thermal energy. In 1827, when the existence of atoms and molecules was not an established fact but a matter of debate, the botanist Robert Brown observed the random motion of pollen grains in water (Brown, 1828). Albert Einstein later related that observation to the motion of molecules. In 1855, Adolf Fick developed two laws describing the flux of particles (Fick, 1855). Given a concentration gradient $\nabla c(\mathbf{r}, t)$, the flux of particles $\mathbf{J}(\mathbf{r}, t)$ is proportional and opposed to the concentration gradient:

$$\mathbf{J}(\mathbf{r}, t) = -D\nabla c(\mathbf{r}, t) \quad (2.4)$$

where D is the diffusion coefficient. Conservation of mass leads to Fick's second law which is also known as diffusion equation:

$$\frac{\partial c(\mathbf{r}, t)}{\partial t} = D\nabla^2 c(\mathbf{r}, t) \quad (2.5)$$

In contrast to Fick's first law, which only describes a steady flow, the second more general law relates the temporal to the spatial changes of the concentration gradients. These laws were initially developed to describe the flow of macroscopic particles,

drifting from higher to lower concentrations, but it was shown that they also hold true in the case of “self-diffusion” where no macroscopic concentration gradient exists. In 1905, Albert Einstein could explain the Brownian motion of macroscopic particles by the collision with molecules in the fluid, and thereby gave evidence for the existence of atoms (Einstein, 1905). “Self-diffusion” of molecules is thus based on their thermal energy. William Sutherland, Albert Einstein and Marian Smoluchowski independently found equations to describe the diffusion:

$$D = \mu k_B T \quad (2.6)$$

where μ is a general mobility of the particles, k_B the Boltzmann constant and T the temperature. The Einstein equation for diffusion describes the 1D displacement x in the diffusion time t :

$$x^2 = 2Dt \quad (2.7)$$

This relation is only valid for free diffusion. In biological tissue however, diffusion may only be free on very short – with MRI hardly realizable – time scales, but as the diffusion time increases water molecules interact with the environment and encounter permeable and non-permeable barriers (Figure 2.7, A). For typical values of $D=10^{-3}\text{mm}^2/\text{s}$ and diffusion time $t=50\text{ms}$ free water molecules diffuse over a distance of $10\ \mu\text{m}$. This is in the same scale as the size of neural compartments, fibers and cells. Diffusion of water molecules thus samples the underlying tissue and reveals information about structures much smaller than the size of a typical MRI voxel. Also, the direction of the diffusion is not necessarily isotropic but may have a certain preference, for example rather along fibers than across them. In order to characterize this anisotropy, the scalar D is extended to a diffusion tensor D .

Measuring the water diffusion means applying an MRI sequence that is especially sensitive to it. The most common approach is based on the early work of Stejskal and Tanner in 1965 (Stejskal and Tanner, 1965), who introduced two pulsed gradients to achieve a diffusion-weighting of a spin echo (Figure 2.7, B). The first gradient pulse is introduced in the dephasing part before the 180° refocusing pulse. This gradient imparts a spatially dependent phase shift which is then inverted by the 180° refocusing pulse. The second gradient pulse in the re-phasing part after the 180° pulse has the same amplitude as the first gradient and thus imparts a phase shift that cancels out the first one and leads overall to an induced phase shift of zero. However, motion along the direction of the gradients leads to differently experienced gradients proportional to the travelled distance and a total induced phase shift different from zero. The incoherent Brownian motion causes phase differences inside a voxel and thus an attenuation of the echo, whereas macroscopic motion and coherent flow lead to a total phase shift, not to phase differences inside the voxel, and thus not per se to a signal attenuation.

Nowadays EPI is used for the image read-out, which introduces negligible inherent diffusion-weighting (the only exception may be micro imaging measurements with extremely strong imaging gradients), so that the signal attenuation is mainly determined by the characteristics of the diffusion gradients: their amplitude G , duration δ and separation Δ . In a simplified approach, when δ is shorter than Δ , the attenuation of the spin echo signal S can be written as:

$$\ln \left[\frac{S_1}{S_0} \right] = -\gamma^2 G^2 \delta^2 \Delta D \quad (2.8)$$

S_1 and S_0 are the signals with and without diffusion weighting, respectively. The b -value (in $[s/mm^2]$) characterizes the sensitivity to diffusion and summarizes all effects of the sequence gradients:

$$\ln \left[\frac{S_1}{S_0} \right] = -bD \quad (2.9)$$

If more images with a range of different b -values are acquired, Eq. 2.9 is fitted to the acquired signal intensities to estimate the diffusion coefficient. Diffusion attenuates the signal exponentially; in diffusion weighted-images areas of high diffusivity appear dark whereas areas of low diffusivity appear bright. However by using this technique, only the diffusion along the gradient direction determines the attenuation of the diffusion-weighted echo (Figure 2.7, C). To be able to describe the diffusion in three dimensions, the scalar D is extended to a tensor:

$$\ln \left[\frac{S_1}{S_0} \right] = -b(u_j \ v_j \ w_j) \times \begin{bmatrix} D_{xx} & D_{xy} & D_{xz} \\ D_{xy} & D_{yy} & D_{yz} \\ D_{xz} & D_{yz} & D_{zz} \end{bmatrix} \times \begin{pmatrix} u_j \\ v_j \\ w_j \end{pmatrix} \quad (2.10)$$

Where u , v and w represent the direction of the diffusion gradient vector and x , y and z represent the reference frame of the measured subject. The sequence is repeated several times ($j = 1 \dots n$) with altered gradient directions. To be able to estimate the diffusion tensor a minimum of seven measurements – six unique directions with diffusion weighting and one without diffusion weighting – are needed. If more directions are measured, a least square fitting approach can be used to estimate the tensor elements. The elements of D are real and D is symmetric, thus D is diagonalizable and can be represented by its eigenvectors ($\lambda_1, \lambda_2, \lambda_3$) and eigenvalues (D_1, D_2, D_3):

$$D = \begin{bmatrix} D_1 & 0 & 0 \\ 0 & D_2 & 0 \\ 0 & 0 & D_3 \end{bmatrix} \quad (2.11)$$

Using MRI to investigate diffusion in this way is referred to as diffusion tensor imaging (DTI). Anisotropic diffusion can intuitively be described by an ellipsoid that is aligned along the main diffusion direction (λ_1). For a quantitative characterization of diffusion properties, several parameters can be computed from λ and D . For example, maps of

each eigenvalue can be created to visualize diffusion parallel (or axial, D_1) or perpendicular (D_2, D_3) to the main direction. The mean diffusivity (MD), which is $\text{trace}(D)/3$, gives a non-directional measure of diffusion and fractional anisotropy (FA) is a measure for the degree of anisotropy. FA ranges from 0, meaning completely free diffusion, to 1, representing the unrealistic case of completely directed diffusion.

$$FA = \sqrt{1.5} \frac{\sqrt{\sum_{i=1}^3 (D_i - D_{avg})^2}}{\sqrt{\sum_{i=1}^3 D_i^2}} \quad (2.12)$$

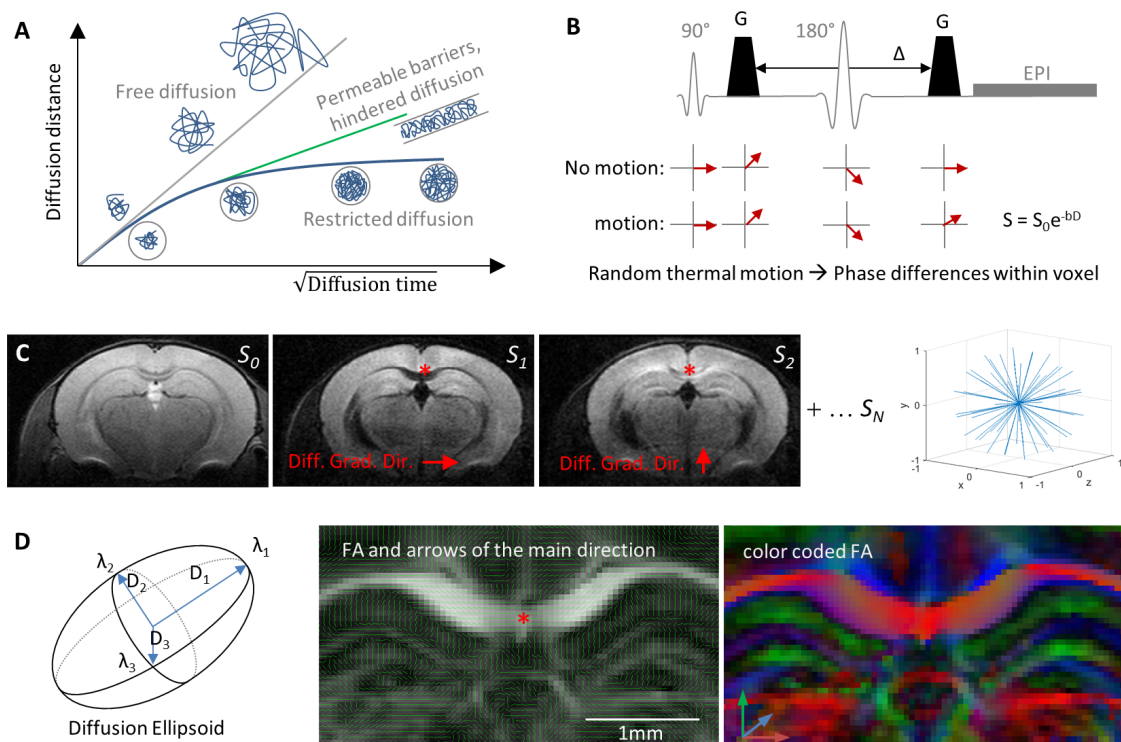


Figure 2.7: From thermal motion to diffusion tensor MRI. **A)** The thermal energy causes the random Brownian motion of molecules. During their diffusion “walk” (blue lines), the molecules encounter obstacles and sample the tissue microstructure (Figure A adapted from (Le Bihan et al., 1991)). **B)** Spin echo EPI with diffusion gradients (G). Motion between the application of these gradients lead to imperfect phase refocusing. The random nature of the diffusion leads to phase differences within the voxels and signal attenuation. **C)** Images without (S_0) and with diffusion weighting (S_1 - S_N) are acquired. The diffusion directions for the applied gradient scheme are illustrated on the right side. In Image S_1 , the diffusion gradients were directed from left to right, which corresponds to the direction of the fibers in the corpus callosum (red asterisk). Relative fast diffusion along the fiber direction leads to strong signal attenuation. Whereas diffusion perpendicular to this direction is hindered leading to a high signal in the corpus callosum if the diffusion direction is perpendicular to it (image S_2). **D)** In DTI, the diffusion properties within a voxel are represented by an ellipsoid that is aligned along the main diffusion direction. In a DTI image, the main diffusion directions can be illustrated by arrows or by a color code (Figure D, middle and right: magnifications of the mouse brain showing the corpus callosum (red asterisk) and the hippocampus).

Using only six measurements of the diffusion directions may lead to direction-dependent variances in the estimates of the diffusion coefficients. Several schemes were therefore developed to optimally resolve the direction dependent diffusion properties. Based on the concept of electrostatic repulsion, Jones et al. developed a scheme with 30 diffusion-directions which is rotationally invariant and optimal to estimate the principal eigenvectors (Jones et al., 1999; Jones, 2011). Besides the gradient directions, the amount of diffusion weighting is crucial. The question of which b-value would be optimal depends, like the gradient-direction scheme, on the specific application. In general, too low b-values lead to insufficient diffusion-weighting, too high b-values lead to low SNR. The optimal b-value for estimating the in-vivo diffusion tensor is approximately equal to $1/D$ and lies in the range $750\text{-}1300\text{ s/mm}^2$ (Alexander and Barker, 2005; Armitage and Bastin, 2001; Jones et al., 1999). In fixed, ex-vivo tissue diffusion rates are significantly reduced, so that higher b-values of approximately 2000 s/mm^2 are needed to achieve a similar diffusion weighting (Sun et al., 2005).

Diffusion in tissue is not free; it's not only much shorter but also depends on the underlying structure, experimental and technical parameters, as well as intra-voxel incoherent motion (Le Bihan et al., 1988). On this account, the measured diffusion coefficients are often referred to as apparent diffusion coefficients (ADC).

It is an ongoing endeavor to find links between the measured diffusion properties and the specific components of the underlying tissue. For example, myelinated axons in the white matter of the human brain are known to exhibit very anisotropic diffusion favoring the direction along the fibers. This was observed early on leading to the rapid success of DTI (Moseley et al., 1991; Thomsen et al., 1987). But even though the myelin sheath does contribute to anisotropy, it is not a prerequisite to find anisotropic diffusion (Beaulieu and Allen, 1994). At b-values $\geq 2000\text{ s/mm}^2$ (in-vivo), the attenuation of the signal intensity shows a deviation from the mono-exponential decay (Figure 2.8) which is referred to as diffusion kurtosis and may reveal further information about restricted diffusion (Fieremans et al., 2011; Hui et al., 2008; Wu and Cheung, 2010). To account for the kurtosis K , equation 2.9 can be expanded to:

$$S = S_0 e^{-bD + b^2 D^2 K/6} \quad (2.13)$$

If a hardly permeable boundary, like the myelin sheath of axons, restricts the diffusion, the diffusion signal will not completely decay into the noise level even at high b-values. Figure 2.8 illustrates that a plateau is reached instead, indicating that the underlying structure limits the maximal displacement of the water molecules. For a rough estimation, taking the measured values for S_0 , $S_{b=10000\text{ s/mm}^2}$, the diffusion time of 40 ms and using equations 2.9 and 2.7 yields a displacement of around $2.6\text{ }\mu\text{m}$. This lies well in the range of the diameter of white matter axons (Liewald et al., 2014).

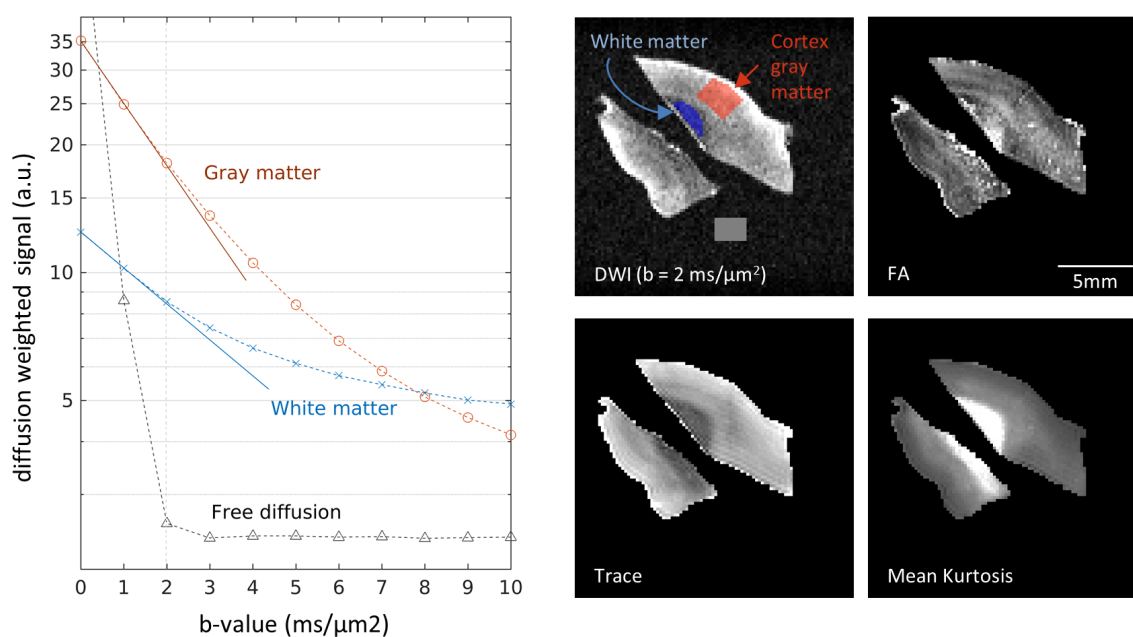


Figure 2.8: Diffusion properties of human brain tissue. **Left)** The averaged intensity of 100 diffusion directions is plotted for regions of interest in cortical gray matter, white matter and in the surrounding buffer solution (gray rectangle). From $b=0$ s/mm² to $b=2000$ s/mm², the signal decays exponentially (note the logarithmic scale of the y-axis). At $b>2000$ s/mm², the signal decay in gray and white matter deviates from the exponential trend. The difference between (quasi) free and hindered diffusion depends on the microstructure and becomes more obvious at stronger diffusion weightings. Especially myelinated axons in the white matter represent hardly permeable boundaries. **Right)** Maps showing different contrasts: fractional anisotropy FA (plotted scale 0-0.4), trace (0-0.0005 mm²/s) and mean kurtosis (0-1.5). (Ex-vivo scan of tissue resected from an epilepsy patient. Sequence: 2D diffusion-weighted spin-echo EPI, diffusion gradients 8 ms duration, 40 ms separation, resolution 200 μ m isotropic, TR 3 s, TE 64 ms, 4 segments, NA 2, scan time 6h41 min. The MRI setup is described in chapter 4.)

Methods employing multiple high b-values and directions (>60) are often summarized under the term high angular-resolution diffusion imaging (HARDI). These approaches provide more information about the microstructure than DTI, but nonetheless an exact one-to-one assignment of a measured diffusion quantity to an individual component (e.g. axons, myelin, glia) or compartment (e.g. intra- and extracellular) remains elusive.

A complementary approach to infer information about the underlying microstructure is termed fiber tractography. The key idea behind tractography is that the anisotropic diffusion in white matter fiber bundles is a measure of their orientation. By following this direction throughout the brain, one can recreate the tracts connecting different brain regions. The different tractography approaches can be categorized based on their algorithm, deterministic or probabilistic, whether they act on local seed points or globally, and whether they utilize the diffusion tensor or the raw diffusion weighted images.

The simplest method is the deterministic approach based on the diffusion tensor. Each voxel is represented by the major eigenvector of the diffusion tensor which creates a vector field. Starting from one or multiple local seed points, “walking” through the

volume along the vectors until a stop criterion (e.g. the decrease below a certain FA threshold) yields the fiber pathways (Figure 2.9, left). The major problem of this method arises from the reduction to a single tensor in each voxel. Given the relative coarse resolution of MRI, a multitude of fiber groups exist in each voxel. These fiber bundles often curve, disperse or converge. For example, if one considers two fiber bundles crossing perpendicularly in a voxel, while each of them may show very anisotropic diffusion, the reduction to a single tensor yields a rather isotropic appearance which prevents the resolution of the individual directions. Additionally to the ubiquitous noise, this leads to an uncertainty of the actual direction. Stepwise progression from the initial seed points then results in a propagation of these errors increasing with the distance and a lack of confidence in the final results.

Probabilistic algorithms take this uncertainty into account during the tracking process. The first step is the determination of orientation distribution functions (ODF) for each voxel which describe the distribution of possible orientations. For example, the simplest approach is to correlate the degree of anisotropy with the fiber orientation. Having set up the ODFs, one option then is to repeatedly apply a deterministic algorithm with random samples from the ODFs. This generates probabilistic maps with the most reproducible connections (Figure 2.9, right).

The idea of the global tractography method used in this work is as follows: 1) the fibers are represented by line segments. These line segments are not of the size of an actual axon, but smaller than the MRI voxel. They are connected and built into a model. 2) A synthetic MRI dataset is simulated from the model and compared to the measured HARDI data. 3) During an iterative optimization process, the number, orientation and connection of the line elements are adjusted until the difference between the model and the measured data is minimal (Reisert et al., 2011).

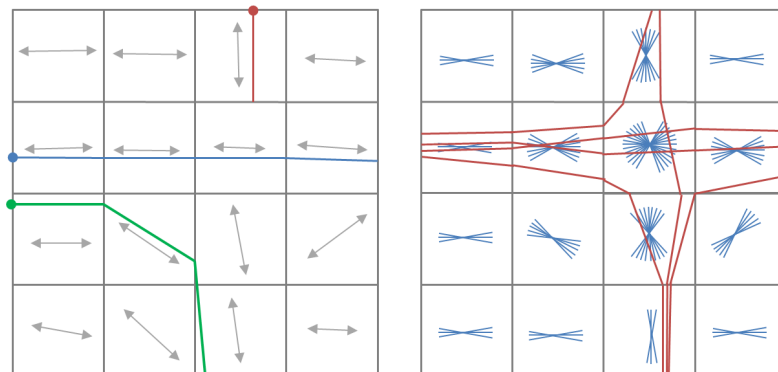


Figure 2.9: Illustration of different tractography approaches. Left) Deterministic seed-based tractography. Following the main direction from a seed point may yield proper connections (blue and green paths). However if fibers cross, the tracking fails because the anisotropy becomes too low or an unrealistic sharp curvature would point in a wrong direction (red path). These limitations are addressed by probabilistic tracking approaches (Figure right).

2.2.2 In-vivo ^1H -NMR Spectroscopy

Typical MRI exploits the water in biological tissue, for which the resonance frequency ω_0 depends on the gyromagnetic ratio γ_{1H} and the magnetic field strength B_0 . In-vivo ^1H spectroscopy detects the signal of hydrogen protons in several metabolic compounds, for example N-Acetyl Aspartate (NAA), creatine (Cr) or neurotransmitters like glutamate (Glu) and γ -aminobutyric acid (GABA). Two properties – the chemical shift and the scalar coupling – lead to a splitting from a single proton resonance peak to a spectrum which is characteristic for each molecule and allows the identification of individual metabolites (De Graaf, 2007).

The chemical environment influences the experienced field at the nucleus, a phenomenon referred to as chemical shift. In the external magnetic field B_0 , electrons surrounding each nucleus will produce a magnetic moment opposed to B_0 . This shields the nucleus from the external field B_0 and reduces the effective field at the nucleus. The resonance condition (Eq. 2.1) is altered to:

$$\omega_0 = \gamma B_0(1 - \sigma) \quad (2.13)$$

where σ is a dimensionless shielding constant. The shift of the resonance frequency depends on the electron density around the nuclei and the type of bonds in the molecule. As the chemical shift is proportional to the external field strength B_0 , it is usually defined as difference between the measured frequency and a reference signal (e.g. tetramethylsilane or certain peaks of Cr or NAA) and specified in parts-per-million (ppm; 1ppm \approx 300 Hz at 7 T). This makes the descriptions of the shifts independent of the field strength and thus allows an easier comparison of different spectra. In-vivo spectra of the brain show the most metabolites between 1 and 4 ppm (water is at 4.7 ppm).

Furthermore, a finer splitting originates from a phenomenon referred to as scalar, spin-spin or J-coupling. The different nuclei in a molecule can influence each other through electrons in their chemical bonds. Considering the case of a single proton, then the nuclear and electron spins are antiparallel as this is energetically favored. This gives rise to two transitions with equal transition energies and thus a single resonance peak is measured. If the proton is coupled to a different nucleus, the Pauli principle demands that the electron spins in the chemical bond are antiparallel. That enforces energetically less favorable states in which the spin of the nucleus is parallel to the electron spin. The allowed transitions then have different energy levels and the resonance frequency is split up. The splitting pattern depends on the chemical bonds in the molecule and is thus not dependent on the magnetic field. The scalar coupling constants for ^1H - ^1H interactions are in the range 1-15 Hz.

A localized acquisition of the spectra is for example achieved by point-resolved spectroscopy (PRESS). This sequence uses three slice selective pulses, 90° - 180° - 180° , to

create an echo signal originating from the intersection volume of these pulses (Figure 2.10). Typical volume sizes are in the order of 10 cm^3 in clinical MRI systems and $4\text{--}10\text{ mm}^3$ in preclinical MRI systems. The concentration of the metabolites is often more than 10,000 times lower than that of the abundant water in the tissue. The water signal at 4.7 ppm therefore obscures the resonances of the metabolites at 1–4 ppm and needs to be suppressed in order to facilitate the metabolite detection. One method to achieve this is: variable pulse powers and optimization relaxation delays (VAPOR). It uses frequency selective r.f. pulses and optimized delays to reduce the longitudinal magnetization of water to zero prior to the PRESS sequence. LCMoDel has been established as a robust method to quantify metabolite concentrations in-vivo (Provencher, 2018). It takes a basis set, which contains either simulated or measured spectra of all relevant metabolites and models the measured spectrum as a linear combination of the single metabolite spectra. The fitted weights for each element of the basis set are then directly related to the concentrations of the respective metabolites.

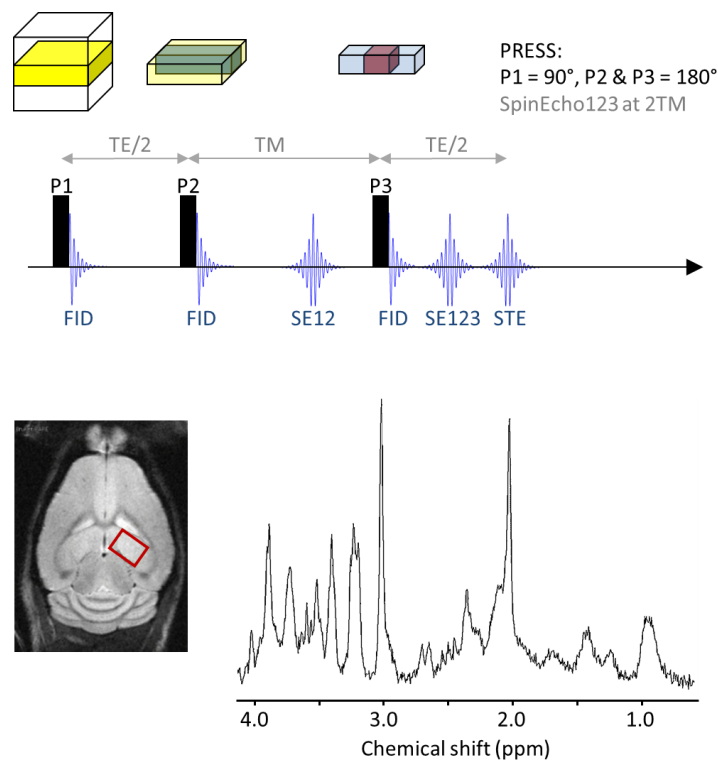


Figure 2.10: Localized Spectroscopy. Three orthogonal slice-selective pulses create a signal originating from the volume of interest only. PRESS ($90^\circ\text{--}180^\circ\text{--}180^\circ$) uses the spin echo (SE123), whereas STEAM ($90^\circ\text{--}90^\circ\text{--}90^\circ$) uses the weaker (50% less signal) stimulated echo (STE). The most prominent peaks in the acquired in-vivo spectrum are from NAA at 2 ppm and tCr at 3 ppm (further details in chapter 4).

2.2.3 Functional MRI

The idea to employ MRI for the study of brain activity arose when it was demonstrated that hemoglobin, which is part of the red blood cells in almost all vertebrates, possesses variable magnetic properties depending on whether oxygen is bound to it or not (Ogawa et al., 1990, 1992). Oxygenated hemoglobin is diamagnetic, but deoxygenated hemoglobin is paramagnetic. When placed in the magnetic B_0 -Field, hemoglobin induces local magnetic field variations around blood vessels. Compared to oxyhemoglobin, the distortions by deoxyhemoglobin are stronger which leads to a faster spin dephasing and thus to a decreased MRI signal. This is the basis of the blood-oxygen-level dependent (BOLD) contrast, which is most pronounced in MR sequences sensitive to T_2^* . Important to note is that BOLD fMRI is not a direct measure of neuronal activity which is an important difference to the detection of neuronal action potentials by electrophysiology for example. BOLD is an indirect effect based on the coupling of neuronal activity, metabolic processes and the corresponding changes in blood supply to meet the local energy demands of the brain. This eventually leads to local changes in blood oxygenation in the tissue. This chapter describes the underlying physiology and the basics of two different methodological approaches: task-based fMRI, which evaluates the activation of brain areas in response to an external stimulus, and resting-state fMRI, which evaluates the connectivity between brain regions at rest without an external stimulus.

Physiology

In order to understand the BOLD effect, one has to examine how neuronal activity leads to changes in blood oxygenation (Huettel et al., 2004). The nerve cells or neurons form the central units in the brain, integrating and transmitting signals. Active and passive channels inside the cell membranes control the inner and outer concentration of ions like sodium (Na^+), chloride (Cl^-), potassium (K^+) and calcium (Ca^{2+}). At rest, an electrochemical concentration gradient is maintained with a resting potential of ca. -70 mV between the inside and outside of the cell. Incoming signals either increase or decrease that potential by generating an excitatory postsynaptic potential (EPSP) or an inhibitory postsynaptic potential (IPSP), respectively. If the potential at a certain location of the neuron – at the axon hillock – increases above a threshold (ca. -50 mV), then voltage-gated sodium channels open. The resting higher Na^+ concentration outside the cell leads to an influx of Na^+ and a further depolarization which again opens further Na^+ channels. This so-called action potential travels in a self-propagating manner down the axon until it reaches the axon terminal. Synapses connect the axon terminals to other neurons. Chemical synapses possess a cleft preventing electrical transmission. After an incoming action potential, this gap is bridged by a presynaptic release of neurotransmitters into the cleft and brief postsynaptic binding of these neurotransmitters where they induce an EPSP or IPSP. The neurotransmitters are subsequently removed from the synaptic cleft and through metabolic recycling transported back into the presynaptic cell. For fMRI,

the aspect of energy demands to support these processes are important. Diffusion along a concentration gradient like the influx of Na^+ or the free diffusion of neurotransmitters in the synaptic cleft is driven by thermal energy and the propagation of the action potentials therefore does not require an external energy supply. However, for restoring the resting potential across cell membranes, channels have to actively pump Na^+ against the concentration gradient out of the cell, for which the brain has to supply energy. Also, the uptake, recycling and synaptic storage of neurotransmitters are active, energy-consuming processes. Adenosine triphosphate (ATP) hydrolysis is the reaction in the brain by which the energy stored in the ATP bonds can be released to provide energy for other chemical processes. ATP can be produced from glucose in the brain in two ways, either involving oxygen (aerobic glycolysis) or not (anaerobic glycolysis) with the latter process being faster but less efficient. As the brain does not hold large energy reservoirs, functional activity is accompanied by locally increased blood flow to deliver glucose and oxygen as energy sources.

Blood is delivered through arteries, which start with a relative thick diameter near the heart and branch into smaller arterioles until they terminate in the capillary bed, where glucose and oxygen is extracted from the blood. As aortic blood is oxygenated, changes in the deoxygenation content manifest at the venous side of the capillary bed. The BOLD effect depends on the total amount of deoxygenated blood. One could therefore assume that increased activity and oxygen consumption lead to a decreased MR signal, but in fact most experiments yield a positive fMRI response upon stimulation. This can be explained by the fact that due to the blood influx, oxygenated hemoglobin replaces deoxygenated hemoglobin, which is flushed out of the active region. Moreover, the increase in blood flow exceeds the consumption of oxygen leading to an increase of the fMRI signal above the initial baseline. However, the shape and timing of the vasculature's response to neuronal activity, which is referred to as hemodynamic response function (HRF), is a complex interplay between the cerebral metabolic rates of oxygen (CMR_{O_2}) and glucose (CMR_{Glc}) consumption and cerebral blood flow (CBF) and volume (CBV).

Task-based fMRI

The BOLD response manifests as a relative temporal deviation from an arbitrary baseline signal intensity. Therefore, one can only detect differences between the baseline and altered signals during rest and stimulation, respectively. Since fMRI is by far more established in humans than in rodents, the basic principles are illustrated here for a human fMRI experiment (Figure 2.11). A flickering checkerboard was presented to a human volunteer as visual stimulation in a block design during which GE EPI images were acquired on a clinical scanner (3T Prisma, Siemens, Germany). Voxels within the visual cortex showed a response to the stimuli. In general, the time course of the HRF can be qualitatively described as an initial dip, a delayed positive overshoot at the be-

ginning of the positive response during the stimulus and a post stimulus undershoot that eventually returns to baseline. But these features are highly variable and depend on the fMRI experiment; the timing of the main peak may vary and its amplitude can even be negative despite increases neuronal activity (Schridde et al., 2008), while the mechanisms and significance of the initial dip and post-stimulus undershoot are still being debated (Hu and Yacoub, 2012; van Zijl et al., 2012).

A model, which represents the estimated response, is fitted to each voxel's time course in the acquired data. The time course of the model is created by the convolution of the block design with basis functions (also called predictors, regressors, or explanatory variables). Several different approaches for these basis functions exist. An overview of the different methods' performance, especially with respect to heterogeneous responses in optogenetic fMRI, can be found in (Liu et al., 2017). General linear modelling (GLM) is then used for a statistical analysis of the fMRI activation. In GLM, the acquired data is expressed as the model multiplied by weighting factors plus residuals (or errors). Various hypotheses, e.g. activation vs. no activation, can then be tested yielding thresholded maps of statistically significant activation.

The fundamentals of the method are the same for preclinical rodent fMRI. A similar visual stimulation experiment is also possible and evaluated in chapter 5. The main differences come from the need of anesthesia and of course the size of the brain. Details for mouse fMRI are covered in chapter 5.

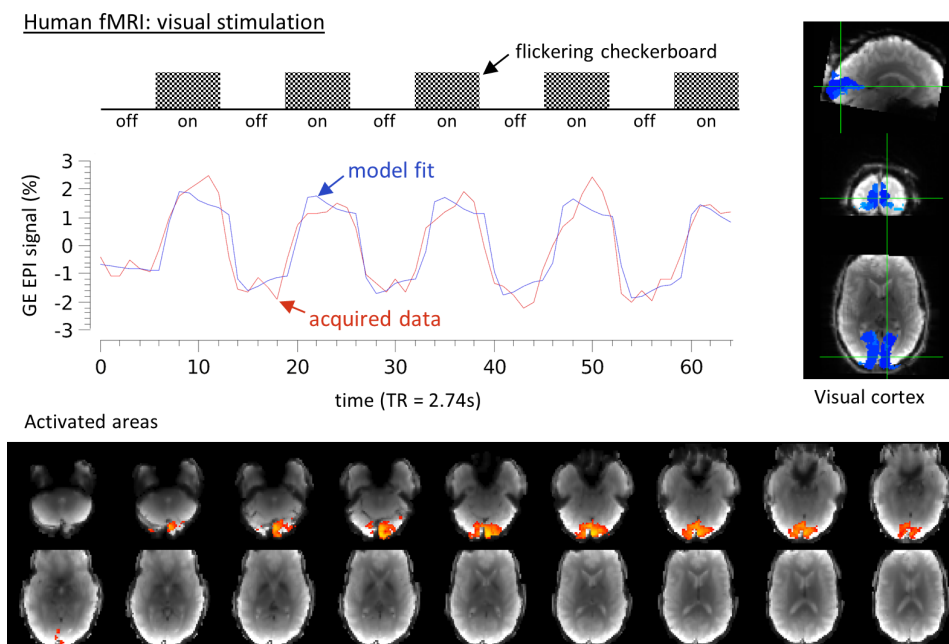


Figure 2.11: Basic task-based fMRI experiment. Five visual stimuli (18s on, 18s off) were presented to a human volunteer (the author of this thesis) during a 3min GE EPI scan (3T Siemens Prisma, TE 30ms, TR 2.74s, 3mm isotropic resolution, 65 recorded volumes). Voxels within the visual cortex (blue label, Jülich brain atlas) showed increased intensities upon stimulation. GLM yields thresholded maps of significant activation (analysis in FSL, model: 3rd order gamma basis functions).

The BOLD effect only leads to signal changes of a few percent. However, this can be quite significant provided that the noise fluctuations are lower. Experimental design, MRI acquisition and post processing steps are aiming to maximize the BOLD effect and minimize residual noise. The main points of the acquisition to consider are:

- *Sensitivity*. It has been shown that BOLD signal changes can be separated into different components; one static dephasing and one dynamic averaging component (Ogawa et al., 1993). GE EPI is sensitive to both and the most widely used sequence for fMRI. TE is chosen according to T_2^* , which is approximately 30ms at 3T. However, T_2^* is variable in the brain and TE is selected according to an overall average or a region-of-interest. Alternatively, multi-echo fMRI is used to acquire a range of TEs. T_2 -weighted spin-echo sequences are only sensitive to the dynamic averaging. Therefore they are less sensitive, but it was reported that they better localize neuronal activity (Norris, 2012).
- *Temporal Signal-to-Noise Ratio (tSNR)*. tSNR is defined as signal amplitude divided by the standard deviation of noise. For a rough orientation, the tSNR of a routine fMRI protocol (3T clinical system, GE EPI with 30ms TE, 2.6s TR and 3mm isotropic resolution) is around 100-200.
- *Temporal Resolution*. FMRI's temporal resolution is determined by the HRF, which, in contrast to the neuronal action potentials that occur in milliseconds, responds in seconds. Standard sequence TR is therefore in the order of 1-2s.

FMRI analysis is carried out on the reconstructed magnitude images. Standard (pre-statistical) post processing steps are applied as follows:

- *Motion correction*. The time course of a voxel must correspond to a consistent anatomical point. Motion causes misalignments and corrupts time courses. Images are therefore registered to a common reference.
- *Removal of non-brain areas*. Signals from outside of the brain should not be smoothed into the brain, therefore non-brain areas are removed. Also, registration of the fMRI images to reference templates requires prior brain extraction.
- *Temporal filtering*. In the frequency domain, BOLD occurs mainly in the range of 0.01-0.1 Hz, whereas much of the noise is either ubiquitous (like thermal noise) or lies outside this frequency range (like respiratory artifacts). Temporal filtering can therefore enhance the contrast between BOLD and noise. High-pass temporal filtering is mandatory to remove low frequency drifts that are often present. Additional low-pass filtering is usually not-recommended but this depends on the application. For consistency, the same temporal filtering must also be applied to the design model in task-based fMRI.
- *Spatial smoothing*. A spatial filter averages adjacent voxels, for example by a convolution with a Gaussian kernel. The FWHM of this curve is usually chosen to be around 2 times the voxel size. This increases SNR and reduces false positives at the cost of a reduced spatial resolution.

Resting-state fMRI

From a macroscopic view, the brain is organized in distinct functional areas. White matter fibers connect these areas within and between the hemispheres and connected areas can therefore quickly exchange signals. In the absence of an external stimulus, cells are not idle. Their resting activity may be lower as compared to stimulated activity but cells are permanently processing information. On the time scale that is relevant for MRI, cells in connected regions show synchronous activity and consequently have a synchronous energy demand and blood supply. If the fMRI time courses are sensitive to changes due to blood supply, this means that fluctuations in the time courses of two connected regions have something in common. Resting-state fMRI takes the correlation of the fMRI time courses as a measure for their connectivity (Figure 2.12).

There are two popular approaches for the investigation of connectivity: seed-based correlation analysis (SBA) and independent component analysis (ICA). SBA takes the fMRI time course of a region-of-interest and analyzes the correlation of different regions to it. ICA decomposes the entire 4D fMRI dataset into different spatial components. These components also have a time course and all together build the complete fMRI data set. The independent components are found by maximizing their statistical independence. According to the central limit theorem, the combination of independent components results in a component that has a more Gaussian shape than the individual components. Maximizing the non-Gaussianity of the individual components therefore yields more independent components.

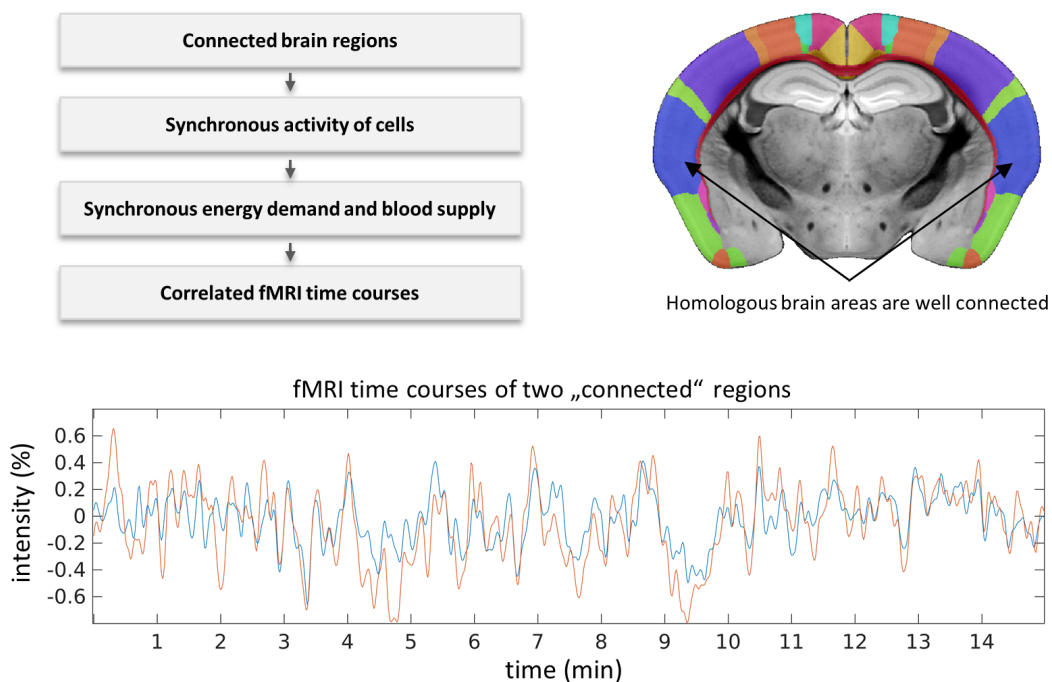


Figure 2.12: Principle idea of resting-state fMRI. Top right) Segmented mouse brain, see section 5.3.3.

Figure 2.13 illustrates SBA of resting-state connectivity and the effect of the applied post processing steps. One voxel in the right somatosensory cortex of the mouse brain is selected as seed. A direct correlation of the seed's time course (TC) yields spurious connections. These false results are caused by drifts present in the TC even after motion correction. Temporal filtering yields the correct TC and connections. Spatial smoothing increases the extent of correlated areas. Brain areas possess several connections; the strongest connection is often between homologous regions. No significant correlation between the TC of neuronal origin in the brain and the TC of noise should be present.

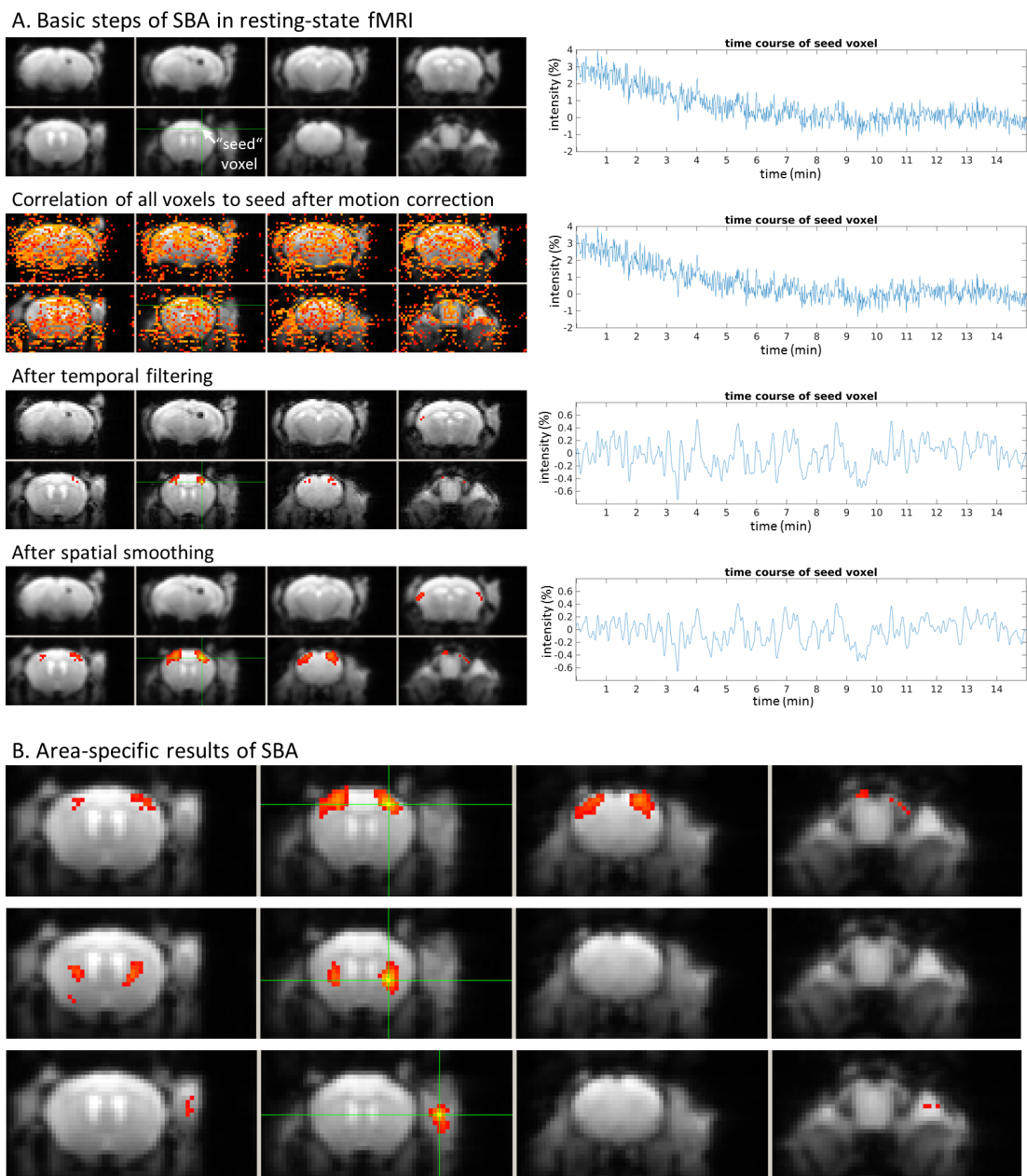


Figure 2.13: Seed-based analysis of mouse brain resting-state connectivity. The reticle points to the voxel chosen as “seed” point. A detailed description of the method is presented in chapter 5.

2.2.4 Chemical Exchange Saturation Transfer (CEST)

Typical MRI is, despite its possibility to infer information about diffusion or functional processes, inherently based on the signal originating from water in the tissue. In contrast to that, chemical exchange saturation transfer (CEST) is an MRI method that offers the possibility to indirectly image endogenous metabolites such as glutamate. CEST can be considered as a subcategory of magnetization transfer (MT) approaches, which is one of the oldest MR techniques with broad applications for imaging and spectroscopy (Forsén and Hoffman, 1963; Wolff and Balaban, 1989; van Zijl et al., 2018). The focus in this work is on the more recent developments of proton related magnetization transfer with the aim to achieve in-vivo images sensitive to endogenously occurring metabolites.

The hydrogen in the brain can be considered to be present in different pools; one small pool of hydrogen in metabolic compounds and one much larger pool of hydrogen in the abundant water. The protons in several chemical groups (e.g. -NH, -NH₂, -OH) may undergo a chemical, physical exchange with the water protons. If in a sufficiently strong magnetic field the chemical shift exceeds the exchange rate, which is referred to as slow to intermediate exchange condition, then these pools can be treated as two discrete pools with specific frequencies (Figure 2.14). It is a convention in the MT community to set water to 0 ppm, then groups with exchangeable protons are found between +0.5 and +4 ppm. The basic principle of CEST is as follows: 1) a saturation pulse is applied at the resonance frequency of a specific chemical group, e.g. +3.5 ppm for -NH₂. The saturation pulse destroys the magnetization in this proton pool. 2) Chemical exchange leads to the transfer of saturated protons into the water pool. The reduction of magnetization in the water pool is an indirect measure for the smaller metabolic pool. 3) The concentration of the water pool vastly exceeds the smaller metabolic pool. Therefore, saturated protons are replaced by unsaturated protons, which in turn can be saturated and exchanged. This process repeats during the application of the saturation pulse (1-2 s). Longitudinal relaxation in the water pool occurs, but the faster chemical exchange leads to an accumulation of saturated protons in the water pool. One advantage of CEST is this strong enhancement effect, which is in contrast to spectroscopy where each proton contributes directly but only once to the measured signal.

CEST has to be delineated from other magnetization transfer processes. First, macromolecules and semi-solid tissue components are also affected by the saturation pulse and transfer of this magnetization to water occurs either via dipolar coupling or chemical exchange. This was the first discovered magnetization transfer pathway and accordingly the method was named magnetization transfer contrast (MTC). However, because of the very short T₂ in semi-solid tissue, MTC exhibits a very large frequency range and even far off-resonant pulses (≥ 10 ppm) lead to saturation. MTC is also nearly symmetric around water; up- and downfield saturation shows minimal differences. This distinguishes MTC from CEST of small metabolites for which the specific frequency range

+0.5 to +4 ppm is characteristic. Another mechanism is referred to as nuclear Overhauser effect (NOE), which originates from inter- and intramolecular cross-relaxation via dipole coupling. There are several possible pathways of magnetization transfer through a molecule to free water which give rise to several resonances mainly observed in the spectral range from -2 to -5 ppm. A detailed review and terminology differentiating MT, CEST, NOE, exchange-relayed NOE and NOE-relayed exchange can be found in (van Zijl et al., 2018).

The saturation pulse in CEST experiments, often in the simplest form of a continuous pulse, is applied immediately before the imaging module, e.g. a RARE sequence. Image acquisition is repeated with different saturation frequencies to sample a certain spectral range, e.g. from +5 to -5 ppm, which results in a so-called z-spectrum for each voxel. The saturation pulse also leads to a direct saturation effect in the water pool. Direct saturation and MT effects are nearly symmetric, therefore CEST effects can typically be identified by analyzing the asymmetry in the z-spectrum.

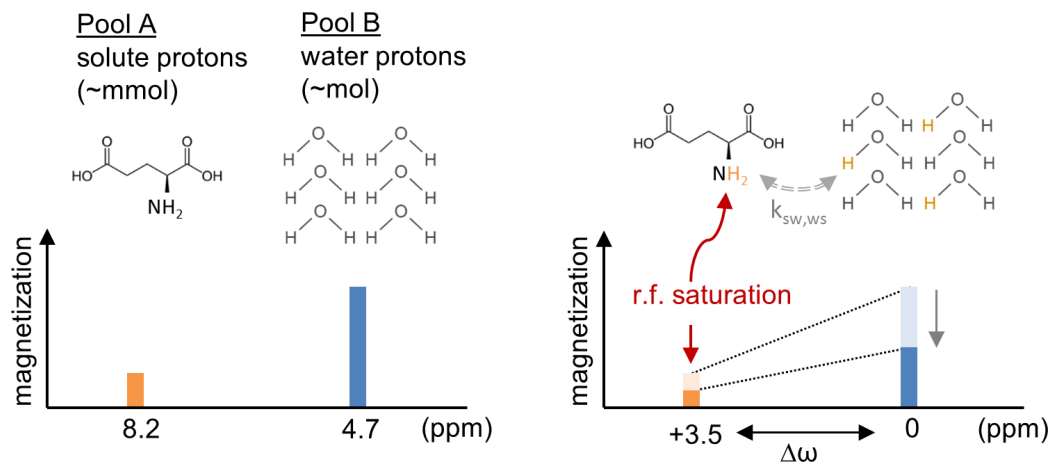


Figure 2.14: Principle of chemical exchange saturation transfer (CEST) MRI. Applying a long r.f. pulse at the resonance frequency of the -NH_2 group in glutamate (+3.5 ppm) destroys the magnetization in this proton pool. Chemical exchange of the protons leads to an accumulation of saturated protons in the water pool and an enhanced reduction of the water signal.

3 Neuroscientific Fields for MRI

3.1 Epilepsy

3.1.1 About Epilepsy

Epilepsy is a neurological disorder that is characterized by recurring and spontaneous seizures, which are episodes of abnormally strong electrical discharges in groups of brain cells. Diverse underlying causes lead to a broad spectrum of epilepsy. Worldwide approximately 50 million people are affected by some form of epilepsy. Around 80% of them live in developing countries and most of them do not receive medical treatment (WHO, 2019b). The effects of the seizures may include involuntary movements, loss of consciousness, impairments of the development during adolescence, depression and social stigmata. The spontaneous nature of the seizures represents a considerable detriment in the quality of life for affected people. Anti-epileptic drugs (AED) are an effective means to inhibit seizures in the majority of epilepsy patients. However, AEDs merely suppress the seizures and do not cure the underlying cause. The success also depends on the type of epilepsy; in focal epilepsies around one third of patients are refractory to AEDs and alternative treatments have to be pursued (Laxer et al., 2014).

At the time the patients arrive at the clinic, they already have a history of seizures. The characterization of the manifestation of a seizure, obtained by description or video recordings during the diagnostics, may give first information about the type of epilepsy. In general, epilepsy syndromes can be divided into symptomatic, when a lesion in the brain can be associated with the seizure, or idiopathic, when no (observable) structural abnormalities exist. Furthermore, when at the onset of the seizure the electrical discharges occur across the whole brain, the seizures are said to be generalized. In contrast, seizures may also arise from a single focus and potentially generalize only as a secondary effect. This can be assessed by electroencephalography (EEG). EEG can also detect conspicuous potentials (e.g. spikes, sharp waves) typical for epilepsy between seizures. In routine clinical practice surface electrodes are used on caps with 20-128 channels. The spatial information of these EEG recordings is limited; inserting depth electrodes into the brain improves localization but is of course highly invasive. MRI is not able to verify the epileptic potentials but may help to identify an epileptic focus if the location of a detected lesion is in accordance with EEG and behavior. If AEDs, after trials with several different ones or in combination, were not sufficient to achieve a control of the seizures, all of the available diagnosis methods may be used for a pre-surgical evaluation. A resection of the lesioned zone is an option if a single focus is identified, whose removal promises seizure freedom and is possible without severe side effects.

3.1.2 Animal Models in Epilepsy Research

Taking AEDs in pharmaco-resistant epilepsy represents only a symptomatic treatment and tissue resection can only provide a permanent cure if the seizure origin was really focal and the pathological area was correctly identified and completely removed. But even after surgery, long-term follow up studies report complete seizure freedom only in 40% of people (de Tisi et al., 2011). Further research is needed to study the mechanisms, based on the molecular or network level, and to identify possible targets to treat the occurrence of seizures (ictogenesis) or the development of epilepsy (epileptogenesis) in the first place. Basic research can systematically be conducted on animal models, which ideally reproduce the molecular, cellular and connectivity changes that drive ictal or epileptogenesis (Pitkänen et al., 2017). Various animal models for different aspects of epilepsy exist. Popular rodent models are the pilocarpine and the kainate model for temporal lobe epilepsy. Systemic injection of pilocarpine or local injection of kainate provokes a status epilepticus (SE), which is a period of sustained seizures that may last several hours. SE results after a latent period in epileptogenesis and eventually in chronic seizures. Very different to these models is for example the kindling model of epilepsy. Kindling exerts repeated low intensity electrical stimuli. At first, these stimuli have a mild local excitation effect, but after some time a single stimulation results in a generalized seizure. However, this is rather a model for acute seizures and not epilepsy per se because only the threshold for seizure occurrences is lowered but without the occurrence of spontaneous seizures (Fritschy, 2004). More rodent models include the traumatic brain injury model and genetic models (Kandratavicius et al., 2014). Other models include flies, zebrafish or even sea-lions, but they have not found widespread use (Grone and Baraban, 2015).

Not every finding in an animal model can directly be related to seizures or epilepsy in humans. On the contrary, the induction of “epilepsy” in animal models in comparison to the “naturally” occurring disease in humans almost guarantees side-effects that are not related to human epilepsy. For example, systemic injection of pilocarpine results in generalized seizures, but they are caused by the brain wide cortical damage induced by the pilocarpine. This situation is different to epilepsy patients and the pilocarpine effect has to be separated from the epilepsy induced alterations. The development of better, more accurate animal models benefits from a better understanding human epilepsy and vice versa. Once established, animal models offer unique opportunities because the time of the initial insult is known and the time span of developments in animals are significantly shorter; weeks or month in animals in comparison to years or decades in humans. This allows studying the development and effects of treatments with the goal to identify biomarkers for at-risk subjects, predict outcome and therapeutic impacts. In the end the relevance of this basic research has to be determined with the hope that the most significant results can be translated to human diagnosis and treatment.

3.1.3 Temporal Lobe Epilepsy and the Kainate Model

Temporal lobe epilepsy (TLE) is the most common type of focal epilepsy and is characterized by focal seizures which originate in the temporal lobe from where they may spread across the brain. TLE can be divided into mesial TLE (mTLE), when seizures arise in the hippocampus (HC), and the rarer lateral TLE (lTLE), where seizures arise in the outer cortex. In the majority of cases, TLE is acquired and emerges during the childhood or adolescence. A cause can be an initial insult like a brain injury, infection or febrile seizure, which initiates the development of TLE. TLE is particularly often refractory to AEDs and in these cases resection of the epileptic tissue is a reasonable approach to gain seizure freedom. Compared to other types of epilepsy, relatively many TLE patients undergo surgical treatment. Many insights about epilepsy therefore come from TLE because the presurgical evaluation often includes intracranial EEG recordings to localize the origin of the seizures and the resected tissue offers the possibility to study the cellular alterations associated with the disease.

A frequent finding in these specimens is hippocampal sclerosis (HS) (Blümcke et al., 2007; Thom, 2014). HS comprises, to a variable degree, neuronal loss in the hippocampal subfields of the dentate gyrus (DG), the hilus and the cornu ammonis (CA), which is a layer of pyramidal cells that can be subdivided into CA1 to CA4 (Figure 3.1). The most severe neurodegeneration in the HC is found in regions CA1 and CA3. So-called mossy fibers connect granule cells in the DG to cells in the hilus and CA3. In response to the loss of the target cells, the axons sprout and form new connections within the HC. This synaptic reorganization is called mossy fiber sprouting. An additional markedly characteristic is the granule cell dispersion (GCD) in the DG. The underlying mechanism of GCD may involve newly generated neurons (neurogenesis) or abnormal migration of mature neurons and result in significant increase in the volume of individual cells as well as the whole DG. HS is accompanied by gliosis, which is a nonspecific reaction of the different glial cells to damage in the central nervous system. One remarkable feature is the radial gliosis in the dispersed DG (Fahrner et al., 2007; Haas and Frotscher, 2010).

The causes and consequences of these alterations are a subject of current research. The seizures itself can cause further cell loss and could promote this development. But epilepsy is defined by the occurrence of spontaneous seizures; permanent structural changes therefore cannot give the full picture of the disease. In general, HS is not a necessary prerequisite for epilepsy and even in mTLE HS is only found in ca. 60% of the patients. Nevertheless, cellular changes that influence neuronal excitation or inhibition and synaptic reorganization that creates recurrent local “short-circuits” may augment epileptogenicity. Also, the finding of HS in resected tissue is a good indicator for a positive outcome for the patient (Thom, 2014).

The kainate mouse model of mTLE replicates several features of the human pathology including HS and the occurrence of spontaneous focal seizures (Fritschy, 2004; Lévesque and Avoli, 2013). Kainate, or kainic acid (KA), is an excitatory neurotoxin that activates glutamate receptors. Local injection of KA into the dorsal HC in one hemisphere leads to an over excitation and a status epilepticus that lasts several hours. This is provoked by the acute effects of the KA, which also causes lesions around the injection site in CA1 as well as in CA3 and the hilus. But this is not sufficient to establish TLE. Only after latent period of 1-2 weeks, spontaneous epileptic seizures occur in the chronic stage. The cellular alterations in human TLE, like neuronal loss, GCD, and gliosis, are also found in the KA mouse model of TLE. That the acute damage is not sufficient to immediately trigger chronic seizures implies that additional mechanisms during the latent period are necessary. The KA mouse model hence offers a good opportunity to study the causal mechanisms during epileptogenesis.

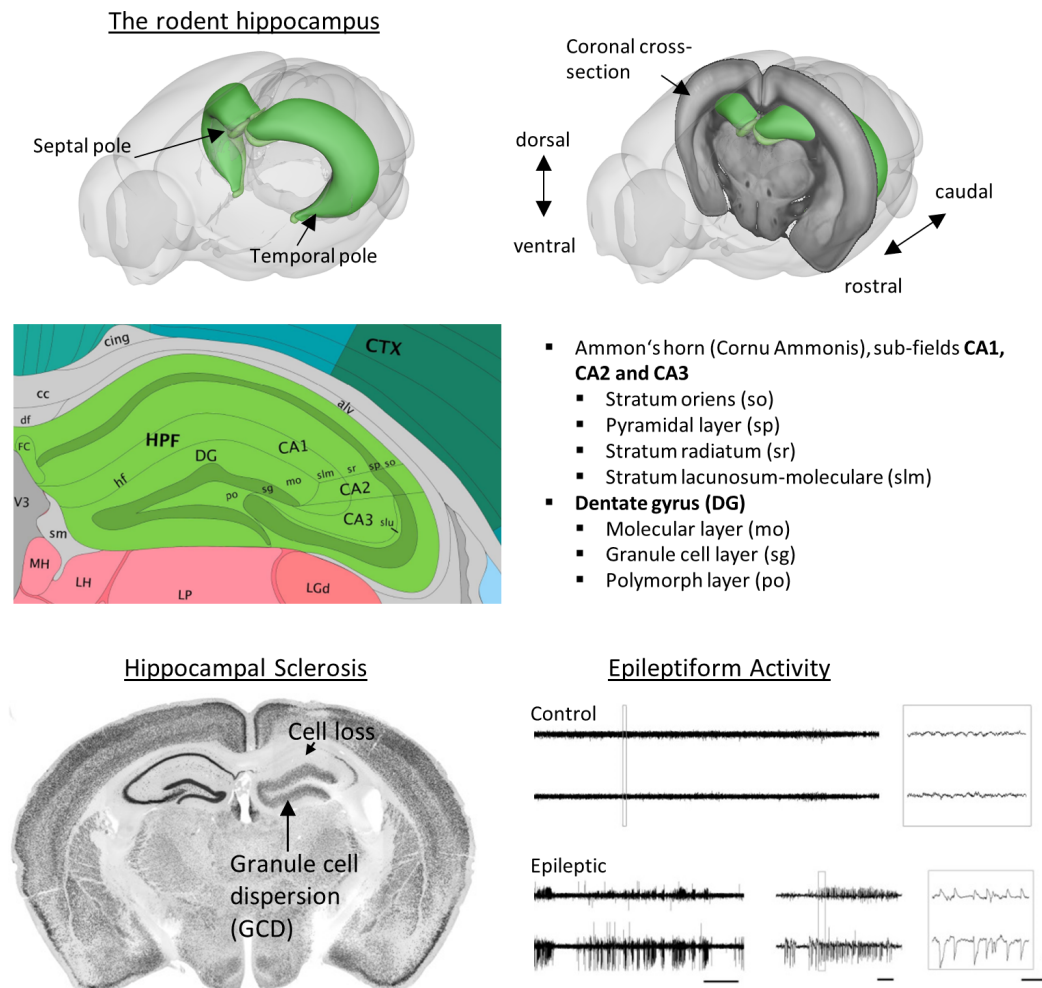


Figure 3.1: Illustration of the rodent hippocampus and the KA model of mTLE. Injection of KA into the right HC causes hippocampal sclerosis (HS) and eventually the occurrence of spontaneous epileptic activity. These features – unilateral HS and epileptic activity originating from this focus – are comparable to human mTLE. (Upper images adapted from scalablebrainatlas.org and the Allen brain atlas).

3.2 Optogenetics

3.2.1 Basic Principles

Optogenetics refers to a method that uses light (“Opto”) to control the function of genetically (“genetics”) modified cells. It enables to trigger or also inhibit action potentials in these cells, typically neurons, and thereby achieve a gain or loss of function. Optogenetics found widespread applications in basic neuroscience as it promises to overcome the limitations of alternative stimulation approaches, such as electrical stimulation, which is unspecific with respect to the stimulated cell types, or drugs, which act only on a very slow timescale. The key components in optogenetics are (1) the expression of light sensitive proteins (opsins) into the cell membranes, (2) the delivery of light via an optical system and (3) the readout of the induced function. The readout may be quantitative behavior, electrical recording or fMRI, which is described in Chapter 5. This section covers the biological basics (for engineers and physicists) and targeting strategies (Figure 3.2).

That cells developed ways to respond to light is most obvious in the visual system of animals or humans. Photoreceptors, which are light sensitive cells, on the retina in the eye are able to absorb photons and thus enable vision. Responsible for this is rhodopsin, which is a light-sensitive protein that consists of two components: opsin and retinal. Opsin belongs to the group of transmembrane proteins, which are proteins that span the membrane of the cell and permit the transport of specific substances through the membrane. Retinal, a form of vitamin A, is a chromophore that is able to absorb photons. In rhodopsin, retinal is bound to the protein and, upon absorption of a photon, isomerizes which triggers a sequence of configuration changes of the protein. The protein then acts as a channel or pump leading to a transport of substances (ions or protons) through the membrane. This alters the membrane potential and may trigger or inhibit subsequent action potentials. The modified retinal afterwards is either replaced by new retinal or transforms itself back into its original configuration, whereby the latter is the case in the opsins used for optogenetics. The bindings of retinal and the environment inside the protein determine the spectral and kinetic characteristics of each individual protein.

Opsins can be divided in two distinct groups; the mentioned opsins for vision belong to type II that are found only in higher life-forms such as animals. Type I opsins can, for example, also be found in unicellular organisms such as green algae. Since these microbial opsins are used (Boyden et al., 2005), the field of optogenetics has expanded rapidly as they offer important advantages. They respond much faster than type II and thus can operate in the same millisecond-timescale as neuronal activity takes place. They also are a single-component in the sense that light-sensing and ion conductance is combined by the same protein. The required retinal was found to be sufficiently present in mammalian cells. Many different opsins have been investigated and designed with

respect to the desired kinetics, wavelength sensitivity and ion selectivity (Adamantidis et al., 2014; Tye and Deisseroth, 2012). For example, bacteriorhodopsin (BR) is sensitive around 500nm and acts as a proton pump, halorhodopsin (HR) is maximally sensitive at 589nm and acts as a chloride pump and channelrhodopsin (ChR) is maximally sensitive at 470nm and acts as an ion channel.

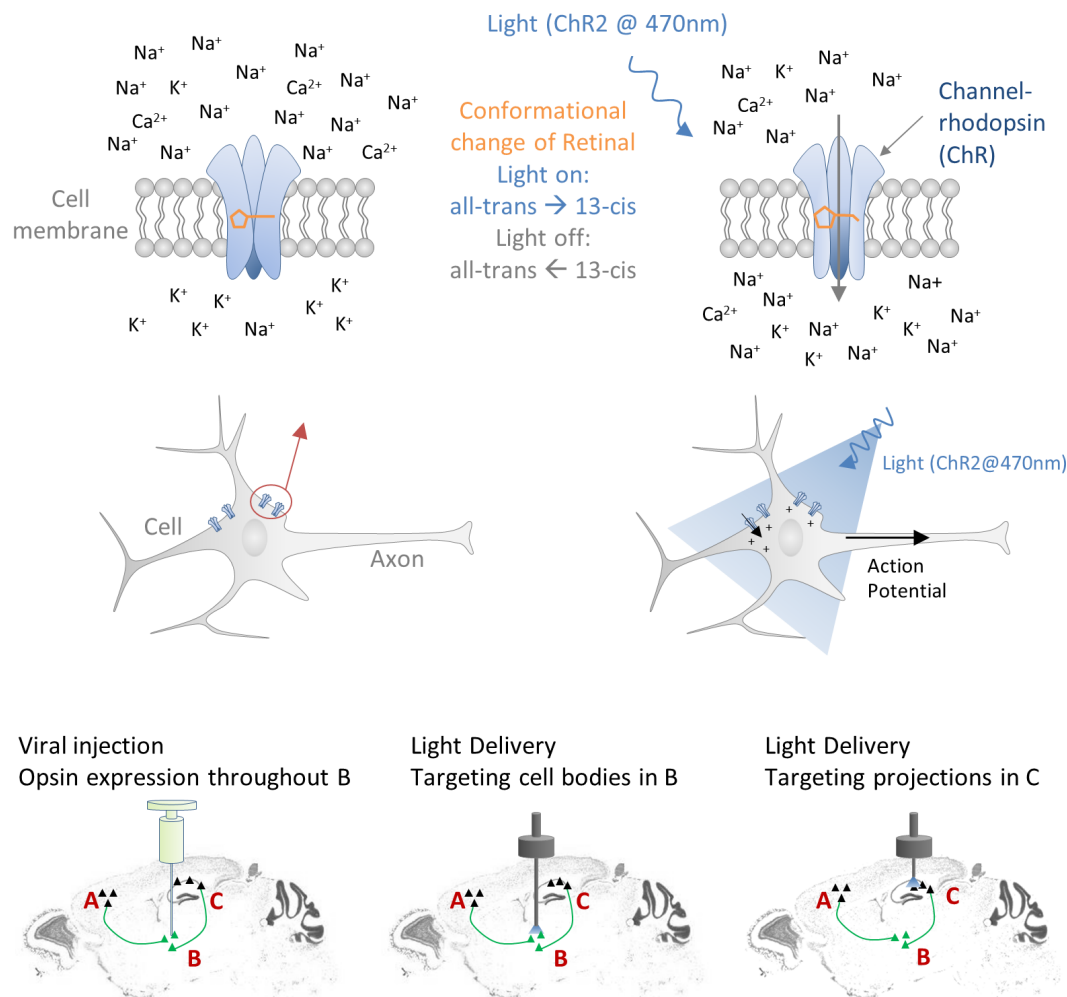


Figure 3.2: Illustration of optogenetic stimulation. Upper rows) The transmembrane protein channelrhodopsin (ChR) is expressed in neuronal cells. The retinal bound in ChR changes its conformation upon absorption of light at 470nm and opens the transmembrane protein allowing diffusion of ions across the membrane. The influx of positive ions depolarizes the cell and triggers an action potential. When the light is turned off, retinal transforms itself back and closes the membrane. The resting potential is subsequently restored. **Bottom row)** Different targeting strategies. The virus is injected into region B and ChR is expressed in cell bodies in B. Applying light in B stimulates all of these cells. Applying light in C stimulates only axonal projections from B to C.

Viral vectors are used to deliver the opsin gene into the cells. The viral vector also contains, adjacent to the opsin gene, a promoter, which is a sequence on the DNA that initiates the transcription of the DNA within the cell. Specific cells can be targeted by specific promoters. Injection of the viral vector then leads to an expression of the engineered opsin in the infected cells. Different spatial targeting strategies may be employed. For example, virus injection and light can be applied at the same anatomical region, which leads to a stimulation of cell bodies in the region while leaving passing fibers unaffected. For comparison, electrical stimulation cannot discriminate axons and cell bodies. Alternatively, the virus can be injected into region A and light is applied to region B, which stimulates only axonal projections from A to B (Yizhar et al., 2011).

3.2.2 Optogenetics in Epilepsy Research

How optogenetic activation or inhibition of cells may help to study the mechanisms of a disease is illustrated here for the field of epilepsy. In focal epilepsies, structural abnormalities may exist, but they are permanent and hence they alone cannot fully explain the spontaneous but intermittent occurrence of seizures. Moreover, the circuit dynamics have to be considered. Research objectives include (1) the seizure focus, besides its location also the identification of specific cells responsible for triggering or maintaining epileptiform activity, (2) the influence of circuits in promoting and spreading the activity and (3) strategies for interference.

In the conventional assumption, epileptic activity is assigned to an imbalance between excitation and inhibition. When for example in the epileptic focus, a degeneration of interneurons leads to a reduced inhibitory function, epileptiform activity may be driven by excessive excitatory principal cells. Several studies investigated this by expressing halorhodopsin in excitatory principal neurons in the epileptic focus and using light stimulation to hyperpolarize and silence these cells. Thereby, epileptiform activity could be suppressed in organotypic hippocampal slices (Tønnesen et al., 2009), tetanus toxin induced focal cortical epilepsy (Wykes et al., 2012) and kainate induced TLE (Berglind et al., 2014). Complementary studies used ChR2 to activate inhibitory GABAergic interneurons in order to suppress epileptic activity in acute hippocampal slices (Ledri et al., 2014) and the kainate model for TLE in-vivo (Krook-Magnuson et al., 2013).

Local short-range reorganizations are thought to be the primary cause of the disease, but in addition long-range connections may also have an influence. Paz et al. demonstrated this by investigating the cortex-thalamus-cortex circuit. In the employed rodent model, epilepsy was induced by a cortical stroke. The thalamus, consisting of excitatory and inhibitory neurons, is remote from the injured cortex but connected to it. Epileptic seizures could be interrupted by inhibiting the output from the thalamus (Paz et al., 2013). Similar to this strategy, the cerebellum was targeted to modulate and inhibit seizures arising in the hippocampus in TLE (Krook-Magnuson et al., 2014).

Recently, the role of the dentate gyrus as a specific node in TLE was investigated using optogenetics. The dentate gyrus forms the input to the hippocampal formation and may prevent an over excitation. Structural alterations in epilepsy may change the normally low to a high excitability of the dentate gyrus. In order to restore the original function, the dentate granule cells were selectively inhibited, which could stop spontaneous seizures in TLE (Bui et al., 2018; Krook-Magnuson et al., 2015).

Several studies could identify critical structures for epileptiform activity. Also, closed-loop systems were developed to detect and inhibit spontaneous seizures (Krook-Magnuson et al., 2013). So far, optogenetics is inherently basic research and because of the necessary genetic manipulation there is no direct translation to human treatment. However, new insights into the disease mechanisms may help to develop new AEDs or find targets for electrical stimulation.

4 Using High-Resolution Diffusion MRI and ¹H-MRS to Monitor Epileptogenesis

Most of the results in this chapter were published in:

“Early tissue damage and microstructural reorganization predict disease severity in experimental epilepsy”, Janz P*, Schwaderlapp N*, Heining K*, Häussler U, Korvink JG, von Elverfeldt D, Hennig J, Egert U, LeVan P*, Haas CA*, eLife, 2017

*Contributed equally. Contributions:

P. Janz: All surgeries (kainate/saline injection and implantation of electrodes), EEG recordings, and histochemistry. Planning of the study and interpretation of the results. Writing and editing on the manuscript.

N. Schwaderlapp: All MR related work (design and optimization of experimental protocols, scanning of animals, all image processing and analysis, and evaluation of the results). Planning of the study and interpretation of the results. Writing and editing on the manuscript.

K. Heining: Analysis of the recorded EEG data.

4.1 Introduction

Epilepsy does not emerge instantly but the development of cellular and structural changes eventually manifest as state in which spontaneous seizures occur. This process is termed epileptogenesis. The earlier prognostic alterations during epileptogenesis are recognized, the more time there is for a possible treatment. One property of TLE that develops over time is hippocampal sclerosis and related cell loss and structural changes can be explored by MR spectroscopy and imaging. The features of human TLE are replicated in the KA mouse model offering a good opportunity for systematic research. MR investigations in the mouse brain require high quality spectra and high-resolution imaging to investigate hippocampal subfields. In our study, state-of-the-art preclinical hard- and software was employed to characterize epileptogenesis in the KA mouse model. The MR findings were retrospectively correlated with histology and electrophysiology. The slower developments in human TLE patients could not be observed in the given time, however we investigated resected sclerotic tissue from TLE patients to validate our preclinical findings and prove the translational value of this study.

4.2 Monitoring of Epileptogenesis by MRI and MRS – State of the Art

Established TLE in humans can be revealed by identification of hippocampal sclerosis (HS). The affected hippocampus shows increased signal intensity in T₂-weighted images and a reduced volume (Gomes and Shinnar, 2011; Urbach et al., 2014). The pathophysiological correlation of the increased signal is not entirely clear but it can easily be identified in unilateral HS by comparison with the contralateral HC. With DTI an increase of the mean diffusivity and a decrease of FA in the ipsilateral hippocampus were reported (Assaf et al., 2003; Gross, 2011; Thivard et al., 2005), although there is variability among different studies which is probably caused by the heterogeneity of patients and the coarse resolution (e.g. only the average FA in the HC was reported and not differentiated into the HC subfields).

MRS findings were first limited to metabolites routinely detectable on 1.5 or 3 T clinical scanners. TLE studies detected an ipsilateral reduction in NAA, suggesting neural loss, and an increase in Cr and Cho, pointing to astrogliosis. The ratio NAA/(Cho+Cr) could thereby be used to lateralize the epileptic focus (Connelly et al., 1994; Cross et al., 1996). Newer studies additionally looked into Glx/Cr or GABA/Cr ratios but did not find significant changes (Simister et al., 2009). Nowadays glutamate and GABA detection is improved by edited spectroscopy, e.g. MEGA PRESS, which was applied to idiopathic generalized epilepsy (Chowdhury et al., 2015), but since this is not routine clinical practice, results in TLE are scarce.

The findings in humans represent the current state or risk factors, but they do not describe the progression during epileptogenesis. Most longitudinal studies focusing on epileptogenesis in humans are limited by small patient cohorts and short follow-up periods. There is one larger prospective study, FEBSTAT (“Consequences of Prolonged Febrile Seizures in Childhood”), addressing the relationship between febrile status epilepticus (FSE) and the development of HS and TLE (Hesdorffer et al., 2012). Approximately 200 children with FSE undergo examinations - including T₁-weighted, T₂-weighted and diffusion weighted MRI – within 72 h and after 1, 5, 10 and 15 years. This study is not completed yet, but preliminary data suggest the predictive value of T₂ hyperintensity for the development of HS (Lewis et al., 2014).

Various magnetic resonance methods were applied in over 50 studies of animal models of epilepsy. A comprehensive overview can be found in (Bertoglio et al., 2017). Anatomical T₂-weighted MRI showed acute signal hyperintensity in different brain areas after pilocarpine-induced SE in rats (Roch et al., 2002). The temporal development of these changes reveal acute edema followed by a normalization and later structural atrophy (Choy et al., 2010). Quantification of T₂ relaxation time was used to track changes during epileptogenesis that correlated with the later epilepsy (Dietrich et al., 2016).

Using diffusion MRI, ADC changes in the hippocampus at acute and chronic time-points were found (Gröhn et al., 2011; Kharatishvili et al., 2014). High-resolution ex-vivo DTI could detect hippocampal subfield specific changes; an increase in FA in the DG was related to a reorganization of the dentate granule cells (Laitinen et al., 2010; Sierra et al., 2015). High-resolution in-vivo DTI showed progressive changes in the DG after induced SE in rats (Salo et al., 2017).

Similar to human epilepsy, ¹H MR spectroscopy detected a reduction of NAA in the rat pilocarpine model in acute and chronic stages (Gomes et al., 2007; Lee et al., 2012). Also changes of GABA and Glu during epileptogenesis were investigated using edited MRS (van der Hel et al., 2013).

Derived from the state of the art, four major points were identified by which our study may be of value for TLE research:

- The KA mouse model is well established but MRI studies of this model are rare. Many of the studies are for example based on the pilocarpine rat model, which might be easier to handle but lacks important features like unilateral hippocampal sclerosis. At the beginning of this project, no longitudinal in-vivo MRI study had been performed in the KA mouse model.
- State of the art hard- (7T and CryoProbe) and software (ParaVision 6) promise more than only better images. The clear identification of hippocampal subfields in mice with a high spatial resolution may be challenging but is important for the interpretation of the MRI findings. Likewise, in early MRS studies the necessary large voxel covered both hemispheres limited the validity of the results.
- Most of the conducted studies focus on a single method like diffusion MRI or spectroscopy. Within the scope of this longitudinal study several MR methods (anatomical MRI, diffusion MRI and spectroscopy) were applied as well as complementary characterization by electrophysiology and histology, which allows the multimodal combination of the individual results and the evaluation of the ability of MRI to act as a non-invasive biomarker of features usually obtained with invasive techniques.
- The infrastructure of the University Medical Center Freiburg allows to run the study of the KA mouse model of TLE as well as to obtain hippocampal tissue resected from TLE patients. These specimens could be investigated with the same methods and the preclinical findings could thereby be directly translated into clinical research.

4.3 Methods

In the wider context of this study experimental epileptogenesis is characterized by multimodal measurements. This chapter focuses on MRI and describes the details of the applied MR methods. Animal treatment, histochemistry, electrophysiology and human ex-vivo tissue preparation are extensively covered in the joint publication (Janz et al., 2017) and described here only insofar it is necessary for the understanding of the respective section.

All MR measurements were conducted on the following system:

- 7 Tesla small animal system (BioSpec 70/20USR by Bruker BioSpin, Ettlingen, Germany), max. gradient strength 660 mT/m, ParaVision 6.0
- ^1H quadrature transmit/receive CryoProbe (closed cycle helium cryocooler)

4.3.1 Experimental Design

KA injection triggers a status epilepticus (SE) that lasts several hours and one to two weeks later epileptic activity begins to occur. To cover this development mice were scanned before KA injection and at five time points following SE (Figure 4.1). To avoid interfering with the animal model, mice were not scanned during SE but 1 day later. After the last MR measurement, electrodes were implanted to record the EEG. These electrodes were not MR compatible therefore EEG recording was not possible during the epileptogenesis (MR compatible electrodes for simultaneous EEG and MRI were tested later in the project, see chapter 5). Five days later animals were sacrificed for immunohistochemistry (IHC). Saline injected animals served as controls. These animals have the same physical injury due to the needle injection but without the KA effect. In total eight KA and five control mice were included in the study.

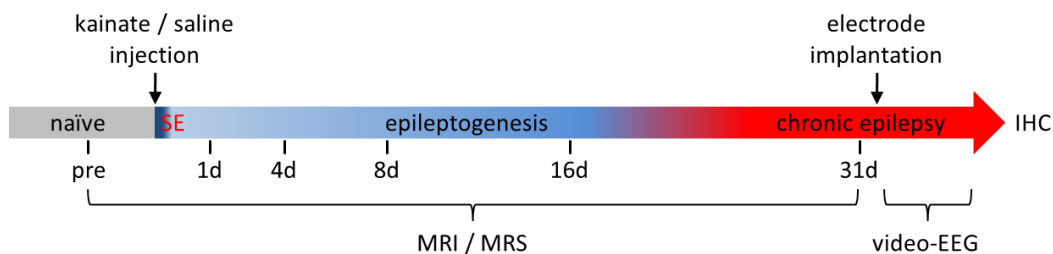


Figure 4.1: Experimental design.

4.3.2 Preclinical in-vivo MR measurements

4.3.2.1 General Setup

The usual procedure is described here in chronological order. The animals are kept in groups of 4-6 mice per cage with sufficient water and food. Initially, a mouse is placed in a box and anesthetized with 2-4% isoflurane added to oxygen at a flow of 3-4 l/min for ca. 1-3 minutes. The mouse is then placed on the dedicated MRI mouse bed (Bruker, Germany) and isoflurane is reduced to 1.2-1.6% at 1.2 l/min. A pressure sensor beneath the mouse body is used to monitor the respiration and isoflurane is adjusted to keep a respiration rate of 70-90 breaths/min throughout the scan. The mouse is restrained on the bed with teeth and ear fixation. The body temperature is monitored by a rectal temperature probe and a closed water heating system is used to maintain a body temperature of 36 ± 1 °C. A blood-oxygen saturation sensor could optionally be attached at the tail. The eyes were covered by a gel (Bepanthen, Bayer) to prevent a dry out. The mouse is then placed inside the MRI system. The total time including the preparation and scanning amounted to 2.5 hours per animal. The method is illustrated in Figures 4.2 and 4.3, the MR protocols are listed in Table 4.1 and described in the following sections.

For the sake of completeness, it should be mentioned that a resting-state fMRI scan was also performed. For this purpose, the anesthesia was induced by sub cutaneous infusion of medetomidine. Unfortunately, rsfMRI did not yield any meaningful results, which is why it is not addressed in this chapter. One probable reason was the too low SNR of the scan. Separate fMRI experiments are covered in chapter 5.

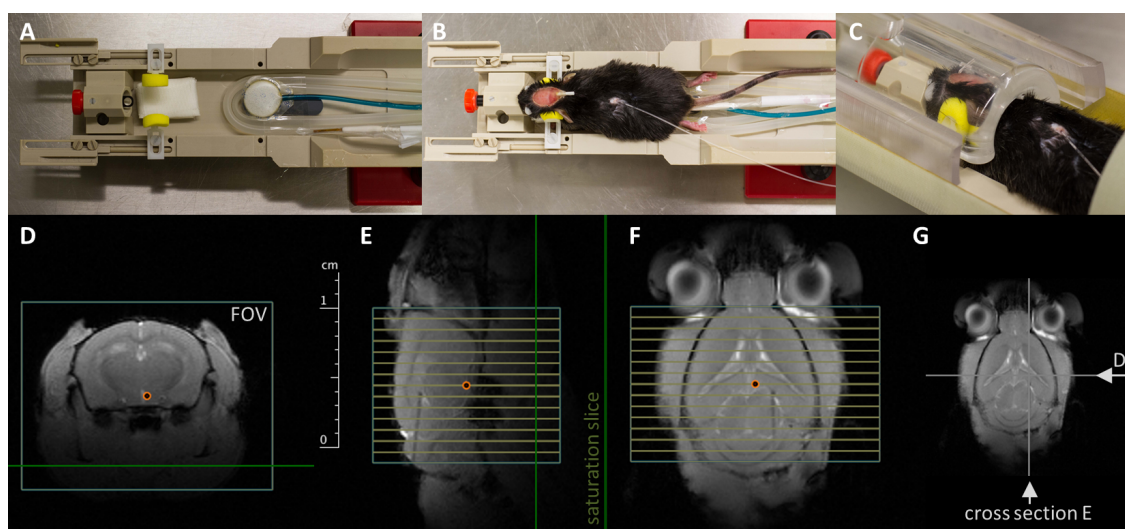


Figure 4.2: Setup for mouse brain MRI. **A)** Mouse-bed with head-fixation, pressure sensor, temperature probe and water tubes for heating. **B)** Attached mouse; anesthesia by isoflurane supply through the nose cone as well as subcutaneous infusion of medetomidine. **C)** Mouse placed into a replica of the CryoProbe. **D-F)** Localizer scan with indicated slice geometry for the anatomical/diffusion MRI scans. The green bar indicates the location of a saturation slice which is applied to eliminate the signal outside of the FOV.

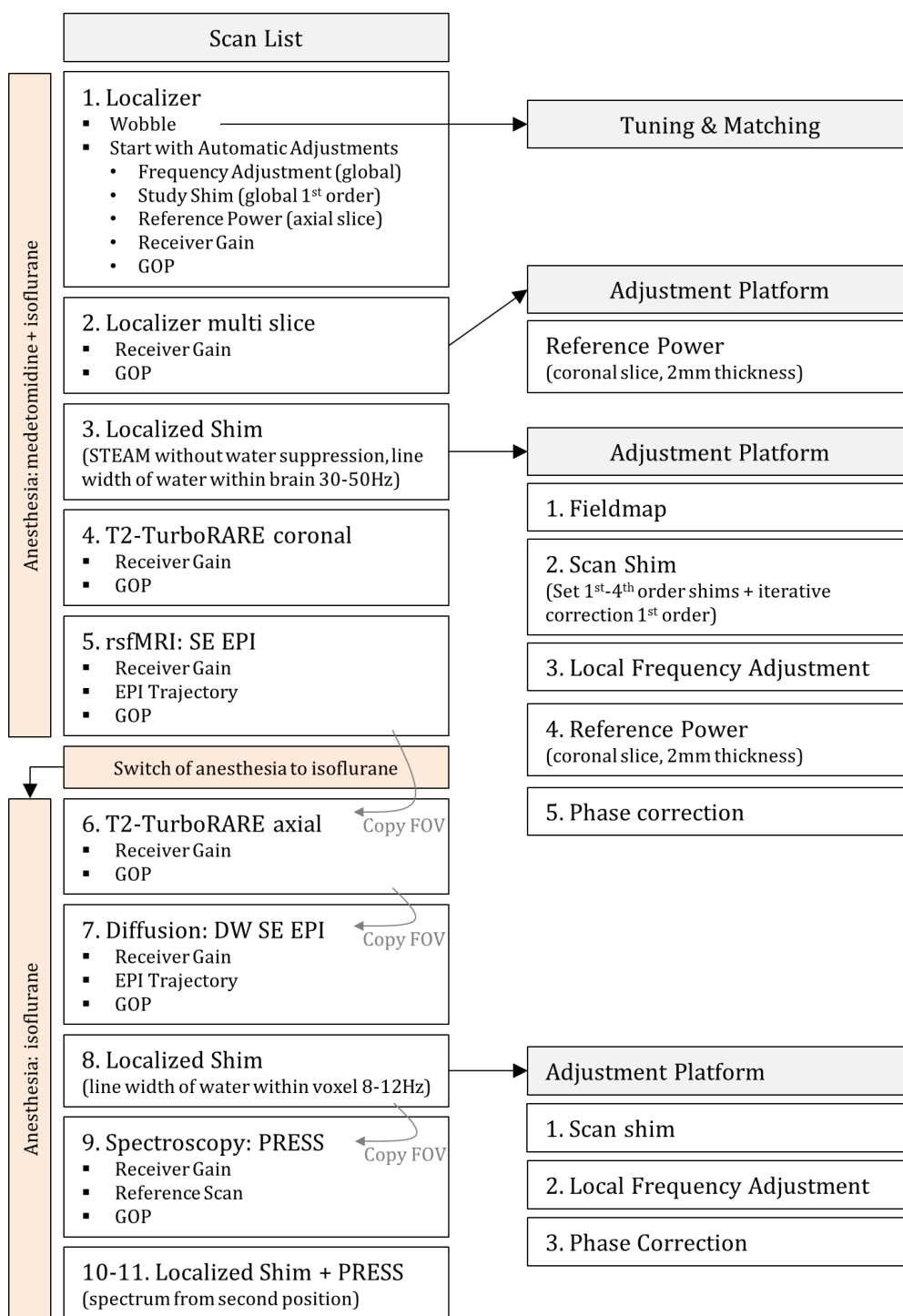


Figure 4.3: Scanning procedure. The main sequences and corresponding adjustments are listed (Orientations “coronal” and “axial” refer to scanner orientations. The Bruker term “GOP” means start of the sequence).

		RARE	DWI	PRESS
Contrast	TR	3 s	2.5 s	2.5 s
	TE	50 ms	33 ms	20 ms TE1=TE2=10ms
Geometry	Matrix Read x Phase	440 x 256	220 x 128	
	FOV Read x Phase	12.76 x 7.424 mm		Voxel 1.4x1.4x2 mm
	In-Plane Resolution	29 x 29 μ m	58 x 58 μ m	Spectral Res. 1.22 Hz/point
	Slices	22, contiguous, interleaved		
	Slice Thick- ness	0.4 mm		
Encoding	Acquisition Matrix	316 x 184	158 x 90	
	Interpolation	Read 1.4, Phase 1.4	Read 1.4, Phase 1.4	
Acquisition		RARE Factor 4	EPI Segments 3	
	Echo Spacing	25 ms	0.632 ms	
	Acq. Band- width	33 kHz	250 kHz	5 kHz (16.65ppm)
	Acquisition Duration		EPI Module 20.86 ms	2048 Points, 409.6 ms
	Exc. Pulse	90°, 2.1 ms, 2 kHz	90°, 2.7 ms, 2.2 kHz	90°, 0.8 ms, 5.3 kHz
	Ref. Pulse	180°, 1.8 ms, 2 kHz	180°, 3 ms, 1.7 kHz	180°, 1.85 ms, 1.8 kHz
Diffusion	Directions A0/A		3/30	
	b-value [s/mm ²]		1000	
	Gradient Duration		2.5 ms	
	Gradient Separation		14 ms	
	Max. Strength		434 mT/m, (64%)	
Time	Averages	6	6	400
	Acq. Time	13 min 48 s	24 m 45 s	16 m 40 s
	Acq. Time Triggered	20-25 min	40-60 min	

Table 4.1: Applied MR protocols.

4.3.2.2 RARE

The protocol was set up with a focus on high resolution so that the hippocampal subfields are distinguishable (Figure 4.4). The anatomy of the rodent brain shows structural changes in the rostro-caudal direction not as subtle as in the dorso-ventral direction. The in-plane resolution therefore was set to be higher than in the slice direction. The same applies to the diffusion MRI protocol.

After the study, one dataset was selected as reference and all other RARE images as well as a labeled brain atlas (AMBMC, University of Queensland, AUS) were registered to it using FLIRT (FSL toolbox, FMRIB, Oxford, UK). Image intensities were normalized by equalizing the mean intensity in the ipsilateral thalamus. Mean signal intensities were quantified in the hippocampal subfields CA1 and DG.

One to some degree neglected issue in the quantification is the displacement of the borders inside the HC due to the granule cell dispersion in the DG. To minimize this effect, the HC was only subdivided into DG and CA1 and not into the even finer individual sublayers. This would only be possible with a manual segmentation.

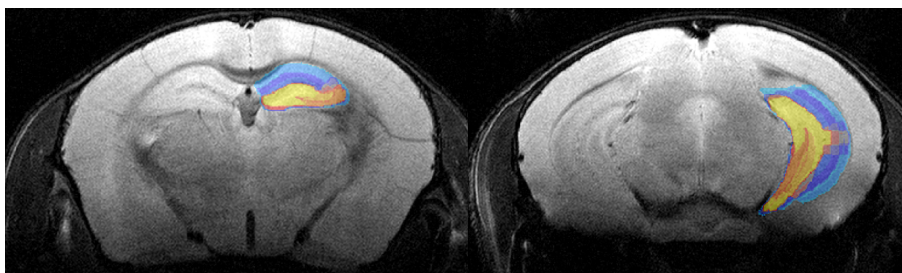


Figure 4.4: Representative RARE images. The registered labels (colored overlay) indicate the hippocampal subfields CA1 (blue), CA3 (orange) and DG (yellow).

4.3.2.3 Diffusion Weighted MRI

The applied protocol is listed in Table 4.1 and representative images are shown in figure 4.5Table. Misalignments of the individual images caused by frequency drifts or actual animal motion were corrected by registration of the images to the first non-diffusion weighted image using FLIRT (FSL toolbox, FMRIB, Oxford, UK). The diffusion tensor and corresponding quantities (Fractional Anisotropy FA, mean- (MD), axial- (AD) and radial- (RD) diffusivity) were calculated using an in-house built MATLAB tool (DTI-FiberTools, Medical Physics, University Medical Center Freiburg). In addition, the dorso-ventral diffusivity (dvD) was assessed by calculating the extent of the diffusion ellipsoid in this direction. All datasets and the labeled atlas were registered to the reference dataset as described previously. Additionally, a fiber tractography approach was applied using the DTI-FiberTool (with default settings regarding tracking, only the visualization was adapted) based on (Reisert et al., 2011).

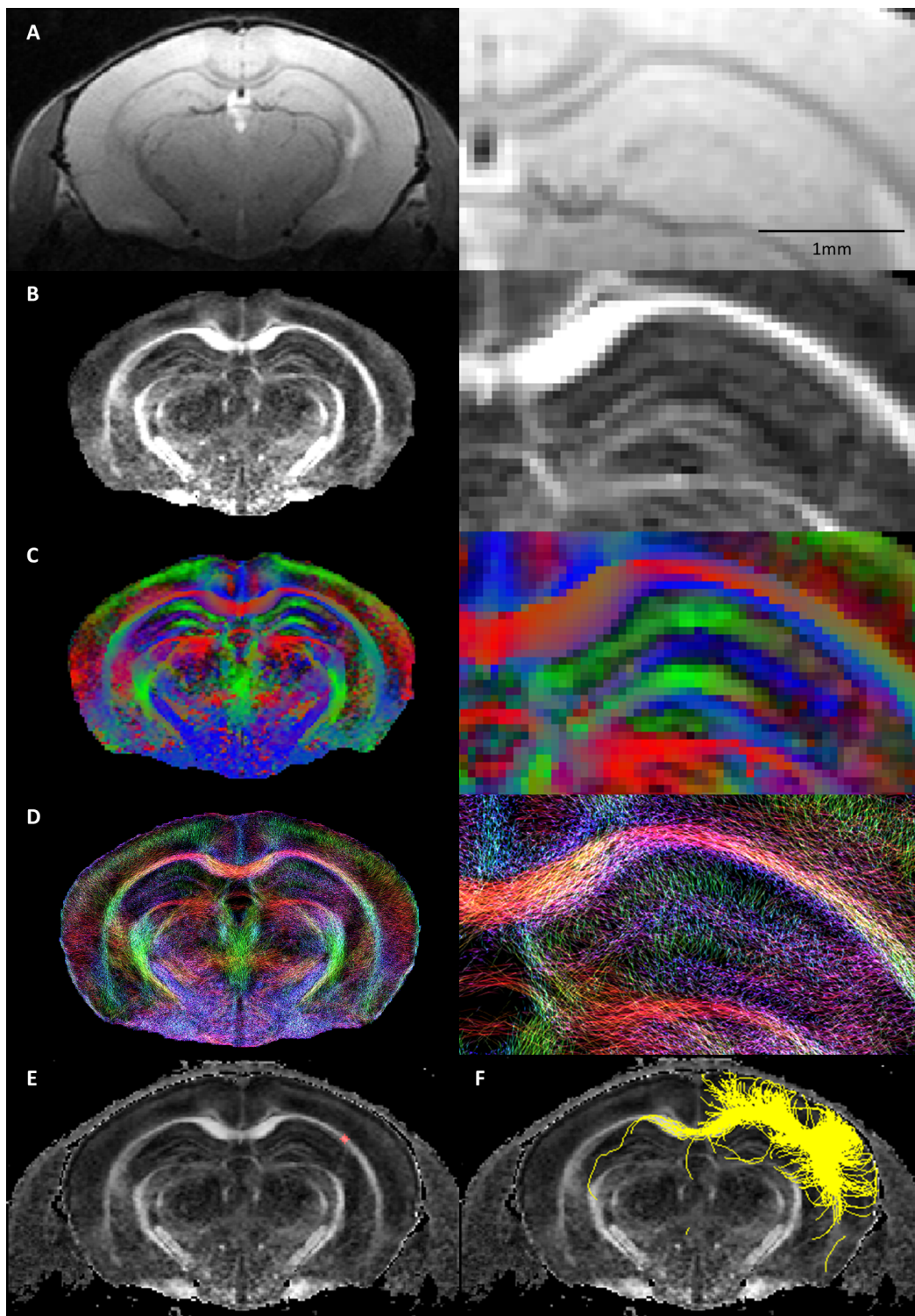


Figure 4.5: Representative results of diffusion MRI. A) Spin-echo EPI without diffusion weighting. Right: Enlargement of the hippocampus. B) Fractional Anisotropy (FA). C) color-coded FA: right-left (red), up-down (green), through-plane (blue). D) Tractography-model. E) Red dot: selected ROI (background figure FA map). F) Illustration of all fibers from the tractography-model passing through the selected ROI.

4.3.2.4 Spectroscopy

MR spectroscopy of several nuclei like proton (^1H), carbon (^{13}C) or phosphorous (^{31}P) would theoretically be interesting. From those, only ^1H MRS is feasible in this study because of the employed CryoProbe. Spectra obtained from an MRI system are of course not as differentiated as those from a dedicated MRS system. However, in-vivo MRS is feasible and in the case of MRS in mice with a focus on the hippocampus (HC) there are even beneficial characteristics; the HC is relatively large in rodents compared to humans and is located towards the top of the brain close to the surface-transmit/receive CryoProbe (Figure 4.6, left). The PRESS sequence was preferred over STEAM as it provides more signal. The parameters are listed in Table 4.1. Spectra from the ipsi- and contralateral septal HC were acquired and quantified with LCModel (S. Provencher, LCModel Inc., Canada). A representative spectrum is shown in figure 4.7.

First estimates for the quality of a spectrum are the linewidth FWHM (full width at half-maximum) and the SNR. In this study, unsuppressed water signals acquired after the shimming showed linewidths in the order of 8-12 Hz (0.025-0.04 ppm). Also, the LCModel evaluation for the representative spectrum resulted in 0.02 ppm FWHM. LCModel specifies the SNR as the ratio of the maximum in the spectrum to twice the root-mean-square residuals, which was in the range of 30 for the acquired spectra. Another important point to consider are frequency drifts (Figure 4.6, right). Navigator signals with low flip angles and no water suppression are acquired to compensate field drifts during the acquisition. For an unknown reason this has worked reliably only since software version PV6 and not with the previous PV5. For water suppression the initial settings in PV6 for the pulse amplitudes in VAPOR were in general appropriate. Only in a few cases, the pulses had to be manually optimized. Outer volume suppression was applied and the working frequency was set to -2.5 ppm to minimize the chemical shift displacement of the metabolites of interest (e.g. Glu).

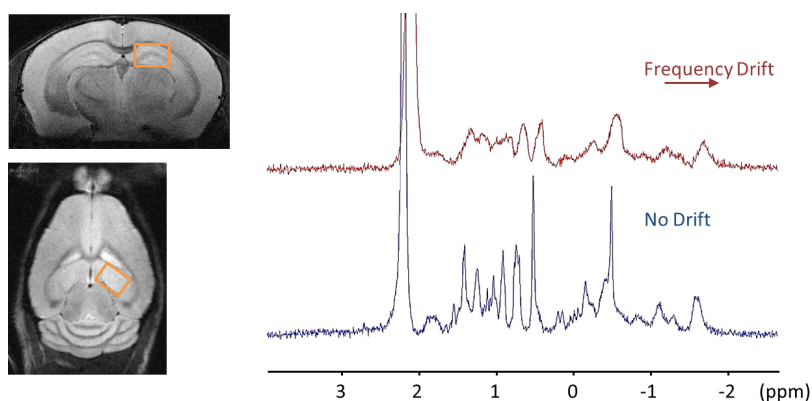


Figure 4.6: In-vivo Mouse brain spectroscopy. **Left)** Location of the PRESS voxel (1.4 x 1.4 x 2mm). **Right)** Acquired spectra. One indication for a low-quality of a spectrum are broad peaks (top). In this example, uncompensated frequency drifts during the 15min acquisition are the reason for the broad peaks. A drift correction during the acquisition yields spectra of a much higher quality (bottom), which is required for the identification of individual metabolites.

A simulated basis set for the evaluation of the acquired spectra (using PRESS, TE=20ms, f=300MHz) was obtained from S. Provencher. As suggested in the LCModel manual, eddy correction was only applied in ParaVision and no zero-filling or exponential filtering was applied. Absolute concentrations were calculated using a reference scan without water suppression. However, MRS on the used scanner was not calibrated using phantoms with known concentrations. This means that the obtained concentrations are consistent but represent “institutional units” probably differing from mM by a constant factor (see LCModel manual).

SNR and linewidths are rough estimates for the quality of a spectrum. The best criteria for high-quality are reliability and reproducibility (assuming that there are no systematic errors in which case even a high reproducibility would be misleading). LCModel gives estimated standard deviations (SD) or Cramér-Rao lower bounds (CRLB), which are lower limits and have to be multiplied by 2 to get 95% confidence interval. Many groups use a SD<15% as acceptance threshold.

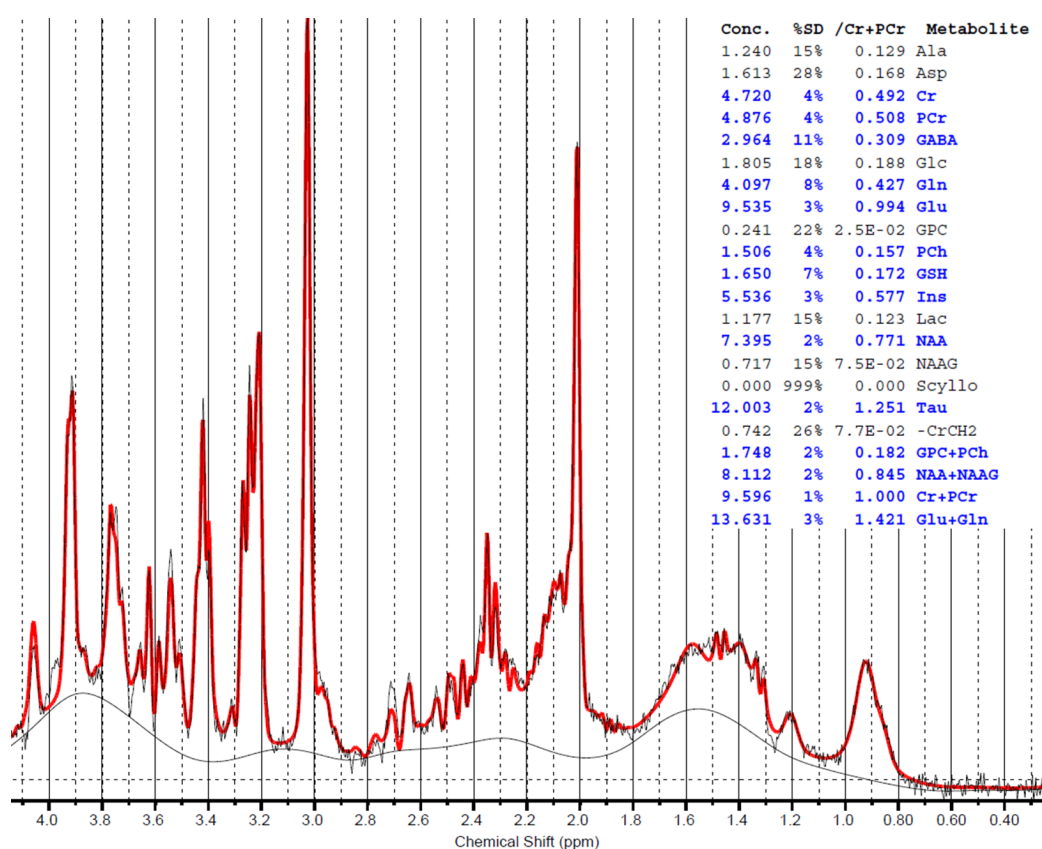


Figure 4.7: In-vivo spectrum evaluated with LCModel. Red line: LCModel fit to the acquired spectrum (gray noisy line below the red line; bottom gray line: baseline). Concentration table: absolute concentrations (Conc.), estimated standard deviations (SD) and ratios to total creatine (/Cr+PCr). Metabolites with a SD<15% are in boldface blue (for individual metabolites see figure 4.8). Metabolites not routinely detectable because of their low concentrations and/or complex spectra are: L-Alanine (Ala), Aspartate (Asp), Glucose (Glc), Glycerophosphocholine (GPC), L-Lactate (Lac), N-Acetylaspartylglutamate (NAAG), scyllo-Inositol (Scyllo).

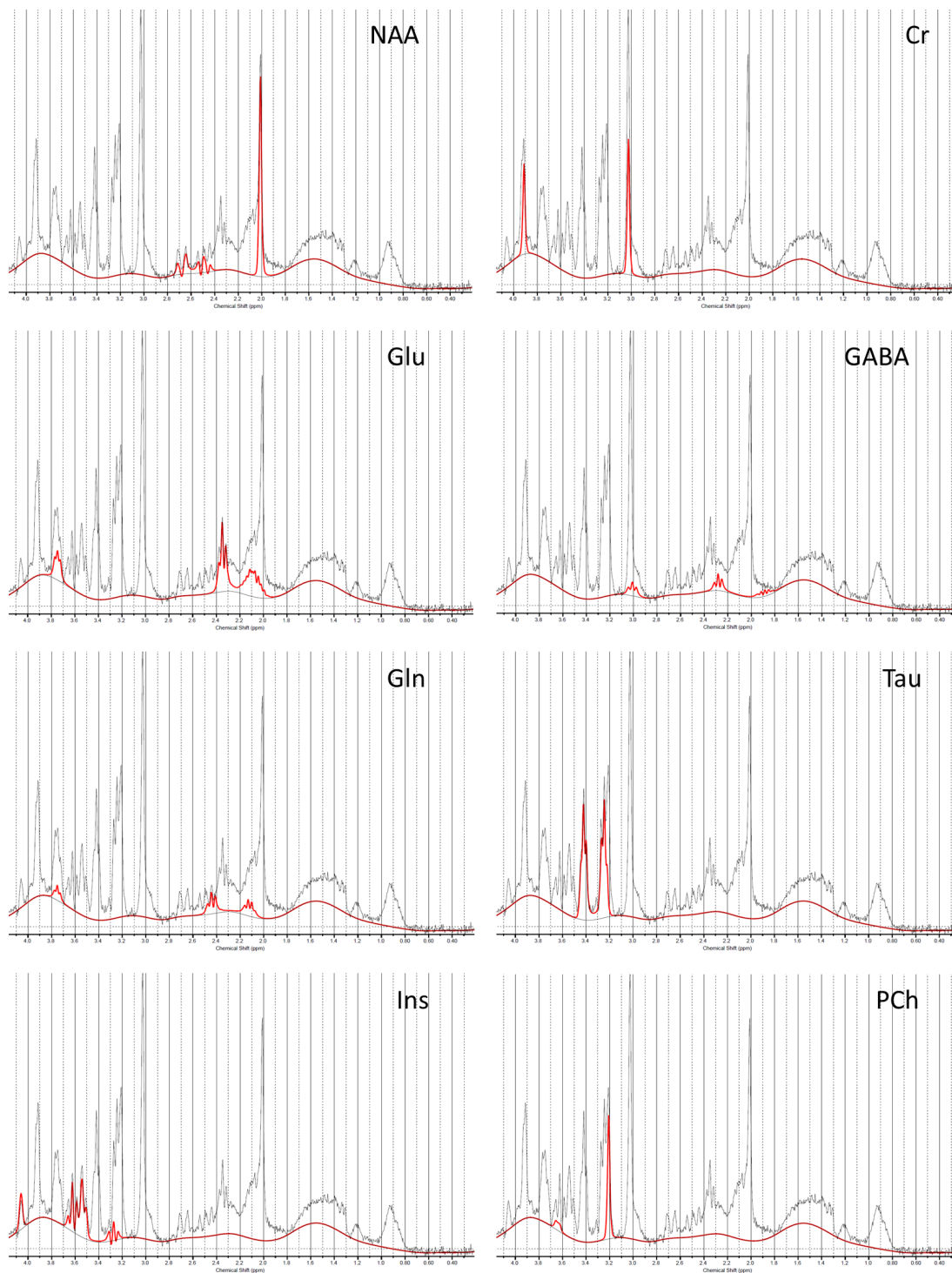


Figure 4.8: Contributions of individual metabolites to the spectrum. N-Acetylaspartate (NAA), Creatine (Cr), Glutamate (Glu), γ -Aminobutyric Acid (GABA), Glutamine (Gln), Taurine (Tau), myo-Inositol (Ins) and Phosphocholine (PCh).

Table 4.2 lists the MRS results of the 13 mice scanned before any treatment. This allows the comparison of the estimated with the real deviations and the determination of the reliability. Usual reference compounds like NAA and total creatine are easily identifiable and have a low CRLB (2-3%). The actual deviation among all animals is only a few percent points higher (4-7%) originating from experimental variations due to differences in voxel position and animal physiology. This is similar to Glu and even GABA which shows that these compounds can be analyzed. The detection of Lactate however with a CRLB of $\approx 18\%$ and an actual deviation of $\approx 33\%$ is not naively possible. Lactate can only be reliably detected in the case of a strong increase. A prediction about the detection of Ins is difficult. A constantly low CRLB of 3-5% but a much higher actual deviation of $\approx 13\%$ indicates a high variability among the animals. The preconditions for the study were nonetheless established. Further optimization is discussed in section 4.5.

NAA, right

	#1	#2	#3	#4	#5	#6	#7	#8	#9	#10	#11	#12	#13	mean	std [%]
Conc.	8.04	8.02	8.68	8.02	8.69	8.17	8.25	7.94	8.32	7.61	8.13	7.69	6.57	8.01	6.7
/Cr+PCr	0.84	0.80	0.84	0.92	0.85	0.86	0.81	0.84	0.91	0.81	0.82	0.82	0.68	0.83	7.0
CRLB	3	3	3	3	3	3	3	3	3	3	2	3	3	2.9	

NAA, left

	#1	#2	#3	#4	#5	#6	#7	#8	#9	#10	#11	#12	#13	mean	std [%]
Conc.	8.24	7.47	8.66	8.40	8.29	8.08	8.44	7.90	8.39	7.94	8.03	7.64	8.00	8.11	4.1
/Cr+PCr	0.85	0.88	0.84	0.97	0.87	0.87	0.85	0.87	0.91	0.92	0.83	0.83	0.80	0.87	5.1
CRLB	2	2	2	3	3	3	2	2	3	2	2	2	3	2.4	

CrPCr, right

	#1	#2	#3	#4	#5	#6	#7	#8	#9	#10	#11	#12	#13	mean	std [%]
Conc.	9.88	10.06	10.30	8.74	10.20	9.47	10.24	9.48	9.17	9.43	9.92	9.36	9.66	9.68	4.8
CRLB	2	2	2	2	2	2	2	2	2	2	2	2	2	2	

CrPCr, left

	#1	#2	#3	#4	#5	#6	#7	#8	#9	#10	#11	#12	#13	mean	std [%]
Conc.	9.66	8.46	10.34	8.65	9.53	9.30	9.93	9.12	9.21	8.68	9.66	9.24	9.97	9.36	6.0
CRLB	2	2	2	2	2	2	2	1	2	2	1	1	2	1.8	

Glu, right

	#1	#2	#3	#4	#5	#6	#7	#8	#9	#10	#11	#12	#13	mean	std [%]
Conc.	10.43	10.40	10.10	9.93	10.58	10.49	10.60	9.90	10.28	9.38	9.76	10.03	9.77	10.1	3.7
/Cr+PCr	1.06	1.03	0.98	1.14	1.04	1.11	1.04	1.04	1.12	1.00	0.98	1.07	1.01	1.05	4.8
CRLB	3	3	3	3	3	3	3	3	3	3	3	3	3	3	

Glu, left

	#1	#2	#3	#4	#5	#6	#7	#8	#9	#10	#11	#12	#13	mean	std [%]
Conc.	10.56	9.39	10.72	10.33	9.68	10.75	11.07	9.94	10.99	8.83	9.62	10.38	11.14	10.26	7.0
/Cr+PCr	1.09	1.11	1.04	1.19	1.02	1.16	1.12	1.09	1.19	1.02	1.00	1.12	1.12	1.10	5.9
CRLB	3	3	3	3	4	3	3	2	3	3	3	3	3	3	

GABA, right

	#1	#2	#3	#4	#5	#6	#7	#8	#9	#10	#11	#12	#13	mean	std [%]
Conc.	3.78	3.99	5.00	3.20	4.11	4.68	4.42	4.25	3.88	4.22	4.03	3.99	3.76	4.10	10.9
/Cr+PCr	0.38	0.40	0.49	0.37	0.40	0.50	0.43	0.45	0.42	0.45	0.41	0.43	0.39	0.42	9.0
CRLB	9	10	7	10	10	8	10	8	9	8	8	9	9	8.8	

GABA, left

	#1	#2	#3	#4	#5	#6	#7	#8	#9	#10	#11	#12	#13	mean	std [%]
Conc.	4.09	4.14	4.62	3.77	4.60	3.97	4.46	4.27	3.71	3.95	4.41	3.38	4.00	4.11	8.9
/Cr+PCr	0.42	0.49	0.45	0.44	0.48	0.43	0.45	0.47	0.40	0.46	0.46	0.37	0.40	0.44	7.9
CRLB	8	7	7	9	9	9	8	7	10	8	7	9	9	8.2	

Lac, right

	#1	#2	#3	#4	#5	#6	#7	#8	#9	#10	#11	#12	#13	mean	std [%]
Conc.	1.97	1.86	1.44	2.71	1.14	2.22	1.90	2.37	2.73	1.45	1.48	2.64	1.29	1.94	28.8
/Cr+PCr	0.20	0.19	0.14	0.31	0.11	0.23	0.19	0.25	0.30	0.15	0.15	0.28	0.13	0.20	32.9
CRLB	14	20	21	11	43	14	20	13	11	22	18	11	26	18.8	

Lac, left

	#1	#2	#3	#4	#5	#6	#7	#8	#9	#10	#11	#12	#13	mean	std [%]
Conc.	1.51	0.66	1.37	2.40	1.24	1.79	1.79	2.61	2.03	1.18	1.12	1.87	1.84	1.65	32.9
/Cr+PCr	0.16	0.08	0.13	0.28	0.13	0.19	0.18	0.29	0.22	0.14	0.12	0.20	0.19	0.18	34.6
CRLB	18	32	18	14	31	15	12	7	13	16	18	10	17	17	

Ins, right

	#1	#2	#3	#4	#5	#6	#7	#8	#9	#10	#11	#12	#13	mean	std [%]
Conc.	7.40	6.52	7.46	4.33	7.09	6.89	7.15	7.24	6.09	5.72	6.85	6.82	7.89	6.73	13.7
/Cr+PCr	0.75	0.65	0.73	0.50	0.70	0.73	0.70	0.76	0.66	0.61	0.69	0.73	0.82	0.69	11.5
CRLB	3	4	3	5	4	4	4	3	4	4	3	4	3	3.7	

Ins, left

	#1	#2	#3	#4	#5	#6	#7	#8	#9	#10	#11	#12	#13	mean	std [%]
Conc.	7.63	6.10	7.72	4.18	8.20	7.81	7.22	6.99	6.85	5.12	7.30	6.81	7.33	6.87	16.5
/Cr+PCr	0.79	0.72	0.75	0.48	0.86	0.84	0.73	0.77	0.74	0.59	0.76	0.74	0.74	0.73	13.4
CRLB	3	3	3	5	4	3	3	3	4	4	3	3	3	3.4	

Table 4.2: MRS results of 13 mice scanned before any treatment. Absolute concentrations and ratios to total creatine (/Cr+PCr).

4.3.3 Ex-vivo MRI of human hippocampal tissue

The resected human specimens had a size of roughly $15 \times 15 \times 5 \text{ mm}^3$ and were kept in 0.1 M phosphate buffer. The samples were placed in a plastic container which was covered with parafilm to prevent the dry out of the samples and the intrusion of air bubbles during the measurements (Figure 4.9). The fixation and the immunohistochemistry are described in (Janz et al., 2017). The parameters of the applied spin-echo diffusion weighted EPI scans are listed in Table 4.3. A total of seven different samples were measured, however two were excluded from the study because the condition of the samples did not allow an identification of the hippocampal structures.

Resolution [μm]	Matrix	Slices	b-values	# Diff. Dir.	DW Grad. Dur. [ms]	DW Grad Sep. [ms]	Acq. Time
200x200 x 500	96x96	9	#5, 1000-5000	30	8	16	41 m 20 s
200x200 x 500	96x96	9	#5, 1000-5000	30	30	38	41 m 20 s
500x500 x 1500	46x46	4	#5, 1000-5000	30	30	38	41 m 20 s
200x200 x 200	98x98x10	3D	#2, 1000, 2000	50	30	38	4 h 40 min

Table 4.3: Applied DW SE EPI protocols. Parameters in common were TE=80ms, TR=4s, NA=1, bandwidth 250 kHz, 4 EPI segments, 5 non-diffusion weighted images.

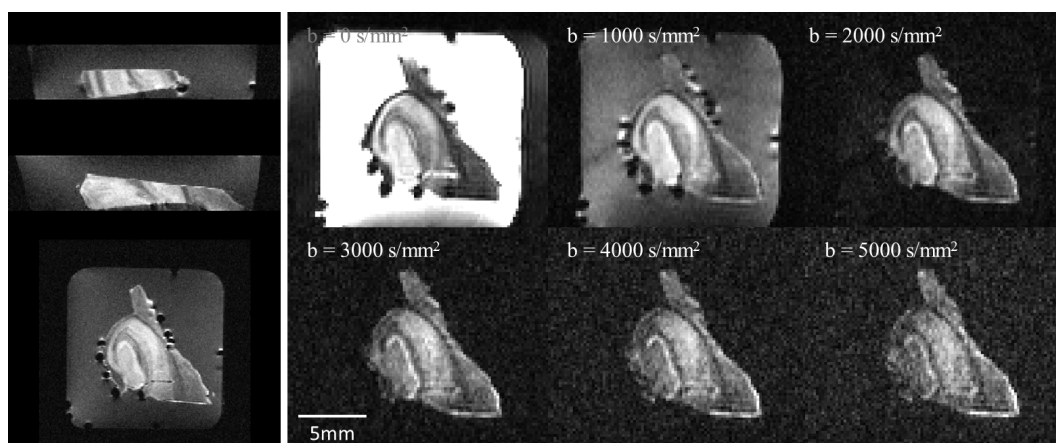


Figure 4.9: Representative RARE and DWI of resected human HC. Left) Orthographic view of RARE images with $100 \mu\text{m}$ isotropic resolution. Right) DWI with $200 \times 200 \times 500 \mu\text{m}^3$ resolution.

T_2 -weighted RARE images were acquired which had the same resolutions and geometry as the DWI scans plus one scan with $100 \mu\text{m}$ isotropic resolution. Other parameters were TR 5 s, TE 40 ms and RARE factor 2. NA and acquisition time depended on the resolution: NA=1 and acq. time 4 min for $200 \times 200 \times 500 \mu\text{m}^3$ (matrix 96×96); NA=8 and acq. time 1 h 5 min for $100 \mu\text{m}$ isotropic (matrix 196×196).

4.4 Results

All MRI/MRS results (acquisition and quantification) were produced by the author of this thesis. P. Janz performed the histochemical/EEG characterization and conducted the statistical tests for multiple comparisons.

4.4.1 Histochemical and Electrophysiological Characterization of Animals

The EEG revealed epileptiform activity in seven out of the eight KA injected mice (Figure 4.10). These animals were considered as the epileptic group. All of them showed cell death-associated microgliosis and granule cell dispersion (GCD). The five saline injected mice served as control group in which no gliosis or GCD was present. Important to note is the inter-individual variability among the eight KA-injected mice. This fact is used for the correlation of the MRI findings and a prognosis of the outcome.

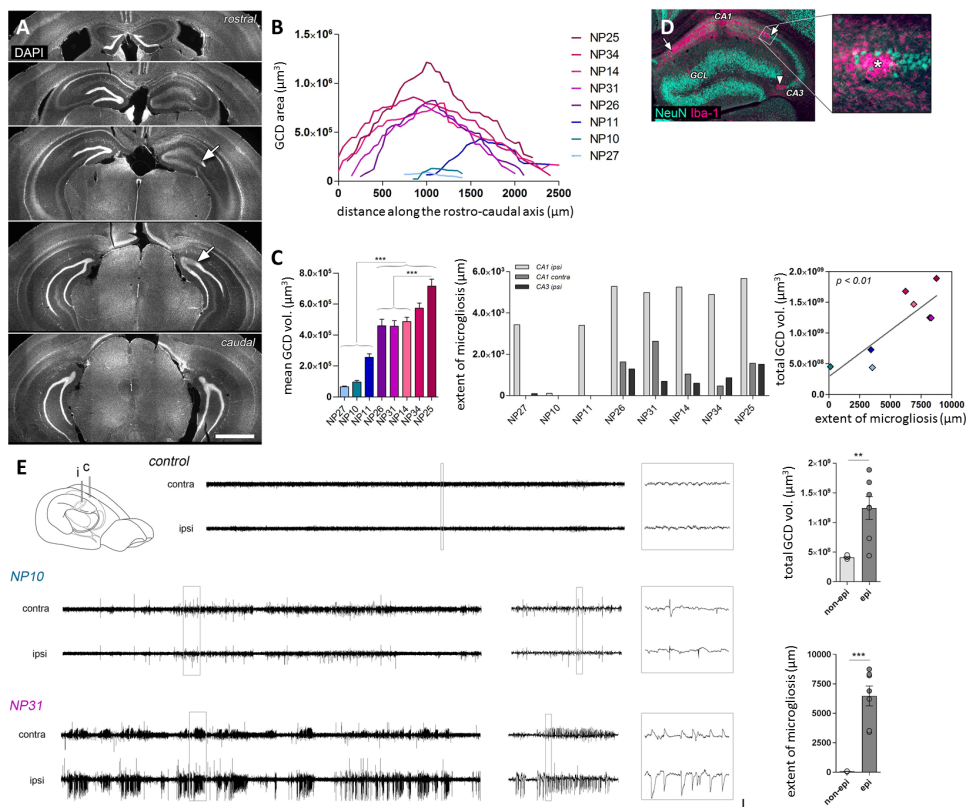


Figure 4.10: Histological and electrophysiological characterization of animals. **A)** Representative DAPI stainings along the hippocampal axis. The arrows indicate the granule cell dispersion (GCD). Scale bar 1mm. **B)** Quantified area of GCD in epileptic mice. **C)** Characterization of GCD (one-way ANOVA, Bonferroni's post-test; ***p<0.001; n = 8) and microgliosis, which represents the cell loss in CA1-3. **D)** Stainings for NeuN (neurons) and Iba-1 (microglia). **E)** Representative EEG traces of non-epileptic (control and NP10) and an epileptic mouse (NP31) displaying spikes and paroxysmal discharges (Horizontal scale bars (left) 50 s, (middle) 5 s, (right) 0.5 s; vertical scale bar 2 mV). Figure adapted from (Janz et al., 2017).

4.4.2 T₂-weighted MRI and ¹H MRS: Early Quantification of Sclerosis

Changes of the signal intensity were most pronounced in the dorsal part of the ipsilateral hippocampus (Figure 4.11). Two characteristics with different time courses can be identified. At first, there was a very strong signal increase especially in CA1, hilus and DG measured at one day after KA injection. By day four, this had returned to baseline. The second process followed and was restricted to the DG, which showed from day 4 to day 31 a gradual increase of signal intensity and a blurry appearance.

The acute changes were caused by the KA induced cell loss. The signal intensity in CA1 at day 1 accordingly correlates with the extent of microgliosis (Figure 4.13, top right). Similar changes of acute edema and a subsequent normalization were also detected in a study of pilocarpine induced SE (Roch et al., 2002) in which an increased water content was suggested as the reason for the increased signal. In the chronic state at days 8 to 31, signal intensities in the DG correlated with the later determined volume of the granule cell layer (Figure 4.13, bottom right).

There is one KA injected mouse (np10), which showed no epileptic activity on the EEG and also no hippocampal sclerosis or GCD in the IHC. This mouse and the control mice showed no abnormalities on the T₂-weighted images. All other KA injected mice showed an early increase of signal intensities pointing to HS (Figure 4.12). Two KA mice (11 and 27) had minimal GCD, which is also reflected in the T₂ images. The direct histological comparison and the quantitative analysis confirms that the early increase in CA1 correlates with microgliosis and later changes in the DG correlate with GCD (Figures 4.13 and 4.14).

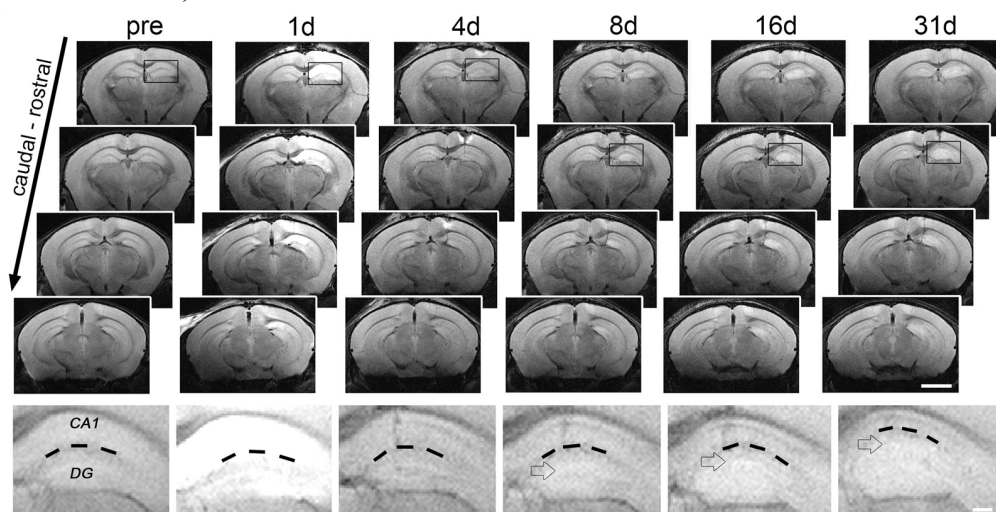


Figure 4.11: T₂-weighted imaging during epileptogenesis revealed early hippocampal damage as well as chronic changes of the DG. Shown are images of one representative epileptic mouse at different time-points (pre, 1 day, 4d, 8d, 16d and 31 d after kainate injection). Bottom row: enlargements of the ipsilateral hippocampus, the dashed lines denote the hippocampal fissure. The hollow arrows indicate the increasing volume of the DG. Scale bars 2 mm (top) and 200 μm (bottom). Figure adapted from (Janz et al., 2017).

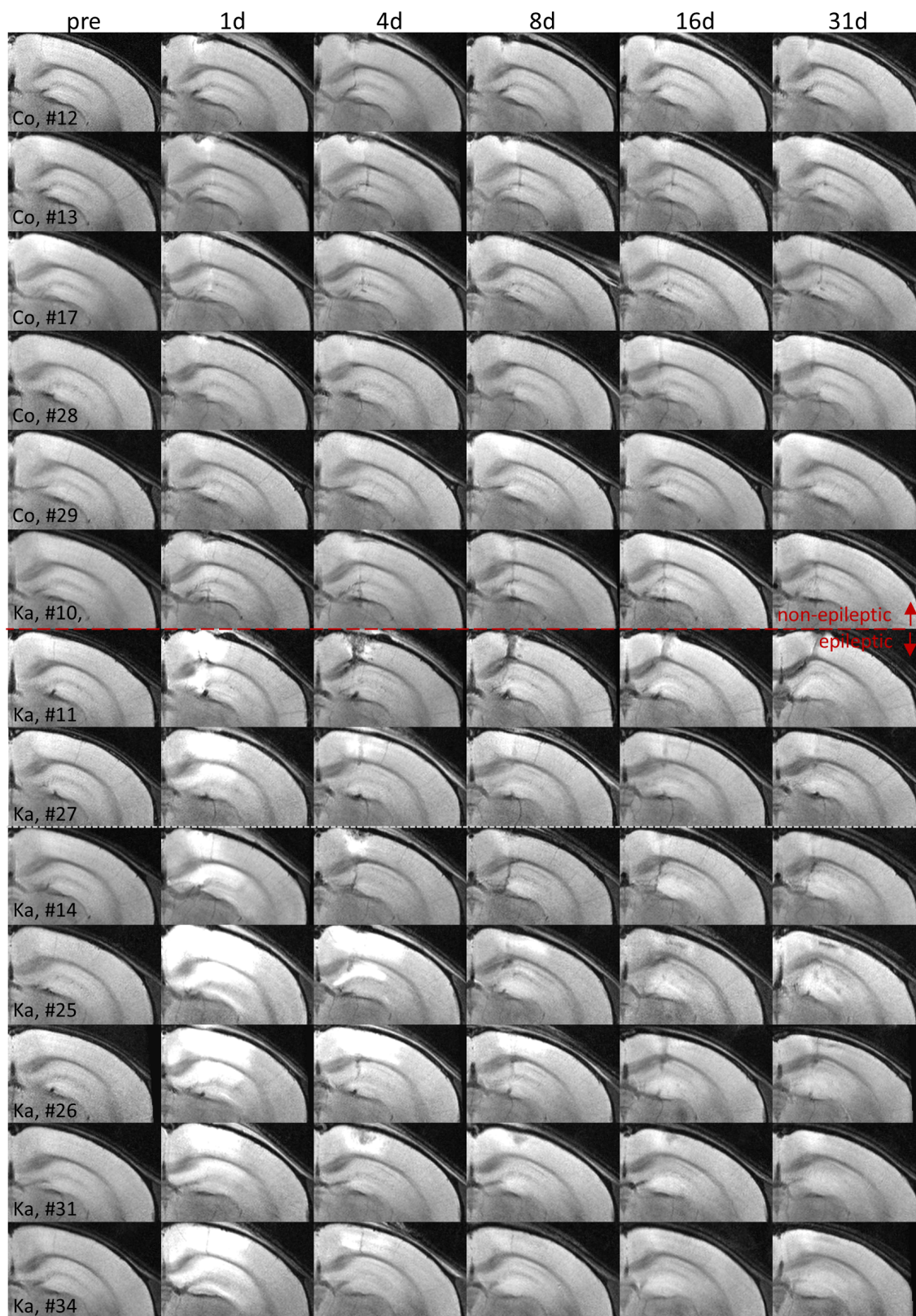


Figure 4.12: Sections of T₂-weighted images for all mice at all time-points (pre and 1-31 days after kainate injection).

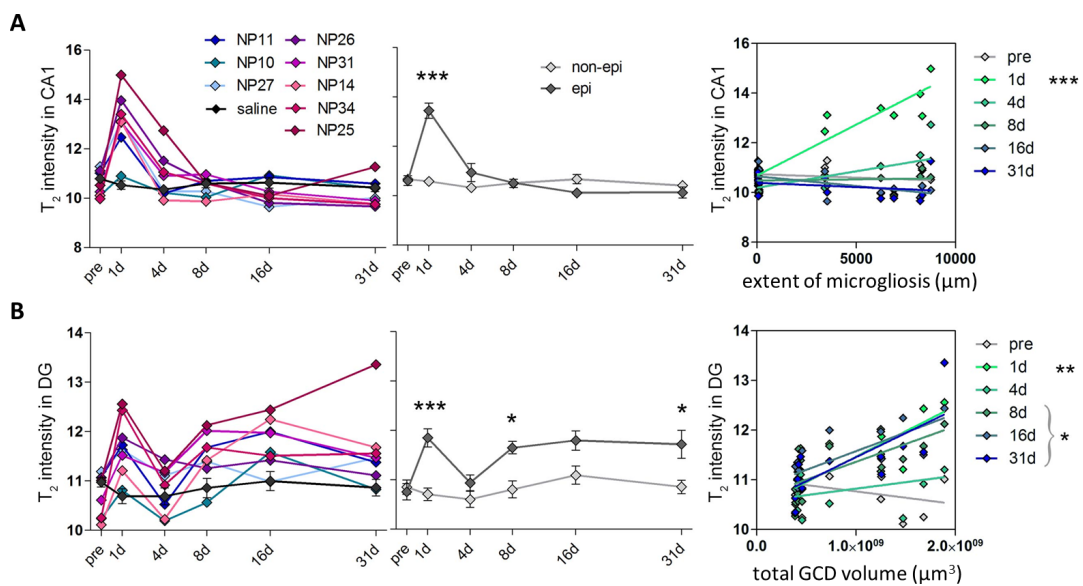


Figure 4.13: Quantified changes of T_2 -weighted signal intensity in CA1 and DG during epileptogenesis. Plotted for individual KA injected animals and control group (left), group comparison (middle, Two-way ANOVA; Bonferroni's post-test; * $p < 0.05$, *** $p < 0.001$) and correlation of intensity with microgliosis (top) and GCL volume (bottom, Pearson's correlation; corrected for multiple testing; * $p < 0.05$, ** $p < 0.01$, *** $p < 0.001$). Figure adapted from (Janz et al., 2017).

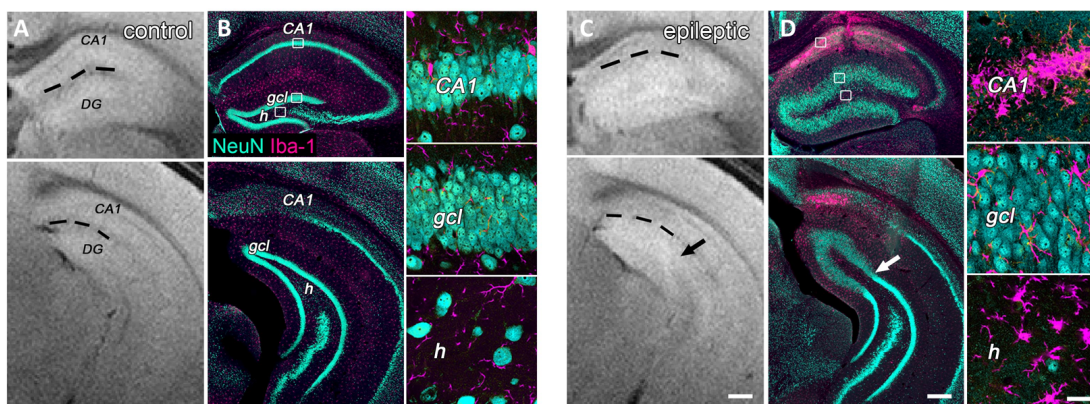


Figure 4.14: Direct comparison of T_2 -weighted images and histological stainings in a control and epileptic mouse. Upper and lower panels show the septal and temporal regions of the hippocampus, respectively. **A-B)** Stainings for NeuN (neurons, color green) show the densely packed cell layers in the control mouse. **C-D)** In the epileptic mouse, cells of the granule cell layer are dispersed and the DG is enlarged, this is reflected in the T_2 -weighted images. Stainings for Iba-1 (color magenta) show the cell death associated microgliosis especially in CA1. Figure right: enlargements of CA1, granule cell layer (gcl) and hilus (h), scale bars 200 μm (A, B, C, D) and 20 μm (enlargements right). Figure adapted from (Janz et al., 2017).

Significant cell loss after KA injection and associated microgliosis can be assessed by ¹H-MR spectroscopy. Substantially decreased concentrations of N-acetyl aspartate (NAA), a marker for neurons, and the neurotransmitters glutamate (Glu) and GABA were detected at day 1. The concentration of these metabolites correlated with the later quantified microgliosis. The lower concentrations for NAA and Glu persisted, whereas GABA concentrations increased from day 4 on (Figure 4.15).

Lactate can be used as a marker for microgliosis. As analyzed in section 4.3.2.4, Lactate cannot be reliably detected in the naive case, but a strong increase here led to a better detectability with a CRLB of 3% in the best case. Consequently, it is possible to conclude that Lactate did increase in the acute stage at day 1 and 4 (group comparison). However, the values for the individual animals and the weak statistical correlation with the microgliosis at later time points should be interpreted with caution. Myoinositol (Ins) can be used as a marker for astroglial activation and showed a significant increase at 8d in the epileptic group. In one animal surprisingly low concentrations of Ins were detected, also already before the KA treatment. However, this animal follows the same trend as the others which revealed increased Ins concentrations from day 4 on. This time course coincides with the development of GCD (see next section).

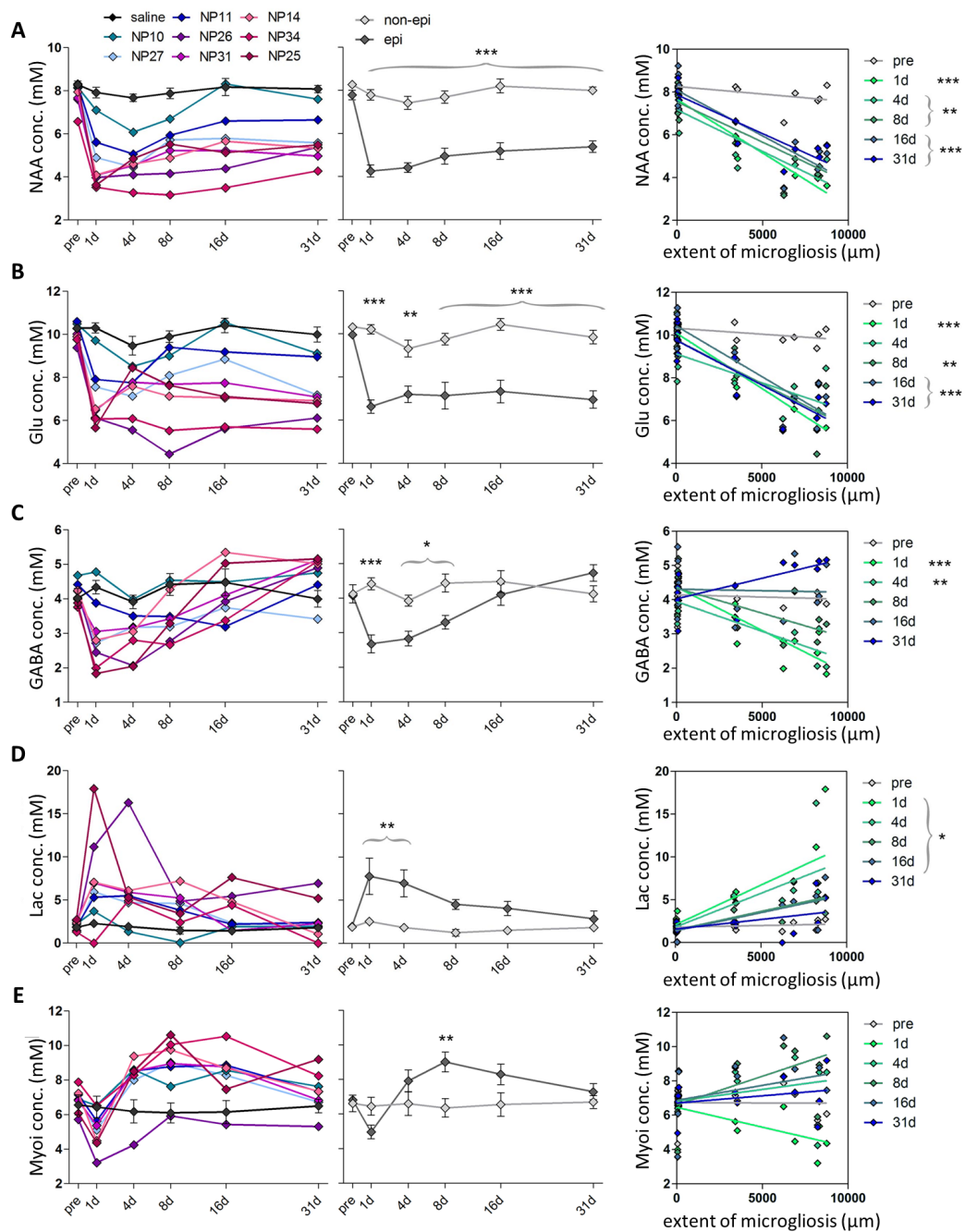


Figure 4.15: ^1H -MR spectroscopy results from the ipsilateral septal hippocampus during epileptogenesis. Concentrations for NAA, Glu, GABA, Lac and Ins for individual mice (left), group comparison (middle, Two-way ANOVA; Bonferroni's post-test; * $p < 0.05$, ** $p < 0.01$, *** $p < 0.001$) and correlation with extent of microgliosis (right, Pearson's correlation, corrected for multiple comparison; * $p < 0.05$, ** $p < 0.01$, *** $p < 0.001$). Figure adapted from (Janz et al., 2017).

4.4.3 Diffusion MRI: Development of Granule Cell Dispersion (GCD)

The most striking finding by diffusion MRI is the development of substantially altered diffusion properties in the ipsilateral dorsal hippocampus, more precisely within the dentate gyrus (Figure 4.16). Spots within the DG with increased dorso-ventral diffusivity can be identified in the images as early as four days after KA treatment. Quantification of the whole DG reveals that diffusivity in general (MD, RD, AD) increased from day 8 on (Figure 4.18). At later time points anisotropy (FA) is also increased. AD not only shows a very significant difference between the control and epileptic group, but also correlates with the histologically determined volume of the dispersed GCL at all later time points.

Diffusion in the dispersed GCL was mainly aligned in the dorso-ventral direction. This was assessed by quantifying the extent of the diffusion tensor ellipsoid in this direction. Already from day 4 on, dvD correlates with the volume of the GCL (Figure 4.20). In the group comparison, dorso-ventral diffusivity (dvD) is significantly increased in the epileptic group from day 8 on. The changed diffusion in the GCL clearly differentiates the DG from all surrounding structures, e.g. the hilus or the CA1-3 regions. This facilitated an automatic segmentation and the quantification of the volume of the dispersed GCL in-vivo.

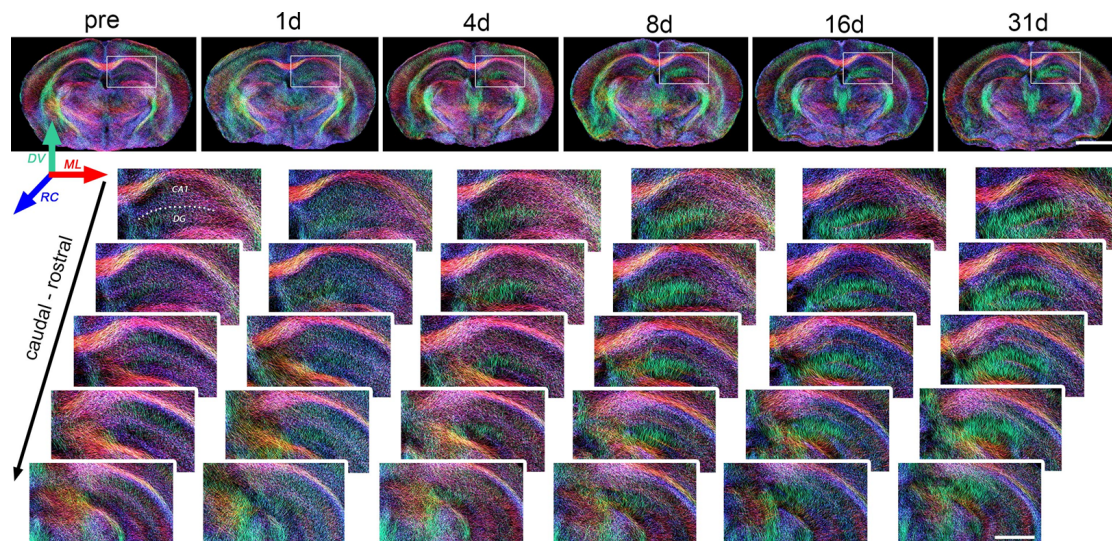


Figure 4.16: Diffusion-weighted tractography during epileptogenesis. Shown are images of one representative epileptic mouse at different time-points (pre, 1 day, 4d, 8d, 16d and 31d after kainate injection). Bottom row: enlargements of the ipsilateral hippocampus, Scale bars 2 mm (top) and 500 μm (bottom). Direction of the diffusion is color-coded, dorso-ventral (green), mediolateral (red), rostrocaudal (blue). From day 4 on, an increased diffusion in the dorsoventral direction in the DG becomes visible. Figure adapted from (Janz et al., 2017).

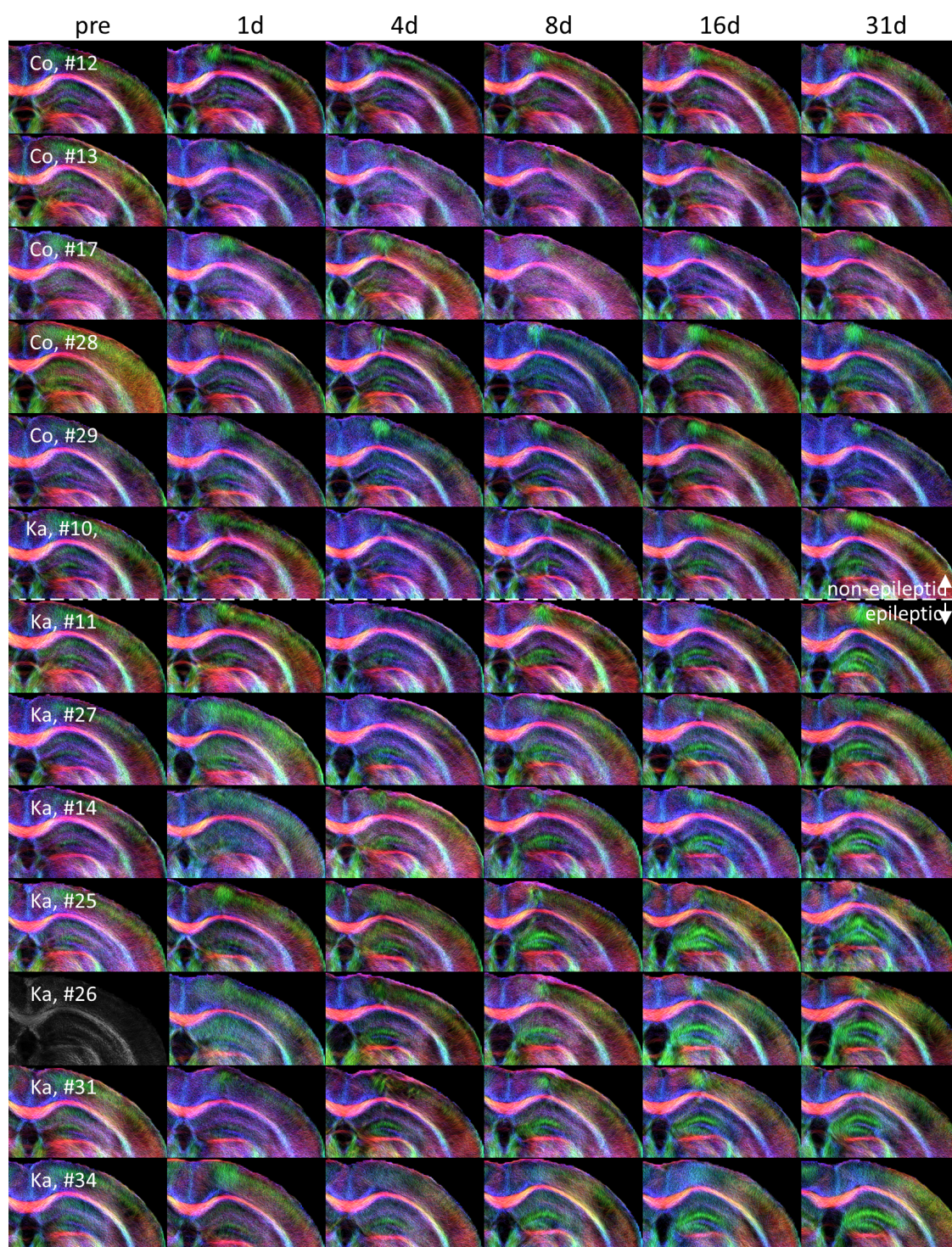


Figure 4.17: Sections of tractography images for all mice at all time-points (pre and 1-31 days after kainate injection). The dataset of #26 at t_0 was excluded because of strong motion artifacts.

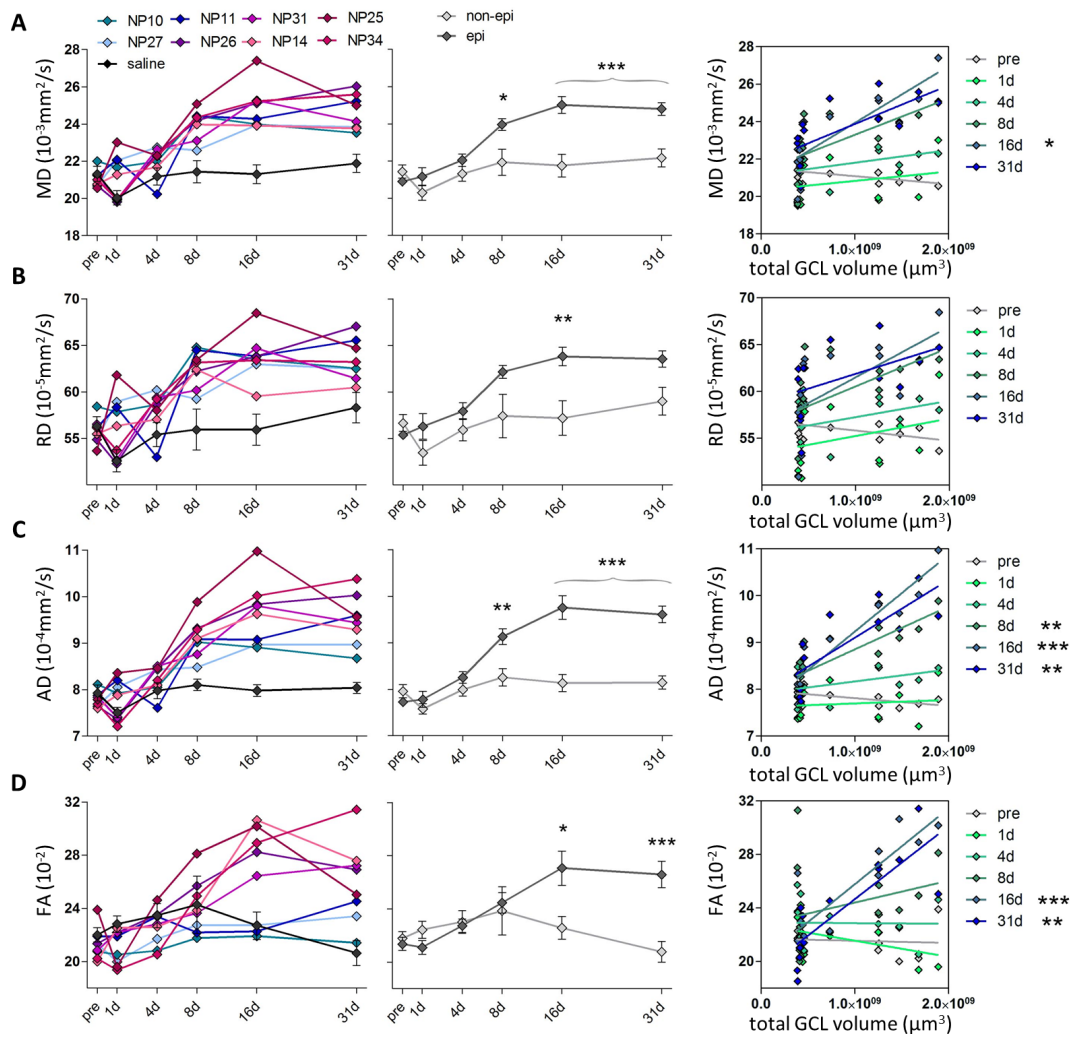


Figure 4.18: Quantitative analysis of DWI in the DG during epileptogenesis. Mean (MD), radial (RD), axial diffusivity (AD) and fractional anisotropy (FA) plotted for individual mice (left), groups (middle; two-way ANOVA, Bonferroni's post-test, $**p < 0.01$; $***p < 0.001$; $n_{\text{non-epi}} = 6$, $n_{\text{epi}} = 7$) and correlation with volume of GCL (right; $n = 13$; Pearson's correlation, corrected for multiple comparison; $*p < 0.05$, $**p < 0.01$, $***p < 0.001$). Figure adapted from (Janz et al., 2017).

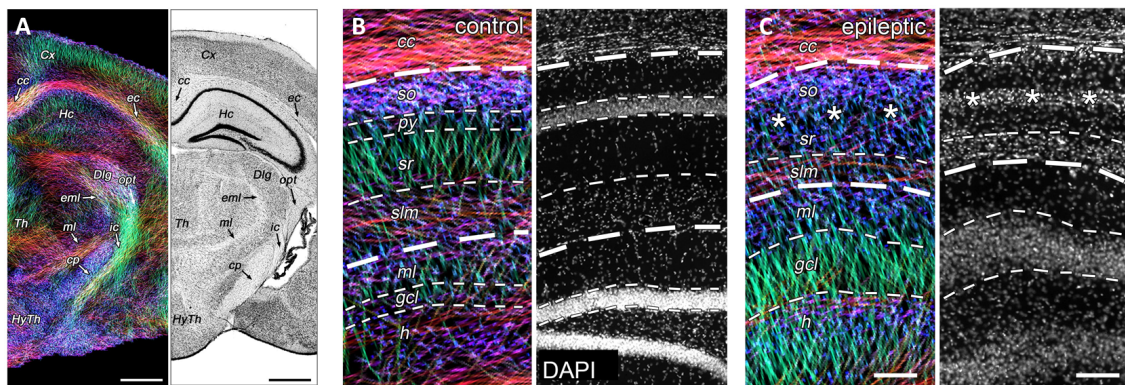


Figure 4.19: Direct comparison of tractography images and histological stainings. **A)** Comparison of tractography image with a Nissl-stained section modified from Paxinos and Franklin, “The Mouse Brain in Stereotaxic Coordinates”, 2001. Computed structures relate to major axonal pathways (cc, corpus callosum; cp, cerebral peduncle; Cx, cortex; Dlg, dorsal lateral geniculate nucleus; ec, external capsule; eml, external medullary lamina; Hc, hippocampus; HyTh, hypothalamus; ic, internal capsule; ml, medial lemniscus; opt, optic nerve; Th, thalamus). **B)** Direct comparison of tractography image with DAPI staining to identify the hippocampal layers (dashed lines; cc, corpus callosum; so, stratum oriens; py, pyramidal layer; sr, stratum radiatum; slm, stratum lacunosum moleculare; ml, molecular layer; gcl, granule cell layer). **C)** Alterations in an epileptic mouse (asterisks denote the region of pyramidal cell loss). Scale bars 500 μm (A) and 100 μm (B and C). Figure adapted from (Janz et al., 2017).

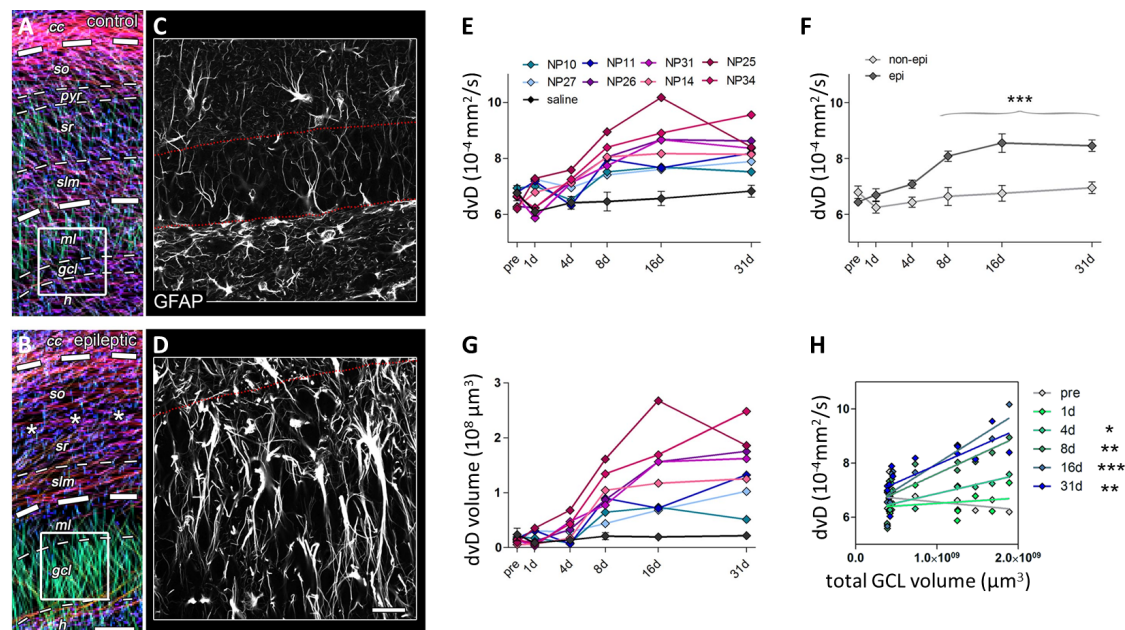


Figure 4.20: Contribution of radial gliosis to the diffusion properties. **A and B)** Tractography images for a representative control and epileptic mouse. Scale bar 100 μm . **C and D)** Magnification of GFAP stainings in the region-of-interest (white boxes in A and B). Scale bar 30 μm . **E and F)** Quantification of dorsoventral diffusivity (dvD) in the DG for individual mice (E) and groups (F). **G)** Volume of the DG quantified by the number of voxels with a dvD above a selected threshold. **H)** Correlation of the DG volume quantified with MRI during epileptogenesis and the volume finally determined by histology (Pearson’s correlation, corrected for multiple comparison; * $p < 0.05$, ** $p < 0.01$, *** $p < 0.001$). Figure adapted from (Janz et al., 2017).

4.4.4 Diffusion MRI in Ex-Vivo Human Tissue: Validation of GCD

In clinical MRI the resolution is lower and histological evaluations are not available during the course of diagnosis. The severity of TLE and the presence of HS also vary between patients; for these reasons evaluating DWI from TLE patients directly would not be the ideal approach to test the validity of the preclinical findings. In cases of refractory epilepsy, temporal lobectomy removes parts of the hippocampus and these tissue samples can be analyzed with histochemistry and MRI. The hippocampal tissues were qualitatively graded by a neuropathologist using the Wyler scale. Grades 1 and 2 represent mild, grades 3 and 4 severe hippocampal sclerosis. The degree of GCD correlates with the Wyler grade (Fahrner et al., 2007).

The results are very similar to the findings obtained in mice. The diffusion in the GCL is radially aligned, and MD and FA in the DG are increased in the samples with Wyler grading 3 and 4 compared to the samples with grading 1. FA is reduced in CA1 (Figure 4.21).

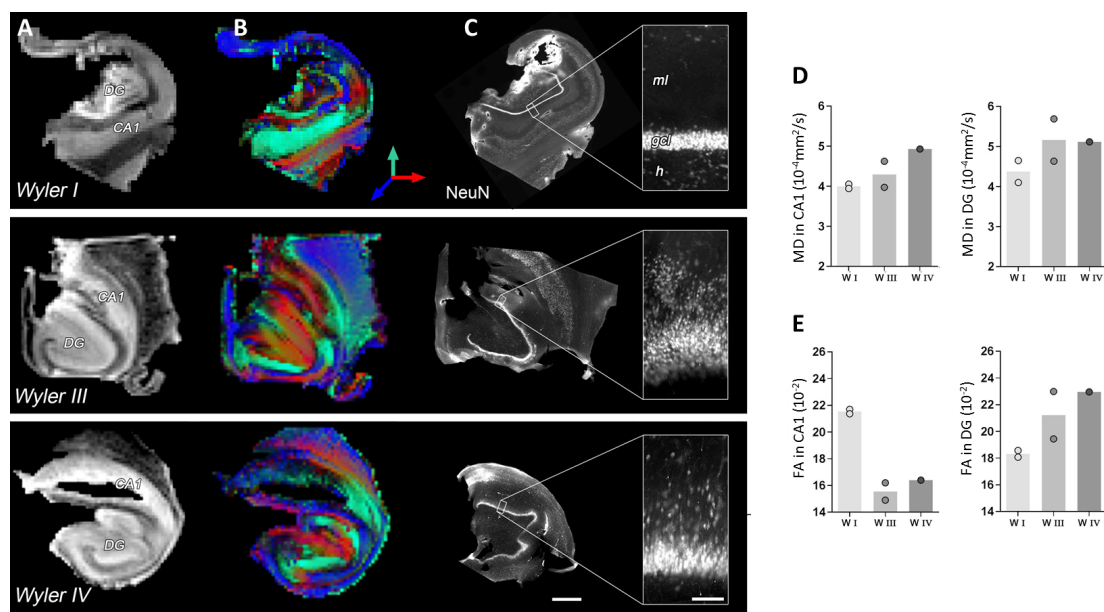


Figure 4.21: Ex-vivo analysis of sclerotic human hippocampi from mTLE patients. The rows show samples with different Wyler grades (W I: mild, W III: moderate, W IV: strong). **A)** Mean diffusion-weighted image. **B)** Color-coded FA. **C)** NeuN stainings and enlargement of the GCL. Scale bar 3 mm, insets 200 μm . **D and E)** Quantified mean diffusivity (MD) and FA in CA1 and DG. Figure adapted from (Janz et al., 2017).

Having validated the background of the diffusion alterations, it was tested whether it would be possible to detect them in-vivo. Acquisition parameters were therefore chosen that would be conceivably achievable on the most recent 7T clinical MRI systems: diffusion gradient duration 30ms, separation 38ms, and spatial resolution $0.5 \times 0.5 \times 1.5 \text{ mm}^3$. The aforementioned changes could still be detected at this lower resolution: In the hippocampi with strong sclerosis (Wyller grades 3 and 4), MD and FA are increased in the DG and FA is reduced in CA1. But the lower resolution of course complicates the identification of small structures like the GCL and partial volume effects reduce the significance (Figure 4.22).

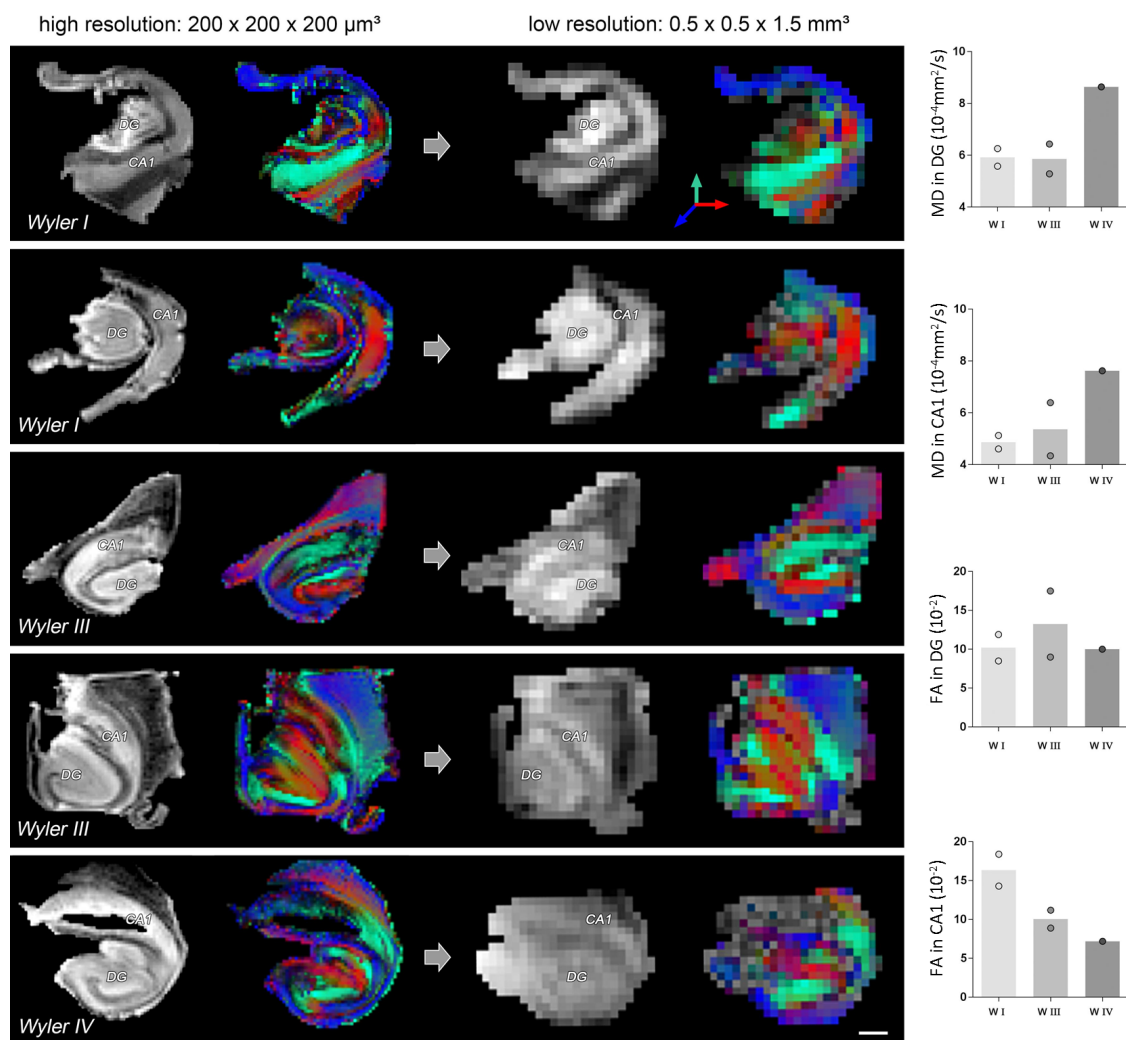


Figure 4.22: Comparison of high- and low-resolution ex vivo DWI. Only the lower resolution would conceivably be achievable in a clinical setting. Scale bar 2 mm. Right: Quantitative analysis of the low-resolution scans. Figure adapted from (Janz et al., 2017).

4.4.5 Combination of MR Modalities

The different MR methods were used to identify early hippocampal sclerosis in CA1 and later developing granule cell dispersion (GCD) in the DG. Histological analysis shows a correlation between microgliosis and GCD. The first can be detected by spectroscopy and the latter with diffusion MRI. Figure 4.23 shows the correlation of these methods at each time point during epileptogenesis. Mice with no (10) or weak microgliosis (11, 27) also develop little GCD. The other kainate mice show that strong HS translates into strong GCD. Combining the results from spectroscopy and diffusion MRI in such a 2D plot therefore can help to better separate the control and epileptic groups.

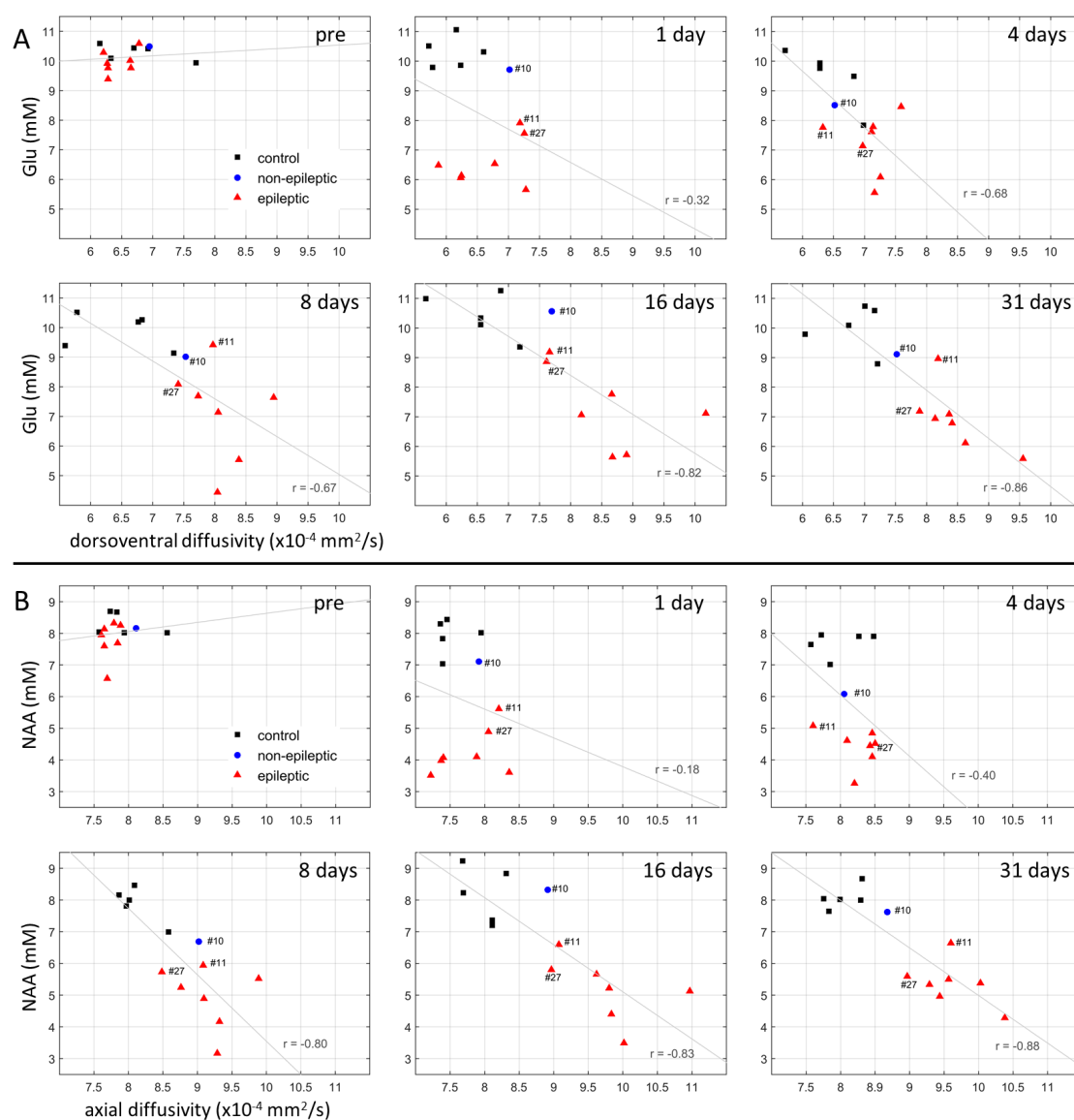


Figure 4.23: Correlation between spectroscopy and diffusion MRI results during epileptogenesis. A) Glutamate concentration in the ipsilateral hippocampus versus dorsoventral diffusivity in the DG. **B)** NAA concentration in the ipsilateral hippocampus versus axial diffusivity in the DG.

4.5 Discussion

Issues related to the animal model are addressed in the paper (Janz et al., 2017). The focus here lies on the main MR methods, their outcome and possible improvements.

Spectroscopy

Metabolite measurements were of course not comparable to the spectra of a dedicated spectrometer, however the field strength of 7T and a good shim (8-12Hz in 4mm³) allowed decent in-vivo spectra. The main goals, the separation of glutamate and glutamine as well as the quantification of glutamate and GABA, were achieved. Absolute concentrations were determined using the unsuppressed water signal as reference and changes of the water content due to cell death therefore could have influenced the quantification. This does not undermine the validity of this study because analyzing concentration ratios to water yielded the same results. However, using an external reference would lead to a more robust quantification. If the focus lies on a single metabolite, for example in a future study, edited spectroscopy may be used to improve the detection. This is especially recommended for metabolites like lactate or GABA, for which a MEGA-PRESS sequence can be used (Guo et al., 2018).

Instead of using a single voxel, further insights may be found with more spatial information. Chemical shift imaging however might not be appropriate as it does not provide sufficiently small voxel sizes that would be needed to separate hippocampal subfields. CEST imaging does not provide an unequivocal identification of a specific metabolite, but it can be made sensitive to glutamate, provides higher spatial information and can in preclinical studies be validated by histology, making CEST a promising option to broaden the insights obtained by single voxel spectroscopy.

Diffusion MRI

The resolution of the in-vivo DWI scans was 60x60x400 μm^3 . The diffusion weighting with a b-value of 1000 s/mm² resulted in images with an SNR of approximately 10, which is the lowest limit for a meaningful quantification. This resolution was chosen because the main focus of the study was on hippocampal subfields, which reveal finer structural details in the in-plane direction as compared to the slice direction. An isotropic resolution could have been chosen only with a lower in-plane resolution in order to maintain the SNR. A stronger diffusion weighting would also have led to a too low SNR. Investigating mouse brain connectivity with tractography is in general difficult because unlike in the human brain there are no strongly myelinated fiber bundles apart from the corpus callosum. Nonetheless, for tractography an isotropic resolution, more and higher b-values together with more directions would have been beneficial, even at the cost of a lower resolution.

For the ex-vivo scans of human tissue, the highest resolution was a 3D scan with $200\ \mu\text{m}^3$ isotropic resolution. Increasing this resolution is of course possible by employing micro coils and longer scan times and, because partial volume effects are reduced, a higher resolution would yield higher FA values. This would be desirable because FA in the samples was relatively low (around 0.2) and differences between the samples were even smaller. However, diffusion MRI is not meant to be a substitute for histology; the long-term goal is to translate the preclinical findings into the clinic and already a $200\ \mu\text{m}^3$ resolution is hardly feasible on a clinical MRI system. An alternative strategy, as opposed to increasing the resolution, would be to improve the contrast for example by using the oscillating gradient spin-echo (OGSE) sequence. It was reported that OGSE shows improved sensitivity to probe the hippocampal microstructure (Aggarwal et al., 2016). However, the reported findings of regional specific gliosis and cell loss were also detected in our study using pulsed gradient spin-echo (PGSE). Also, the contrast from OGSE diverges from PGSE mainly at high frequencies and b-values (Portnoy et al., 2013), which again might not be achievable by the gradient system of a clinical MRI system.

EEG

EEG was used to detect epileptic spikes and paroxysmal discharges and was therefore essential to classify the animals into epileptic and non-epileptic groups. Though, one goal was to use the MR biomarkers to predict the quantity of spontaneous generalized seizures, which could not be achieved because these seizures were only detected in a few cases. The main reason for this was presumably the short recording time of 3 hours per day. A significant improvement would be the use of MR compatible electrodes and EEG recordings already during the whole epileptogenesis. That would also allow correlating early structural changes to ictogenesis.

4.6 Conclusions and Outlook

In section 4.2 “Monitoring Epileptogenesis by MRI and MRS – State of the art” four points were identified how this study may contribute to TLE research:

- Longitudinal study on the kainate mouse model; the observed changes in this mouse model of TLE are in good accordance with what is known from human TLE. After an initial damage there was a return to baseline and only after a silent period chronic changes limited to a single focus occurred. Other regions (i.e. the amygdala and the piriform cortex) were, unlike in other animal models, not affected.

- High-resolution MRI; the imaging was able to reveal regional specific developments in different hippocampal subfields. Initial cell loss mainly in CA1, the hilus and the DG triggered the further developments. At later time points, microstructural changes in the DG continuously increased during epileptogenesis until eventually the chronic epileptic state was established. Opposing changes highlight the importance of high-resolution MRI: FA increased in the DG due to granule cell dispersion, whereas FA decreased in CA1 due to cell loss. Quantifying an overall FA across the entire hippocampus may consequently show no or minimal changes in FA.
- Combination of MR methods; different MR methods are sensitive to different processes. Spectroscopy was well suited to detect the reduction of metabolite concentrations due to cell death and diffusion MRI was optimal to detect structural changes due to granule cell dispersion. Both processes were validated by immunohistology. Importantly, these features are correlated. It was shown (Section 4.4.5) that the combination of MRS and DWI in a 2D plot can be used to easily separate the control and epileptic group. In the clinic, MRI is used to analyze patients. However, measurements are done at a single time point and MR results might be ambiguous because of a low resolution or bad quality. Combining the results from different methods (MRS, DWI) therefore could improve the sensitivity of the diagnosis.
- Ex-vivo human sclerotic tissue; the imaging results from the mouse model could be validated in a high-resolution scan of human tissue, which again shows that this model is adequate to study epilepsy. Theoretically, this means the process of epileptogenesis can be detected and, more importantly, be predicted in human epilepsy. Though, the in-vivo detection of subtle changes in hippocampal subfields over years remains challenging in a routine clinical setting.

Instead of looking at human epilepsy and following the longitudinal changes of a possible at-risk cohort, two different strategies were pursued:

- BOLD fMRI was used to study optogenetically induced epileptic activity as well as connectivity changes which aims at identifying new targets for a possible intervention (Chapter 5).
- Glutamate, which is an excitatory neurotransmitter, was counterintuitively reduced in epileptic animals. GluCEST and GluCEST fMRI was developed to study the local glutamate distribution and the release during epileptic activity (Chapter 6).

5 Optogenetic fMRI

All surgeries, virus and kainate/saline injection, fiber implantation and histochemistry were carried out by Enya Paschen and Philipp Janz, members of the experimental epilepsy research group headed by Prof. Dr. Carola Haas. All MRI-related work, planning of the experiments and evaluation of the results was performed by Niels Schwaderlapp.

5.1 Introduction

Epilepsy manifests at different levels, from molecular changes to large scale network modulations, and can be characterized by different methods like EEG, optical imaging or fMRI (Wykes et al., 2019). fMRI offers the possibility to directly translate the results from basic research to clinical treatment and vice versa. Especially in epilepsy this is important because in humans only interictal periods can be studied in practice. The systematic study of epileptic seizures is only possible in animal experiments.

With the advent of optogenetics, manipulation of specific cells has become possible. This is a significant advantage over other types of stimulation. Seizures can for example be triggered by optogenetic or electrical stimulation. However, if the aim is to induce seizures that mimic spontaneous activity, a stimulation that is as specific as possible is necessary. In the KA mouse model of mTLE, spontaneous seizures arise from a single focus in the septal pole of the ipsilateral hippocampus. In our study, ChR2-expressing cells in the perforant path were stimulated to trigger seizures that were similar to spontaneous seizures. fMRI was used to monitor the seizure propagation across the brain.

Epileptic seizures were more severe in epileptic than in healthy animals; they lasted longer and spread to more brain areas, for example to motor-related areas. Additional to ofMRI of induced activity, resting-state fMRI was used to study network alterations. This gives the full picture why seizures are more severe in epileptic animals and may also indicate possible targets to interfere with the seizures.

5.2 State of the Art

Shortly after optogenetics had been established, it was shown that optogenetic excitation of neurons can be detected by fMRI at the stimulation site as well as at downstream, axonal projections (Lee et al., 2010). A fast setup was developed to enable real time ofMRI experiments (Fang and Lee, 2013), which maybe aimed at closed-loop feedback interactions. However, because of the temporal delay of the BOLD signal, closed-loop systems aiming at interfering with epileptic activity might be better based on EEG (Krook-Magnuson et al., 2013). More appropriate is to use ofMRI as a tool to visualize induced activity and infer causal information about the network circuits.

Using block design stimulations, frequency-specific responses in the hippocampus (Weitz et al., 2015) or thalamus (Liu et al., 2015) were investigated. Especially the direct optogenetic control of neuronal functions may lead to heterogeneous BOLD responses and different fMRI analysis methods in block design studies were investigated (Liu et al., 2017). MR compatible optrodes, which are fibers combined with an electrode, were developed and used in combination with ofMRI to study seizure-like afterdischarges (Duffy et al., 2015). More recently, dynamic causal modelling was applied to ofMRI experiments to study the causal relationships among regions of a network (Bernal-Casas et al., 2017; Ryali et al., 2016).

In the recent years, rsfMRI in rodents has become well-established (Bukhari et al., 2017; Grandjean et al., 2014, 2017; Paasonen et al., 2018; Zerbi et al., 2015). One study also combined rsfMRI and ofMRI using a transmit-only birdcage and receive-only surface coil (Chan et al., 2017).

This chapter advances the current state of the art by the following points:

- Combination of ofMRI with the CryoProbe. Usually room-temperature coils have been used previously because of the easier incorporation of the optical fiber in the setup. The enhanced SNR by the CryoProbe is beneficial for all of the following points.
- Imaging of the dynamic response during seizures. Because of the heterogeneous animals/responses it is important to be able to study single seizures, their onset and propagation. A high SNR and temporal resolution are required for this.
- Acquisition of resting-state fMRI immediately before seizure induction. Studies using optogenetic stimulation were rarely combined with rsfMRI during the same fMRI session. The probable reason for this is that basically all of the ofMRI studies until now have used room-temperature coils, whereas rsfMRI requires the CryoProbe technology due to its higher tSNR.
- Application of multi-echo fMRI (ME fMRI). FMRI based on more than one echo image is not entirely novel (Poser and Norris, 2009; Kundu et al., 2017), however this has mainly been applied in human fMRI. So far, very few preclinical fMRI studies utilize ME fMRI.
- Applications in the KA mouse model of mTLE. Epileptiform activity has been induced in other studies, e.g. in (Duffy et al., 2015). However, as outlined in chapter 3, the significance for epilepsy crucially depends on the studied animal model. Block design or seizure induction in naïve mice or rats therefore had only a limited explanatory value for epilepsy research.

5.3 Methods

fMRI experiments were performed on the same MR system as described in chapter 4; this chapter therefore covers only the details relevant for optogenetic-fMRI.

5.3.1 Optogenetic Setup

An in-vivo optogenetics toolbox (Prizmatix, USA/Canada) was used for stimulation. The optical fiber was plugged to the implanted cannula before each of MRI scan. The cannulas consisted of a ferrule and the fiber (diameter 200 μm , $NA\ 0.66$) and were implanted two days before the start of the ofMRI experiments. The fiber sleeve and ferrules were made of zirconia to ensure MR- and biocompatibility. An LED source delivered blue ($\sim 460\text{nm}$) light with an optical power of $>15\text{mW}$ and irradiance $>440\text{mW}/\text{mm}^2$ at the fiber tip (according to the Prizmatix datasheet).

Self-written software (Matlab, Mathworks, USA) and a data acquisition device (NI USB 6251 BNC, National Instruments, USA) connected to the MRI scanner and the LED system were used to trigger the stimulation.

The MR CryoProbe consists of a thin outer ceramic layer heated to 37°C to allow in-vivo measurements. This limited the free space above the head of the mice and required a flat-implantation of the fiber through the cerebellum (figure 5.1). The usage of an alternative low-profile cannula is discussed at the end of the chapter.

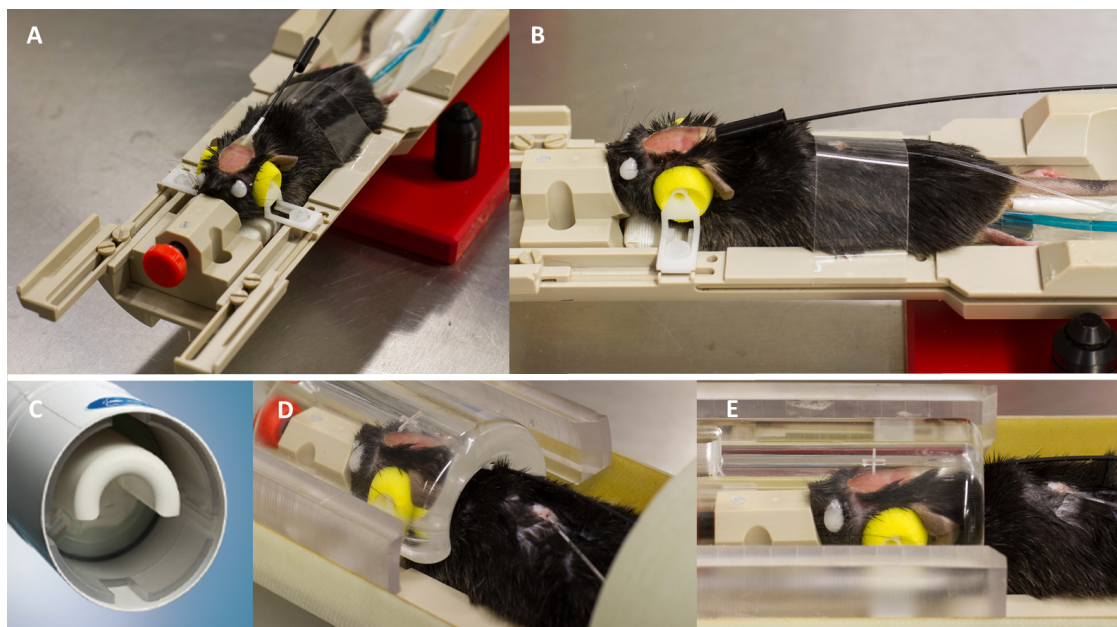


Figure 5.1: CryoProbe compatible ofMRI setup. **A and B)** Photographs of a mouse placed on the animal bed and attached optical fiber. **C)** Image of the CryoProbe (Bruker BioSpin, Germany). **D and E)** Mouse placed into a replica of the CryoProbe.

The virus AAV1.CamKII.ChR2-mCherry was injected into the right entorhinal cortex of ≈ 13 weeks old Thy1-eGFP mice. Blue light delivered via an optical fiber excited ChR2-expressing cells of the perforant path in the dorsal part of the intermediate hippocampus (figure 5.2). At the same time point as the virus injection, either kainate, in order to engender epileptic mice, or saline, in order to engender control mice, was injected into the right septal hippocampus. MRI experiments were performed around 2.5 to 3.5 weeks later, when the virus expression was sufficient and the kainate injected mice had developed chronic epilepsy.

Generalized seizures may have a relatively long-lasting effect of several hours until the baseline state is reached again. Successive stimulations within the limited time of an fMRI session (~ 1 h) are therefore not completely comparable. Thus, animals were stimulated only once per day and scans were repeated on 4-8 consecutive days.

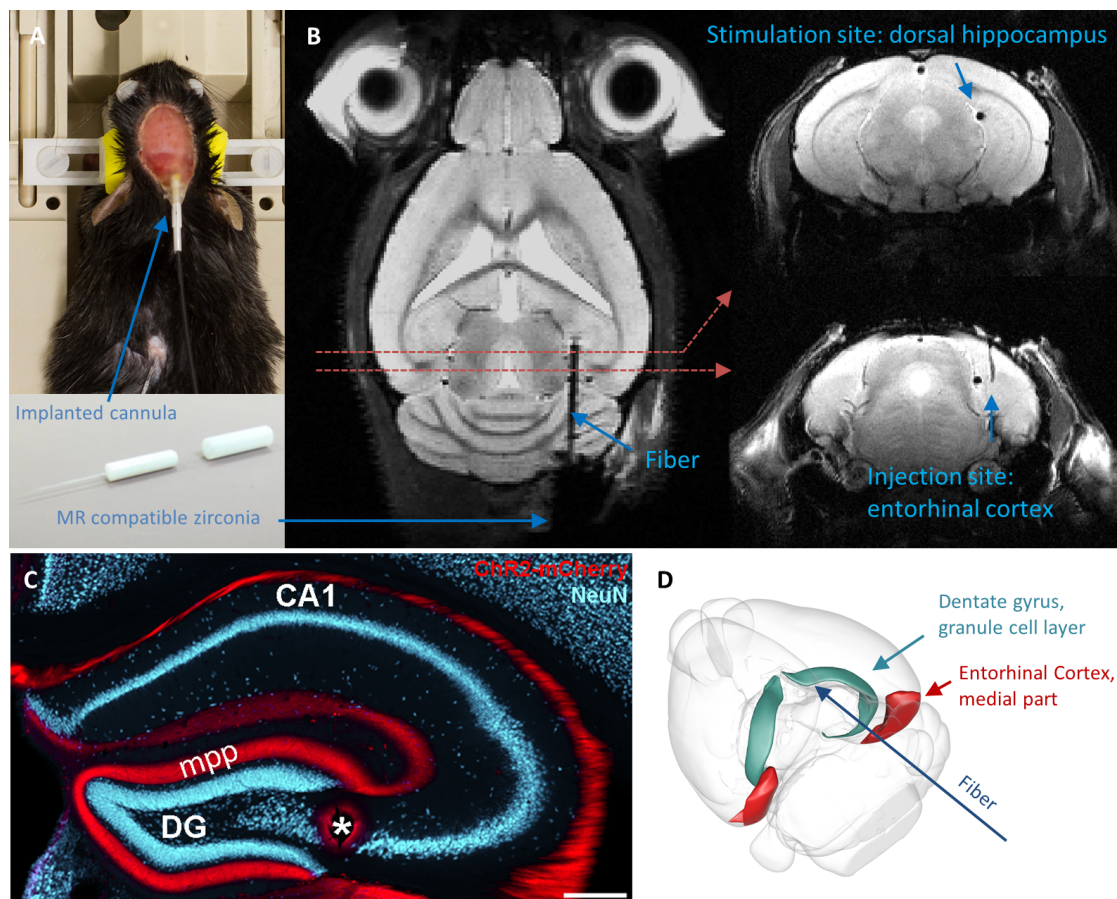


Figure 5.2: ofMRI setup. A) After the surgery, the skull was sealed with dental cement to which the implanted cannula adhered to. The optical fiber with ceramic sleeve at the end could be plugged to the cannula before each experiment. B) RARE images showing the injection and the stimulation site. C) Histological staining for mCherry (red) shows the ChR2-expressing cells of the medial perforant path (mpp) which represents the axonal projections from the entorhinal cortex to the hippocampus. These cells form the input to the granule cells of the dentate gyrus (Asterisk: location of the fiber tip. Blue color: NeuN staining for neuronal cell bodies. Scale bar 400 μm . Figure C produced by E. Paschen). D) Illustration of the fiber direction (generated using scalablebrainatlas.incf.org/composer/?template=ABA_v3).

5.3.2 fMRI Setup and Acquisition

Anesthesia is needed for rodent fMRI and the effects of different anesthetics on the measured fMRI connectivities have been studied (Bukhari et al., 2017; Paasonen et al., 2018). For example, brain connectivities under propofol or urethane anesthesia were similar to the awake condition in rats. Also, α -chloralose and a combination of medetomidine with a low dose of isoflurane ($\leq 0.5\%$) produced similar results. However, in the study of epilepsy it is important that the applied anesthesia does not act as an anticonvulsant and suppresses epileptiform activity. This is known for propofol, urethane and also isoflurane (Airaksinen et al., 2010, 2012; De riu et al., 1992). In our preliminary experiments a combination of medetomidine and 0.5% isoflurane was used. While it was possible to induce seizures in control mice, isoflurane at 0.5% completely suppressed epileptic activity in kainate mice. α -chloralose might be an alternative but it was reported that it leads to unstable physiological conditions in mice (Low et al., 2016). Therefore, we used only medetomidine sedation which does not suppress epileptic activity. Medetomidine (Domitor, Pfizer, Germany) was administered as a subcutaneous (s.c.) initial bolus (200 μ L, 0.3 mg/kg) and a continuous s.c. infusion (200 μ L/h, 0.6 mg/kg). Mice freely breathed a mixture of 70% N₂ – 30% O₂ during the MRI scans.

However, under medetomidine sedation alone mice often resisted the fMRI scan, which resulted in severe motion and the abortion of the scan. Increasing the medetomidine concentration up to tenfold showed no improvements. The animals' reluctance was caused by the fixation. In the routine setup (figure 5.3, A-C) as developed by Bruker, ear pins were used for the fixation. They fit only into the CryoProbe at the innermost position which left a too small distance between the pins. Also, the angle of the pins (figure 5.3, B) did not match the angle of the ear canals (figure 5.3, C). This may have produced strong pressure on the head and maybe pain, which the mice only tolerated at a deeper anesthesia ($>1\%$ isoflurane). This setup was therefore modified (figure 5.3, D-E). The ear pins were removed and replaced by a soft cushion which improved the animals' compliance significantly.

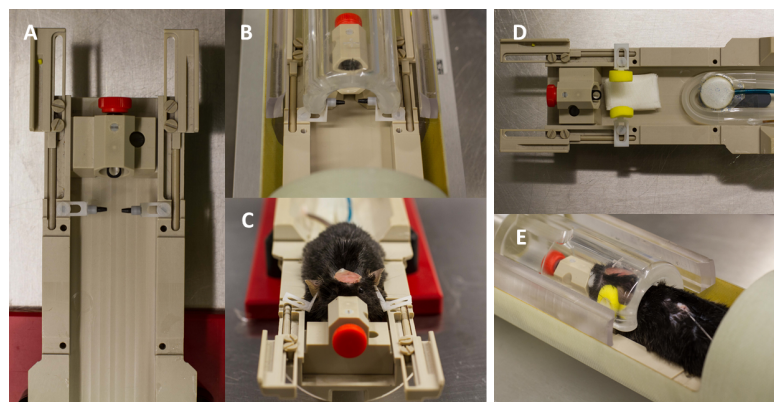


Figure 5.3: Animal fixation for fMRI. A-C) The usual fixation with ear pins was not suitable for fMRI. D-E) Modified fixation.

fMRI datasets with the following protocol parameters were acquired:

- Gradient-Echo EPI; 2 echo images with TE 13.9 ms and 22.6 ms, respectively
- TR 1 s, flip angle 60°, NA 1
- Matrix 60 (read) x 32 (phase), bandwidth 250 kHz
- Resolution 0.28 x 0.28 mm², FOV 16.8 x 8.96 mm²
- Slices 12, slice thickness 0.8 mm, slice gap 0.2 mm

The two echo images were combined into a single image before further analysis. Compared to a simple summation, a weighted summation based on the contrast-to-noise ratio was reported to be beneficial (Kundu et al., 2017; Poser and Norris, 2009). The voxelwise weighting factors w for the images acquired at the echo times TE_1 and TE_2 are:

$$w_n = \frac{tSNR * TE_n}{\sum tSNR * TE_n} \quad (5.1)$$

The temporal SNR was determined during the rest period. The two weighted echo images were then combined into a single multi-echo (ME) dataset:

$$ME = w_1 * TE_1 + w_2 * TE_2 \quad (5.2)$$

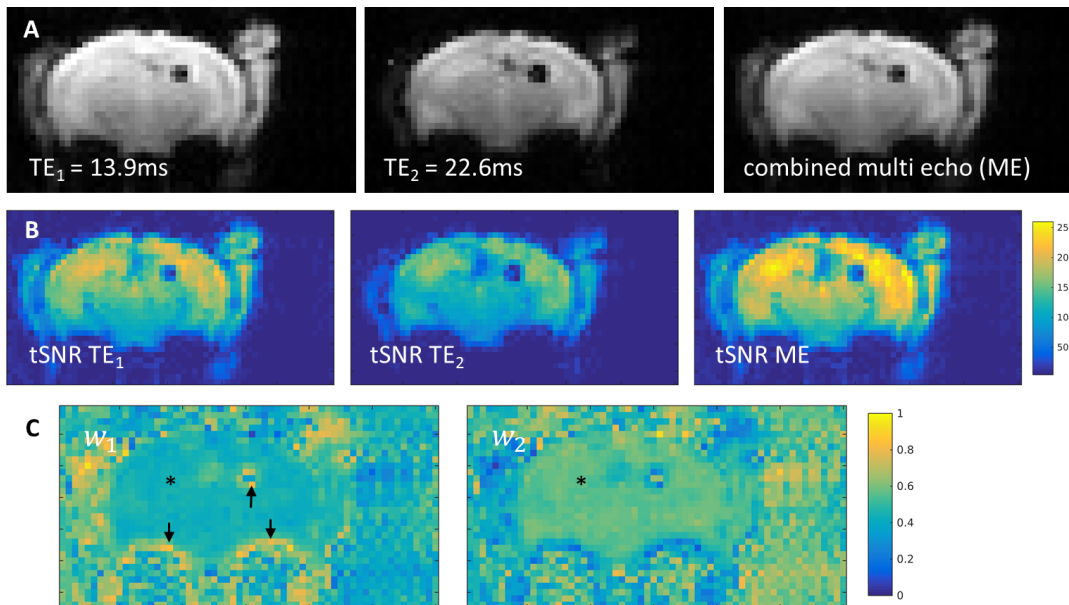


Figure 5.4: Combination of multi-echo fMRI datasets. A) Individual and combined echo images. B) tSNR maps. C) Maps showing the voxelwise weighting factors. For example, the weighting factors at the asterisk are $w_1 \approx 0.45$ and $w_2 \approx 0.55$. Strong weighting for TE1 are at areas of short T_2^* around the fiber and at the lower border of the brain (arrows).

The post processing for the resting state fMRI data is described in chapter 2.2.3 and included motion correction, removal of non-brain areas, bandpass temporal filtering

(0.01 Hz-0.5 Hz) and spatial smoothing (0.42 μm Gaussian Kernel; FSL, FMRIB Oxford, UK). The temporal filtering for datasets with seizure induction differed; this is described in section 5.4.6.

A slice gap was introduced to minimize the crosstalk between neighboring slices, which is present even when using an interleaved acquisition. Figure 5.5 shows the signal intensity and tSNR depending on the gap size. The signal increased with the gap size because the saturation by neighboring slices decreased. However, larger gaps lead to unsaturated areas between the slices and a higher susceptibility to motion. This may be the reason why the tSNR did not increase accordingly.

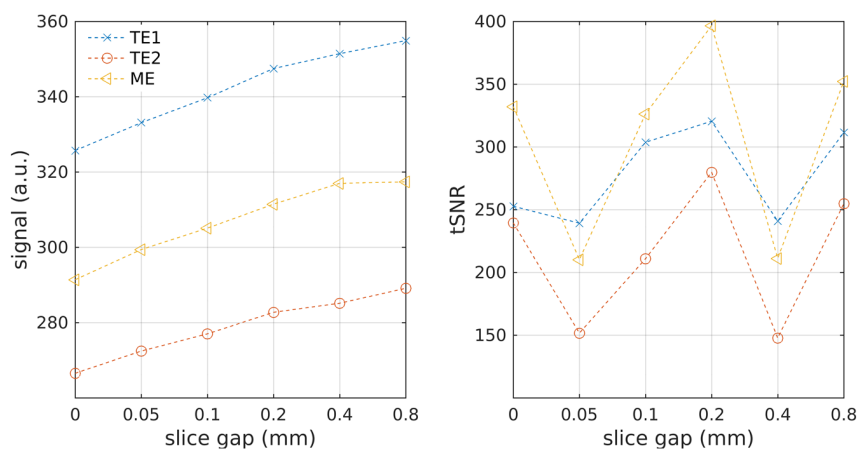


Figure 5.5: Effect of slice gaps. Mean signal intensity (left) and tSNR (right). 5 slices were acquired and a ROI in the middle slice was selected, so that the position of the ROI remained exactly the same while the position of the neighboring slices changed at different the gap sizes (interleaved acquisition).

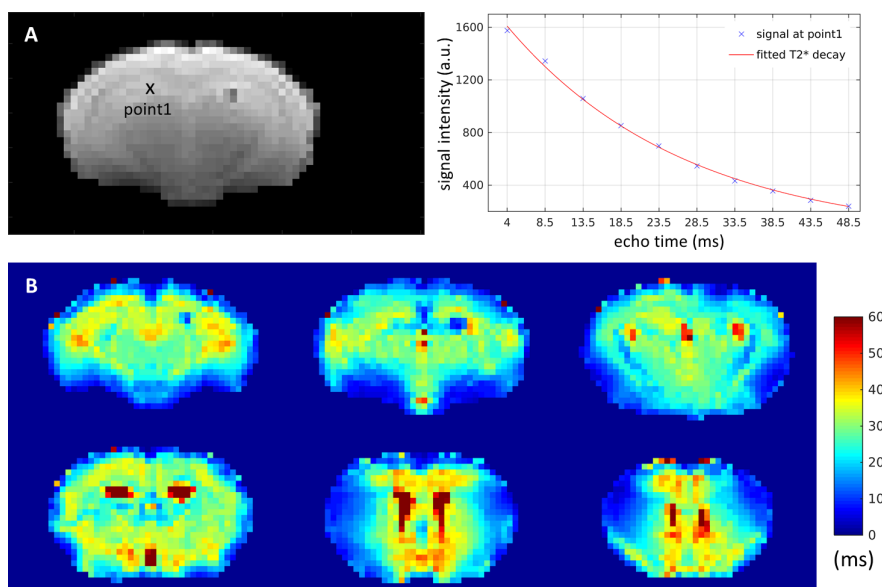
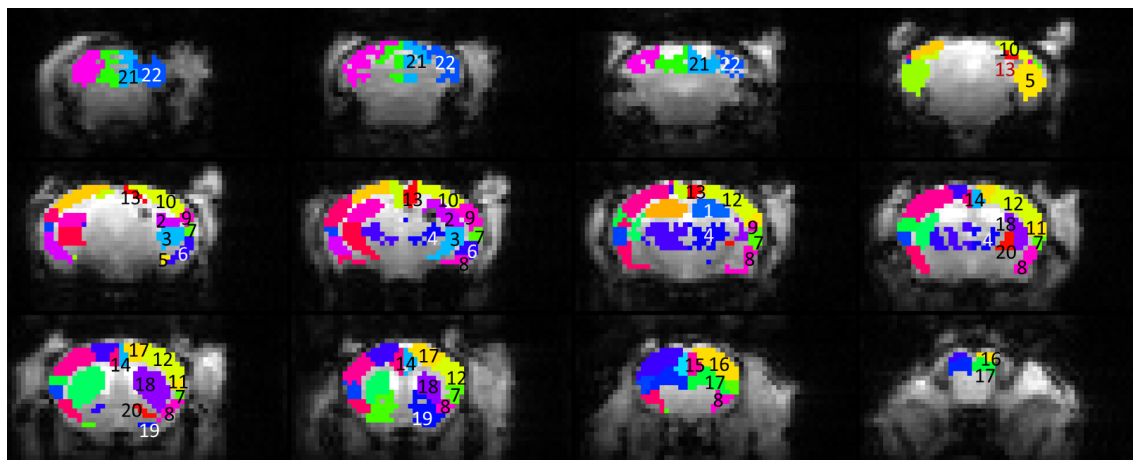


Figure 5.6: T₂* relaxation in the mouse brain. A) T₂* was quantified by a multi-gradient-echo (MGE) scan (right: signal decay at point1). B) T₂* maps. The MGE scan had the same geometry as the fMRI scans (10 echoes, 3.5-48.5 ms with 5 ms echo spacing, TR 1 s, FA 60°, NA 2, acq. time 1 min 4 s).

5.3.3 Mouse Brain Atlas

A reference brain atlas based on the AMBMC (Australian Mouse Brain Mapping Consortium) datasets was created to segment the brain into different areas (figure 5.7). The original AMBMC atlas, which is based on 15 μm isotropic ex-vivo MR scans, as well as the Allen mouse brain atlas, which is based on gene expression mapping, are extremely detailed and not suitable for fMRI analysis at a much lower resolution.

In each hemisphere 22 areas were defined and this labeled dataset was linearly registered to the fMRI datasets using FSL Flirt (FMRIB Oxford, UK).



- | | |
|---|--|
| 1: Hippocampus, septal pole | 13: Cingulate Cortex, retrosplenial area |
| 2: Hippocampus, intermediate, dorsal part | 14: Cingulate Cortex, anterior area |
| 3: Hippocampus, intermediate, ventral part | 15: Cingulate Cortex, prelimbic area |
| 4: Thalamus | 16: Frontal Cortex, somatomotor area |
| 5: Entorhinal Cortex, medial part | 17: Frontal Cortex, orbital area |
| 6: Entorhinal Cortex, dorsal part | 18: Basal Ganglia, dorsal striatum |
| 7: Insular Cortex, ectorhinal / perirhinal area | 19: Basal Ganglia, ventral striatum |
| 8: Ventral Cortex, piriform area | 20: Basal Ganglia, pallidum |
| 9: Temporal Cortex, auditory and temporal association | 21: Cerebellum, cerebellar vermis |
| 10: Occipital Cortex, visual cortex | 22: Cerebellum, cerebellar hemispheres |
| 11: Parietal Cortex, sec. somatosensory cortex | |
| 12: Parietal Cortex, prim. somatosensory cortex | |

Figure 5.7: Segmented and labeled mouse brain atlas.

5.4 Results I: Methodological Characterization

The results of this chapter are divided into two parts. In the first part, section 5.4, several methods and their outcome are characterized. The aim of this part was to establish a solid foundation for optogenetic-fMRI and resting-state fMRI. This was the precondition to apply these methods to the study of epilepsy which is the focus of section 5.5.

5.4.1 Side Effects in ofMRI: Visual Stimulation and Thermal Effects

Light leaking out of the fiber-cannula conjunction implies the possibility of a visual stimulation which has to be differentiated from the optogenetic stimulation. There are cumbersome approaches to regulate this (Schmid et al., 2017) or to completely block the light leakage. Here, visual stimulation was intentionally performed to assess which brain areas are involved. The fiber tip was for this purpose not connected to the cannula but placed in front of the eyes. Figure 5.8 shows the effect of the visual stimulation.

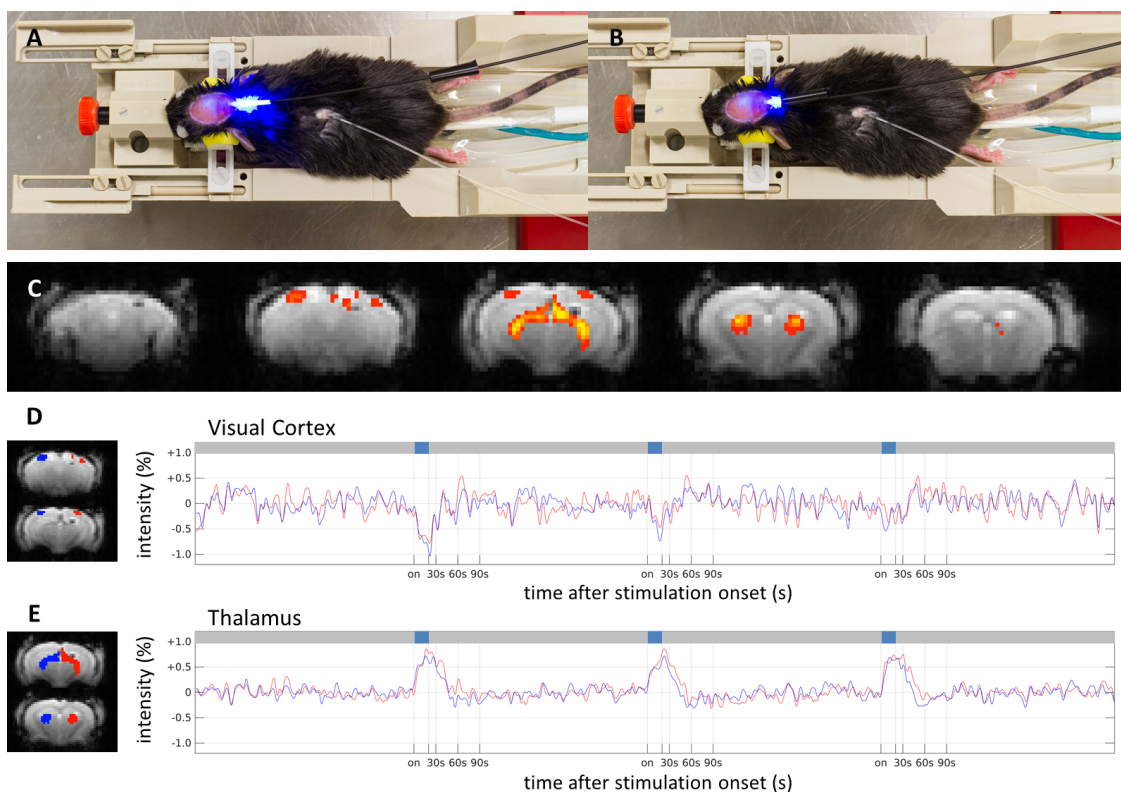


Figure 5.8: fMRI during visual stimulation. **A)** Photography of the connected fiber during stimulation shows the light leakage. **B)** The cannula could not be completely covered because it was partly glued to the skull. **C-E)** The fiber was not connected to the cannula. **C)** Visual stimulation analyzed with FSL FEAT (15 min scan, 3 stimulations of 20s at 10Hz, 3rd order gamma basis functions, corrected voxel p threshold 0.01). **D, E)** fMRI time courses in the right (red) and left (blue) hemisphere of the visual cortex and thalamus.

The second unwanted side effect could be a thermal effect. This could be best studied in animals without virus injection. Thermal effects could then be identified by differences to the visual stimulation and/or by differences between the right and left hemisphere because a thermal effect would mainly be cell unspecific and manifest at the fiber end. Experiments without virus injection were not carried out, however some animals revealed no or minimal virus expression and the induction of seizures was impossible. Figure 5.9 illustrates such a case. This stimulation shows no differences between right and left hemispheres and also no response that could not be attributed to the visual effect.

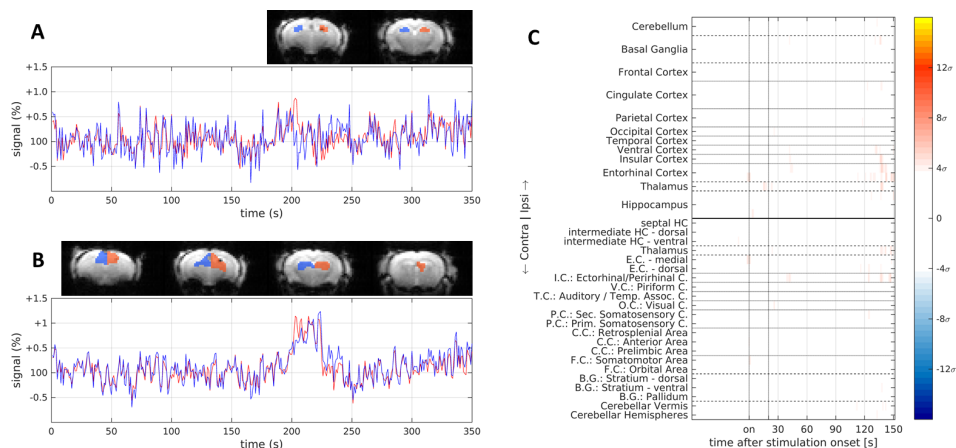


Figure 5.9: Failed induction of epileptic activity. A, B) Time courses in the hippocampus and thalamus during a single 20s stimulation (at time point 200s). C) Mean time courses in all brain regions. Scale bar in standard deviations (σ) during baseline rest periods. This is the same representation as for the later seizure evaluations and, compared to the seizure activity, shows no relevant visual or thermal effects.

In section 5.5 epileptic seizures are induced and it is important to know how the mentioned side effects could influence their analysis. Seizures are induced by a single 20s stimulation and instead of fitting a design model to the data, the fMRI intensity (above or below a certain threshold) is directly analyzed. This evaluation is less sensitive. Visual effects could be present in the thalamus but compared to the much stronger fMRI response during epileptic activity, can be neglected (Figure 5.9, C vs Figure 5.23). There are no indications that a thermal effect is present.

5.4.2 Optogenetic-fMRI Block Design

An fMRI block design experiment was performed and analyzed similar to the visual experiment. At a low light power of 5%, activation was only visible around the fiber tip (figure 5.10, A). When the light power was increased to 10%, the activity spread to the contralateral side and along the hippocampus to the entorhinal cortex (figure 5.10, B). The visual effect is not present because of the low light amplitude. Thermal effects can again be neglected as figure 5.10, B shows no differences in the time courses between the right and left septal hippocampi.

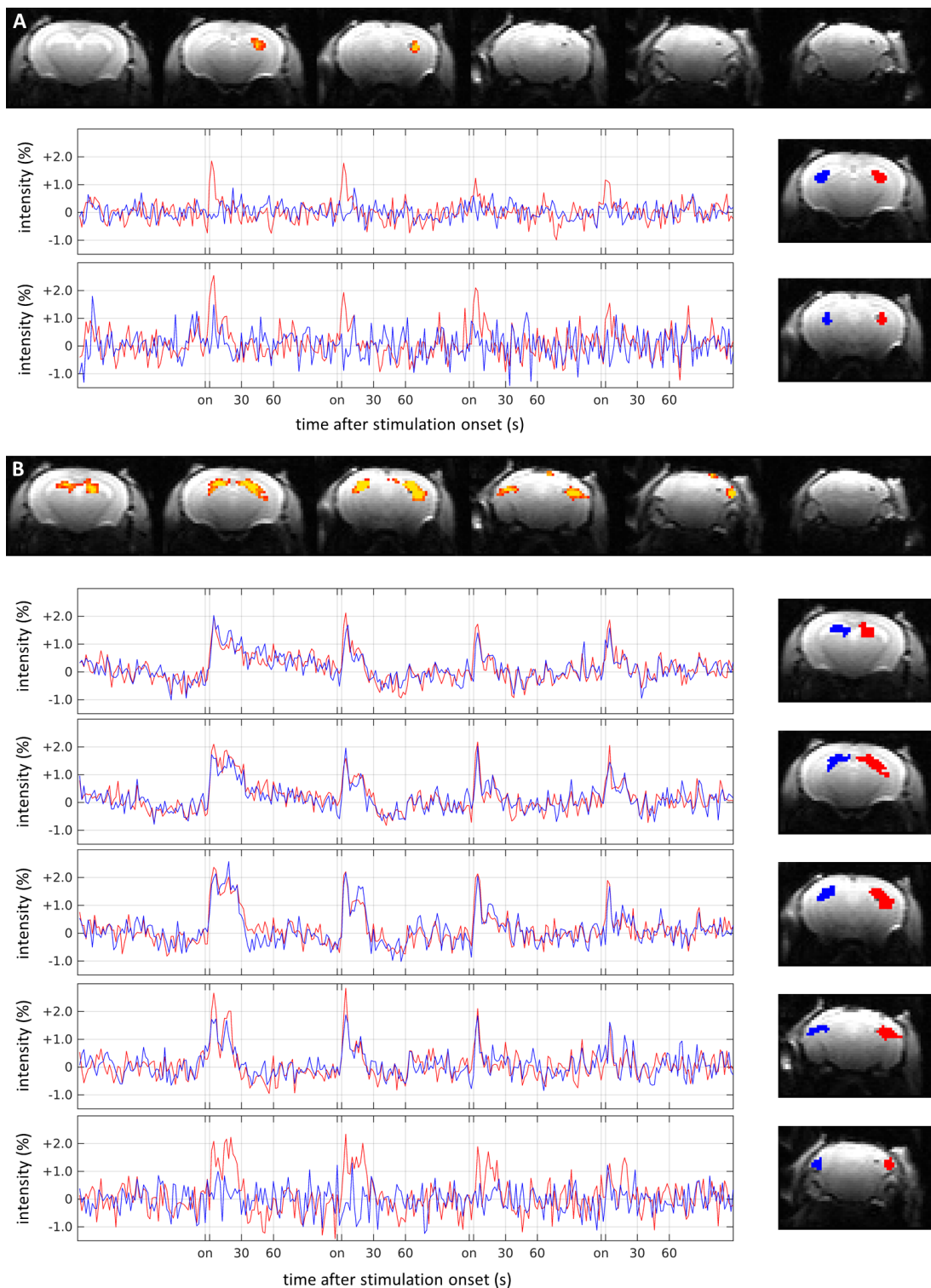


Figure 5.10: fMRI of optogenetic stimulation below seizure threshold. The light power was increased from 5% (A) to 10% (B). This shows the spread of activity, initially only at the right hippocampus, throughout the hippocampal-entorhinal network for the stronger stimulation (4 stimulations, 10 Hz, 20 ms pulse duration, amplitude settings 5% and 10% of the max. power, block design analyzed in FSL, red and blue time courses of the areas illustrated in the right column).

5.4.3 Resting State fMRI

15-minute resting state fMRI (rsfMRI) scans were analyzed by ICA with 30 components. Figure 5.11 shows around 10 components that are in accordance with the location and extent of anatomical brain regions as for example defined by the Allen brain atlas.

7 control mice were scanned 2-5 times and figure 5.12 shows the two components indicating the hippocampus and somatosensory cortex for every rsfMRI scan. Figure 5.11 represents the best case based on the used method and not every component is perfectly reproducible. However, figure 5.12 shows that rsfMRI is reasonably reproducible in the sense that in every animal and every scan bilateral connectivity is detectable. Improvements are discussed at the end of the chapter.

The selection of ICA components and their interpretation as “meaningful” or “noise” may lead to a bias during evaluation. Therefore, rsfMRI connectivity is mainly evaluated in this work using the seed-correlation approach of anatomically defined brain regions (Figure 5.13).

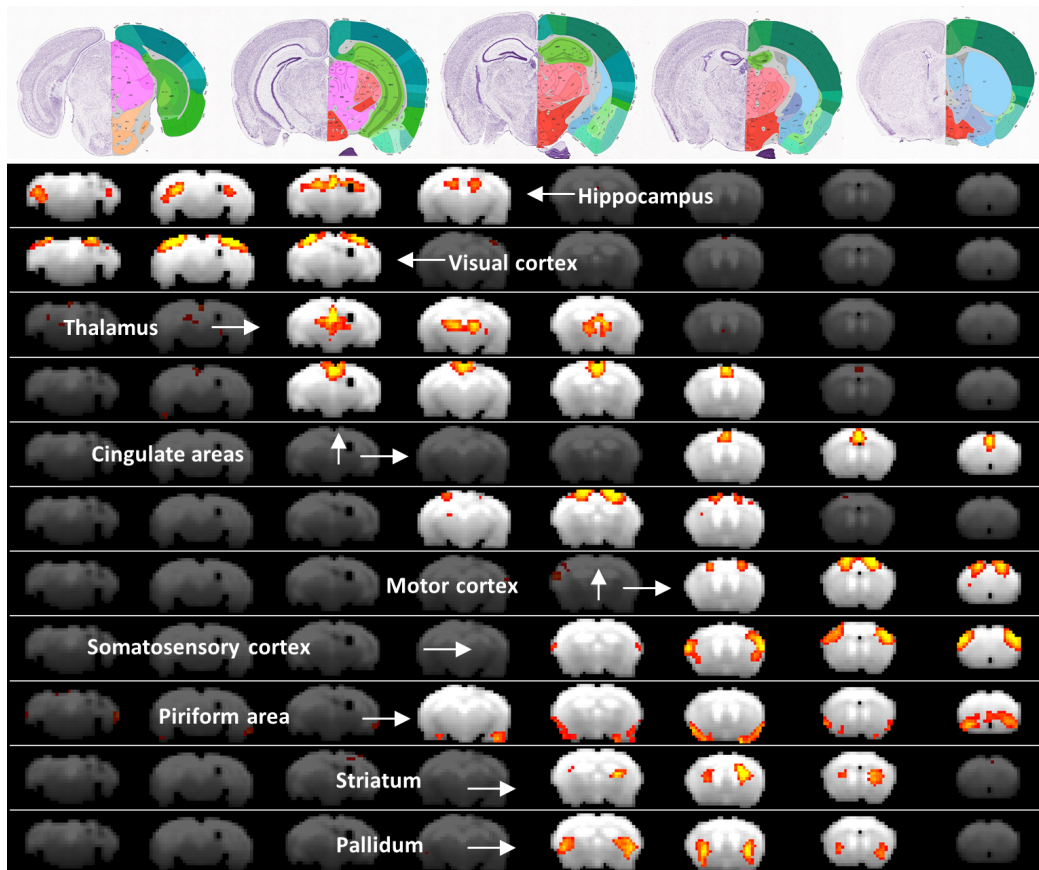


Figure 5.11: ICA components of single subject resting-state fMRI. Top) Allen mouse brain atlas. Below) selected rsfMRI ICA components (FSL MELODIC). Each row represents a different network, with each network overlaid on the same slices. Slices with only negligible activation are grayed out.

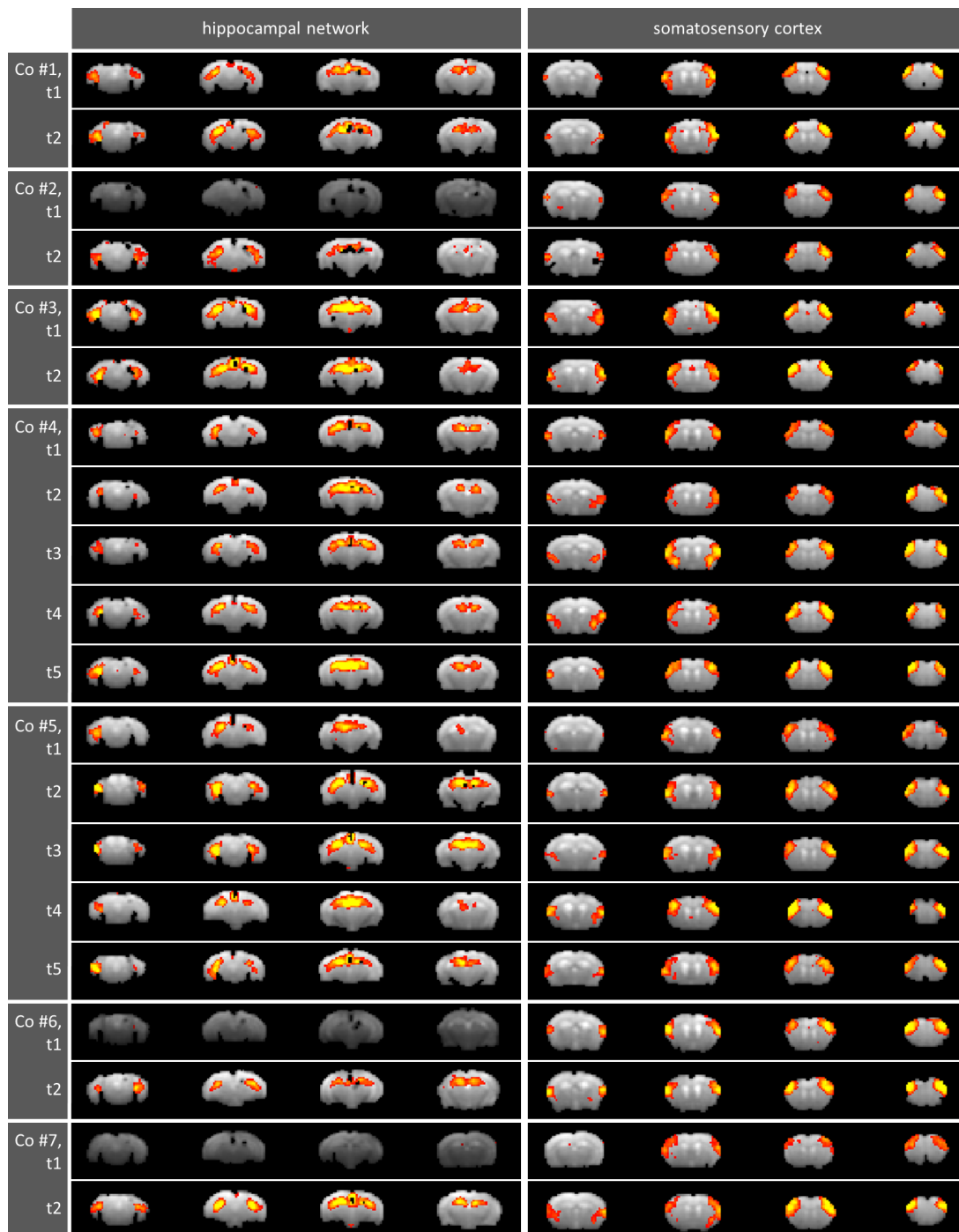


Figure 5.12: Reproducibility of resting-state fMRI ICA. 7 control (CO #1-7) mice were scanned 2-5 times (t1-t5) and the two ICA components corresponding to the hippocampi (HC) and the somatosensory cortex (SSC) are shown. The HC component was present in 17/20 measurements (absent components are shown as grayed out slices), the SSC was present in 20/20 measurements.

Figure 5.13 shows the pairwise correlations of the mean time courses in the defined brain regions. Correlations of fMRI time courses are not directionally dependent; for two brain regions A and B, $\text{corr}(A,B)$ equals $\text{corr}(B,A)$. The correlation matrix is thus symmetric, so only the lower left half is shown. The diagonal from top left to bottom right represents the trivial correlations $\text{corr}(A, A)$ and is thus also not shown.

The regions are ordered by hemispheres. That leads to three different areas in the matrix: The upper left triangle shows the correlations only within the ipsilateral (right) hemisphere, the lower right triangle within the contralateral (left) hemisphere and the remaining quadrant shows the correlations between the hemispheres. The diagonal in this quadrant, from the lower left corner to top right, shows the correlations between homologous areas in each hemisphere which are usually well connected.

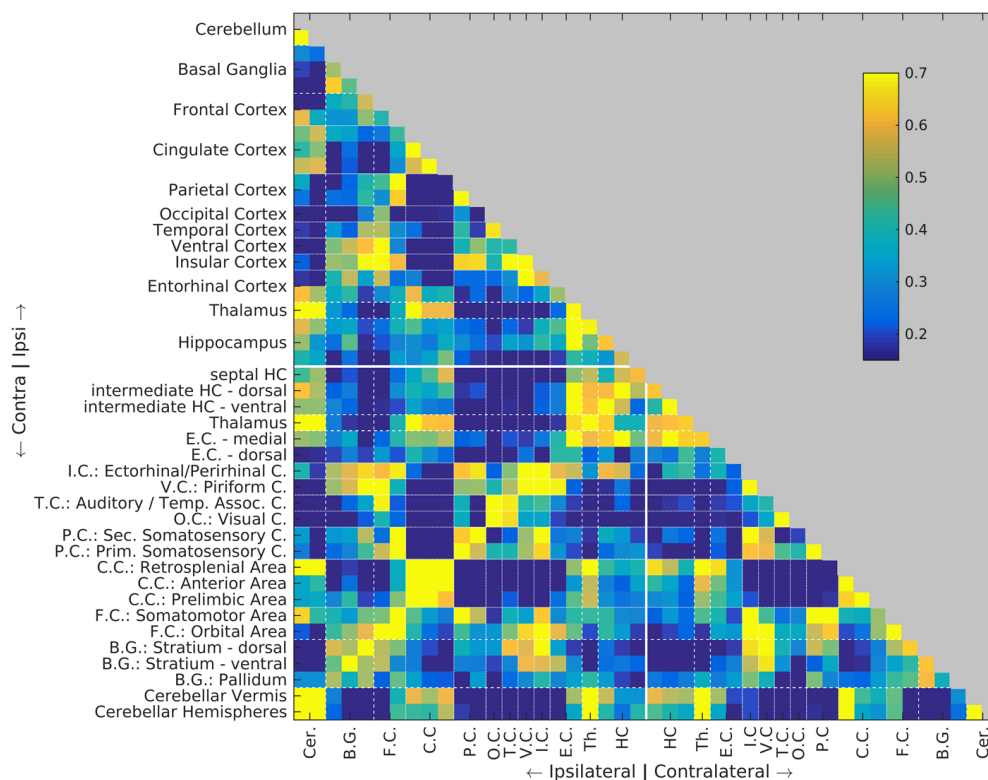


Figure 5.13: Seed-based resting-state fMRI connectivity. Result from a 15-minute rsfMRI scan (Fisher-z transformed correlation coefficients, color range 0.15-0.7).

5.4.4 Sliding Window Analysis of Resting State fMRI

The rsfMRI time courses (TC) of the kainate mice often showed unusual fluctuations (figure 5.14 C, arrow) that could not be attributed to motion artifacts (figure 5.14, A). The correlation of the whole 15 min TC results in an anomalous pattern (figure 5.14, G). A sliding window analysis was used to only analyze time periods without these conspicuous signals (figure 5.14 D). To obtain a reference for the range of “normal” connectivities, all control mice were analyzed in this way. The mean correlation across all brain regions plus 3 times the standard deviation was ≈ 0.51 . This was set as threshold to define “normal” and anomalous connectivity patterns. Only time windows with a mean correlation below this threshold were used and averaged.

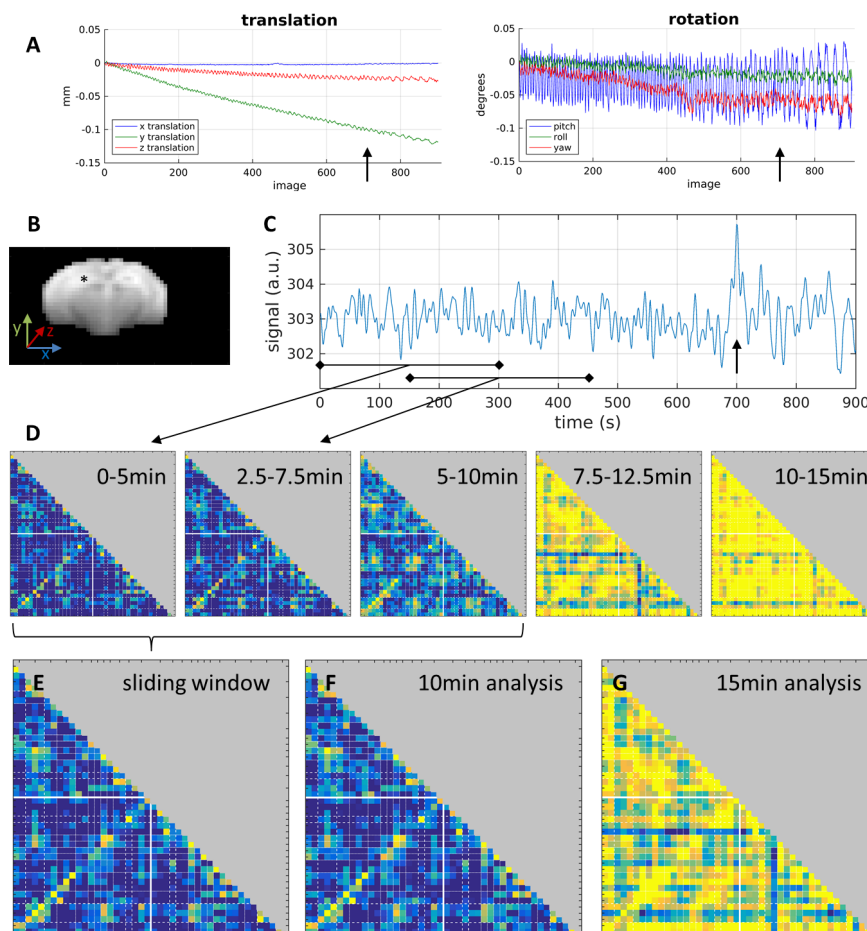


Figure: 5.14. Sliding window analysis of rsfMRI. **A)** motion estimates of the rsfMRI scan (SPM, MATLAB). **B and C)** selected time course (asterisk). **D)** Analysis of 5min time windows, shifted by 2.5min. **E)** Average of the first 3 windows. **F)** Static analysis of the first 10 min. **G)** Static analysis of the whole 15 min (correlation coefficients color range 0.15-0.7).

In control animals, 1 out of 20 scans showed these abnormally strong connectivities, which was related to irregular breathing during this scan. In contrast to this, 6 out of 7 kainate mice were affected and 11/25 scans from those 6 mice were conspicuous. EEG recordings would be necessary to identify the origin of these large synchronous fluctua-

tions. However, because of the much higher incidence in epileptic animals, it can be assumed that at least to some degree spontaneous interictal epileptic activity is present and responsible for these effects. Discarding windows with abnormally strong correlations ensured that only true resting-state connectivity was analyzed.

For the control group, the static correlation of the whole 15 min TC was compared to the sliding window approach yielding no significant differences (figure 5.15). The sliding window approach was therefore used to analyze control and kainate mice (Figures 5.16 and 5.17).

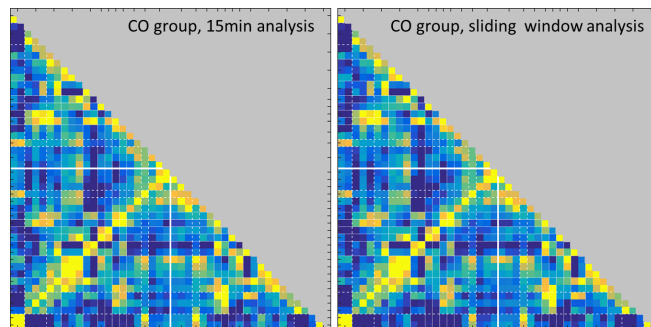


Figure 5.15: Comparison of static and sliding window analysis. A false-discovery-rate (FDR) corrected t-test revealed no differences between these approaches.

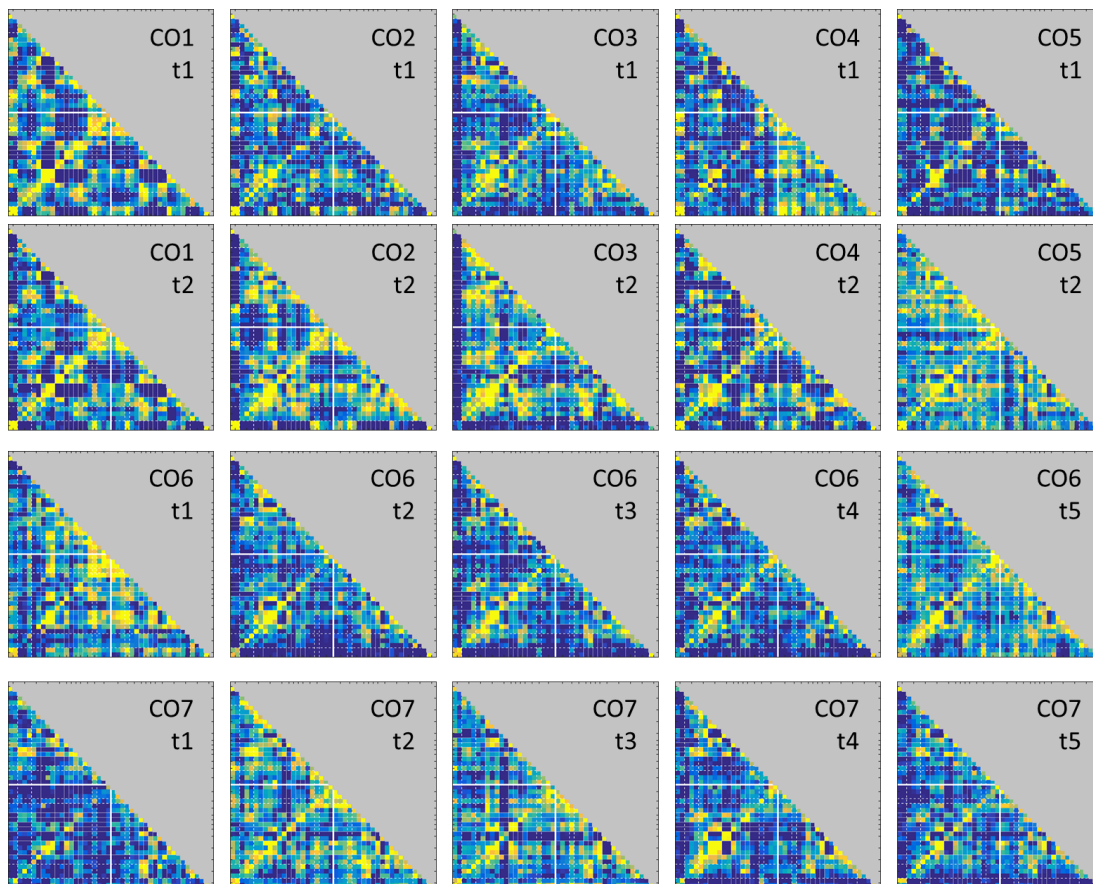


Figure 5.16: Resting-state fMRI correlations for all measurements of control mice.

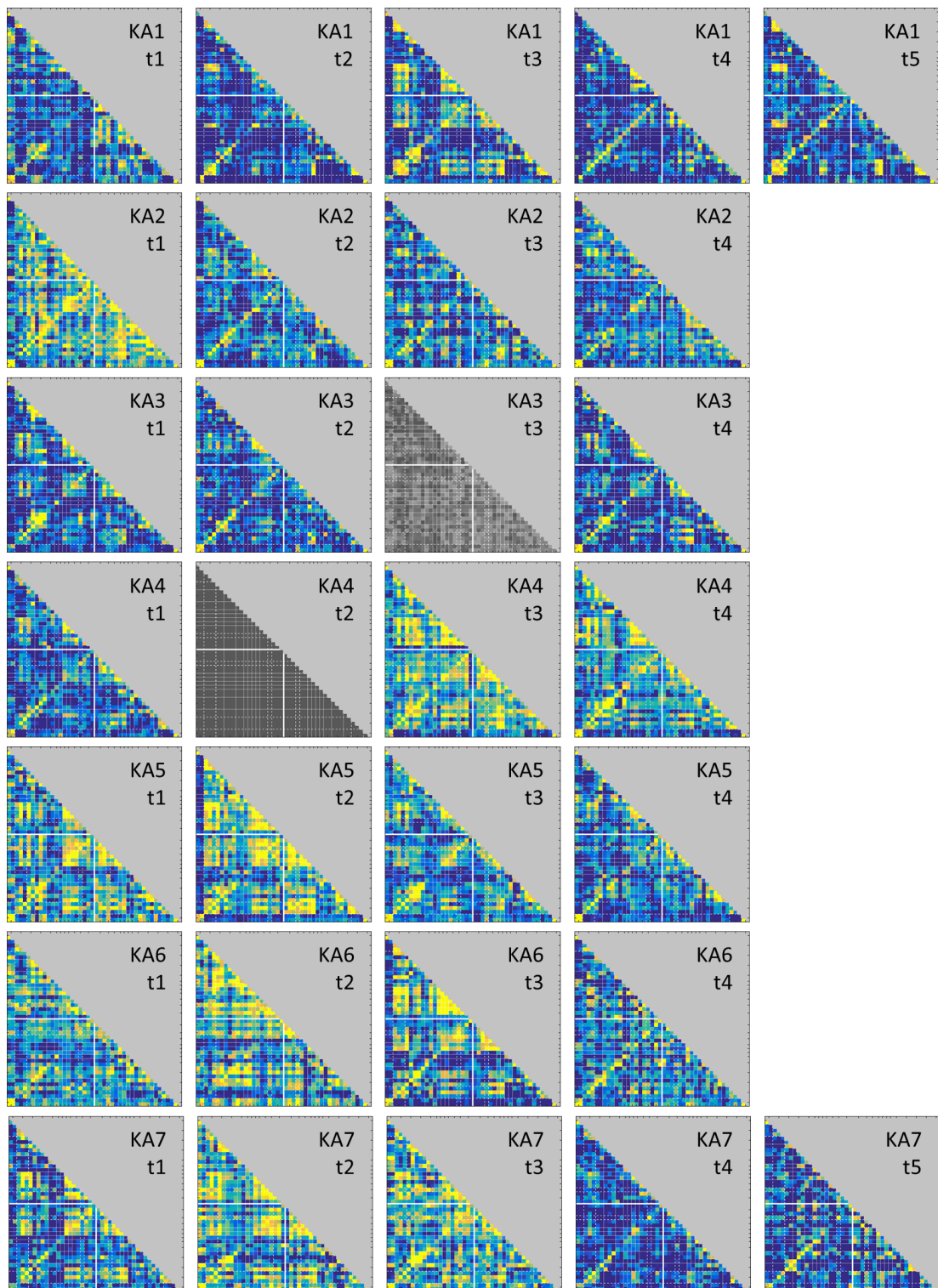


Figure 5.17: Resting-state fMRI correlations for all measurements of kainate mice. Two datasets were dismissed because only a period of 5 minutes or less was free of artefacts and abnormally strong correlations.

5.4.5 Comparison of Single-Echo and Multi-Echo fMRI

The performance of single-echo fMRI was compared to the combined multi-echo (ME) fMRI datasets (figure 5.18). This was done with the control group datasets (figure 5.16).

In comparison to the first echo image ET1, ME fMRI showed substantially increased correlations. Significant differences were found especially in the basal ganglia and hippocampal regions, which are located towards the middle of the brain where T_2^* is much longer than the first echo time of 13.9 ms. The ME datasets benefit from the higher sensitivity due to the second echo image.

In comparison to the second echo image ET2, ME fMRI showed only weakly increased correlations. A false-discovery-rate (FDR) corrected t-test showed no significant differences. However, the weak increases were not unspecific. Increased values were mainly observed in regions with a high correlation. Therefore, one may conclude that ME could help detect connectivities slightly better. The T_2^* in many brain areas was around 25-35 ms or longer (figure 5.6). Thus, adding the first echo image (at 13.9 ms) to the second (at 22.6 ms) increases the SNR but hardly improves the sensitivity. Adding a third echo at an echo time of 31ms however may further improve the ME fMRI performance.

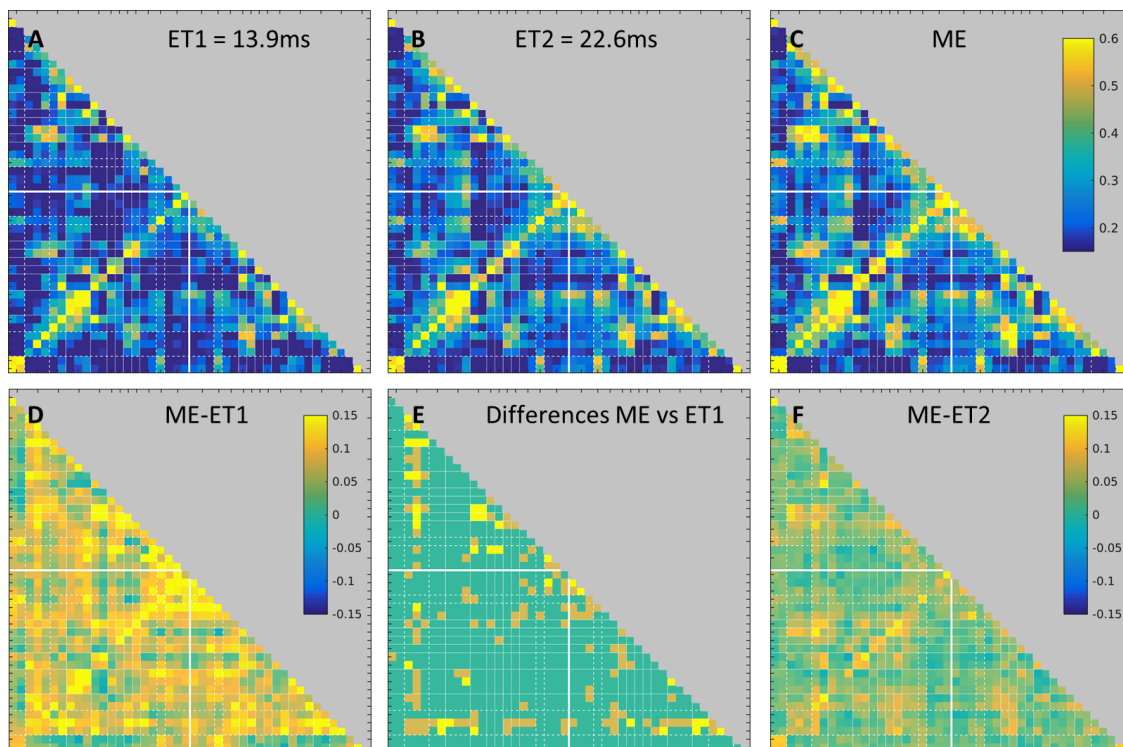


Figure 5.18: Comparison of single-echo and multi-echo fMRI. Seed-based resting state fMRI correlations using only the first echo time (A), the second echo time (B) or the combined multi-echo data (C). D) Correlation coefficients of ME minus ET1. E) FDR-corrected t-test shows significantly increased correlations in the ME data (p value yellow 0.01, orange 0.05). F) Correlation coefficients of ME minus ET2.

5.4.6 Dynamic fMRI Response of Epileptic Seizures

The fMRI response during an epileptic seizure is variable and (so far) unpredictable. For example, it is possible that after a short activation in the hippocampus a prolonged depression occurs, but this is not guaranteed. In contrast to the block design experiments there is only a single stimulation. Therefore, it is impossible fit a design model to the data for evaluation. Seizure activity is evaluated in this work simply by means of the signal intensity. The 90s before the stimulation are defined as baseline and the "fMRI response" is given in standard deviations (σ) of the baseline in the respective region.

The long-lasting signal changes influence the choice for the temporal filtering during postprocessing. The routinely applied high-pass temporal filtering (HPTF) would lead to corrupted time courses (figure 5.19, A). Therefore, no HPTF was applied, and only linear drifts detected before the stimulation were removed from the time courses. Low-pass temporal filtering (LPTF) was applied to reduce the fast, non-BOLD related fluctuations (figure 5.19, B). For this, a moving average window filter replaced every point in the time course with the average of three consecutive points (the time point plus the preceding and subsequent one).

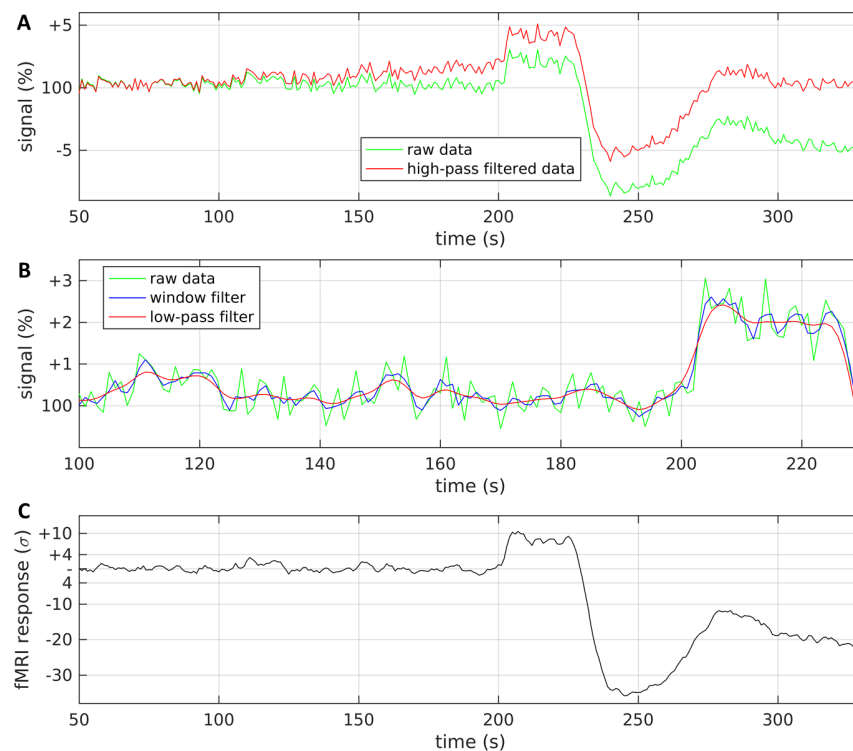


Figure 5.19: FMRI temporal filtering for seizure activity. **A)** fMRI time course without and with applied high-pass temporal filter. As expected, the high-pass filter distorts the slow BOLD fluctuations associated with the epileptic seizure. **B)** Unfiltered data and low-pass temporal filter implemented as Gaussian smoothing (red line; FSL, 0.5Hz cutoff) or moving average window filter (blue line; MATLAB). **C)** Time course of seizure activity after post-processing steps: linear drift removal, low-pass filtering and spatial smoothing.

5.5 Results II: Epileptic networks

During fMRI scans, mice rested for 20 minutes and then an epileptic seizure was triggered. This allowed to analyze the seizure activity as well as the resting-state connectivity immediately before it. Sections 5.5.1 and 5.5.2 describe the seizure activity and resting-state connectivity, respectively. In section 5.5.3, relationships between seizure spread and connectivity are outlined.

The control (CO) group consisted of 7 mice and a total of 20 scans. Seizure induction was successful in 5 CO mice with a total of 16 seizures. The kainate (KA) group consisted of 7 mice and a total of 28 scans. Seizure induction was successful only in 2 KA mice with a total of 5 evaluable seizures. All scans were used for the resting-state fMRI analysis.

5.5.1 fMRI during Optogenetically-Induced Epileptiform Activity

Figure 5.20 shows the fMRI response upon seizure induction in a CO mouse. Detected activity started in the hippocampus at the stimulus location, quickly spread along the hippocampus to the entorhinal cortex and then spread further to other cortical areas and the frontal part of the brain. The meaning of the negative in the somatosensory cortex is unclear; it could represent neuronal depression, but also activation as this can also lead to negative fMRI responses under certain circumstances (Schridde et al., 2008). The strong and long-lasting negative response in the hippocampus however followed an initial strong positive response and may be related to neuronal depression. This effect was observed for > 1 h. The propagation in the right and left hemisphere was symmetric.

The seizure propagation in a KA mouse (figure 5.21) on the contrary was not quite symmetric. At the onset, there was a clearly stronger involvement of the ipsilateral hemisphere. In comparison to the CO mouse, the KA mouse showed an increased spread and seizure duration.

In Figure 5.22 the response in the hippocampus for all CO and KA mice is plotted. Figure 5.23 represents an overview of the mean response across the entire brain. Obvious differences between CO and KA mice are that seizures in KA mice last longer and spread to more cortical regions. The areas of the hippocampus, entorhinal cortex and thalamus are involved in CO and KA mice. Significantly different is the delayed response in the contralateral hippocampus in KA mice.

Figure 5.24 shows these overview maps for all datasets.

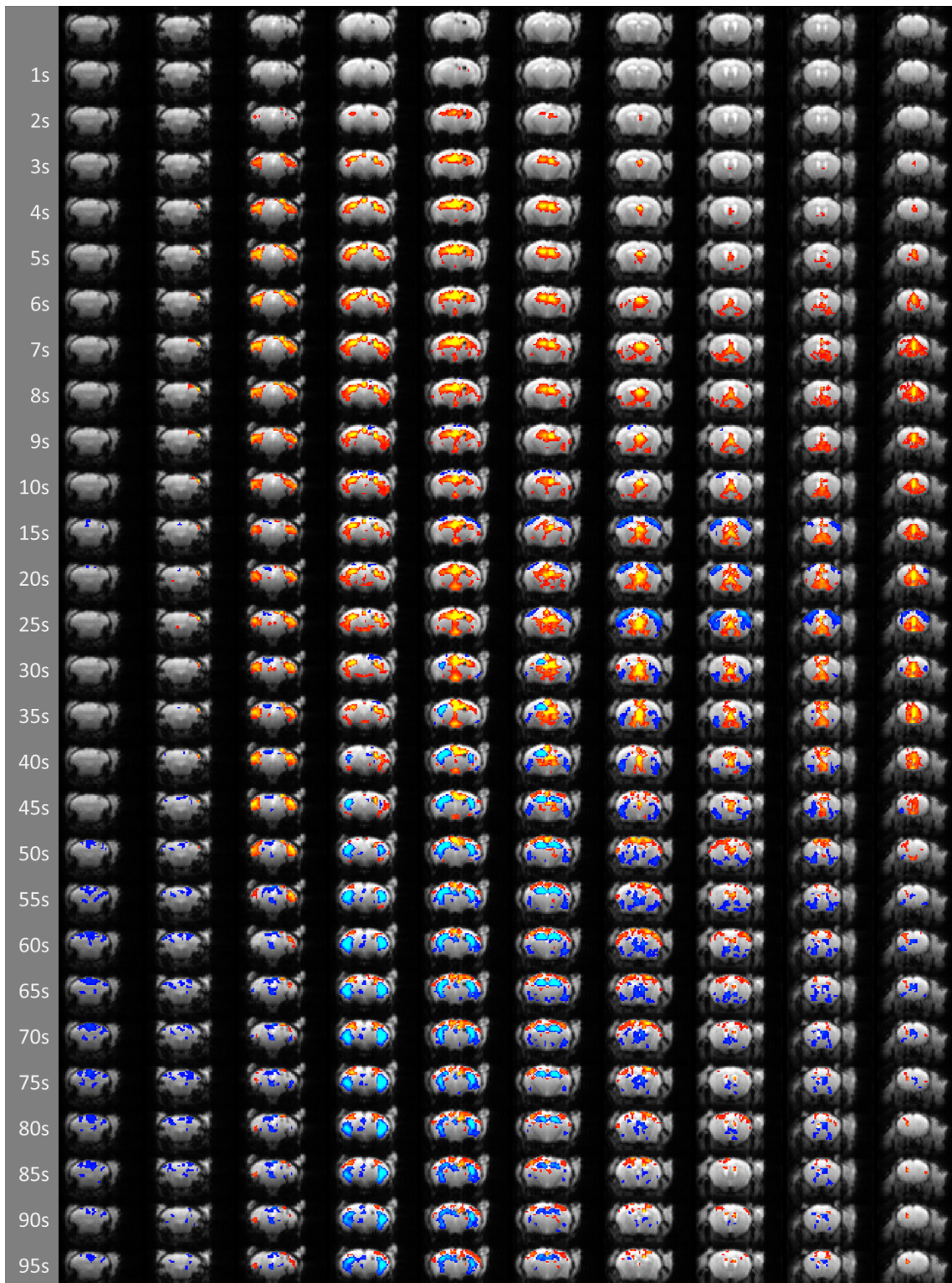


Figure 5.20: Seizure propagation in a control mouse. Left column) time after stimulation onset. Corresponding rows) fMRI responses, positive responses in red-yellow, negative responses in blue-light blue (voxelwise threshold for activation $\pm 4.89\sigma$).

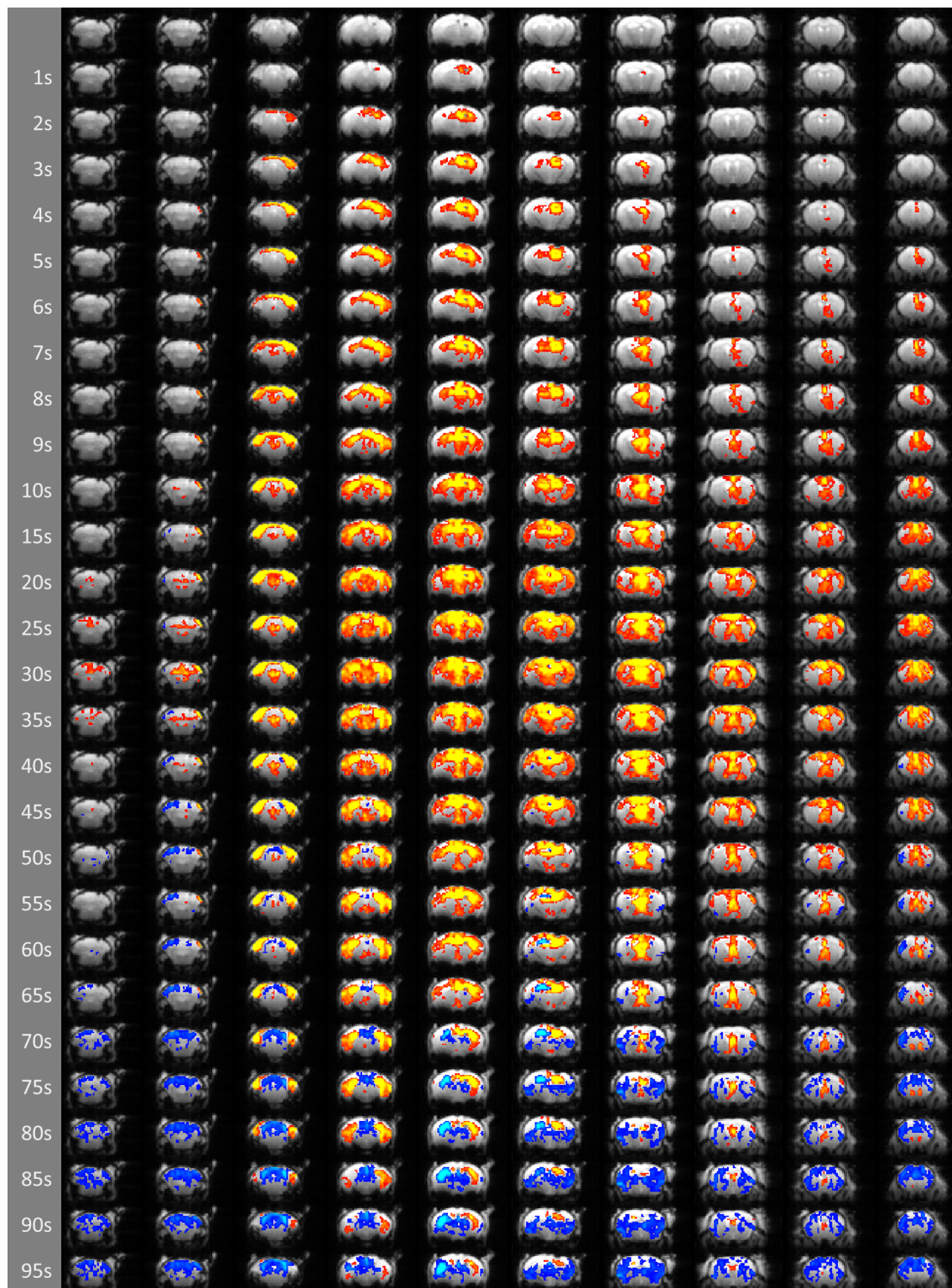


Figure 5.21: Seizure propagation in a kainate mouse. Left column) time after stimulation onset. Corresponding rows) fMRI responses, positive responses in red-yellow, negative responses in blue-light blue (voxelwise threshold for activation $\pm 4.89 \sigma$).

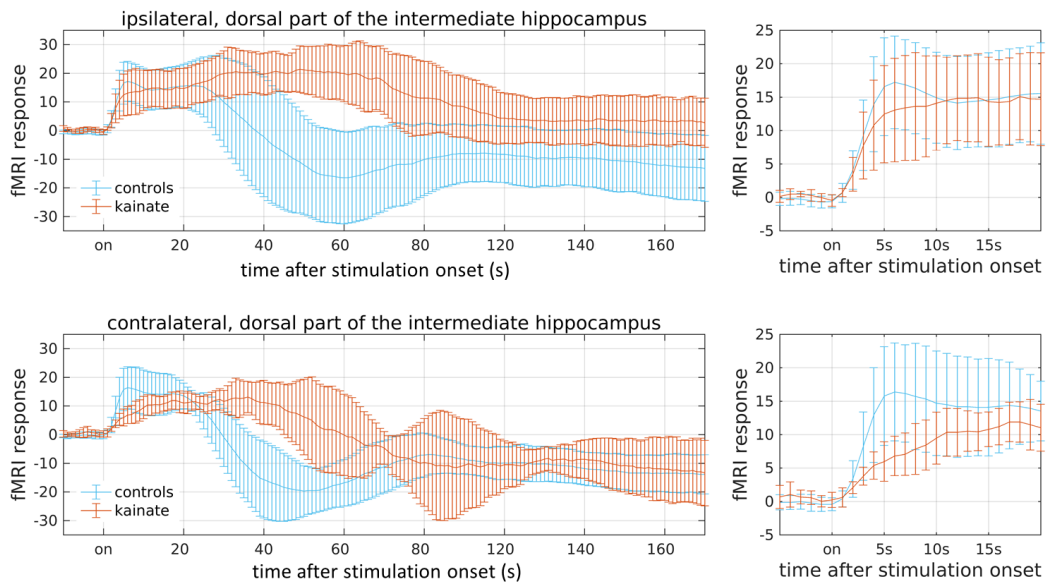


Figure 5.22: fMRI time courses during epileptic seizures. Ipsilateral (top) and contralateral (bottom) time courses in the dorsal part of the intermediate hippocampus for kainate (red) and control (blue) mice. Right) Enlarged view of the first 20s. “FMRI response” in standard deviations (σ) of the baseline. Error bars represent the standard deviations among the animals.

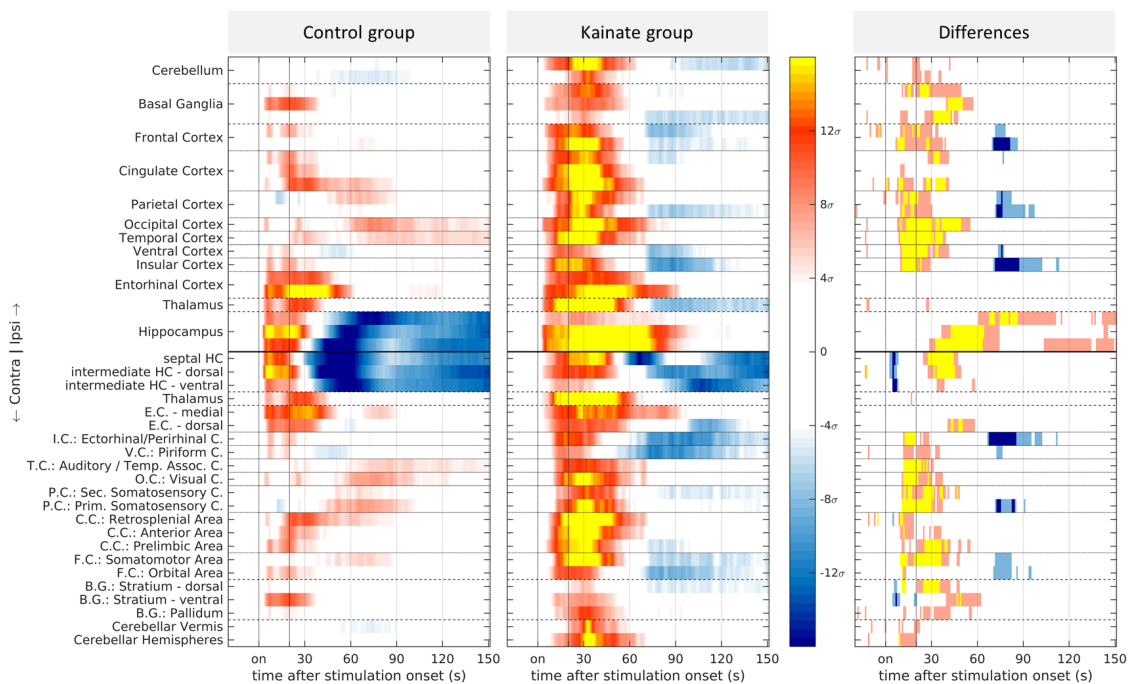


Figure 5.23: Mean seizure response in control and kainate mice. Mean time courses in the defined brain regions averaged for all seizures induced in control (left) and kainate (middle) mice. Scale bar in standard deviations (σ) of the baseline. Right) Increased activity in kainate mice in orange-yellow (p 0.05-0.01) and decreases in light blue-blue (p 0.05-0.01, FDR corrected t-test).

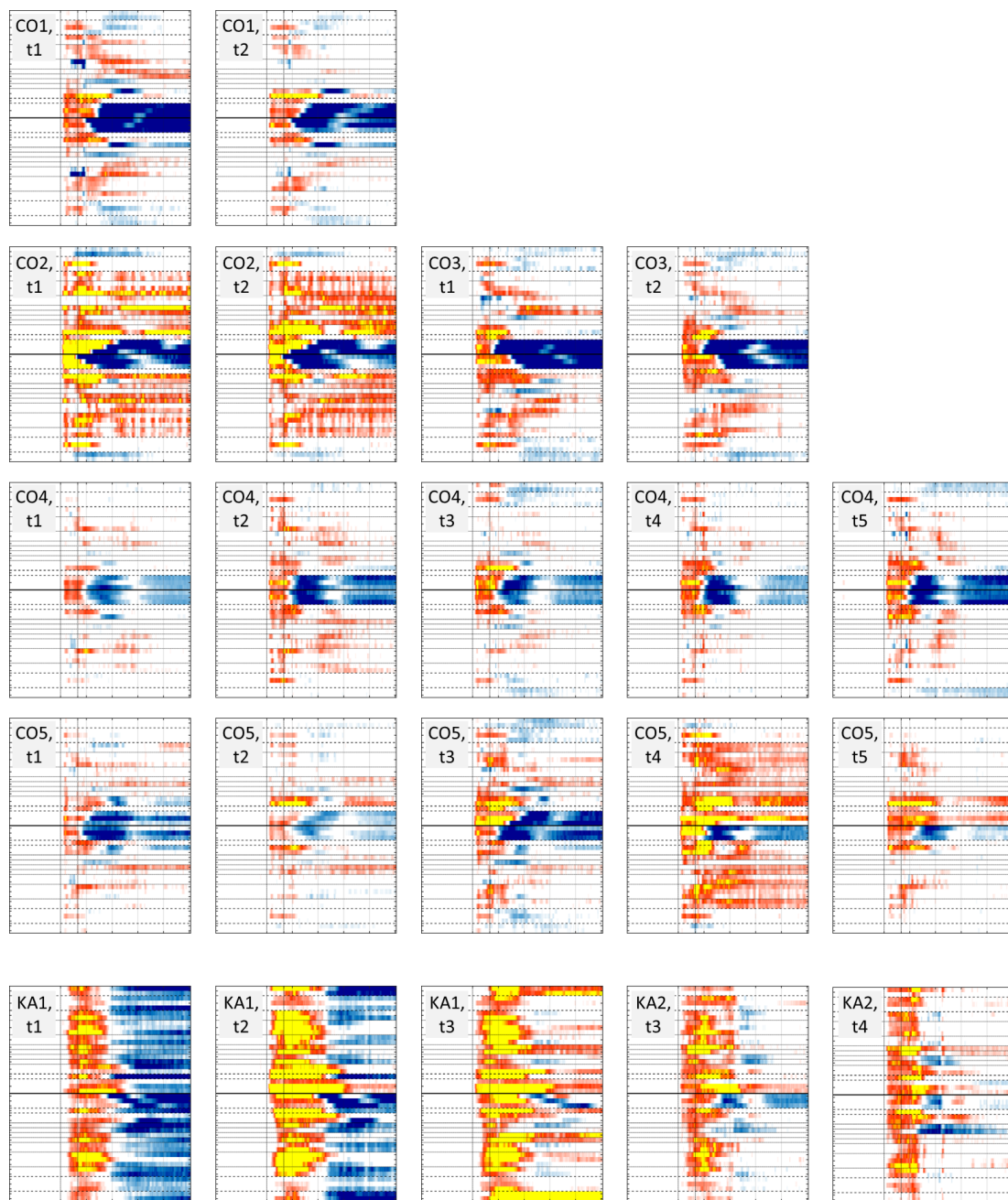


Figure 5.24: Overview of all induced seizures. fMRI of seizure activity in 5 control mice with 2-5 repetitions. In 2 kainate mice, 5 seizures were evaluable in total.

The strength of the fMRI signal is somewhat related to the strength of the underlying neuronal activity. However, fMRI is not a truly quantitative method. If responses in certain brain areas are frequently present, they may also be important even if they show a relatively low (albeit significant) signal change. Figure 5.25 illustrates the probability of significant responses. This shows that the responses in the basal ganglia and cingulate cortex may be relatively weak, but they were often present in CO mice.

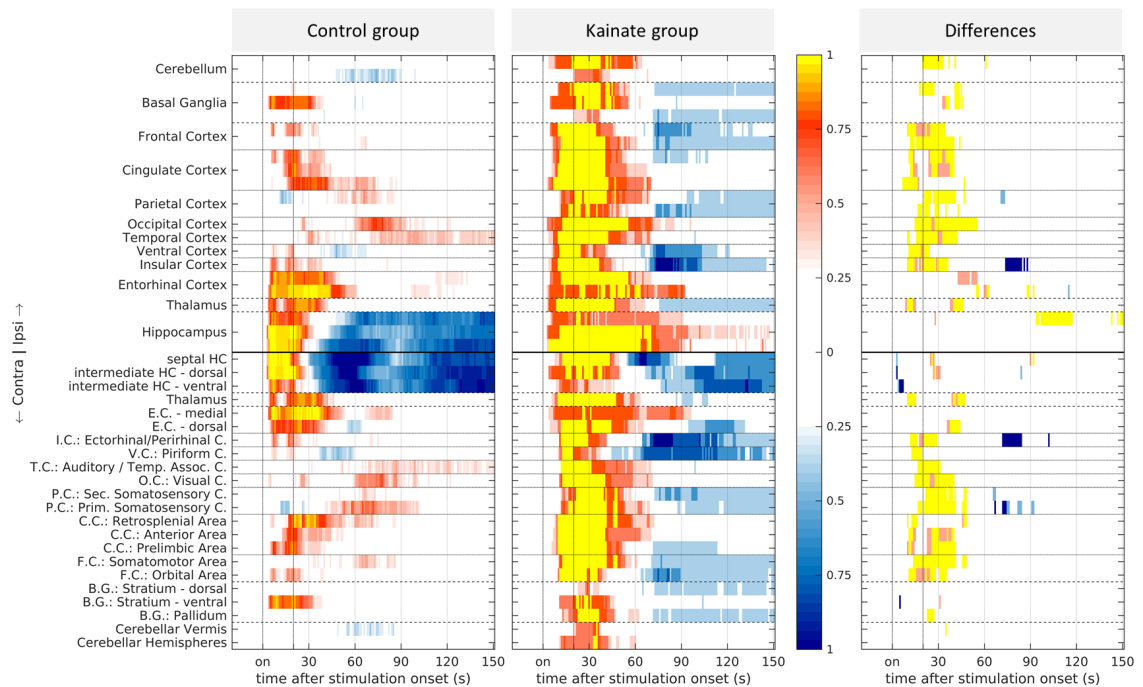


Figure 5.25: Probability of seizure activity in control and kainate mice. These maps show the incidence ($\pm 6\sigma$) of significantly ($\pm 6\sigma$) increased or decreased activity for control and kainate mice. Significant differences obtained by an FDR-corrected t-test.

5.5.2 Resting State fMRI Connectivity Changes

Figure 5.26 shows the mean functional connectivity in control mice. This is also illustrated in figure 5.27 in which the regions with the strongest connections to the seed regions are colored. These illustrations show that fMRI correlations are not randomly distributed but represent plausible connections. In general, regions are functionally connected to the homologous region on the contralateral hemisphere, to adjacent regions and/or within established networks, for example hippocampus-entorhinal cortex, hippocampus-thalamus or primary to secondary somatosensory cortex. Also, the connectivity patterns are similar regardless of whether the seed is placed on the right or left hemisphere.

Figure 5.28 shows the mean functional connectivity in kainate mice and figure 5.29 shows the significant differences. Figure 5.30 illustrates the strongest connections for CO and KA mice to facilitate a direct comparison. In general, connectivity patterns are more bilateral and symmetric in CO than KA mice. As one unforeseen result, resting-state fMRI showed stronger connections of the hippocampal regions to the frontal part of the brain in KA mice (see figure 5.30, regions of the intermediate HC, the ventral striatum of the basal ganglia and the frontal cortex).

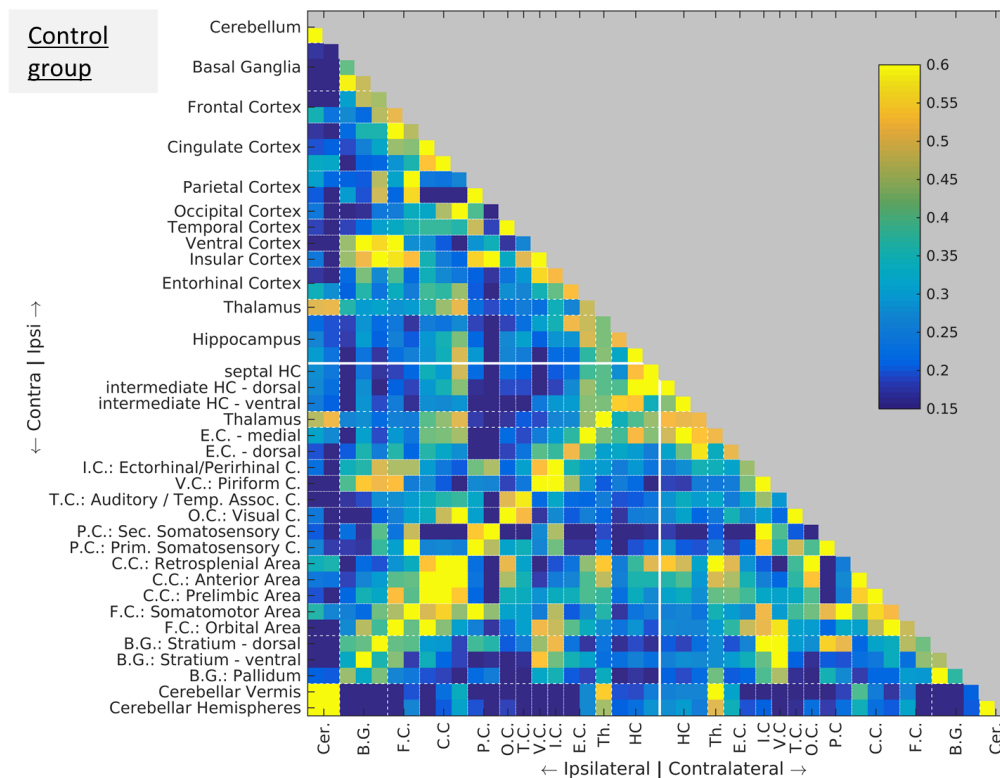


Figure 5.26: Mean resting-state fMRI connectivity in control mice. Fisher-z transformed correlation coefficients; color range blue-yellow 0.15-0.6.

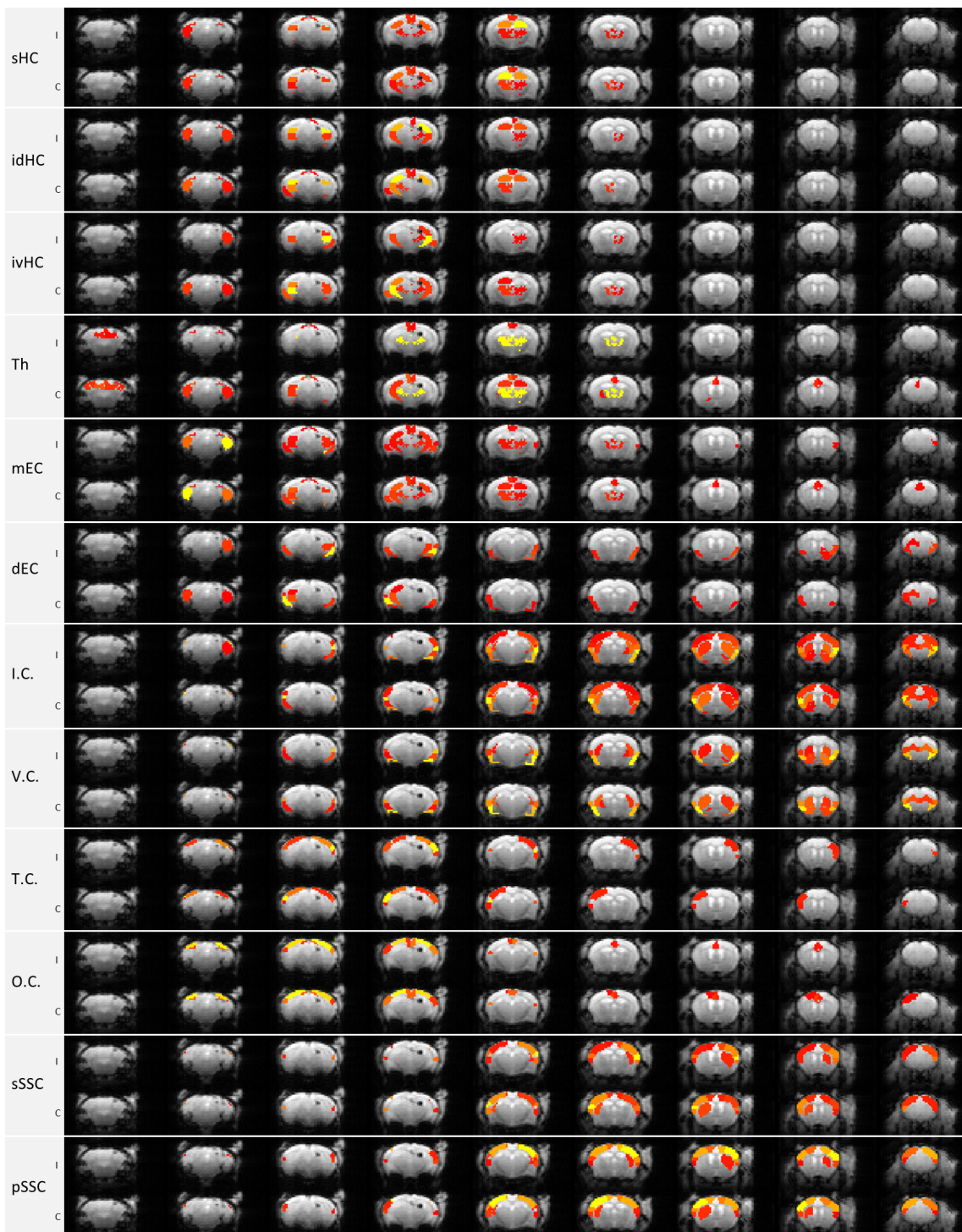
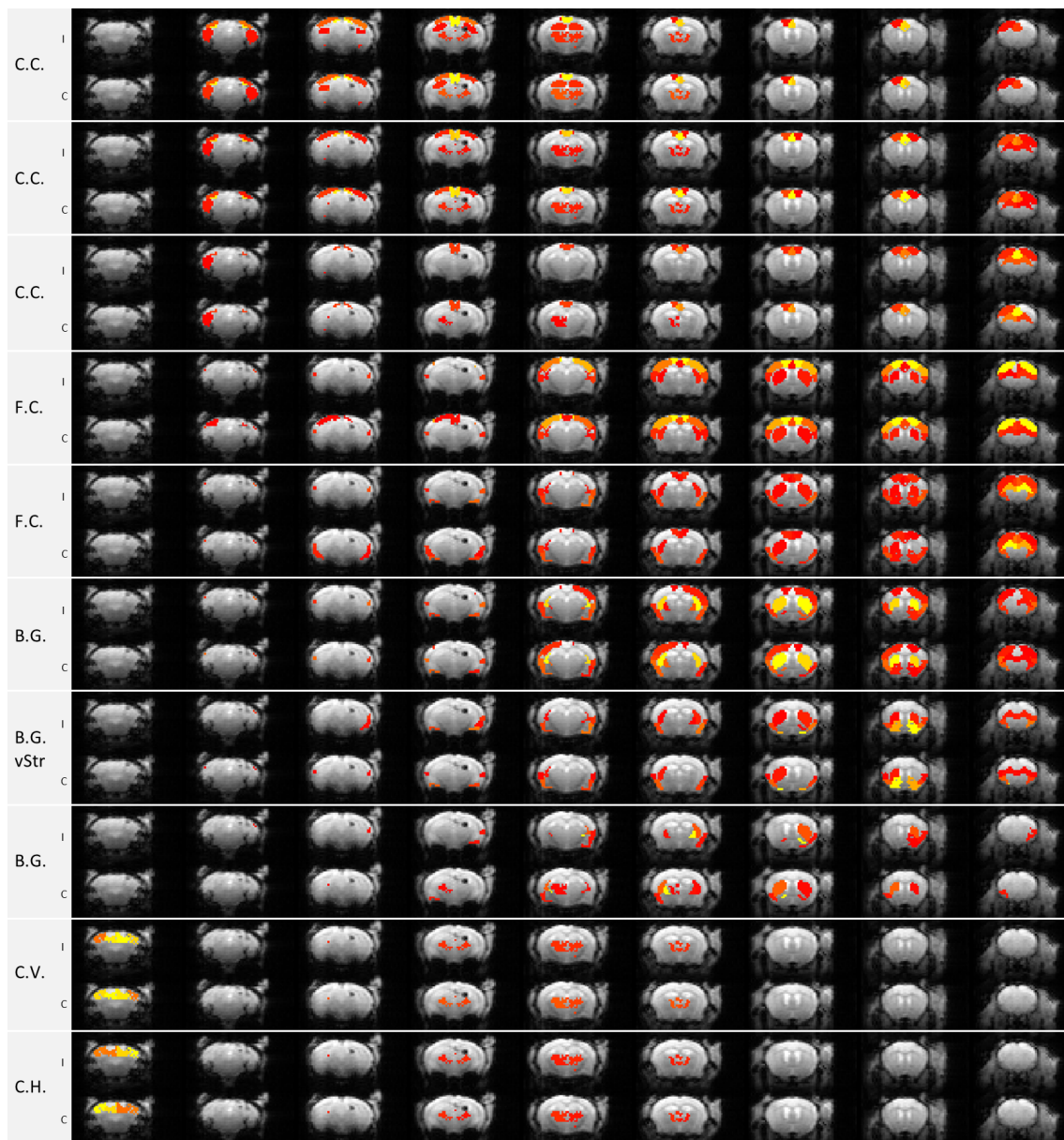


Figure 5.27: Anatomical representation of the mean resting-state fMRI connectivity in control mice. Left column) seed-region on the ipsi- (I) or contralateral (C) hemisphere. A brain region is color coded if the correlation of this region to the seed region is >0.4 . Color code of the correlation coefficient: red (0.4) – yellow (1). The seed regions are colored in yellow. Abbreviations: septal pole of the hippocampus (sHC), intermediate dorsal HC (idHC), intermediate ventral HC (ivHC), thalamus (Th), medial entorhinal cortex (mEC), dorsal EC (dEC), insular cortex (I.C.), ventral cortex (V.C.), temporal cortex (T.C.), occipital cortex (O.C.), secondary somatosensory cortex (sSSC), primary SSC (pSSC).



Continuation of figure 5.27. Abbreviations: cingulate cortex (C.C.), frontal cortex (F.C.), basal ganglia (B.G.), ventral striatum (vStr), cerebellar vermis (C.V.), cerebellar hemispheres (C.H.).

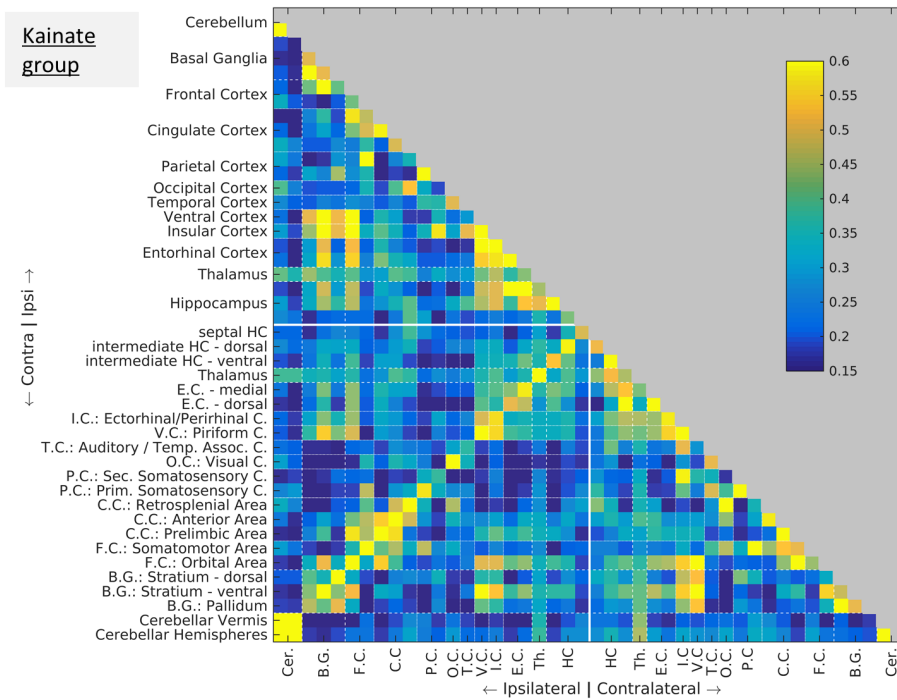


Figure 5.28: Mean resting-state fMRI connectivity in kainate mice. Fisher-z transformed correlation coefficients; color range blue-yellow 0.15-0.6.

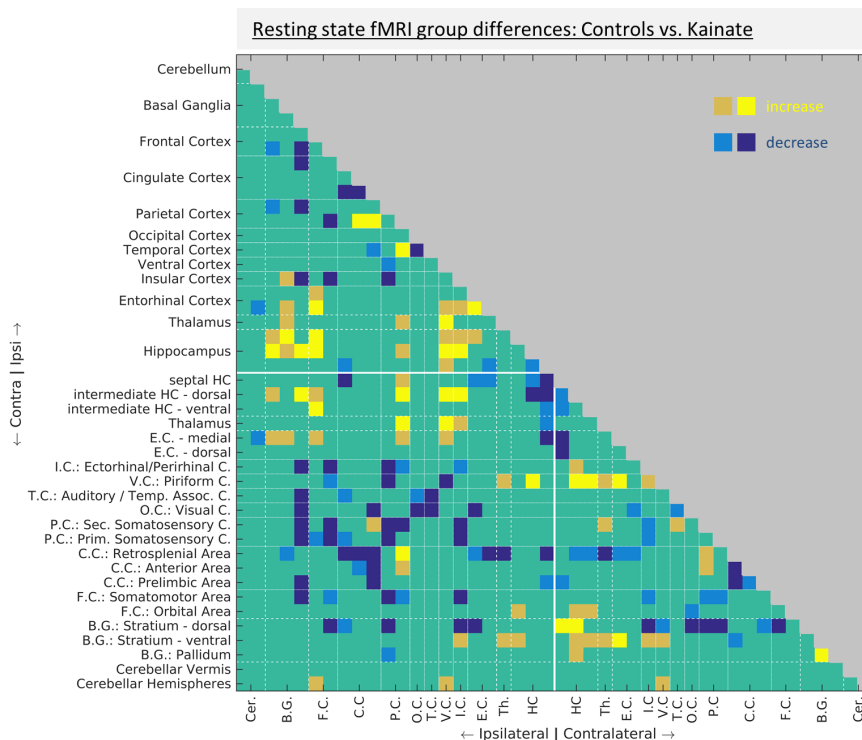


Figure 5.29: Resting-state fMRI differences between the CO and KA group. Increased correlations in KA mice in orange ($p < 0.05$) and yellow ($p < 0.01$). Significant decreases in KA mice in light-blue ($p < 0.05$) and blue ($p < 0.01$). FDR-corrected t-test comparison.

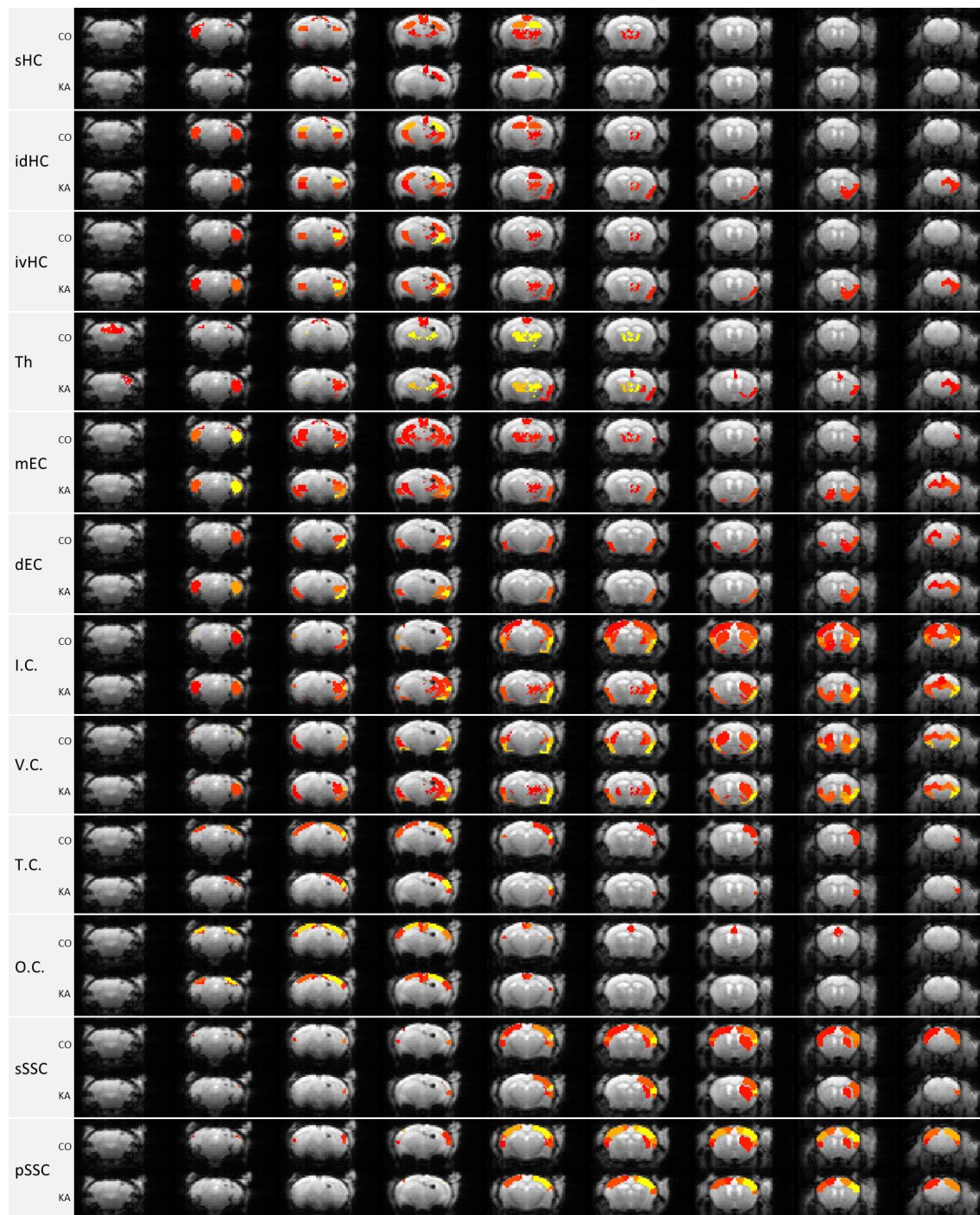
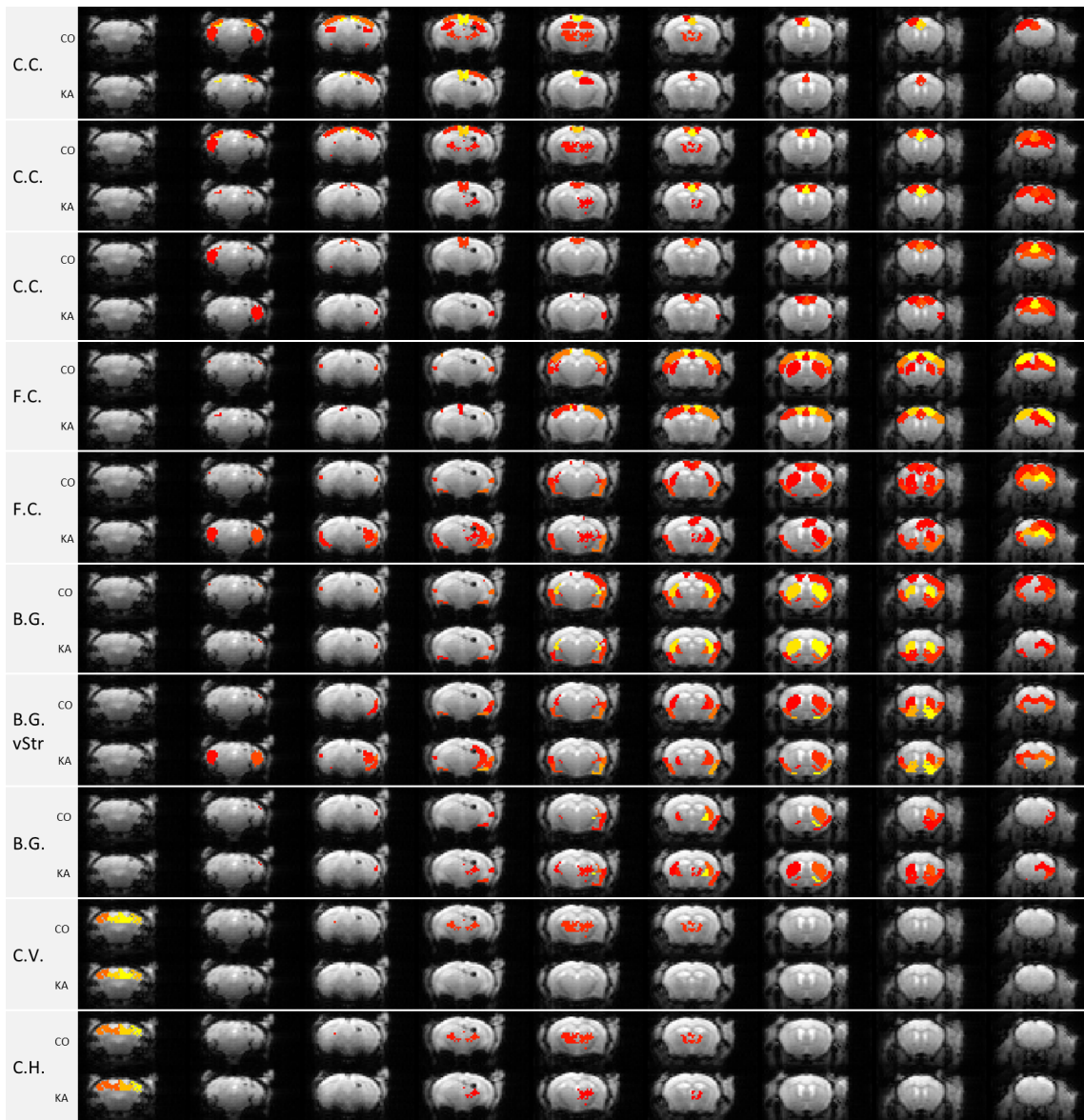


Figure 5.30: Anatomical representation of connectivity differences between CO and KA mice. Left column) seed-region on the ipsilateral hemisphere for the control (CO) and kainate (KA) group. A brain region is color coded if the correlation of this region to the seed region is >0.4 . Color code of the correlation coefficient: red (0.4) – yellow (1). The seed regions are colored in yellow. Abbreviations: septal pole of the hippocampus (sHC), intermediate dorsal HC (idHC), intermediate ventral HC (ivHC), thalamus (Th), medial entorhinal cortex (mEC), dorsal EC (dEC), insular cortex (I.C.), ventral cortex (V.C.), temporal cortex (T.C.), occipital cortex (O.C.), secondary somatosensory cortex (sSSC), primary SSC (pSSC).



Continuation of figure 5.30. Abbreviations: cingulate cortex (C.C.), frontal cortex (F.C.), basal ganglia (B.G.), ventral striatum (vStr), cerebellar vermis (C.V.), cerebellar hemispheres (C.H.).

Group ICA for the KA and CO mice were analyzed. To create two completely comparable groups, only two datasets per animal were taken because some control mice were only scanned two times. For each scan, a 10-minute period free of any “unusual” fluctuations or artifacts was selected. Figures 5.31 and 5.32 show a selection of ICA components for the KA and CO group, respectively. The most obvious difference is that in CO mice, there was one single component that represents the hippocampus. Whereas in KA mice, such a component was not present but two separate components were found representing the right and left hippocampus. There were also fewer components showing bilateral cortical connectivity in KA mice.

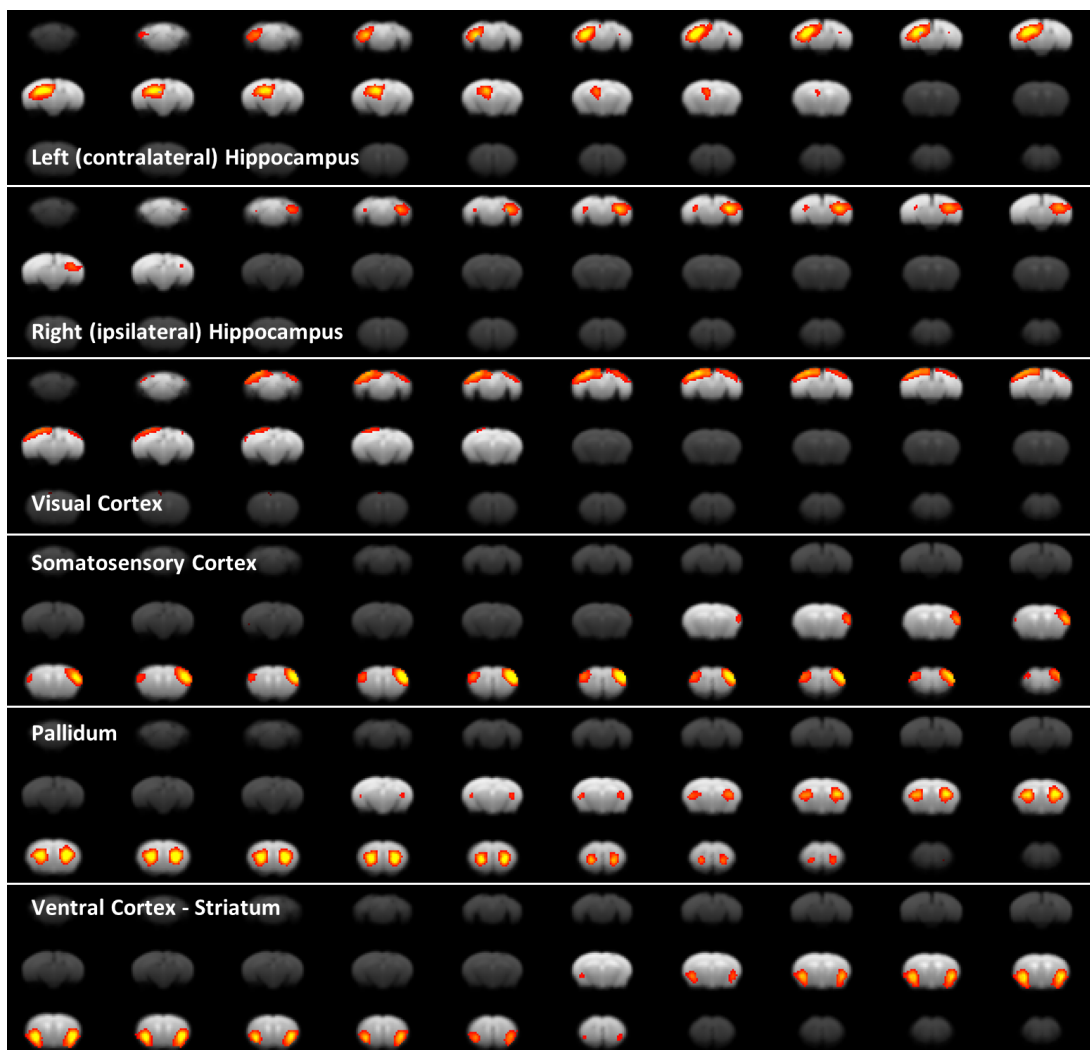


Figure 5.31: Group ICA of KA mice (two 10-minute long datasets per animal, FSL MELODIC with 30 components).



Figure 5.32: Group ICA of CO mice. Only selected components for the hippocampus, cortex and basal ganglia are shown (two 10-minute long datasets per animal, FSL MELODIC with 30 components).

5.5.3 Epileptic Networks and Seizure Propagation

This section provides an overall picture of the differences between healthy and epileptic mice. The rsfMRI connectivity between the ipsi- and contralateral HC was reduced, also further reductions of several interhemispheric connections were found. Conversely, the enhanced seizure spread and duration in KA mice have already implied strengthened connections. Some increases that count as statistically significant can be neglected at first because the increases in correlation coefficients are still very low; for example, in the ipsilateral hemisphere the correlation between the parietal and the cingulate cortex only increased from 0.03 to 0.17 and the correlation between the temporal and the parietal cortex increased from 0.18 to 0.36. The highlighted areas on the ipsilateral hemisphere (Figure 5.33, A and B) showed stronger connections in controls as well as stronger increases in KA mice, therefore these changes appear to be more relevant.

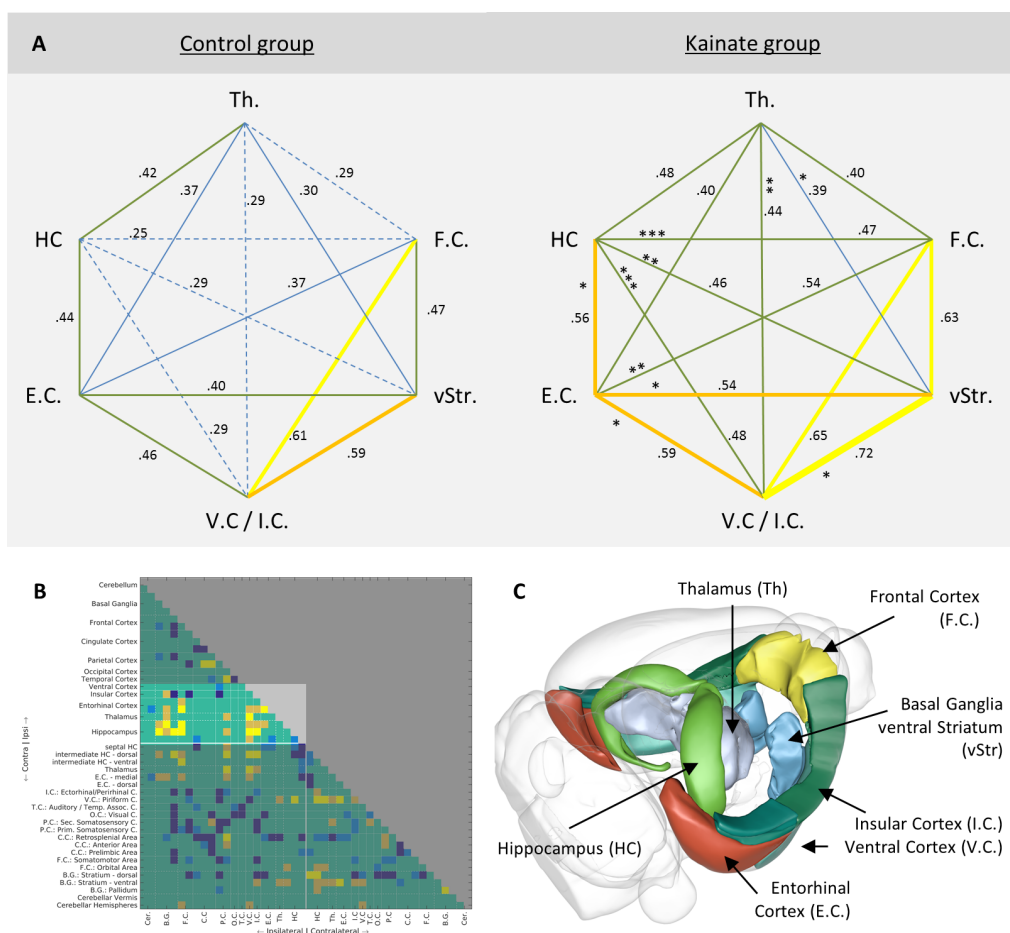


Figure 5.33: Resting-state fMRI connections in CO and KA mice. A) Areas with altered connections in KA mice and their correlation coefficients in CO (left) and KA (right) mice (** $p < 0.001$, ** $p < 0.01$, * $p < 0.05$). **B)** Group comparison of CO and KA mice (same as figure 5.29). Highlighted areas on the ipsilateral hemisphere with meaningful (because of their relatively high correlation coefficients) and significantly increased connections. **C)** Representation of these areas (generated using scalablebrainatlas.incf.org).

Areas on the ipsilateral hemisphere with significantly increased and meaningful connections (Figure 5.33, B; highlighted area) include the hippocampus (HC), the entorhinal cortex (E.C.), the thalamus (Th), the ventral/insular cortex (V.C./I.C.) and the orbital area of the frontal cortex (F.C.). These areas constitute possible networks connecting the HC to the frontal part of the brain (Figure 5.33, C). The connectivity between the HC and the F.C. was significantly increased. However, these two areas are relatively wide apart. Therefore, they are probably not directly connected (via axonal projections) and the increased connectivity may reflect an indirect effect. Most of the connections between the HC and the F.C. (e.g. HC to E.C. or E.C. to I.C., etc.) were increased or were already strong, as for example the correlation between V.C./I.C. and F.C. of around 0.6.

These areas were also significantly involved in the spread of activity during seizure onset (figures 5.34 and 5.35). In control animals, the activation was first detected at the stimulation site in the dorsal HC. The activity then propagated to the ventral part of the HC, and further to the entorhinal cortex, thalamus, ventral striatum, ventral and insular cortex and the frontal cortex. These are exactly the previously mentioned areas whose rsfMRI connectivity was increased in KA animals. Other recruited areas are the temporal (auditory) and occipital (visual) cortex. These areas did not show widespread connections to other brain areas (figure 5.30) and the only rsfMRI change involving these areas was the increased correlation between the temporal and the parietal (somatosensory) cortex (discussed in the first paragraph). The delay of activation may indicate how the different areas of the cingulate cortex were involved. The retrosplenial area, close to the HC, is activated relatively quickly; however, the prelimbic area at the frontal cortex is activated before the anterior area which lies between the retrosplenial and the prelimbic area. There are also no relevant increased rsfMRI connections of the cingulate areas. The areas described in figure 5.33 are therefore more relevant for the seizure spread.

The seizure spread in control animals was remarkably symmetric. In KA animals, the connectivity between ipsi- and contralateral HC was reduced and also the activation during the seizure spread was delayed in the contralateral areas. The regions that were involved during the seizure onset in CO mice were also activated in KA animals first. These regions were better connected in KA mice which might support the fact that the activity did not decline (or remained constant) like in CO mice but rather increased. Additional areas, like the somatosensory and the somatomotor cortex or the cerebellum, may thus be recruited more efficiently.

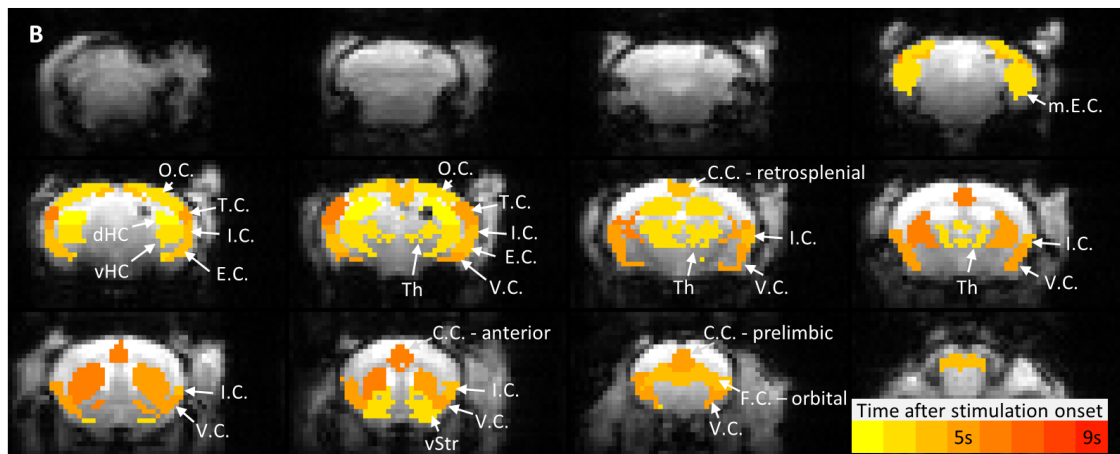
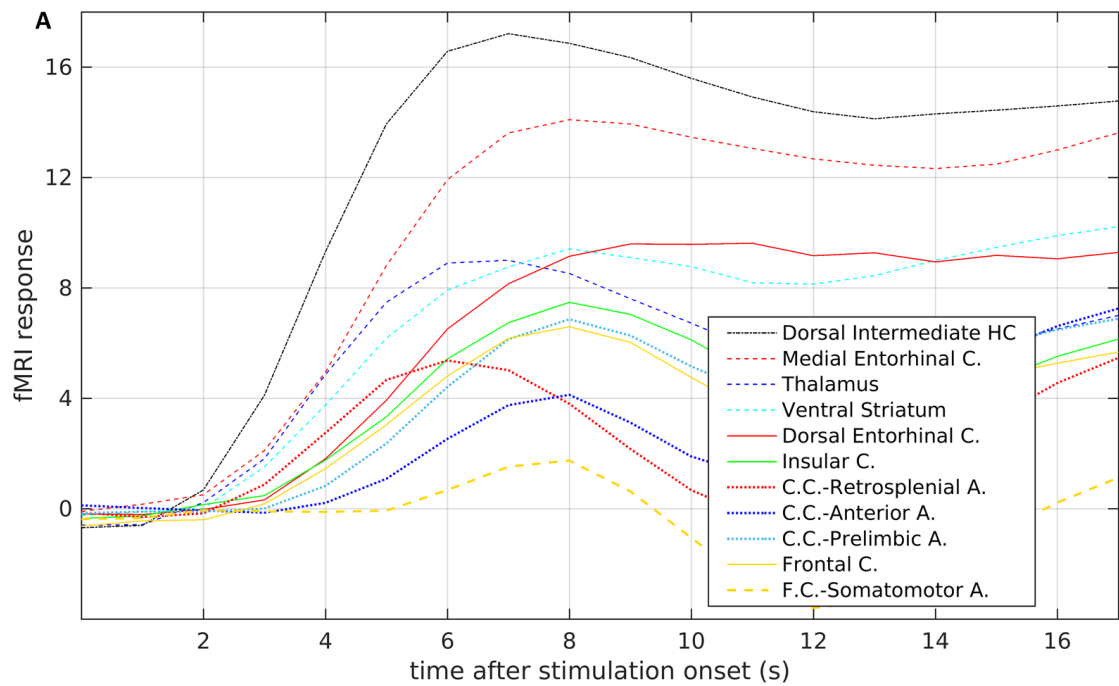


Figure: 5.34: Seizure propagation in CO mice. A) Mean response in selected ipsilateral regions. FMRI response in standard deviations (σ) of the baseline. **B)** Illustration of the activation timings. The time from the stimulation onset until the activation (threshold at $+3\sigma$) was translated into a color code. Only areas with significant ($+3\sigma$) activation within the first 10 seconds were color coded.

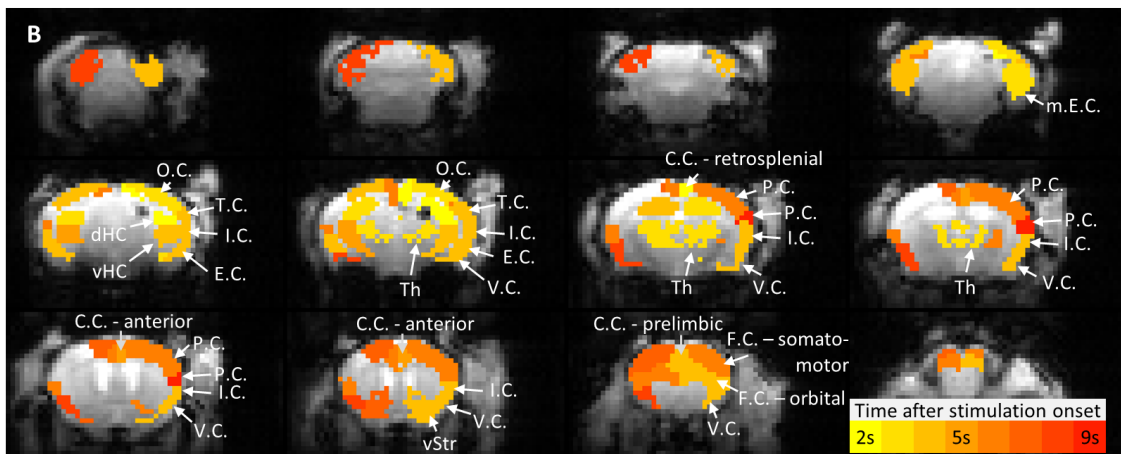
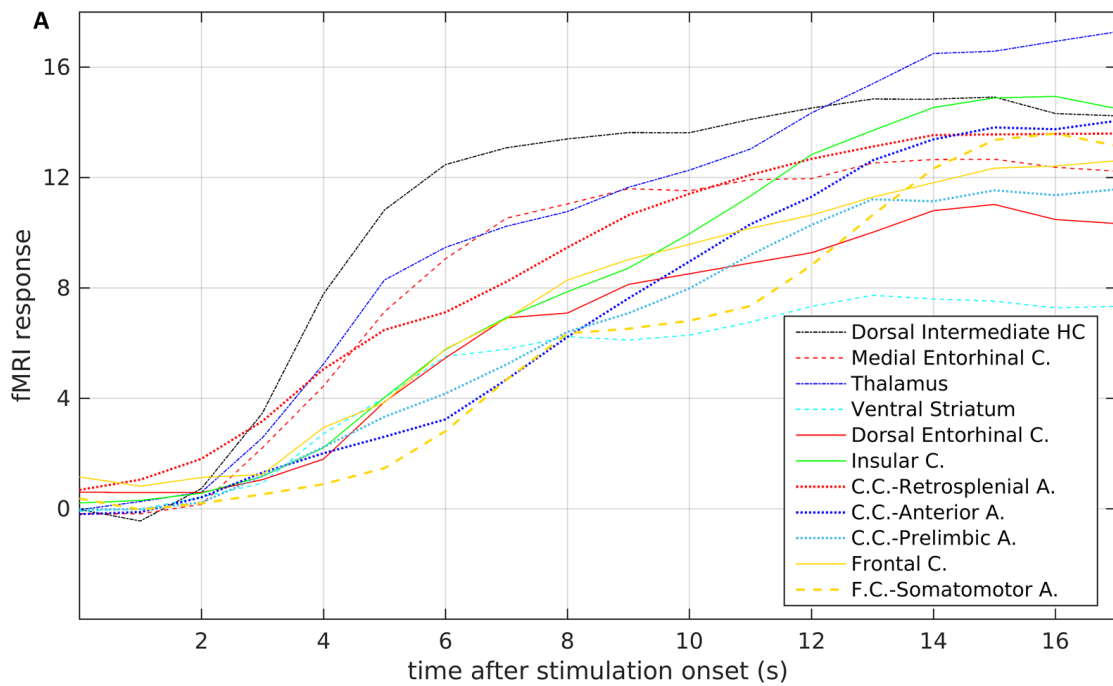


Figure 5.35: Seizure propagation in KA mice. A) Mean response in selected ipsilateral regions. FMRI response in standard deviations (σ) of the baseline. **B)** Illustration of the activation timings. The time from the stimulation onset until the activation (threshold at $+3\sigma$) was translated into a color code. Only areas with significant ($+3\sigma$) activation within the first 10 seconds were color coded.

5.6 Discussion

Resting-State fMRI

As described in section 5.3.2, the optimal choice of anesthesia for rsfMRI in rodents might be a combination of medetomidine and isoflurane. The application in epileptic animals however restricted the anesthesia to medetomidine alone. There is currently no evidence that any other anesthetic would be more suitable. Motion-related artefacts were minimized by a fixation that the animals still tolerated. Prospective motion correction and physiological noise detection by fast sequences, as used in human fMRI (Barth et al., 2016; Akin et al., 2017), is so far not possible in mouse fMRI. Other groups developed setups for mechanical ventilation under anesthesia (Grandjean et al., 2014; Paasonen et al., 2018). This would allow the retrospective removal of respiratory artefacts and the use of a muscle relaxant also minimizes motion artefacts.

Another approach to improve the fMRI performance is based on multi-echo fMRI. There was no statistically significant difference between the results obtained by the second echo image alone and the combined echoes. However, this was probably due to the relatively short echo times (≈ 14 and 23 ms), whereas T_2^* was around 25 - 35 ms in many brain regions. The acquisition of a third echo is therefore probably useful, even if the TR in that case would need to be increased from 1 s to 1.5 s to keep a similar gradient duty cycle. Furthermore, ME fMRI with three echoes would provide the possibility to separate BOLD and noise components based on their TE dependence (Kundu et al., 2017).

Optogenetic Block Design Stimulation

Using ofMRI during block design experiments, it was possible to detect the response first at the stimulus location and, at increased light amplitude, at remote but connected regions. Thus, ofMRI is a great method able to reveal causal relations between brain regions; this is a significant advantage compared to the detection of undirected connections based on correlations.

In the used setup with a focus on epileptic activity however, the probability of inducing an epileptic seizure compromised the use of this approach. Block design stimulation is only possible with light amplitudes below the threshold for seizure induction. This threshold was variable due to differences in light-leakage, fiber position, virus expression and the animals' susceptibility to seizures. For comparable datasets, a broad range of amplitudes had to be tested in each animal, which is very time consuming. Also, this technique is limited to a single stimulus location. The focus of this study was on the brain wide propagation of seizure activity. This could better be combined with resting-state fMRI.

Optogenetic Seizure Induction

When considering only experiments that strictly avoided isoflurane during fMRI, 7 control and 7 kainate mice were measured. Seizure induction was successful in 5 control mice but only in 2 kainate mice. In the two non-excitable control mice, an insufficient virus expression was identified by histochemical evaluation. However, at least 3 non-excitable kainate mice did reveal sufficient virus expression. The unreliable outcome may be explained by the anatomical structure of the medial perforant path (mpp), whose cells ought to be stimulated, and the alignment of the optical fiber (figure 5.36). The implanted fiber in the caudal-rostral orientation aims only at the cross-section of the mpp and the stimulation efficacy in this case crucially depends on the exact fiber position and penetration depth of the light. For ChR2 the light intensity required to induce spiking has been reported to be around $\geq 1 \text{ mW/mm}^2$ (Aravanis et al., 2007). In this study the light propagation through cortical tissue was analyzed. Light emitting from a $200 \mu\text{m}$ optical fiber with $\approx 380 \text{ mW/mm}^2$ was capable of evoking spiking up to a distance of 1.4mm from the fiber tip. This distance would be sufficient to target the cells at the dentate gyrus in our setup. However, it is not known how many cells have to be stimulated to evoke an epileptic seizure. Additionally, the hippocampal subfields in epileptic mice were significantly deformed. It is possible that the light in our setup was not capable of reaching enough cells and the stimulation therefore was not reliable, especially in kainate mice. This can be improved by a dorso-ventral direction of the fiber and light emittance, because the extent of the ChR2-expressing cells viewed from this direction is much larger.

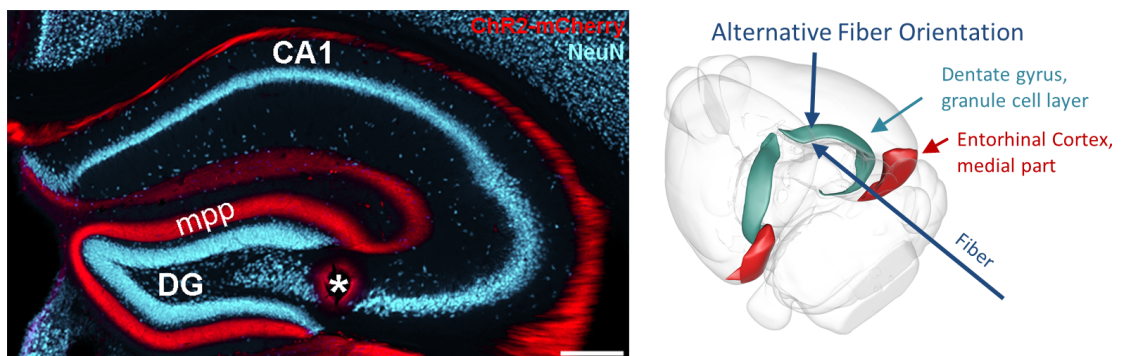


Figure: 5.36: Stimulation target and fiber orientation. Left) ChR2-expressing cells (red) of the medial perforant path. Asterisk: location of the fiber tip. Scale bar $400 \mu\text{m}$. Histology performed by E. Paschen. **Right)** The amount of excitable cells within the irradiated volume depends on the fiber orientation because of the “flat” geometry of the dentate gyrus.

MR-compatible intracranial EEG

In the very first of fMRI experiments, concurrent EEG recordings were also performed. This was helpful because the fMRI response during stimulation was unknown at that

time, whereas neuronal activation could easily be identified by EEG. The EEG results thus guided the fMRI optimization at the beginning. However, the electrodes for concurrent EEG-fMRI have to be MR-compatible, CryoProbe-compatible, biocompatible and must be connected to the EEG amplifier before the experiments

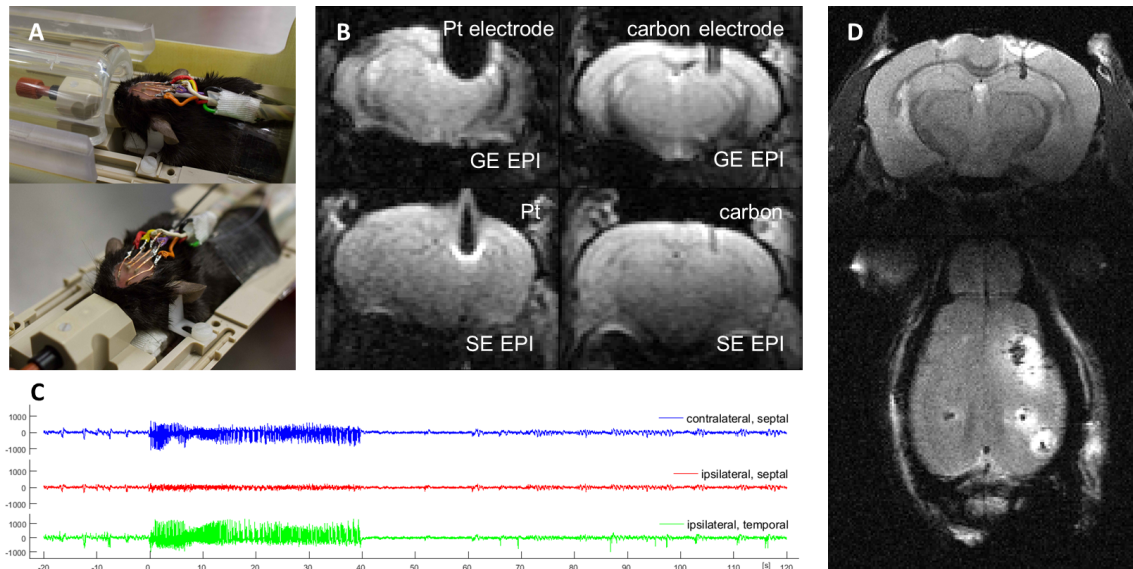


Figure 5.37: EEG-ofMRI. **A)** Images of a mouse with implanted electrodes and connected optical fiber. **B)** Gradient- (GE) and spin-echo (SE) EPI images of a mouse with implanted platinum electrodes and one with implanted carbon electrodes. **C)** Recorded EEG traces of an induced seizure during fMRI. **D)** Cortical lesions around the electrode locations.

Standard platinum electrodes caused large signal dropouts around the electrodes (figure 5.37, B). Therefore, carbon electrodes were built which were covered with nail polish and glued to copper wire outside the brain to facilitate the connection. The electrodes were then soldered to the amplifier cables before each experiment (figure 5.37, A). This setup provided the MR-compatibility, fitted inside the CryoProbe and allowed EEG recordings during fMRI (figure 5.37, C). However, in many animals lesions around the electrode locations in the cortex became visible (figure 5.37, D). It was unclear whether the electrodes or the soldering caused these lesions. Since this induced cortical damage was not foreseen, these experiments were stopped. Further electrode development had to be postponed until the anesthesia protocol, resting-state fMRI and the stimulation are optimized. For the prospective electrode design, the nonconductive polymer polyvinylidene difluoride (PVDF) was reported to be a suitable insulation for carbon electrodes that provides biocompatibility for chronic electrode implantations (Duffy et al., 2015; Dunn et al., 2009).

As a result of this work, several benefits of combined ofMRI and EEG recordings were identified for future studies: 1) During resting-state fMRI in epileptic mice, interictal epileptic events could be characterized. 2) The exact time delay of the activation during seizure propagation could be quantified. 3) The seizure spread could be correlated to the

EEG patterns. In general, epileptiform activity in humans is characterized by EEG. These recordings therefore help to translate the results between basic research and clinical treatment. 4) Optogenetic inhibition will be used to interfere with the seizure spread. The absence of a BOLD signal however would be no perfect proof that neuronal activity has been successfully inhibited.

5.7 Conclusions and Outlook

This work showed the feasibility of combining ofMRI with the CryoProbe. Because of the higher sensitivity of this coil this may be the optimal approach; in future ofMRI studies, the setup (fiber and electrodes) should be made CryoProbe-compatible.

fMRI was capable of monitoring the propagation of activity during epileptic seizures as well as revealing plausible connectivity differences between control and epileptic mice. Resting-state fMRI could also show these connectivity patterns in each fMRI scan. There are basically two approaches how the fMRI performance can be improved further: First, the full potential of multi-echo fMRI should be used to enhance the SNR and sensitivity. ME fMRI is especially suited in combination with invasive probes because a short first echo time minimizes signal losses around the probes. The second approach is to reduce residual artefacts due to motion and respiration; this can be achieved in rodents by mechanical ventilation in combination with applied anesthesia and muscle relaxant.

Established resting-state fMRI also allows investigating alternative stimulation protocols. For example, 30 minute continuous stimulation at 1 Hz may not lead to a direct response as for example the applied block design or seizure induction, instead brain connectivities may change (Chan et al., 2017). Fast fMRI and the dynamic sliding window analysis may even be able to track these changes during the stimulation.

Resting-state fMRI revealed several brain regions strongly connected in epileptic mice. However, using rsfMRI alone it is not possible to conclude whether these areas were connected in a directed way or whether they formed a network with connections equally strong in all directions. Block-design fMRI during optogenetic stimulation at different regions could elucidate this. Dynamic causal modelling in combination with ofMRI has also been reported to be able to describe causal influences (Bernal-Casas et al., 2017).

The induced epileptic seizures were triggered at the stimulus location and then spread across the brain. Using the same methods developed in this work, optogenetic inhibition of cells can be used to study which brain areas are crucial for the spread of activity. Optogenetics cannot be translated to human treatment; however, the identified regions may then be targeted by electrical stimulation.

6 CEST fMRI

The MRI experiments were performed in the same animals as described in the previous chapters. Most of the results from conventional CEST were presented at the ISMRM 2017 (Schwaderlapp et al., 2017).

6.1 Introduction

BOLD fMRI is the most widely used method to study task-induced brain activity. However, BOLD fMRI does not detect neuronal metabolism directly. In fact, neuronal activity triggers a series of events that lead to a hemodynamic response to meet the local energy demand. Local changes of the concentrations of oxygenated and deoxygenated blood eventually manifest changes of the relaxation times T_2^* and T_2 . As one important consequence, BOLD fMRI is not directly sensitive to neuronal metabolism. For example, the BOLD response associated with the pre-synaptic release of neurotransmitters may not be able to distinguish between subsequent post-synaptic excitatory or inhibitory potentials. Also, BOLD cannot distinguish neuronal activity from astrocyte activity and its associated metabolism of neurotransmitters.

Relating to the study of experimental epilepsy, the BOLD response of seizures in the ipsilateral septal hippocampus showed differences between epileptic and control mice; the positive response was stronger and longer in epileptic mice and was not followed by a prolonged depression. However, the spectroscopy results showed a significant reduction of glutamate - the main excitatory neurotransmitter - in epileptic mice, whereas GABA - the main inhibitory neurotransmitter - was not reduced or even increased at the chronic stage. This seems to be counterintuitive as epilepsy is usually associated with a higher excitability. Different scenarios may be considered to elucidate this: At first, a changed distribution of glutamate within the hippocampus, although overall reduced, may alter the interplay between hippocampal subfields. CEST MRI has already been suggested in chapter 4 to investigate this. Second, the kinetics of glutamate upon activity - its release, uptake and conversion to glutamine - may be different in epilepsy. A slower uptake of glutamate by astrocytes for example would mean that glutamate remains longer in the extracellular space where it potentially could activate more cells. Indeed, one study used micro dialysis to measure the extracellular glutamate concentration and found elevated levels in patients before seizures (During and Spencer, 1993). These aspects cannot be studied by BOLD fMRI because of the lack of sensitivity to neurotransmitters. CEST MRI can be made sensitive to glutamate, but so far, has only been employed to detect static changes of Glu concentration levels under various pathologies (Crescenzi et al., 2014; Pépin et al., 2016).

The main aim of this chapter is to investigate neuronal activity-induced, temporary changes of the GluCEST effect. Establishment of such an fMRI method would allow studying glutamate metabolism upon activity and would thus optimally complement the results obtained from spectroscopy and BOLD fMRI.

6.2 Glutamate CEST fMRI - Hypothesis

If glutamatergic cells die, for example due to a disease or intervention, the remnants of these cells are removed from the brain tissue and changes of the GluCEST effect occur trivially due to the reduction in the total amount of glutamate. During an fMRI experiment however, such drastic changes are not expected. Activity related changes of the GluCEST effect may come from two causes; First, the concentration of glutamate may change because of the conversion from glutamate to glutamine or the synthesis of new glutamate. Secondly, because the CEST effect depends on the exchange properties between glutamate and water, different environments during the metabolic cycling may lead to changes in the CEST effects.

A brief overview of the glutamate metabolism is given: Glutamate molecules are stored in vesicles at the synaptic boutons. An incoming action potential triggers the fusion of the vesicles with the presynaptic membrane and the release of the glutamate molecules into the synaptic cleft. This cleft is in continuity with the general extracellular space. Glutamate acts as excitatory neurotransmitter; therefore, it is important that it is rapidly removed from the extracellular space. Glutamate is taken up by astrocytes where it is converted into glutamine. Glutamine is then released by astrocytes, taken up by neurons and converted into glutamate which is then packed into the synaptic vesicles. The environment of the glutamate molecules thus changes during the metabolic cycle, between being packed in small, crowded vesicles and being quasi free. This motivates the hypothesis that the exchange properties of GluCEST may change during activity.

Let's consider a simplified estimate: Synaptic vesicles have a size of approximately 20-45 nm and contain 400-4300 glutamate molecules (Danbolt, 2001). A vesicle is now represented by a sphere with a diameter of 45 nm and contains 4300 glutamate molecules. Assuming that the vesicle membrane is impermeable to water and the water content inside is the same as in gray matter, which is around 44 mol/L (LCModel Manual, 2019), this would yield around 1.26 million water molecules inside the vesicle. On the other hand, a CEST enhancement factor of around 700 compared to spectroscopy was reported (Cai et al., 2012). If we take this as the number of water molecules that each single glutamate molecule can saturate, multiplying 4300 glutamate molecules with 700 yields around 3 million. The maximal CEST effect in that scenario would be limited by the number of available water molecules inside the vesicle and would in-

crease if all glutamate molecules are released from the vesicle. This shows that inside the vesicles, the basic assumption that the water pool is “infinitely” greater than the metabolic pool is not necessarily true. In reality, this effect depends on the exact content inside the vesicles, the mobility within them and the permeability of the vesicle membrane, which are not precisely known.

There are around 200 vesicles in a synaptic terminal. Various works showed that one can define vesicle pools with different release probabilities (Alabi and Tsien, 2012; Denker and Rizzoli, 2010; Rizzoli and Betz, 2005; Südhof, 2004). Only 4-8 ($\approx 5\%$) of these vesicles are immediately releasable and another 20 vesicles ($\approx 10\%$) serve to replenish this pool if it is exhausted. These two pools can be described as “readily releasable pool” and “reserve pool”, respectively. Under normal physiological activity however, the remaining majority of vesicles ($\approx 85\%$) does not directly participate in signal transmission; these vesicles can be defined as a “resting pool”.

This has consequences for CEST fMRI experiments; All glutamate molecules probably contribute to the total CEST effect, but under “normal” conditions only a few of them are involved during metabolic activity. Therefore, even if the exchange properties between these glutamate molecules and water change, their contribution to the total CEST effect will be small. The same applies for the synthesis of new glutamate molecules, for example in the TCA cycle.

However, the various vesicle pools were defined according to their release under specific stimulation protocols; they are not actually structurally different. The release depends on the exact stimulation: the pattern, duration and frequency. It was shown that under continuous, low-frequency stimulation (0.2 Hz over 10 min) the majority of vesicles can be released (Ikeda and Bekkers, 2009).

In summary, it is hypothesized that upon neuronal activity, changes of the GluCEST effect may occur and that these changes would mainly be caused by different exchange properties between water and glutamate during the metabolic cycling. However, common stimulation protocols like the visual block design for BOLD experiments, are not expected to yield significant GluCEST effects. In order to show the general possibility of GluCEST fMRI, the experimental designs in this chapter are aiming at releasing as much glutamate as possible. Epileptic activity is by definition not physiological and is associated with the excessive release of glutamate, which makes the ofMRI experiments described in chapter 5 the ideal platform to test GluCEST fMRI responses. As an alternative, continuous stimulation is tested.

6.3 Methods

The general setup of preclinical mouse MRI is described in chapter 4. CEST fMRI experiments were conducted in the same animals as BOLD fMRI; details of the animals, anesthesia, fiber implantation, optogenetic stimulation and fMRI are described in chapter 5. Only points relevant for CEST are described here.

Saturation	Pulse	Duration	Frequency [ppm]	B ₁
	continuous wave	2s	-10.5 to +10.5	1-8 μ T
Encoding	Sequence	RARE factor	Enc. Order	TE
	RARE	32	centric	4.6ms
	TR	NA		
4s	1			
Geometry	Resolution [mm x mm]	#Slices (Thickness)	Matrix (Read x Phase)	FOV [mm x mm]
	0.4 x 0.4	1 (1mm)	40 x 32	16 x 12.8
other	Fat sup.	FOV sat.		
	off	off		

Table 6.1: CEST MRI protocol.

Spatial B₀ variations were corrected by using the “water saturation shift referencing” (WASSR) approach (Kim et al., 2009). A z-spectrum acquired with a short (50 ms) and low power (0.25 μ T) saturation pulse shows only the direct water saturation and thereby allows an easy identification of the exact B₀ frequency. If complete z-spectra were acquired, B₀ was retrospectively corrected on a voxel-by-voxel basis. For CEST fMRI with only 2-4 saturation offsets, WASSR was run beforehand and saturation frequencies were corrected according to a region of interest (left septal hippocampus).

For CEST fMRI, images with different saturation offsets were assigned to individual time courses (Figure 6.1). Linear drifts in the time courses before the stimulation were removed and images were spatially smoothed using FSL (0.6 mm Gauss Kernel).

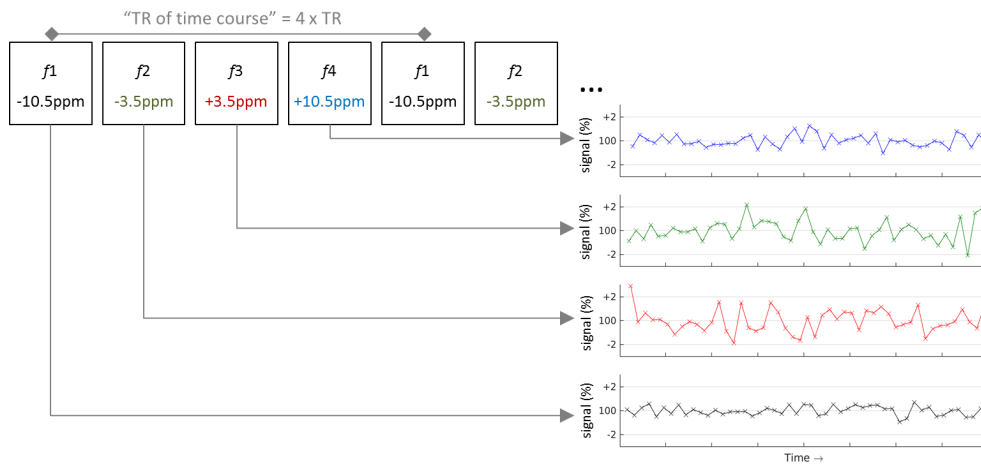


Figure 6.1: CEST fMRI. Either four (-10.5ppm to +10.5ppm) or two (\pm 3.5ppm) different saturation offsets were used.

6.4 Results I – Establishment of GluCEST MRI

As a prerequisite for CEST fMRI studies, the basic GluCEST method had to be established since it had not been used in our group before. This section shows a proof-of-principle application of the method, the optimization of the sensitivity in a phantom and the possibility to detect glutamate changes in-vivo.

6.4.1 Proof-of-Principle

A phantom was built that consisted of two chambers (Figure 6.2). Both were filled with a buffer solution, but glutamate was added only to the left chamber. Z-spectra were acquired with different saturation pulse strengths (Figure 6.2, B and C). Only the glutamate containing chamber shows asymmetries (2-20%) demonstrating the GluCEST effect.

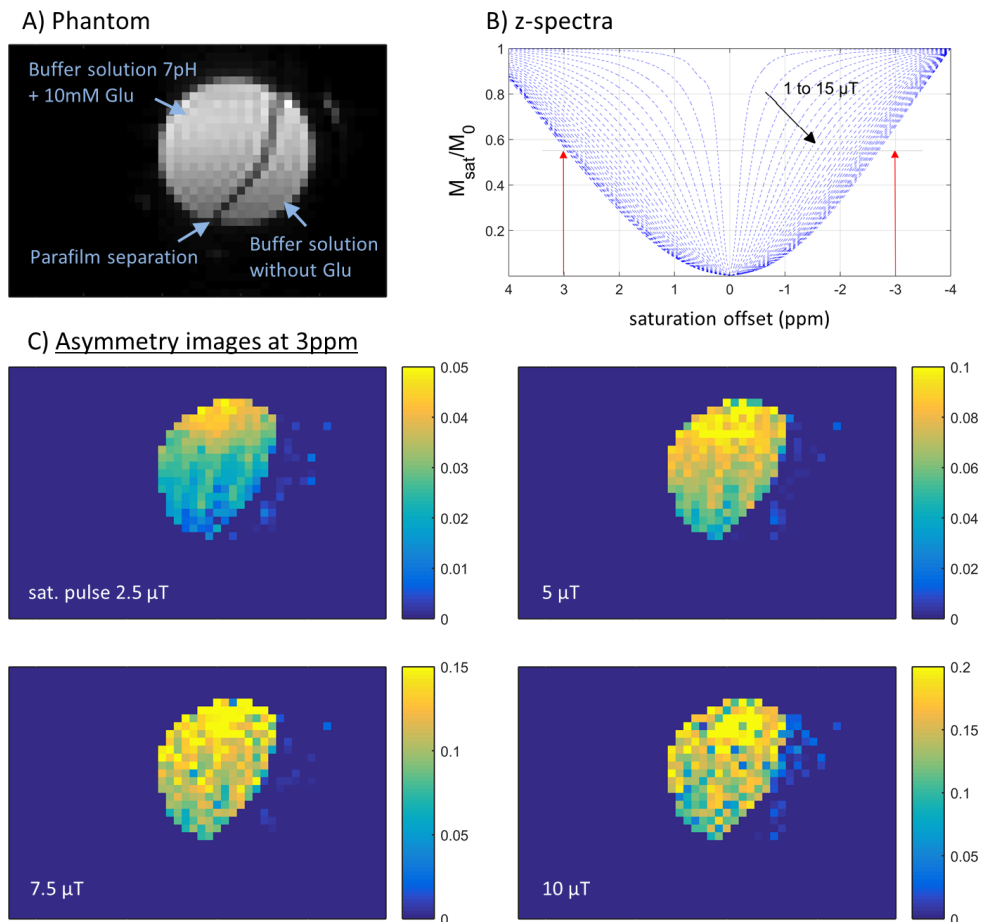


Figure 6.2: Proof-of-principle of glutamate CEST MRI. **A)** Cross-section of a syringe divided into two chambers (syringe diameter 5 mm). Glutamate is added to the buffer solution in the upper left chamber. No glutamate is added in the other chamber. **B)** Z-spectra of the glutamate containing solution acquired with different saturation pulse strengths (1-15 μT). **C)** Asymmetry of the intensity between the images acquired with a saturation frequency of plus and minus 3ppm (scale bar in %/100).

6.4.2 Optimization of sensitivity

The saturation was applied in the form of a continuous pulse giving two adjustable parameters; the pulse duration and amplitude. Z-spectra of phantoms were acquired with different saturation durations (Figure 6.3; left column 2s, middle 1s, right 0.5s) and amplitudes (black lines 1, 2, 3, 4 μT – blue 8, 12, 16 μT – orange 20 and 24 μT). This was tested for glutamate (first row), glutamine (second row) and glucose (third row).

CEST MRI aiming for glutamate utilizes the proton exchange of the $-\text{NH}_2$ group detectable at around 3 to 3.5 ppm. There, glutamate shows a CEST effect almost linearly dependent on the saturation strength, whereas glutamine and glucose do not show significant effects. The CEST effect at around 1ppm originates from the $-\text{OH}$ group present in all of these compounds.

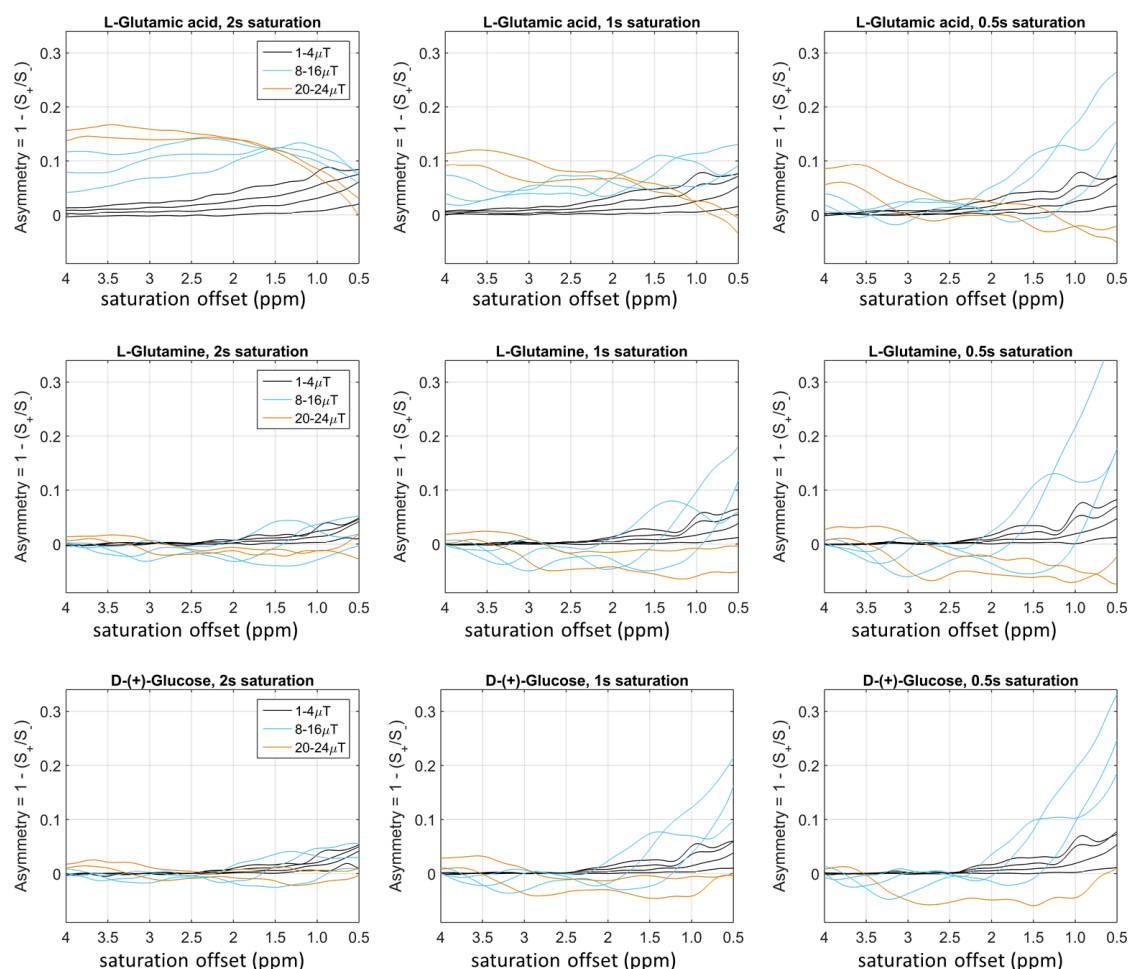


Figure 6.3: Impact of the saturation pulse on the CEST effect. Data acquired from a phantom filled with a buffer solution (7pH) and added glutamate (10mM, top row), glutamine (10mM, middle row) or glucose (5mM, bottom row).

6.4.3 In-vivo validation: Reduction of Glu after KA-induced status epilepticus

To establish GluCEST MRI in-vivo, its ability to detect well-known changes has to be demonstrated. In chapter 4 it was shown that the injection of kainate leads to significant cell death in the ipsilateral hippocampus. As this involved a loss of glutamatergic cells, a significant reduction of the glutamate concentration was detected by ^1H spectroscopy at one day after KA injection and at later time points. Since this is already an established result, the ability of GluCEST MRI to detect these changes is tested.

Figure 6.4 illustrates the procedure of in-vivo CEST MRI. A pre-processed RARE image is shown in A. B shows the direct water saturation of point1 in the right septal hippocampus. The shift of the minimum from 0 is used to correct the B_0 offset on a voxel-by-voxel basis, even though the localized shim and frequency adjustment have already led to a quite homogeneous B_0 field (C). The CEST spectra were acquired with a 0.2 ppm step size (D). These spectra were interpolated and corrected for B_0 shifts (E). The asymmetry at 3 ppm was taken as GluCEST effect (F).

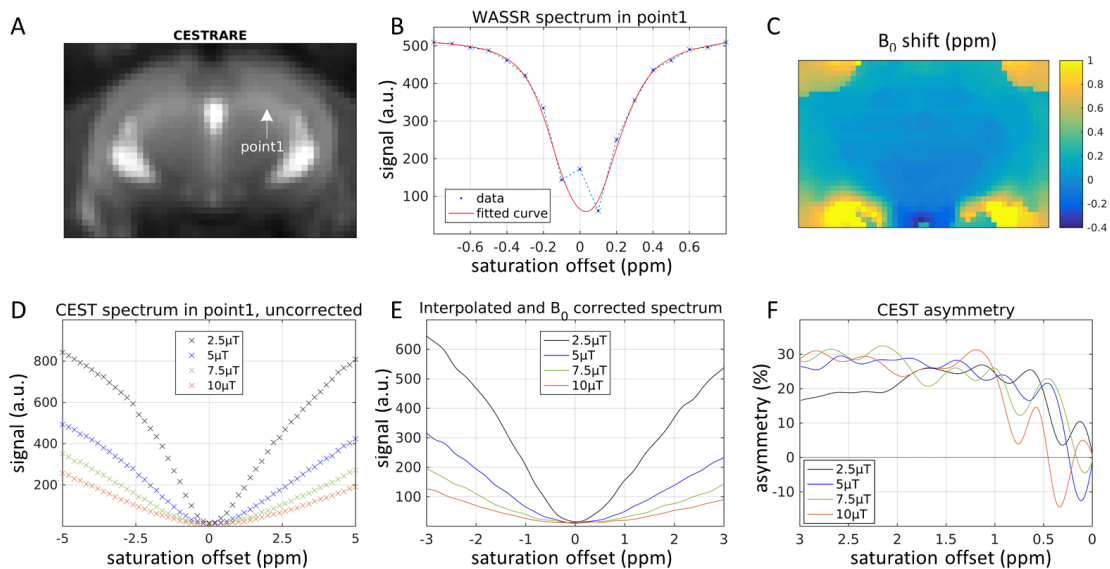


Figure 6.4: In-vivo CEST MRI. A) spatially smoothed CEST RARE image. B) WASSR spectrum showing the direct water saturation only. C) Map showing the deviation from the ideal B_0 frequency. D) CEST spectra acquired with saturation strengths between 2.5 μT and 10 μT . E) interpolated and shifted CEST spectra. F) Asymmetry of the spectra shown in E.

Two mice were scanned at three time points: before any treatment and 1 and 8 days after kainate injection. Figure 6.5 shows the GluCEST images of one mouse at the three time points. The mean CEST effect was quantified in the right hippocampus (white border) as well as in the subfields CA1 and DG. At 1 and 8 days after KA injection, the mean CEST effect in the hippocampus was reduced. Since this is in good agreement with the spectroscopy results (chapter 4) it can be concluded that the applied CEST method is sensitive to glutamate and that the reduction of the CEST effect is due to the glutamatergic cell loss after KA injection. The subdivision into DG and CA1 suggests that the DG is much more strongly affected than CA1. However, this should be interpreted with caution since it is established that cell loss after KA injection occurs in many hippocampal subfields including CA1 and DG.

The data of the second mouse were similar but not shown here because the three acquired slices were unintentionally positioned differently and thus do not allow an ideal comparison.

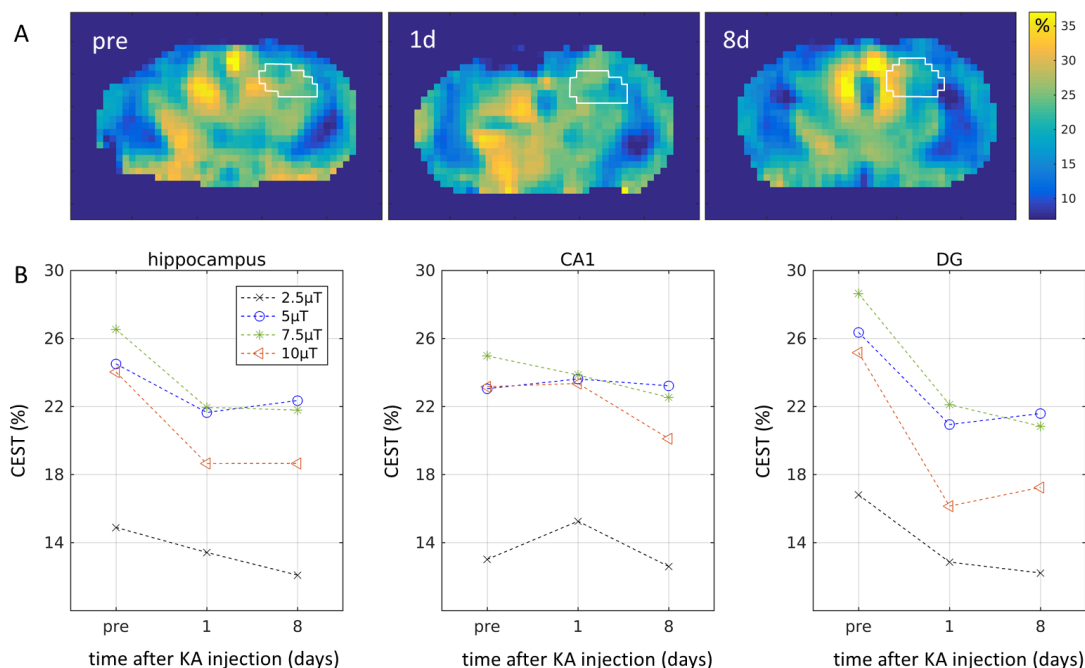


Figure 6.5: GluCEST MRI detects the reduction of Glu after KA-induced status epilepticus. A) Maps showing the CEST asymmetry at 3 ppm before any treatment and 1 and 8 days after KA injection. The region of the right HC was selected according to a reference image at higher resolution. **B)** Quantified CEST effect in the right septal hippocampus (white borders) and in the subfields CA1 and DG.

6.5 Results II – GluCEST fMRI

The main objective is to test whether it is in general possible to detect activity-related changes of the GluCEST effect. This is indicated in this chapter by the investigation of epileptic seizures and prolonged stimulation.

6.5.1 GluCEST response during induced epileptic seizures in naïve mice

Mice were scanned like described in chapter 5. After 20 min of rest, epileptic seizures were induced by 20s optogenetic stimulation in the right septal hippocampus. Like before, epileptic seizures in naïve mice were mainly confined to the right and left hippocampus. CEST fMRI time courses during an epileptic seizure are plotted in Figure 6.6, A1. The time course of the saturation offsets -10.5 ppm, -3.5 ppm and +10.5 ppm were alike and also very similar to the BOLD time courses of the GE EPI scans (chapter 5). However, the time course at +3.5 ppm, where a potential GluCEST effect is expected, shows a clear deviation. Note that an increase of the CEST effect would also lead to reduced signal intensities.

In the same MRI session, this mouse was stimulated a second time around 30 min after the first stimulation (Figure 6.6, A2). This second run is not entirely comparable; this time 0.5% isoflurane was applied in order to prevent motion that sometimes occurred after the first seizure and the physiological condition was not at the “true” baseline because of the long-lasting effect of the first seizure. However, the time course at +3.5 ppm again shows a clearly different response. The same experiments were performed in a second animal, sampled with only two saturation offsets to increase the temporal resolution (Figure 6.7, A1 and A2).

These experiments were repeated on the following day with the only difference that a saturation pulse duration of 100ms was chosen. Compared to the 2s saturation, 100ms saturation leads to negligible CEST effects. In these experiments all time courses are similar (Figures 6.6 and 6.7, B1 and B2).

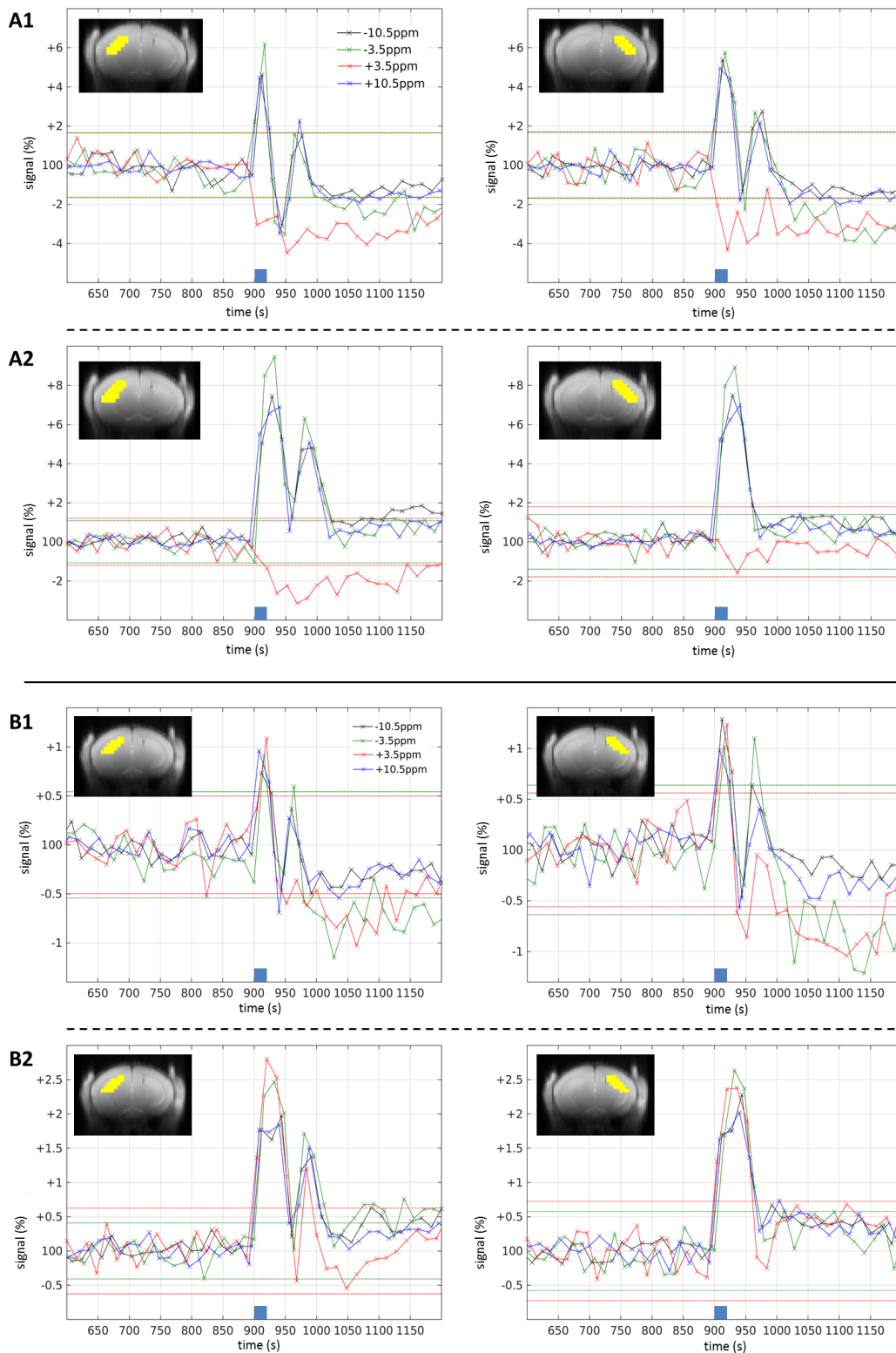


Figure 6.6: CEST fMRI during epileptic seizures sampled with four saturation frequencies. A) Time courses in the left and right hippocampus (yellow ROIs) of two consecutive stimulations (A1 and A2) acquired with a saturation duration of 2 s. **B)** Repetition of the same experiment on the following day, acquired with a saturation duration of 100 ms. (The horizontal red and green lines indicate the range of ± 3 times the standard deviation of the baseline. The blue bars indicate the stimulation periods.)

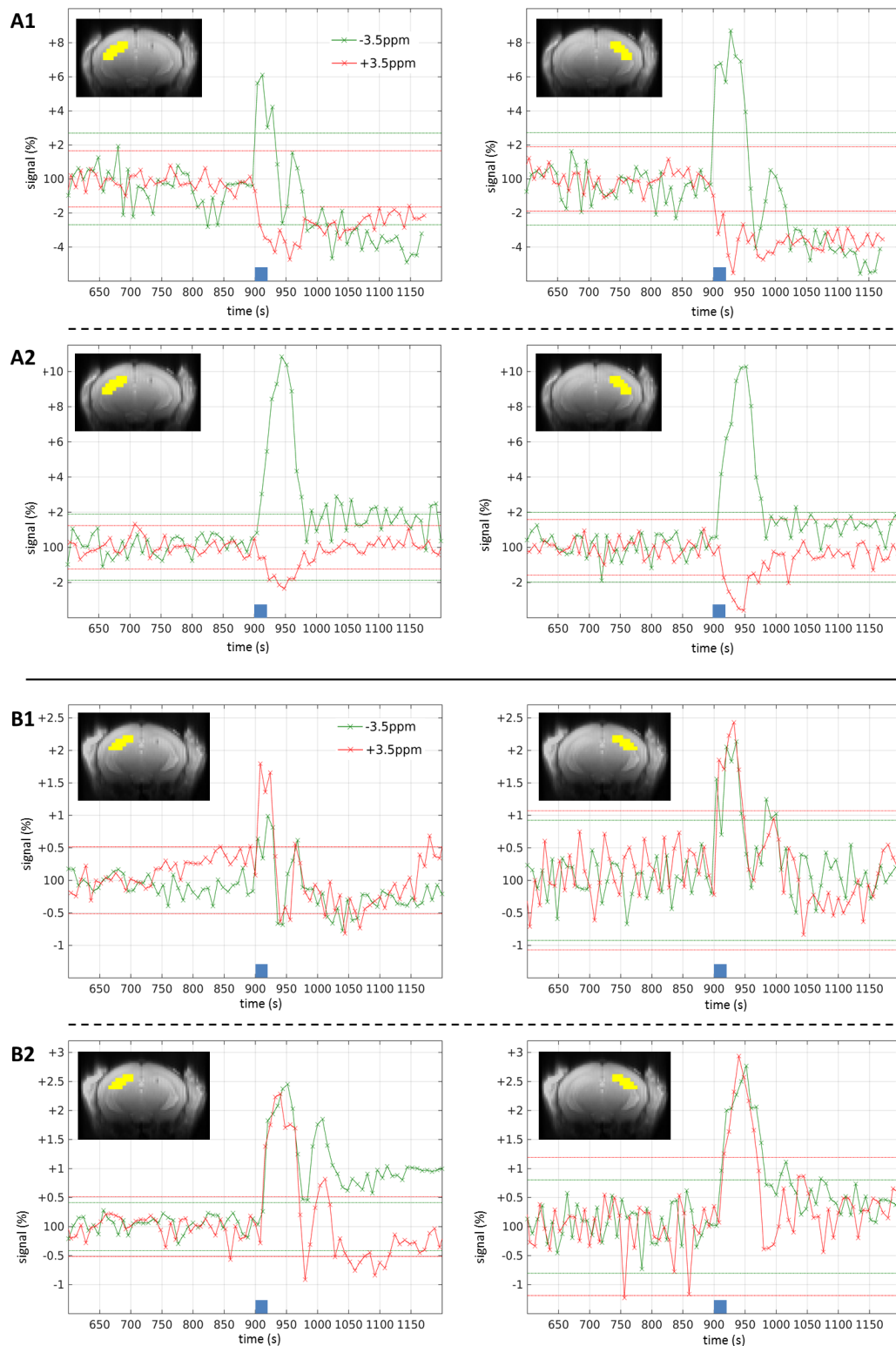


Figure 6.7: CEST fMRI during epileptic seizures sampled with two saturation frequencies. A) Time courses in the left and right hippocampus (yellow ROIs) of two consecutive stimulations (A1 and A2) acquired with a saturation duration of 2s. **B)** Repetition of the same experiment on the following day, acquired with a saturation duration of 100ms. (The horizontal red and green lines indicate the range of ± 3 times the standard deviation of the baseline. The blue bars indicate the stimulation periods.)

6.5.2 GluCEST response during continuous stimulation in naïve mice

The original focus of the study was on epileptic activity. The stimulation therefore targets cells in the dentate gyrus. High-frequency (10Hz) stimulation there always provoked epileptic seizures, which is a very specific kind of activity. To test a more general scenario and avoid the induction of epileptic activity, different low frequency stimulation protocols were chosen. Different frequencies, 0.2Hz and 1Hz at different duty cycles, as well as continuous illumination were tested. Stimulation at 0.2Hz (pulse durations of 0.5 s and 1 s) did not yield any response, neither BOLD nor CEST. However, stimulation at 1Hz induced detectable activity: Pulse durations of 0.2 s, 0.5 s and 0.9 s led to BOLD responses (Figure 6.8) and especially pulse durations of 0.2 s and 0.5 s showed again the decreased signal in the +3.5 ppm time course. Also, non-pulsed continuous light stimulation showed a frequency specific response at +3.5 ppm.

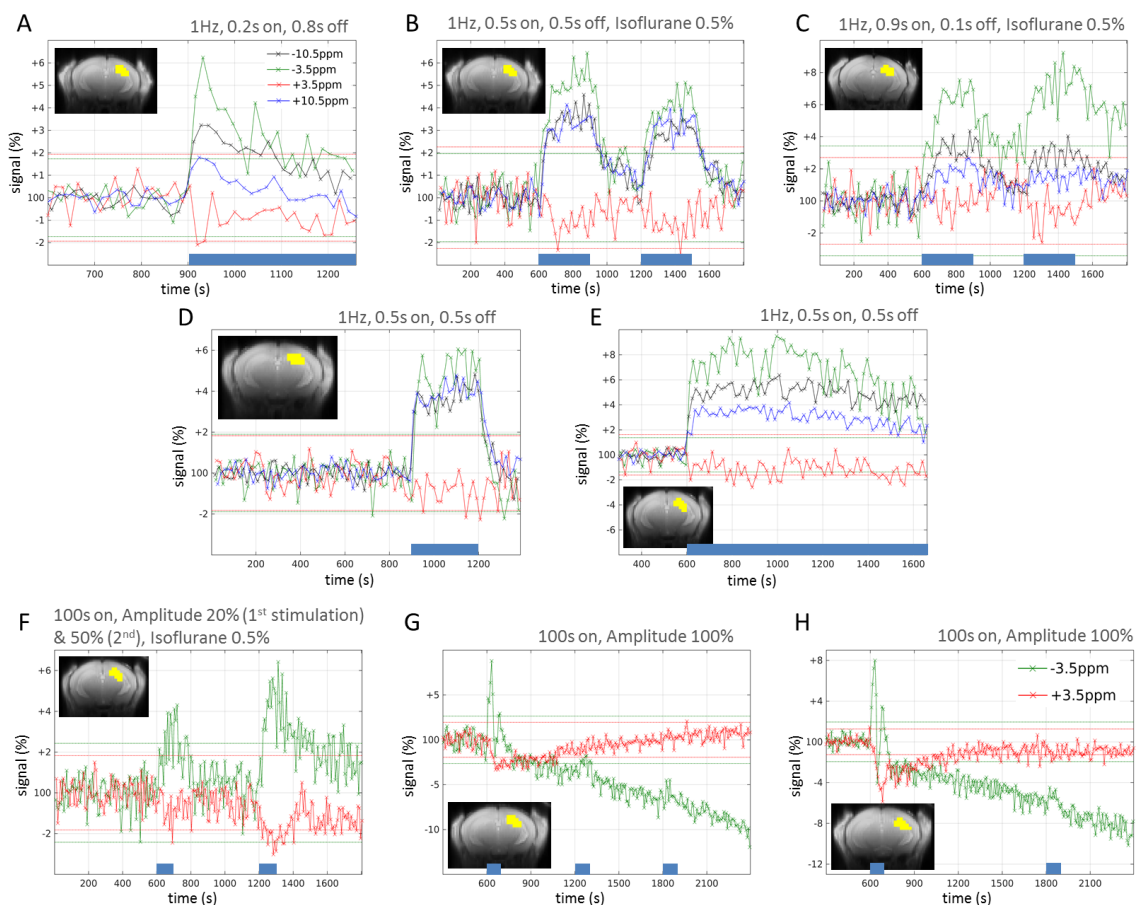


Figure 6.8: CEST fMRI during low-frequency optogenetic stimulation. A-E) Different 1 Hz stimulation experiments. **F-H)** 100s continuous light stimulation. (The horizontal red and green lines indicate the range of ± 3 times the standard deviation of the baseline. The blue bars indicate the stimulation periods.)

6.5.3 GluCEST response in epileptic mice

CEST fMRI during epileptic seizures was also tested in two kainate injected mice. Unfortunately, these datasets had to be discarded because of either a failed stimulation or too severe motion during the seizures.

6.6 Discussion

Saturation parameters were chosen that led to the maximal glutamate CEST effect while glutamine and glucose did not show significant CEST effects. During the detection of epileptic activity, the time courses at -10.5 ppm, -3.5 ppm and +10.5 ppm appeared identical and reflected the BOLD response. The time courses at +3.5 ppm however clearly deviates from these and showed only decreased signal intensities. This is the frequency at which a possible GluCEST effect is expected and decreased signals are in agreement with the assumption that the CEST effect increases upon activity and thus reduces the water signal. Given that the experiments show a frequency specific response and are reproducible in different mice, the initial hypothesis about GluCEST fMRI can be kept.

One possible confounding factor is a frequency shift potentially caused by the hemodynamic response. Let's assume that no CEST effect but only the direct water saturation would have been present and only a frequency shift caused the signal decrease at +3.5 ppm. Then the signal at +10.5 ppm should have been affected in the same manner and should be different from the opposite frequency offsets at -3.5 ppm and -10.5 ppm. This was not the case; all saturation frequencies apart from +3.5 ppm yielded similar, BOLD-like responses. Another point may be a thermal effect. Theoretically, light supply via the optical fiber could be used to heat the tissue which may lead to pH-changes and ostensible CEST effects. However, the short stimulation did not lead to any thermal effects (discussed in chapter 5) and CEST fMRI effects were also visible at regions remote from the fiber end, like in the contralateral hippocampus. Thermal effects are consequently not relevant here.

Maybe the most important confounding factor is the interplay between BOLD and the impact of the saturation pulse on the tissue. Several interactions were reported; for example, magnetization transfer (MT) reduces the signal in tissue more than in blood (Zhou et al., 2005) and MT decreases with increased blood oxygenation (Cai et al., 2013). The relative contributions of individual tissue components to the overall BOLD signal can thereby be amplified or reduced. The time course of the concentration of deoxygenated hemoglobin (dHb), as for example measured in (Lachert et al., 2017), is roughly the opposite of oxygenated hemoglobin. After a stimulation, the concentration of dHb decreases at the beginning and then returns to baseline, which is indeed similar

to the time courses measured in the CEST fMRI experiments at +3.5 ppm. As a control experiment to test whether the measured CEST effect was only due to the tissue saturation, experiments with shorter (0.1 s) saturation pulses at the same strength (7.5 μ T) were conducted. This shorter time leads to tissue saturation but without GluCEST because of the significantly shorter time for proton exchange. In these experiments, the time course at +3.5 ppm followed the other ones and did not show any GluCEST effect. However, this is still no definite proof for the glutamate-origin of the CEST fMRI response, because the tissue saturation was of course different to the actual CEST experiments.

One recent publication suggests the ability of CEST fMRI to detect glucose metabolism during activity and found a negative contrast during stimulation (Roussel et al., 2019). However, these results were also obtained in naïve animals only and were not confirmed by any complementary technique or animal model. The above-mentioned concerns about the interaction of MT and BOLD remain.

6.7 Conclusions and Outlook

Conventional CEST MRI was made sensitive to glutamate and was investigated in phantoms and validated in KA-injected mice in-vivo. In general, GluCEST MRI benefits from higher field strengths and therefore is being increasingly used in preclinical studies (Crescenzi et al., 2014; Pépin et al., 2016).

Using the GluCEST contrast in fMRI experiments suggests the possibility to detect glutamate metabolism during activity. However, because of the complex interaction between MT and BOLD there is no unequivocal proof that glutamate is responsible for the measured changes. Complementary approaches to clarify this can be pursued; At first, the experiments in epileptic mice will be repeated. Different glutamate concentrations between the left and right hippocampus, as well as differences between epileptic and healthy mice might be helpful to disentangle BOLD and GluCEST responses. Secondly, in-vitro experiments do not show BOLD responses. Acute slices offer several possibilities for interference, including optogenetic stimulation, and could be prepared to examine GluCEST fMRI responses in the absence of BOLD.

7 Concluding remarks

All points that were directly related to the results of this thesis and the possible next steps have already been discussed within each chapter. Some points shall now be set in the broader context.

The high-resolution diffusion MRI results of epileptogenesis could be clearly related to established features of epilepsy. The significance of these results for the field of research has been described by (Gröhn and Sierra, 2017). Meanwhile, a longitudinal study of human epileptogenesis came in part to similar results (Yokoi et al., 2019). The value of preclinical MRI research is immediately visible in this context. The MR results in this thesis showed opposing trends in different hippocampal subfields; FA increased in the DG and decreased in CA1. If such a high spatial resolution is not achieved, like in most clinical studies, different biological alterations may become averaged out. Therefore, it is not surprising that the published studies in humans yielded somewhat variable results. MR results that do not distinguish hippocampal subfields should be interpreted with caution.

As already described in chapter 1, there are attempts to model the microstructure with the aim to identify the individual components in-vivo by diffusion MRI. This thesis also showed that several structures, including neuronal axons but also glia, can contribute to anisotropic diffusion. A realistic model containing all structures that theoretically contribute to the diffusion results would need to be extremely detailed. However, such a model cannot be unambiguously confirmed because diffusion MR results do not contain sufficient information (simple signal decay). Attempts to gain more information are based on the use of more diffusion directions and higher b-values, which has to be traded off against reasonable scan times in-vivo.

Another application for diffusion is diffusion-fMRI (dfMRI). It has been assumed that neuronal cell swelling during activity can directly be detected by dfMRI. Measured dfMRI effects have been reported (Bihan et al., 2006; Tsurugizawa et al., 2013), but the method of dfMRI has so far not been broadly accepted because of the difficulty to separate dfMRI from the confounding BOLD effect in-vivo. In-vitro approaches without the BOLD effect could not find evidence for dfMRI effects in low-field MR systems (Bai et al., 2016). Current work explores dfMRI at high field. One advantage of the proposed CEST fMRI method is that, because of the application of the saturation pulse and the frequency specific responses, there are more adjustable parameters to separate possible CEST fMRI effects from BOLD. Furthermore, instead of “just” detecting structural differences during activity, CEST fMRI could be used to measure the kinetics of glutamate metabolism, in-vivo and in-vitro, and could be developed into a truly

quantitative fMRI method. However, it has to be emphasized that the proposed CEST fMRI method is also in an exploratory status and limitations are discussed in chapter 6.

Already several studies combining optogenetics and fMRI have been published. The impact of this work for the field of research is based on the one hand on the studied disorder and on the other hand on methodological advancements. So far, no comparable work in the kainate mouse model of TLE has been published and the combination of ofMRI with the CryoProbe provided higher sensitivity and allowed resting-state fMRI, which is also novel in this combination. Furthermore, this work is the beginning for further planned work on seizure interference.

Especially resting-state fMRI will be important to translate the preclinical results into clinical relevance. For example, it allows studying the question if activity propagates accordingly along the strongest resting-state connections. This work also shows that brain areas with increased resting-state fMRI connectivity in epileptic mice are critically involved during seizure spread. FMRI therefore has to be continually improved in order to be sensitive enough to detect all relevant changes.

Deep brain stimulation has already been performed in tens of thousands of patients and will continue to be a treatment tool as it provides an immediate therapeutic effect with fewer side-effects than drugs. However, the long-term efficacy of the stimulation may change due to the disease progression which requires adjustments of the stimulation parameters (Limousin and Foltynie, 2019). Currently, MRI is mainly used to check the position of the electrodes. There are reports discussing the safety and possibility of resting-state fMRI in DBS patients (Boutet et al., 2019; Carmichael et al., 2007). Using fMRI to observe the response to the stimulation is the subject of current research and may improve the effectiveness of DBS in the future.

Bibliography

Adamantidis, A.R., Zhang, F., Lecea, L. de, and Deisseroth, K. (2014). *Optogenetics: Opsins and Optical Interfaces in Neuroscience*. Cold Spring Harbor Protocols 2014, 815-822, DOI:10.1101/pdb.top083329.

Aggarwal, M., Gröhn, O., and Sierra, A. (2016). *Altered hippocampal microstructure in the epileptogenic rat brain revealed with diffusion MRI using oscillating field gradients*. Annual Meeting of the International Society for Magnetic Resonance in Medicine (ISMRM) in Singapore 2016, Abstract #1083

Airaksinen, A.M., Niskanen, J.-P., Chamberlain, R., Huttunen, J.K., Nissinen, J., Garwood, M., Pitkänen, A., and Gröhn, O. (2010). *Simultaneous fMRI and local field potential measurements during epileptic seizures in medetomidine-sedated rats using raser pulse sequence*. Magnetic Resonance in Medicine 64(4), 1191–1199.

Airaksinen, A.M., Hekmatyar, S.K., Jerome, N., Niskanen, J.-P., Huttunen, J.K., Pitkänen, A., Kauppinen, R.A., and Gröhn, O.H. (2012). *Simultaneous BOLD fMRI and local field potential measurements during kainic acid-induced seizures*. Epilepsia 53(7), 1245–1253.

Akin, B., Lee, H.-L., Hennig, J., and LeVan, P. (2017). *Enhanced subject-specific resting-state network detection and extraction with fast fMRI*. Human Brain Mapping 38(2), 817–830.

Alabi, A.A., and Tsien, R.W. (2012). *Synaptic Vesicle Pools and Dynamics*. Cold Spring Harbor Perspectives in Biology 2012, 4(8), 1-18, DOI: 10.1101/cshperspect.a013680

Alexander, D.C., and Barker, G.J. (2005). *Optimal imaging parameters for fiber-orientation estimation in diffusion MRI*. Neuroimage 27(2), 357–367.

Aravanis, A.M., Wang, L.-P., Zhang, F., Meltzer, L.A., Mogri, M.Z., Schneider, M.B., and Karl Deisseroth (2007). *An optical neural interface: in vivo control of rodent motor cortex with integrated fiberoptic and optogenetic technology*. Journal of Neural Engineering. 4(3), 143-156.

Armitage, P.A., and Bastin, M.E. (2001). *Utilizing the diffusion-to-noise ratio to optimize magnetic resonance diffusion tensor acquisition strategies for improving measurements of diffusion anisotropy*. Magnetic Resonance in Medicine 45(6), 1056–1065.

Assaf, B.A., Mohamed, F.B., Abou-Khaled, K.J., Williams, J.M., Yazeji, M.S., Haselgrove, J., and Faro, S.H. (2003). *Diffusion Tensor Imaging of the Hippocampal Formation in Temporal Lobe Epilepsy*. American Journal of Neuroradiology 24(9), 1857–1862.

Bai, R., Stewart, C.V., Plenz, D., and Basser, P.J. (2016). *Assessing the sensitivity of diffusion MRI to detect neuronal activity directly*. Proceedings of the National Academy of Sciences of the United States of America (PNAS) 113(12), 1728–1737.

Barth, M., Breuer, F., Koopmans, P.J., Norris, D.G., and Poser, B.A. (2016). *Simultaneous multislice (SMS) imaging techniques*. Magnetic Resonance in Medicine 75(1), 63–81.

Beaulieu, C. (2002). *The basis of anisotropic water diffusion in the nervous system – a technical review*. Nuclear Magnetic Resonance (NMR) in Biomedicine 15(7-8), 435–455.

Beaulieu, C., and Allen, P.S. (1994). *Water diffusion in the giant axon of the squid: Implications for diffusion-weighted MRI of the nervous system*. Magnetic Resonance in Medicine 32(5), 579–583.

Berglind, F., Ledri, M., Sørensen, A.T., Nikitidou, L., Melis, M., Bielefeld, P., Kirik, D., Deisseroth, K., Andersson, M., and Kokaia, M. (2014). *Optogenetic inhibition of chemically induced hypersynchronized bursting in mice*. Neurobiology of Disease 65, 133–141.

Bernal-Casas, D., Lee, H.J., Weitz, A.J., and Lee, J.H. (2017). *Studying Brain Circuit Function with Dynamic Causal Modeling for Optogenetic fMRI*. Neuron 93(3), 522–532.

Bernstein, M.A., King, K.F., and Zhou, Z.J. (2004). *Handbook of MRI pulse sequences*. Burlington, Massachusetts, USA: Academic Press.

Bertoglio, D., Verhaeghe, J., Dedeurwaerdere, S., and Gröhn, O. (2017). *Neuroimaging in animal models of epilepsy*. Neuroscience 358, 277–299.

Bewernick, B.H., Kayser, S., Gippert, S.M., Switala, C., Coenen, V.A., and Schlaepfer, T.E. (2017). *Deep brain stimulation to the medial forebrain bundle for depression-long-term outcomes and a novel data analysis strategy*. Brain Stimulation 10(3), 664–671.

Bihan, D.L., Urayama, S., Aso, T., Hanakawa, T., and Fukuyama, H. (2006). *Direct and fast detection of neuronal activation in the human brain with diffusion MRI*. Proceedings of the National Academy of Sciences of the United States of America (PNAS) 103(21), 8263–8268.

Bloch, F. (1946). *Nuclear Induction*. Physical Review. 70(7-8), 460–474.

Bloch, F., Hansen, W.W., and Packard, M. (1946). *The Nuclear Induction Experiment*. Physical Review 70(7-8), 474–485.

Blümcke, I., Pauli, E., Clusmann, H., Schramm, J., Becker, A., Elger, C., Merschhemke, M., Meencke, H.-J., Lehmann, T., von Deimling, A., et al. (2007). *A new clinico-*

pathological classification system for mesial temporal sclerosis. *Acta Neuropathologica* 113(3), 235–244.

Boutet, A., Hancu, I., Saha, U., Crawley, A., Xu, D.S., Ranjan, M., Hlasny, E., Chen, R., Foltz, W., Sammartino, F., et al. (2019). *3-Tesla MRI of deep brain stimulation patients: safety assessment of coils and pulse sequences*. *Journal of Neurosurgery* 1-9. DOI: 10.3171/2018.11.JNS181338. [Electronic publication ahead of print].

Boyden, E.S., Zhang, F., Bamberg, E., Nagel, G., and Deisseroth, K. (2005). *Millisecond-timescale, genetically targeted optical control of neural activity*. *Nature Neuroscience* 8(9), 1263–1268.

Brown, R. (1828). *A brief account of microscopical observations made in the months of June, July and August 1827, on the particles contained in the pollen of plants; and on the general existence of active molecules in organic and inorganic bodies*. *The Philosophical Magazine* 4(21), 161–173.

Bui, A.D., Nguyen, T.M., Limouse, C., Kim, H.K., Szabo, G.G., Felong, S., Maroso, M., and Soltesz, I. (2018). *Dentate gyrus mossy cells control spontaneous convulsive seizures and spatial memory*. *Science* 359(6377), 787–790.

Bukhari, Q., Schroeter, A., Cole, D.M., and Rudin, M. (2017). *Resting State fMRI in Mice Reveals Anesthesia Specific Signatures of Brain Functional Networks and Their Interactions*. *Frontiers in Neural Circuits* 11(5),1-11.

Cai, K., Haris, M., Singh, A., Kogan, F., Greenberg, J.H., Hariharan, H., Detre, J.A., and Reddy, R. (2012). *Magnetic resonance imaging of glutamate*. *Nature Medicine* 18(2), 302–306.

Cai, K., Haris, M., Singh, A., Li, L.Z., and Reddy, R. (2013). *Blood oxygen level dependent magnetization transfer (BOLDMT) effect*. In: Welch W.J., Palm F., Bruley D.F., Harrison D.K. (editors) *Oxygen Transport to Tissue XXXIV*. *Advances in Experimental Medicine and Biology*, vol 765, 31-37. Springer, New York, USA

Callaghan, P., (2009). *Introduction to k-space*. <http://www.magritek.com/support/videos> (Access on 5th December 2019).

Carmichael, D.W., Pinto, S., Limousin-Dowsey, P., Thobois, S., Allen, P.J., Lemieux, L., Yousry, T., and Thornton, J.S. (2007). *Functional MRI with active, fully implanted, deep brain stimulation systems: Safety and experimental confounds*. *Neuroimage* 37(2), 508–517.

Chan, R.W., Leong, A.T.L., Ho, L.C., Gao, P.P., Wong, E.C., Dong, C.M., Wang, X., He, J., Chan, Y.-S., Lim, L.W., et al. (2017). *Low-frequency hippocampal–cortical activity drives brain-wide resting-state functional MRI connectivity*. *Proceedings of the National Academy of Sciences of the United States of America (PNAS)* 114(33), 6972–6981.

- Chowdhury, F.A., O’Gorman, R.L., Nashef, L., Elwes, R.D., Edden, R.A., Murdoch, J.B., Barker, G.J., and Richardson, M.P. (2015). *Investigation of glutamine and GABA levels in patients with idiopathic generalized epilepsy using MEGAPRESS*. *Journal of Magnetic Resonance Imaging* 41(3), 694–699.
- Choy, M., Cheung, K.K., Thomas, D.L., Gadian, D.G., Lythgoe, M.F., and Scott, R.C. (2010). *Quantitative MRI predicts status epilepticus-induced hippocampal injury in the lithium–pilocarpine rat model*. *Epilepsy Research* 88(2-3), 221–230.
- Coffey, R.J. (2009). *Deep Brain Stimulation Devices: A Brief Technical History and Review*. *Artificial Organs* 33(3), 208–220.
- Connelly, A., Jackson, G.D., Duncan, J.S., King, M.D., and Gadian, D.G. (1994). *Magnetic resonance spectroscopy in temporal lobe epilepsy*. *Neurology* 44(8), 1411–1417.
- Crescenzi, R., DeBrosse, C., Nanga, R.P.R., Reddy, S., Haris, M., Hariharan, H., Iba, M., Lee, V.M.Y., Detre, J.A., Borthakur, A., et al. (2014). *In vivo measurement of glutamate loss is associated with synapse loss in a mouse model of tauopathy*. *Neuroimage* 101, 185–192.
- Cross, J.H., Connelly, A., Jackson, G.D., Johnson, C.L., Neville, B.G., and Gadian, D.G. (1996). *Proton magnetic resonance spectroscopy in children with temporal lobe epilepsy*. *Annals of Neurology* 39(1), 107–113.
- Danbolt, N.C. (2001). *Glutamate uptake*. *Progress in Neurobiology* 65(1), 1–105.
- De Graaf, R.A. (2007). *In vivo NMR spectroscopy: principles and techniques*. Chichester, West Sussex, England: John Wiley & Sons Ltd.
- De riu, P.L., Petruzzi, V., Testa, C., Mulas, M., Melis, F., Caria, M.A., and Mameli, O. (1992). *Propofol anticonvulsant activity in experimental epileptic status*. *British Journal of Anaesthesia* 69(2), 177–181.
- Denker, A., and Rizzoli, S.O. (2010). *Synaptic Vesicle Pools: An Update*. *Frontiers in Synaptic Neuroscience* 2(135), 1-12.
- Deuschl, G., Schade-Brittinger, C., Krack, P., Volkmann, J., Schäfer, H., Bötzel, K., Daniels, C., Deuschländer, A., Dillmann, U., Eisner, W., et al. (2006). *A Randomized Trial of Deep-Brain Stimulation for Parkinson’s Disease*. *New England Journal of Medicine* 355(9), 896–908.
- Dietrich, Y., Eliat, P., Dieuset, G., Saint-Jalmes, H., Pineau, C., Wendling, F., and Martin, B. (2016). *Structural and functional changes during epileptogenesis in the mouse model of medial temporal lobe epilepsy*. In: 2016 38th Annual International Conference of the IEEE Engineering in Medicine and Biology Society (EMBC), Orlando, USA, pp. 4005–4008.

-
- Duffy, B.A., Choy, M., Chuapoco, M.R., Madsen, M., and Lee, J.H. (2015). *MRI compatible optrodes for simultaneous LFP and optogenetic fMRI investigation of seizure-like afterdischarges*. *Neuroimage* 123, 173–184.
- Dunn, J.F., Tuor, U.I., Kmech, J., Young, N.A., Henderson, A.K., Jackson, J.C., Valentine, P.A., and Teskey, G.C. (2009). *Functional brain mapping at 9.4T using a new MRI-compatible electrode chronically implanted in rats*. *Magnetic Resonance in Medicine* 61(1), 222–228.
- During, M.J., and Spencer, D.D. (1993). *Extracellular hippocampal glutamate and spontaneous seizure in the conscious human brain*. *The Lancet* 341(8861), 1607–1610.
- Einstein, A. (1905). *Über die von der molekularkinetischen Theorie der Wärme geforderte Bewegung von in ruhenden Flüssigkeiten suspendierten Teilchen*. *Annalen Der Physik* 322, 549-560.
- Elster, A. D., (2019). *Questions and Answers in MRI*. <http://www.mriquestions.com> (Access on 5th December 2019).
- Englot, D.J., Konrad, P.E., and Morgan, V.L. (2016). *Regional and global connectivity disturbances in focal epilepsy, related neurocognitive sequelae, and potential mechanistic underpinnings*. *Epilepsia* 57(10), 1546–1557.
- Fahrner, A., Kann, G., Flubacher, A., Heinrich, C., Freiman, T.M., Zentner, J., Frotscher, M., and Haas, C.A. (2007). *Granule cell dispersion is not accompanied by enhanced neurogenesis in temporal lobe epilepsy patients*. *Experimental Neurology* 203(2), 320–332.
- Fang, Z., and Lee, J.H. (2013). *High-throughput optogenetic functional magnetic resonance imaging with parallel computations*. *Journal of Neuroscience Methods* 218(2), 184–195.
- Fick, A. (1855). *Ueber Diffusion*. *Annalen Der Physik* 170, 59–86.
- Fieremans, E., Jensen, J.H., and Helpert, J.A. (2011). *White matter characterization with diffusional kurtosis imaging*. *Neuroimage* 58(1), 177–188.
- Forsén, S., and Hoffman, R.A. (1963). *Study of Moderately Rapid Chemical Exchange Reactions by Means of Nuclear Magnetic Double Resonance*. *The Journal of Chemical Physics* 39(11), 2892–2901.
- Fritschy, J.-M. (2004). *A New Animal Model of Temporal Lobe Epilepsy*. *Epileptologie* 21, 21-28.
- Gomes, W.A., and Shinnar, S. (2011). *Prospects for imaging-related biomarkers of human epileptogenesis: a critical review*. *Biomarkers in Medicine* 5(5), 599–606.
- Gomes, W.A., Lado, F.A., Lanerolle, N.C. de, Takahashi, K., Pan, C., and Hetherington, H.P. (2007). *Spectroscopic imaging of the pilocarpine model of human*

epilepsy suggests that early NAA reduction predicts epilepsy. *Magnetic Resonance in Medicine* 58(2), 230–235.

Grandjean, J., Schroeter, A., Batata, I., and Rudin, M. (2014). *Optimization of anesthesia protocol for resting-state fMRI in mice based on differential effects of anesthetics on functional connectivity patterns*. *Neuroimage* 102(2), 838–847.

Grandjean, J., Zerbi, V., Balsters, J.H., Wenderoth, N., and Rudin, M. (2017). *Structural Basis of Large-Scale Functional Connectivity in the Mouse*. *Journal of Neuroscience*. 37(34), 8092–8101.

Gröhn, O., and Sierra, A. (2017). *Searching for epilepsy's crystal ball*. *eLife* 2017;6:e29853, 1-3, DOI: 10.7554/eLife.29853

Gröhn, O., Sierra, A., Immonen, R., Laitinen, T., Lehtimäki, K., Airaksinen, A., Hayward, N., Nairismagi, J., Lehto, L., and Pitkänen, A. (2011). *Multimodal MRI assessment of damage and plasticity caused by status epilepticus in the rat brain*. *Epilepsia* 52(s8), 57–60.

Grone, B.P., and Baraban, S.C. (2015). *Animal models in epilepsy research: legacies and new directions*. *Nature Neuroscience* 18(3), 339–343.

Gross, D.W. (2011). *Diffusion tensor imaging in temporal lobe epilepsy*. *Epilepsia* 52(s4), 32–34.

Guo, J., Gang, Z., Sun, Y., Laine, A., Small, S.A., and Rothman, D.L. (2018). *In vivo detection and automatic analysis of GABA in the mouse brain with MEGA-PRESS at 9.4 T*. *Nuclear Magnetic Resonance (NMR) in Biomedicine* 31(1):e3837, 1-11.

Haas, C.A., and Frotscher, M. (2010). *Reelin deficiency causes granule cell dispersion in epilepsy*. *Experimental Brain Research* 200(2), 141–149.

Haase, A., Odoj, F., Kienlin, M.V., Warnking, J., Fidler, F., Weisser, A., Nittka, M., Rommel, E., Lanz, T., Kalusche, B., et al. (2000). *NMR probeheads for in vivo applications*. *Concepts in Magnetic Resonance* 12(6), 361–388.

Hahn, E.L. (1950). *Spin Echoes*. *Physical Review*. 80(4), 580–594.

Hanson, L.G. (2008). *Is quantum mechanics necessary for understanding magnetic resonance?*. *Concepts in Magnetic Resonance* 32A, 329–340.

van der Hel, W.S., Eijdsen, P. van, Bos, I.W.M., Graaf, R.A. de, Behar, K.L., Nieuwenhuizen, O. van, Graan, P.N.E. de, and Braun, K.P.J. (2013). *In vivo MRS and histochemistry of status epilepticus-induced hippocampal pathology in a juvenile model of temporal lobe epilepsy*. *Nuclear Magnetic Resonance (NMR) in Biomedicine* 26(2), 132–140.

Hennig, J., Nauerth, A., and Friedburg, H. (1986). *RARE imaging: A fast imaging method for clinical MR*. *Magnetic Resonance in Medicine* 3(6), 823–833.

-
- Hesdorffer, D.C., Shinnar, S., Lewis, D.V., Moshé, S.L., Nordli, D.R., Pellock, J.M., MacFall, J., Shinnar, R.C., Masur, D., Frank, L.M., et al. (2012). *Design and phenomenology of the FEBSTAT study*. *Epilepsia* 53(9), 1471–1480.
- Hu, X., and Yacoub, E. (2012). *The story of the initial dip in fMRI*. *Neuroimage* 62(2), 1103–1108.
- Huettel, S.A., Song, A.W., and McCarthy, G. (2004). *Functional magnetic resonance imaging*. Sunderland, Massachusetts, USA: Sinauer Associates, Inc.
- Hui, E.S., Cheung, M.M., Qi, L., and Wu, E.X. (2008). *Towards better MR characterization of neural tissues using directional diffusion kurtosis analysis*. *Neuroimage* 42(1), 122–134.
- Ikeda, K., and Bekkers, J.M. (2009). *Counting the number of releasable synaptic vesicles in a presynaptic terminal*. *Proceedings of the National Academy of Sciences of the United States of America (PNAS)* 106(8), 2945–2950.
- Janz, P., Schwaderlapp, N., Heining, K., Häussler, U., Korvink, J.G., von Elverfeldt, D., Hennig, J., Egert, U., LeVan, P., and Haas, C.A. (2017). *Early tissue damage and microstructural reorganization predict disease severity in experimental epilepsy*. *eLife* 2017;6:e25742, 1-26. DOI: 10.7554/eLife.25742
- Jones, D.K., Horsfield, M.A., and Simmons, A. (1999). *Optimal strategies for measuring diffusion in anisotropic systems by magnetic resonance imaging*. *Magnetic Resonance in Medicine* 42(3), 515–525.
- Jones, D.K. (2011). *Diffusion MRI: Theory, Methods, and Applications*. New York City, New York, USA: Oxford University Press.
- Kandratavicius, L., Balista, P.A., Lopes-Aguiar, C., Ruggiero, R.N., Umeoka, E.H., Garcia-Cairasco, N., Bueno-Junior, L.S., and Leite, J.P. (2014). *Animal models of epilepsy: use and limitations*. *Neuropsychiatric Disease and Treatment* 10, 1693–1705.
- Kharatishvili, I., Shan, Z.Y., She, D.T., Foong, S., Kurniawan, N.D., and Reutens, D.C. (2014). *MRI changes and complement activation correlate with epileptogenicity in a mouse model of temporal lobe epilepsy*. *Brain Structure and Function* 219(2), 683–706.
- Kim, M., Gillen, J., Landman, B.A., Zhou, J., and Zijl, P.C.M. van (2009). *Water saturation shift referencing (WASSR) for chemical exchange saturation transfer (CEST) experiments*. *Magnetic Resonance in Medicine* 61(6), 1441–1450.
- Krack, P., Batir, A., Van Blercom, N., Chabardes, S., Fraix, V., Ardouin, C., Koudsie, A., Limousin, P.D., Benazzouz, A., LeBas, J.F., et al. (2003). *Five-Year Follow-up of Bilateral Stimulation of the Subthalamic Nucleus in Advanced Parkinson's Disease*. *New England Journal of Medicine* 349(20), 1925–1934.

- Krook-Magnuson, E., Armstrong, C., Oijala, M., and Soltesz, I. (2013). *On-demand optogenetic control of spontaneous seizures in temporal lobe epilepsy*. *Nature Communications* 4:1376, 1-8.
- Krook-Magnuson, E., Szabo, G.G., Armstrong, C., Oijala, M., and Soltesz, I. (2014). *Cerebellar Directed Optogenetic Intervention Inhibits Spontaneous Hippocampal Seizures in a Mouse Model of Temporal Lobe Epilepsy*. *eNeuro* 1(1) 1-15, DOI: 10.1523/ENEURO.0005-14.2014.
- Krook-Magnuson, E., Armstrong, C., Bui, A., Lew, S., Oijala, M., and Soltesz, I. (2015). *In vivo evaluation of the dentate gate theory in epilepsy*. *The Journal of Physiology* 593(10), 2379–2388.
- Kundu, P., Voon, V., Balchandani, P., Lombardo, M.V., Poser, B.A., and Bandettini, P.A. (2017). *Multi-echo fMRI: A review of applications in fMRI denoising and analysis of BOLD signals*. *Neuroimage* 154, 59–80.
- Lachert, P., Janusek, D., Pulawski, P., Liebert, A., Milej, D., and Blinowska, K.J. (2017). *Coupling of Oxy- and Deoxyhemoglobin concentrations with EEG rhythms during motor task*. *Scientific Reports* 7(15414), 1–9.
- Laitinen, T., Sierra, A., Pitkänen, A., and Gröhn, O. (2010). *Diffusion tensor MRI of axonal plasticity in the rat hippocampus*. *Neuroimage* 51(2), 521–530.
- Laxer, K.D., Trinkka, E., Hirsch, L.J., Cendes, F., Langfitt, J., Delanty, N., Resnick, T., and Benbadis, S.R. (2014). *The consequences of refractory epilepsy and its treatment*. *Epilepsy & Behavior* 37, 59–70.
- Le Bihan, D., Breton, E., Lallemand, D., Aubin, M.L., Vignaud, J., and Laval-Jeantet, M. (1988). *Separation of diffusion and perfusion in intravoxel incoherent motion MR imaging*. *Radiology* 168(2), 497–505.
- Le Bihan, D., Turner, R., Moonen, C.T.W., and Pekar, J. (1991). *Imaging of diffusion and microcirculation with gradient sensitization: Design, strategy, and significance*. *Journal of Magnetic Resonance Imaging* 1(1), 7–28.
- Ledri, M., Madsen, M.G., Nikitidou, L., Kirik, D., and Kokaia, M. (2014). *Global Optogenetic Activation of Inhibitory Interneurons during Epileptiform Activity*. *Journal of Neuroscience* 34(9), 3364–3377.
- Lee, E.M., Park, G.Y., Im, K.C., Kim, S.T., Woo, C.-W., Chung, J.H., Kim, K.S., Kim, J.S., Shon, Y.-M., Kim, Y.I., et al. (2012). *Changes in glucose metabolism and metabolites during the epileptogenic process in the lithium-pilocarpine model of epilepsy*. *Epilepsia* 53(5), 860–869.
- Lee, J.H., Durand, R., Gradinaru, V., Zhang, F., Goshen, I., Kim, D.-S., Fenno, L.E., Ramakrishnan, C., and Deisseroth, K. (2010). *Global and local fMRI signals driven by neurons defined optogenetically by type and wiring*. *Nature* 465, 788–792.

-
- Lévesque, M., and Avoli, M. (2013). *The kainic acid model of temporal lobe epilepsy*. *Neuroscience & Biobehavioral Reviews* 37(10 Part 2), 2887–2899.
- Levitt, M. (2008). *Spin Dynamics: Basics of Nuclear Magnetic Resonance*. Chichester, West Sussex, England: John Wiley & Sons Ltd.
- Lewis, D.V., Shinnar, S., Hesdorffer, D.C., Bagiella, E., Bello, J.A., Chan, S., Xu, Y., MacFall, J., Gomes, W.A., Moshé, S.L., et al. (2014). *Hippocampal sclerosis after febrile status epilepticus: the FEBSTAT study*. *Annals of Neurology* 75(2), 178–185.
- Liewald, D., Miller, R., Logothetis, N., Wagner, H.-J., and Schüz, A. (2014). *Distribution of axon diameters in cortical white matter: an electron-microscopic study on three human brains and a macaque*. *Biological Cybernetics* 108(5), 541–557.
- Limousin, P., and Foltynie, T. (2019). *Long-term outcomes of deep brain stimulation in Parkinson disease*. *Nature Reviews Neurology* 15(4), 234–242.
- Liu, J., Lee, H.J., Weitz, A.J., Fang, Z., Lin, P., Choy, M., Fisher, R., Pinskiy, V., Tolpygo, A., Mitra, P., et al. (2015). *Frequency-selective control of cortical and subcortical networks by central thalamus*. *eLife* 2015;4:e09215, 1-27. DOI: 10.7554/eLife.09215.
- Liu, J., Duffy, B.A., Bernal-Casas, D., Fang, Z., and Lee, J.H. (2017). *Comparison of fMRI analysis methods for heterogeneous BOLD responses in block design studies*. *Neuroimage* 147, 390–408.
- Low, L.A., Bauer, L.C., and Klaunberg, B.A. (2016). *Comparing the Effects of Isoflurane and Alpha Chloralose upon Mouse Physiology*. *Public Library of Science (PLOS) One* 11(5): e0154936, 1-14. DOI:10.1371/journal.pone.0154936
- Lozano, A.M., Lipsman, N., Bergman, H., Brown, P., Chabardes, S., Chang, J.W., Matthews, K., McIntyre, C.C., Schlaepfer, T.E., Schulder, M., et al. (2019). *Deep brain stimulation: current challenges and future directions*. *Nature Reviews Neurology* 15(3), 148–160.
- Mansfield, P. (1977). *Multi-planar image formation using NMR spin echoes*. *Journal of Physics C: Solid State Physics* 10(3), 55-58.
- Mayberg, H.S., Lozano, A.M., Voon, V., McNeely, H.E., Seminowicz, D., Hamani, C., Schwalb, J.M., and Kennedy, S.H. (2005). *Deep Brain Stimulation for Treatment-Resistant Depression*. *Neuron* 45(5), 651–660.
- van Mierlo, P., Papadopoulou, M., Carrette, E., Boon, P., Vandenberghe, S., Vonck, K., and Marinazzo, D. (2014). *Functional brain connectivity from EEG in epilepsy: seizure prediction and epileptogenic focus localization*. *Progress in Neurobiology* 121, 19–35.
- Miocinovic, S., Somayajula, S., Chitnis, S., and Vitek, J.L. (2013). *History, Applications, and Mechanisms of Deep Brain Stimulation*. *Journal of the American Medical Association (JAMA) Neurology* 70(2), 163–171.

- Moseley, M.E., Kucharczyk, J., Asgari, H.S., and Norman, D. (1991). *Anisotropy in diffusion-weighted MRI*. *Magnetic Resonance in Medicine* 19(2), 321–326.
- Norris, D.G. (2012). *Spin-echo fMRI: The poor relation?* *Neuroimage* 62(2), 1109–1115.
- Ogawa, S., Lee, T.M., Kay, A.R., and Tank, D.W. (1990). *Brain magnetic resonance imaging with contrast dependent on blood oxygenation*. *Proceedings of the National Academy of Sciences of the United States of America (PNAS)* 87(24), 9868–9872.
- Ogawa, S., Tank, D.W., Menon, R., Ellermann, J.M., Kim, S.G., Merkle, H., and Ugurbil, K. (1992). *Intrinsic signal changes accompanying sensory stimulation: functional brain mapping with magnetic resonance imaging*. *Proceedings of the National Academy of Sciences of the United States of America (PNAS)* 89(13), 5951–5955.
- Ogawa, S., Menon, R.S., Tank, D.W., Kim, S.G., Merkle, H., Ellermann, J.M., and Ugurbil, K. (1993). *Functional brain mapping by blood oxygenation level-dependent contrast magnetic resonance imaging. A comparison of signal characteristics with a biophysical model*. *Biophysical Journal* 64(3), 803–812.
- Paasonen, J., Stenroos, P., Salo, R.A., Kiviniemi, V., and Gröhn, O. (2018). *Functional connectivity under six anesthesia protocols and the awake condition in rat brain*. *Neuroimage* 172, 9–20.
- Parker, C.S., Clayden, J.D., Cardoso, M.J., Rodionov, R., Duncan, J.S., Scott, C., Diehl, B., and Ourselin, S. (2017). *Structural and effective connectivity in focal epilepsy*. *Neuroimage Clinical* 17, 943–952.
- Paz, J.T., Davidson, T.J., Frechette, E.S., Delord, B., Parada, I., Peng, K., Deisseroth, K., and Huguenard, J.R. (2013). *Closed-loop optogenetic control of thalamus as a tool for interrupting seizures after cortical injury*. *Nature Neuroscience* 16(1), 64–70.
- Pépin, J., Francelle, L., Carrillo-de Sauvage, M.-A., de Longprez, L., Gipchtein, P., Cambon, K., Valette, J., Brouillet, E., and Flament, J. (2016). *In vivo imaging of brain glutamate defects in a knock-in mouse model of Huntington's disease*. *Neuroimage* 139, 53–64.
- Pitkänen, A., Buckmaster, Galanopoulou, and Moshé, S.L. (2017). *Models of Seizures and Epilepsy: Second Edition*. Cambridge, Massachusetts, USA: Elsevier Academic Press.
- Portnoy, S., Flint, J.J., Blackband, S.J., and Stanisiz, G.J. (2013). *Oscillating and pulsed gradient diffusion magnetic resonance microscopy over an extended b-value range: Implications for the characterization of tissue microstructure*. *Magnetic Resonance in Medicine* 69(4), 1131–1145.
- Poser, B.A., and Norris, D.G. (2009). *Investigating the benefits of multi-echo EPI for fMRI at 7 T*. *Neuroimage* 45(4), 1162–1172.

Provencher, S. (2018). *LCModel's home page*. <http://s-provencher.com/lcmodel.shtml> (Access on 5th December 2019).

Reisert, M., Mader, I., Anastasopoulos, C., Weigel, M., Schnell, S., and Kiselev, V. (2011). *Global fiber reconstruction becomes practical*. *Neuroimage* 54(2), 955–962.

Rizzoli, S.O., and Betz, W.J. (2005). *Synaptic vesicle pools*. *Nature Reviews Neuroscience* 6(1), 57–69.

Roch, C., Leroy, C., Nehlig, A., and Namer, I.J. (2002). *Predictive Value of Cortical Injury for the Development of Temporal Lobe Epilepsy in 21-day-old Rats: An MRI Approach Using the Lithium-pilocarpine Model*. *Epilepsia* 43(10), 1129–1136.

Roussel, T., Frydman, L., Bihan, D.L., and Ciobanu, L. (2019). *Brain sugar consumption during neuronal activation detected by CEST functional MRI at ultra-high magnetic fields*. *Scientific Reports* 9(4423), 1–11.

Ryali, S., Shih, Y.-Y.I., Chen, T., Kochalka, J., Albaugh, D., Fang, Z., Supekar, K., Lee, J.H., and Menon, V. (2016). *Combining optogenetic stimulation and fMRI to validate a multivariate dynamical systems model for estimating causal brain interactions*. *Neuroimage* 132, 398–405.

Salo, R.A., Miettinen, T., Laitinen, T., Gröhn, O., and Sierra, A. (2017). *Diffusion tensor MRI shows progressive changes in the hippocampus and dentate gyrus after status epilepticus in rat – histological validation with Fourier-based analysis*. *Neuroimage* 152, 221–236.

Schmid, F., Wachsmuth, L., Albers, F., Schwalm, M., Stroh, A., and Faber, C. (2017). *True and apparent optogenetic BOLD fMRI signals*. *Magnetic Resonance in Medicine* 77(1), 126–136.

Schridde, U., Khubchandani, M., Motelow, J.E., Sangahalli, B.G., Hyder, F., and Blumenfeld, H. (2008). *Negative BOLD with Large Increases in Neuronal Activity*. *Cerebral Cortex* 18(8), 1814–1827.

Schwaderlapp, N., Janz, P., Leupold, J., Elverfeldt, D., Korvink, J.G., Hennig, J., Haas, C., LeVan, P. (2017). *Imaging of glutamate alterations in a mouse model of temporal lobe epilepsy*. Annual Meeting of the International Society for Magnetic Resonance in Medicine (ISMRM) in Honolulu, USA, Abstract #4092.

Sierra, A., Gröhn, O., and Pitkänen, A. (2015). *Imaging microstructural damage and plasticity in the hippocampus during epileptogenesis*. *Neuroscience* 309, 162–172.

Simister, R.J., McLean, M.A., Barker, G.J., and Duncan, J.S. (2009). *Proton MR spectroscopy of metabolite concentrations in temporal lobe epilepsy and effect of temporal lobe resection*. *Epilepsy Research* 83(2-3), 168–176.

- Stejskal, E.O., and Tanner, J.E. (1965). *Spin Diffusion Measurements: Spin Echoes in the Presence of a Time-Dependent Field Gradient*. *The Journal of Chemical Physics* 42(1), 288–292.
- Südhof, T.C. (2004). *The Synaptic Vesicle Cycle*. *Annual Review of Neuroscience* 27, 509–547.
- Sun, S.-W., Neil, J.J., Liang, H.-F., He, Y.Y., Schmidt, R.E., Hsu, C.Y., and Song, S.-K. (2005). *Formalin fixation alters water diffusion coefficient magnitude but not anisotropy in infarcted brain*. *Magnetic Resonance in Medicine* 53(6), 1447–1451.
- Thivard, L., Lehericy, S., Krainik, A., Adam, C., Dormont, D., Chiras, J., Baulac, M., and Dupont, S. (2005). *Diffusion tensor imaging in medial temporal lobe epilepsy with hippocampal sclerosis*. *Neuroimage* 28(3), 682–690.
- Thom, M. (2014). *Review: Hippocampal sclerosis in epilepsy: a neuropathology review*. *Neuropathology and Applied Neurobiology* 40(5), 520–543.
- Thomsen, C., Henriksen, O., and Ring, P. (1987). *In vivo measurement of water self diffusion in the human brain by magnetic resonance imaging*. *Acta Radiologica* 28(3), 353–361.
- de Tisi, J., Bell, G.S., Peacock, J.L., McEvoy, A.W., Harkness, W.F., Sander, J.W., and Duncan, J.S. (2011). *The long-term outcome of adult epilepsy surgery, patterns of seizure remission, and relapse: a cohort study*. *The Lancet* 378(9800), 1388–1395.
- Tønnesen, J., Sørensen, A.T., Deisseroth, K., Lundberg, C., and Kokaia, M. (2009). *Optogenetic control of epileptiform activity*. *Proceedings of the National Academy of Sciences of the United States of America (PNAS)* 106(29), 12162–12167.
- Tsurugizawa, T., Ciobanu, L., and Bihan, D.L. (2013). *Water diffusion in brain cortex closely tracks underlying neuronal activity*. *Proceedings of the National Academy of Sciences of the United States of America (PNAS)* 110(28), 11636–11641.
- Tye, K.M., and Deisseroth, K. (2012). *Optogenetic investigation of neural circuits underlying brain disease in animal models*. *Nature Reviews Neuroscience* 13(4), 251–266.
- Urbach, H., Huppertz, H.J., Schwarzwald, R., Becker, A.J., Wagner, J., Bahri, M.D., and Tschampa, H.J. (2014). *Is the type and extent of hippocampal sclerosis measurable on high-resolution MRI?* *Neuroradiology* 56(9), 731–735.
- Weitz, A.J., Fang, Z., Lee, H.J., Fisher, R.S., Smith, W.C., Choy, M., Liu, J., Lin, P., Rosenberg, M., and Lee, J.H. (2015). *Optogenetic fMRI reveals distinct, frequency-dependent networks recruited by dorsal and intermediate hippocampus stimulations*. *Neuroimage* 107, 229–241.
- WHO (2019a) *Neurology and public health*
https://www.who.int/mental_health/neurology/en/ (Access on 5th December 2019).

WHO (2019b) *Mental health*

https://www.who.int/mental_health/neurology/epilepsy/en/ (Access on 5th December 2019).

Wolff, S.D., and Balaban, R.S. (1989). *Magnetization transfer contrast (MTC) and tissue water proton relaxation in vivo*. *Magnetic Resonance in Medicine* 10(1), 135–144.

Wu, E.X., and Cheung, M.M. (2010). *MR diffusion kurtosis imaging for neural tissue characterization*. *Nuclear Magnetic Resonance (NMR) in Biomedicine* 23(7), 836–848.

Wykes, R.C., Heeroma, J.H., Mantoan, L., Zheng, K., MacDonald, D.C., Deisseroth, K., Hashemi, K.S., Walker, M.C., Schorge, S., and Kullmann, D.M. (2012). *Optogenetic and Potassium Channel Gene Therapy in a Rodent Model of Focal Neocortical Epilepsy*. *Science Translational Medicine* 4(161):161ra152, 1-10.

Wykes, R.C., Khoo, H.M., Caciagli, L., Blumenfeld, H., Golshani, P., Kapur, J., Stern, J.M., Bernasconi, A., Dedeurwaerdere, S., and Bernasconi, N. (2019). *WONOE appraisal: Network concept from an imaging perspective*. *Epilepsia* 60(7), 1293–1305.

Yizhar, O., Fenno, L.E., Davidson, T.J., Mogri, M., and Deisseroth, K. (2011). *Optogenetics in Neural Systems*. *Neuron* 71(1), 9–34.

Yokoi, S., Kidokoro, H., Yamamoto, H., Ohno, A., Nakata, T., Kubota, T., Tsuji, T., Morishita, M., Kawabe, T., Naiki, M., et al. (2019). *Hippocampal diffusion abnormality after febrile status epilepticus is related to subsequent epilepsy*. *Epilepsia* 60, 1306–1316.

Zerbi, V., Grandjean, J., Rudin, M., and Wenderoth, N. (2015). *Mapping the mouse brain with rs-fMRI: An optimized pipeline for functional network identification*. *Neuroimage* 123, 11–21.

Zhou, J., Payen, J.-F., and Zijl, P.C.M. van (2005). *The interaction between magnetization transfer and blood-oxygen-level-dependent effects*. *Magnetic Resonance in Medicine* 53(2), 356–366.

van Zijl, P.C.M., Hua, J., and Lu, H. (2012). *The BOLD post-stimulus undershoot, one of the most debated issues in fMRI*. *Neuroimage* 62(2), 1092–1102.

van Zijl, P.C.M., Lam, W.W., Xu, J., Knutsson, L., and Stanis, G.J. (2018). *Magnetization Transfer Contrast and Chemical Exchange Saturation Transfer MRI. Features and analysis of the field-dependent saturation spectrum*. *Neuroimage* 168, 222–241.

List of Figures

- Figure 1.1** Longitudinal study of experimental epilepsy and ex-vivo analysis of resected tissue from epilepsy patients.
- Figure 1.2** fMRI shows the propagation of an optogenetically induced seizure in an epileptic mouse.
- Figure 1.3** CEST fMRI response during an optogenetically induced epileptic seizure.
- Figure 2.1** Signal evolution for Gradient and Spin Echoes.
- Figure 2.2** Spatial Encoding by Gradients.
- Figure 2.3** Relation between k-space and image space.
- Figure 2.4** Image Artifacts.
- Figure 2.5** RARE.
- Figure 2.6** EPI.
- Figure 2.7** From thermal motion to diffusion tensor MRI.
- Figure 2.8** Diffusion properties of human brain tissue.
- Figure 2.9** Illustration of different tractography approaches.
- Figure 2.10** Localized Spectroscopy.
- Figure 2.11** Basic task-based fMRI experiment.
- Figure 2.12** Principle idea of resting-state fMRI.
- Figure 2.13** Seed-based analysis of mouse brain resting-state connectivity.
- Figure 2.14** Principle of chemical exchange saturation transfer (CEST) MRI.
- Figure 3.1** Illustration of the rodent hippocampus and the KA model of mTLE.
- Figure 3.2** Illustration of optogenetic stimulation.
- Figure 4.1** Experimental design.
- Figure 4.2** Setup for mouse brain MRI.
- Figure 4.3** Scanning procedure.
- Figure 4.4** Representative RARE images.
- Figure 4.5** Representative results of diffusion MRI.
- Figure 4.6** In-vivo Mouse brain spectroscopy.
- Figure 4.7** In-vivo spectrum evaluated with LCModel.
- Figure 4.8** Contributions of individual metabolites to the spectrum.
- Figure 4.9** Representative RARE and DWI of resected human HC.
- Figure 4.10** Histological and electrophysiological characterization of animals.
- Figure 4.11** T₂-weighted imaging during epileptogenesis revealed early hippocampal damage as well as chronic changes of the DG.
- Figure 4.12** Sections of T₂-weighted images for all mice at all time-points.
- Figure 4.13** Quantified changes of T₂-weighted signal intensity in CA1 and DG during epileptogenesis.
- Figure 4.14** Direct comparison of T₂-weighted images and histological stainings in a control and epileptic mouse.
- Figure 4.15** ¹H-MR spectroscopy results from the ipsilateral septal hippocampus during epileptogenesis.
- Figure 4.16** Diffusion-weighted tractography during epileptogenesis.
- Figure 4.17** Sections of tractography images for all mice at all time-points.
- Figure 4.18** Quantitative analysis of DWI in the DG during epileptogenesis.
- Figure 4.19** Direct comparison of tractography images and histological stainings.
- Figure 4.20** Contribution of radial gliosis to the diffusion properties.
- Figure 4.21** Ex-vivo analysis of sclerotic human hippocampi from mTLE patients.

- Figure 4.22** Comparison of high- and low-resolution ex vivo DWI.
- Figure 4.23** Correlation between spectroscopy and diffusion MRI results during epileptogenesis.
- Figure 5.1** CryoProbe compatible ofMRI setup.
- Figure 5.2** ofMRI setup.
- Figure 5.3** Animal fixation for fMRI.
- Figure 5.4** Combination of multi-echo fMRI datasets.
- Figure 5.5** Effect of slice gaps.
- Figure 5.6** T_2^* relaxation in the mouse brain.
- Figure 5.7** Segmented and labeled mouse brain atlas.
- Figure 5.8** fMRI during visual stimulation.
- Figure: 5.9** Failed induction of epileptic activity.
- Figure 5.10** fMRI of optogenetic stimulation below seizure threshold.
- Figure 5.11** ICA components of single subject resting-state fMRI.
- Figure 5.12** Reproducibility of resting-state fMRI ICA.
- Figure 5.13** Seed-based resting-state fMRI connectivity.
- Figure 5.14** Sliding window analysis of rsfMRI.
- Figure 5.15** Comparison of static and sliding window analysis.
- Figure 5.16** Resting-state fMRI correlations for all measurements of control mice.
- Figure 5.17** Resting-state fMRI correlations for all measurements of kainate mice.
- Figure 5.18** Comparison of single-echo and multi-echo fMRI.
- Figure 5.19** FMRI temporal filtering for seizure activity.
- Figure 5.20** Seizure propagation in a control mouse.
- Figure 5.21** Seizure propagation in a kainate mouse.
- Figure 5.22** fMRI time courses during epileptic seizures.
- Figure 5.23** Mean seizure response in control and kainate mice.
- Figure 5.24** Overview of all induced seizures.
- Figure 5.25** Probability of seizure activity in control and kainate mice.
- Figure 5.26** Mean resting-state fMRI connectivity in control mice.
- Figure 5.27** Anatomical representation of the mean resting-state fMRI connectivity in control mice.
- Figure 5.28** Mean resting-state fMRI connectivity in kainate mice.
- Figure 5.29** Resting-state fMRI differences between the CO and KA group.
- Figure 5.30** Anatomical representation of connectivity differences between CO and KA mice.
- Figure 5.31** Group ICA of KA mice.
- Figure 5.32** Group ICA of CO mice.
- Figure 5.33** Resting-state fMRI connections in CO and KA mice.
- Figure 5.34** Seizure propagation in CO mice.
- Figure 5.35** Seizure propagation in KA mice.
- Figure 5.36** Stimulation target and fiber orientation.
- Figure 5.37** EEG-ofMRI.
- Figure 6.1** CEST fMRI.
- Figure 6.2** Proof-of-principle of glutamate CEST MRI.
- Figure 6.3** Impact of the saturation pulse on the CEST effect.
- Figure 6.4** In-vivo CEST MRI.
- Figure 6.5** GluCEST MRI detects the reduction of Glu after KA-induced status epilepticus.
- Figure 6.6** CEST fMRI during epileptic seizures sampled with four saturation frequencies.
- Figure 6.7** CEST fMRI during epileptic seizures sampled with two saturation frequencies.
- Figure 6.8** CEST fMRI during low-frequency optogenetic stimulation.

List of Tables

- Table 4.1** Applied MR protocols.
Table 4.2 MRS results of 13 mice scanned before any treatment.
Table 4.3 Applied DW SE EPI protocols.
- Table 6.1** CEST MRI protocol.

List of Abbreviations

AD	Axial Diffusivity
ACQ	Acquisition
ADC	Apparent Diffusion Coefficient
AEDs	Anti-Epileptic Drugs
B.G.	Basal Ganglia
B ₀	Main Magnetic Field
B ₁	Radiofrequency Field
BOLD	Blood-Oxygen-Level-Dependent
BW	Bandwidth
C.C.	Cingulate Cortex
CA1-4	Cornu Ammonis
CBF	Cerebral Blood Flow
CBV	Cerebral Blood Volume
Cer.	Cerebellum
CEST	Chemical Exchange Saturation Transfer
Cho	Choline
ChR2	Channelrhodopsin 2
CMR _{Glc}	Cerebral Metabolic Rates of Glucose Consumption
CMR _{O2}	Cerebral Metabolic Rates of Oxygen Consumption
CO	Control
Cr	Creatine
CRLB	Cramér-Rao Lower Bounds
DBS	Deep Brain Stimulation
dfMRI	diffusion-fMRI
DG	Dentate Gyrus
DKI	Diffusion Kurtosis Imaging
DTI	Diffusion Tensor Imaging
dvD	dorso-ventral diffusivity
DWI	Diffusion Weighted Imaging
E.C.	Entorhinal Cortex
EEG	Electroencephalography
EPI	Echo Planar Imaging
ESP	Echo Spacing
ETL	Echo Train Length
F.C.	Frontal Cortex
FA	Fractional Anisotropy
FDR	False Discovery Rate
fMRI	functional MRI
FOV	Field of View
FWHM	Full Width at Half-Maximum
GABA	γ -Aminobutyric Acid
GCD	Granule Cell Dispersion
GCL	Granule Cell Layer
GE	Gradient Echo
GLM	General Linear Modelling
Gln	Glutamine
Glu	Glutamate
GluCEST	Glutamate CEST
Glx	Glutamate + Glutamine

HARDI	High Angular-Resolution Imaging
HC	Hippocampus
HRF	Hemodynamic Response Function
HS	Hippocampal Sclerosis
I.C.	Insular Cortex
ICA	Independent Component Analysis
IHC	Immunohistochemistry
Ins	myo-Inositol
KA	Kainate
Lac	Lactate
MD	Mean Diffusivity
ME	Multi Echo
MR	Magnetic Resonance
MRI	Magnetic Resonance Imaging
MRS	Magnetic Resonance Spectroscopy
MT	Magnetization Transfer
mTLE	mesial TLE
Myoi	myo-Inositol
NA	Number of Averages
NAA	N-Acetyl Aspartate
NMR	Nuclear Magnetic Resonance
O.C.	Occipital Cortex
ODF	Orientation Distribution Function
ofMRI	optogenetic-fMRI
OGSE	Oscillating Gradient Spin-Echo
P.C.	Parietal Cortex
PGSE	Pulsed Gradient Spin-Echo
PRESS	Point-Resolved Spectroscopy
r.f.	Radio Frequency
RARE	Rapid Acquisition with Relaxation Enhancement
RD	Radial Diffusivity
ROI	Region of Interest
rsfMRI	resting-state fMRI
SBA	Seed-Based Correlation Analysis
SE	Spin Echo
SE	Status Epilepticus
SNR	Signal to Noise Ratio
STEAM	Stimulated Echo Acquisition Mode
T.C.	Temporal Cortex
T ₁	Longitudinal or Spin-Lattice Relaxation Time
T ₂	Transversal or Spin-Spin Relaxation Time
T ₂ *	„effective“ T ₂
TC	Time Course
TE	Echo Time
Th	Thalamus
TLE	Temporal Lobe Epilepsy
TR	Repetition Time
tSNR	temporal SNR
V.C.	Ventral Cortex
vStr	ventral Striatum

The abbreviation “SE” appears twice with the meanings of “Spin Echo” and “Status Epilepticus”. This was not modified because both are well established in the respective community.

Own publications in peer-reviewed journals

Janz P*, **Schwaderlapp N***, Heining K*, Häussler U, Korvink JG, von Elverfeldt D, Hennig J, Egert U, LeVan P*, Haas CA*.

*contributed equally

Early tissue damage and microstructural reorganization predict disease severity in experimental epilepsy.

2017, eLife 6:e25742, 1-26. DOI: 10.7554/eLife.25742

Schmidt AB, Berner S, Schimpf W, Müller C, Lickert T, **Schwaderlapp N**, Knecht S, Skinner JG, Dost A, Rovedo P, Hennig J, von Elverfeldt D, Hövener JB.

Liquid-state carbon-13 hyperpolarization generated in an MRI system for fast imaging.

2017, Nature Communications 8(14535), 1-8. DOI:10.1038/ncomms14535

Hövener JB, Knecht S, **Schwaderlapp N**, Hennig J, von Elverfeldt D.

„Continuous re-hyperpolarization of nuclear spins using parahydrogen: theory and experiment“

2014, Chemical Physics and Physical Chemistry (ChemPhysChem) 15(12), 2451-2457.

DOI: 10.1002/cphc.201402177

Hövener JB, **Schwaderlapp N**, Borowiak R, Lickert T, Duckett SB, Mewis RE, Adams RW, Burns MJ, Highton LA, Green GG, Oлару A, Hennig J, von Elverfeldt D.

“Toward biocompatible nuclear hyperpolarization using signal amplification by reversible exchange: quantitative in situ spectroscopy and high-field imaging.”

2014, Analytical Chemistry 86(3), 1767-1774. DOI: 10.1021/ac403653q

Hövener JB, **Schwaderlapp N**, Lickert T, Duckett SB, Mewis RE, Highton LA, Kenny SM, Green GG, Leibfritz D, Korvink JG, Hennig J, von Elverfeldt D.

“A hyperpolarized equilibrium for magnetic resonance.”

2013, Nature Communications 4(2946), 1-5. DOI: 10.1038/ncomms3946

Borowiak R, **Schwaderlapp N**, Huethe F, Lickert T, Fischer E, Bär S, Hennig J, von Elverfeldt D, Hövener JB.

„A battery-driven, low-field NMR unit for thermally and hyperpolarized samples.“

2013, Magnetic Resonance Materials in Physics, Biology and Medicine (MAGMA)

26(5),491-499. DOI: 10.1007/s10334-013-0366-7

International Talks & Conference Contributions, selection

- 2019 Invited Talk at the “10th Krakow Workshop on Novel Applications of Imaging and Spectroscopy in Medicine, Biology and Material Sciences”. Title “Optogenetic-fMRI in experimental lobe epilepsy”. 23.09.2019
- 2017 Annual Meeting of the International Society for Magnetic Resonance in Medicine (ISMRM) in Honolulu, USA
Schwaderlapp, N., Janz, P., Leupold, J., von Elverfeldt, D., Korvink, J.G., Hennig, J., Haas, C.A. and LeVan, P. (2017). *Imaging of glutamate alterations in a mouse model of temporal lobe epilepsy*. Electronic poster presentation in session “Neuro: Animal Studies: Probing Disease”, Abstract #4092
- 2016 Annual Meeting of the International Society for Magnetic Resonance in Medicine (ISMRM) in Singapore.
Schwaderlapp N, Janz P, Häussler U, Korvink J, Elverfeldt D, Hennig J, Haas C, LeVan P, *MRI Monitoring of epileptogenesis with direct histological validation*. Talk in session “Epilepsy”, Abstract #0776
- 2015 Annual Meeting of the Organization for Human Brain Mapping (OHBM) in Honolulu, USA
Schwaderlapp N, Burak A, Beume L, Schmidt C, Hoeren M, Kaller C, Korvink J, Egger K, Urbach H, Weiller C, Hennig J, LeVan P,. *Dynamic resting-state fMRI connectivity reflects behavioral measures in stroke patients*. Talk in session “Neurological Disorders” and Poster, Abstract #1252
- 2015 Annual Meeting of the International Society for Magnetic Resonance in Medicine (ISMRM) in Toronto, Canada
Schwaderlapp N, Janz P, Leupold J, Häussler U, Lange T, Elverfeldt D, Haas C, Hennig J, Harsan LA, LeVan P,. *A longitudinal study of MR correlates during epileptogenesis in a mouse model of temporal lobe epilepsy*. Poster presentation in session “Epilepsy”, Abstract #1377
- 2013 Annual Meeting of the International Society for Magnetic Resonance in Medicine (ISMRM) in Salt Lake City, USA
Schwaderlapp N, Lickert T, Bär S, Hennig J, Elverfeldt D, Hövener J,. *Earth’s field MRI using continuous SABRE hyperpolarization*. Poster presentation in session “Hyperpolarized Contrast Agents”. Abstract #1924

Danksagung

Mein Dank gilt Jürgen Hennig und Jan Korvink für die Möglichkeit am Thema der Dissertation zu arbeiten und vor allem dabei frei zu forschen, unterschiedlichsten Ideen nachzugehen und so meinen weiteren wissenschaftlichen Weg zu finden. Ganz besonders möchte ich Pierre LeVan für die direkte Betreuung während dieser Zeit danken; für die Unterstützung, kritisches Feedback und seinen anhaltenden Optimismus, dass auch resting-state fMRI eines Tages funktionieren würde.

Des Weiteren möchte ich ganz herzlich Philipp Janz, Enya Paschen und Carola Haas danken für die über Jahre hinweg sehr gute und ergebnisreiche Kooperation. Ebenso danke ich Thomas Lange, vor allem für die Unterstützung bezüglich Spektroskopie zu Beginn meiner Arbeit, und Dominik v. Elverfeldt und der gesamten Medizin Physik für jegliche Unterstützung.

Niels Schwaderlapp